Impacts of Increasing Greenhouse Gas Concentrations and of Ozone Changes on the Atmospheric and Oceanic Circulation in the Southern Hemisphere

Dissertation

in fulfillment of the requirements for the Degree of

Doctor of Natural Sciences

(Dr. rer. nat)

to the **Faculty of Mathematics and Natural Sciences**

of the **Christian-Albrechts-Universität zu Kiel**

by

Ioana Ivanciu

Kiel, September 2022

Main Supervisor and First Examiner:	**Prof. Dr. Katja Matthes** GEOMAR - Helmholtz Centre for Ocean Research Kiel
Second Examiner:	**Prof. Dr. Mojib Latif** GEOMAR - Helmholtz Centre for Ocean Research Kiel Research Division: Ocean Circulation and Climate Dynamics Research Unit: Maritime Meteorology and Kiel University
Additional Supervisor:	**Prof. Dr. Arne Biastoch** GEOMAR - Helmholtz Centre for Ocean Research Kiel Research Division: Ocean Circulation and Climate Dynamics Research Unit: Ocean Dynamics and Kiel University
Date of Submission:	**16th of September 2022**
Date of Oral Examination:	**25th of November 2022**
Approved for Publication:	
Signature of the Dean:	**Prof. Dr. Frank Kempken**

Abstract

For over a century, anthropogenic activities have led to the release of greenhouse gases (GHGs) and ozone depleting substances (ODSs) into the atmosphere, having a profound impact on our climate system. Anthropogenic GHGs have warmed the troposphere, cooled the stratosphere and altered the meridional temperature gradient at the tropopause, leading to changes in dynamics. At the same time, anthropogenic emissions of ODSs led to ozone depletion and the development of the Antarctic ozone hole. Stratospheric ozone strongly absorbs solar radiation in the ultraviolet spectral band, warming the stratosphere. The development of the ozone hole therefore cooled the polar stratosphere, affecting the atmospheric dynamics in the Southern Hemisphere. As the threat that ozone depletion poses to human health was recognized, action has been taken through the Montreal Protocol, signed in 1987, and its amendments and adjustments to phase out ODSs. As a consequence, the ozone in the Antarctic stratosphere is expected to recover in the middle of this century and the effects of ozone depletion are expected to reverse. In contrast, GHG concentrations in the atmosphere continue to increase and, under the most extreme emission scenarios, the global surface temperature is predicted to increase by over 4°C compared to pre-industrial values.

The main aim of this thesis is to separate the effects of the increase in anthropogenic GHGs and of changes in stratospheric ozone on the atmospheric and oceanic circulation in the Southern Hemisphere during the second half of the twentieth century and the twenty-first century. These effects are studied for the first time in a state-of-the-art coupled climate model that includes both a module for interactively simulating the ozone chemistry and a high, eddy-resolving resolution in parts of the ocean. While the response of the Southern Hemisphere atmospheric circulation to the two forcings has been widely studied, so far the focus was on the changes occurring in the zonal mean. This thesis provides new insights into the future atmospheric circulation changes by analyzing their spatial patterns. It is found that the springtime stratospheric effect of the increase in GHGs exhibits a planetary wavenumber 1 structure with changes of opposite sign in the Eastern and Western Hemispheres. This pattern can be identified in several fields, such as temperature, zonal winds, or the flux of wave activity propagating from the troposphere. Another novel result of this thesis is that both ozone recovery and increasing GHGs drive a weakening of the Brewer-Dobson Circulation (BDC) in the Southern Hemisphere in November in the future. This contrasts the effect of the GHGs on the BDC during the rest of the year.

The response of the Southern Hemisphere oceanic circulation to GHGs and ozone changes is more uncertain than that of the atmospheric circulation. This is because a high resolution ocean is required to resolve the mesoscale features that are important for many processes

in the ocean and to accurately simulate changes in ocean circulation. Coupled climate models typically do not include such high resolution in their ocean components due to high computational costs. The nesting capabilities of the model used in this thesis allows for a compromise, whereby the ocean resolution is increased only in the areas of interest, namely the South Atlantic Ocean and the western Indian Ocean. This allows for the separation of the effects of increasing GHGs and of ozone recovery during the twenty-first century on the Agulhas Current System and on the Southern Ocean circulation, for the first time. The Agulhas leakage and the Antarctic Circumpolar Current (ACC) weaken in the future due to ozone recovery, but strengthen due to the increase in GHGs, with the GHG effect dominating under the high-emission scenario SSP5-8.5. However, as the ACC is in an ”eddy-saturated” state, the future ACC changes are rather small, with the total change at the end of the century representing 6% of the current-day ACC transport. This thesis clearly shows that although high-emissions of GHGs dictate the direction of change in the tropospheric and oceanic circulation, ozone recovery plays an important role by mitigating the changes due to GHGs.

A particular emphasis is placed on the Southern African region in this thesis, not just on the changes in the neighboring oceanic circulation, as mentioned above, but also on the changes in precipitation on land. Specifically, the influence of Rossby wave breaking (RWB) at tropopause levels on ridging highs over South Africa and the associated precipitation is studied. It is found that about 44% of ridging highs occur accompanied by RWB and that these ridging highs exhibit a different evolution and bring more precipitation over South Africa than those that occur in the absence of RWB. Furthermore, RWB appears to mediate the effect of increasing GHGs on ridging highs, with only ridging highs accompanied by RWB experiencing changes in the future. These findings represent novel results of this thesis.

A secondary aim of this thesis is to investigate the sensitivity of the simulated dynamical changes to how the ozone field is treated in simulations. To this end, simulations in which the ozone field is calculated interactively are compared to simulations in which the CMIP6 ozone field was prescribed. For both past and future, the effects of ozone changes are weaker and the effects of increasing GHGs are more dominant in the simulations in which the CMIP6 ozone field is prescribed. The differences between the simulated changes with interactive and with prescribed ozone highlight the uncertainties in future projections related to the ozone field, as the majority of the models used in CMIP6 for future projections prescribe the ozone field.

Overall, this thesis presents new insights into the future changes in the atmospheric and oceanic circulation in the Southern Hemisphere during the twenty-first century and underlines the uncertainties associated with the ozone field.

Zusammenfassung

Seit über einem Jahrhundert werden durch anthropogene Aktivitäten Treibhausgase (THG) und ozonabbauende Stoffe (ODS) in die Atmosphäre freigesetzt, was tiefgreifende Auswirkungen auf unser Klimasystem hat. Die anthropogenen THG haben die Troposphäre erwärmt, die Stratosphäre abgekühlt und den meridionalen Temperaturgradienten an der Tropopause verändert, was zu Veränderungen der Dynamik des Klimasystems führt. Gleichzeitig haben die anthropogenen Emissionen von ODS zum Ozonabbau und zur Bildung des antarktischen Ozonlochs geführt. Stratosphärisches Ozon absorbiert Sonnenstrahlung stark im ultravioletten Spektralbereich. Das Ozonloch kühlt dadurch die polare Stratosphäre ab, was sich auf die atmosphärische Dynamik in der südlichen Hemisphäre auswirkt. Da die Bedrohung des Ozonabbaus für die menschliche Gesundheit erkannt wurde, wurden im Rahmen des Montrealer Protokolls (1987) und der dazugehörigen Zusätze und Anpassungen Maßnahmen zum schrittweisen Ausstieg aus ODS ergriffen. Daraus resultierend wird sich das Ozonloch voraussichtlich in der Mitte dieses Jahrhunderts erholen. Es wird erwartet, dass sich die Auswirkungen des Ozonlochs dann wieder umkehren. Im Gegensatz dazu nehmen die Treibhausgaskonzentrationen in der Atmosphäre immer weiter zu. Unter dem extremsten Emissionsszenario wird ein globaler Temperaturanstieg von mehr als 4°C im Vergleich zum vorindustriellen Zeitraum projiziert.

Das Hauptziel dieser Arbeit ist es, die Auswirkungen des Anstiegs der anthropogenen THG und der Veränderungen des stratosphärischen Ozons auf die atmosphärische und ozeanische Zirkulation in der südlichen Hemisphäre in der zweiten Hälfte des zwanzigsten und im einundzwanzigsten Jahrhunderts zu separieren. Diese Auswirkungen werden zum ersten Mal in einem hochmodernen gekoppelten Klimamodell untersucht, das sowohl ein Modul zur interaktiven Simulation der Ozonchemie als auch eine hohe, wirbelauflösende Auflösung in Teilen des Ozeans umfasst. Die vergangene und künftige Reaktion der atmosphärischen Zirkulation der südlichen Hemisphäre durch THG und Ozon wurde bereits umfassend untersucht. Allerdings lag der Schwerpunkt auf den Veränderungen im zonalen Mittel. Diese Arbeit gibt völlig neue Einblicke in die zukünftigen Veränderungen der atmosphärischen Zirkulation, indem sie die räumlichen Muster dieser Veränderungen analysiert. Es zeigt sich, dass die Auswirkungen des Anstiegs der THG ein Muster aufweisen, das stark mit der geografischen Länge variiert. Dieses Muster ist durch eine planetarische Wellenzahl-1-Struktur mit Änderungen mit entgegengesetztem Vorzeichen in der östlichen und westlichen Hemisphäre gekennzeichnet. Dieses Muster lässt sich in mehreren Parametern erkennen, wie z.B. in der Temperatur, den zonalen Winden und dem Fluss der Wellenaktivität, die sich von der Troposphäre aus ausbreitet. Ein weiteres neues Ergebnis ist, dass sowohl die Erholung des

Ozons als auch die steigenden THG zu einer Abschwächung der Brewer-Dobson Zirkulation (BDC) in der südlichen Hemisphäre im November führen. Dieser Effekt ist entgegengesetzt des Einflusses der THG auf die BDC im restlichen Jahr.

Die Reaktion der Ozeanzirkulation der südlichen Hemisphäre auf Treibhausgas- und Ozonveränderungen ist unsicherer als die der atmosphärischen Zirkulation. Es ist eine hohe Auflösung des Ozeans erforderlich, um die mesoskaligen Merkmale aufzulösen, die für viele Prozesse im Ozean wichtig sind, und um Änderungen der Ozeanzirkulation genau zu simulieren. Gekoppelte Klimamodelle enthalten wegen der hohen Rechenkosten in der Regel keine derartig hochauflösenden Ozeankomponenten. Das gekoppelte Klimamodell, das in dieser Arbeit verwendet wird, ermöglicht einen Kompromiss, bei dem die Ozeanauflösung nur in dem Gebiet von Interesse, nämlich dem Südatlantik und dem westlichen Indischen Ozean, erhöht wird. Dies ermöglicht zum ersten Mal eine getrennte Betrachtung der Effekte des Treibhausgasanstiegs und der Erholung des Ozonlochs auf das Agulhasstromsystem und die Zirkulation im Südlichen Ozean im einundzwanzigsten Jahrhundert. Die Agulhas Leakage und der Antarktische Zirkumpolarstrom (ACC) schwächen sich in der Zukunft aufgrund der Erholung des Ozons ab. Gleichzeitig verstärkt sich aber beides aufgrund des Anstiegs der THG, wobei letzteres unter dem hohen Emissionsszenario SSP5-8.5 dominiert. Da sich der ACC jedoch in einem wirbelgesättigten Zustand befindet, sind die künftigen Änderungen des ACCs eher gering, wobei die Gesamtänderung am Ende des Jahrhunderts 6% des heutigen ACC-Transports ausmacht. Diese Arbeit zeigt deutlich, dass, obwohl hohe THG Emissionen die Richtung der Veränderungen in der troposphärischen und ozeanischen Zirkulation vorgeben, die Erholung des Ozons eine wichtige Rolle spielt, indem sie die durch THG verursachten Veränderungen abschwächt.

In dieser Arbeit wird ein besonderer Schwerpunkt auf die Region des südlichen Afrikas gelegt, und zwar nicht nur auf die oben erwähnten Veränderungen der benachbarten ozeanischen Zirkulation, sondern auch auf die Veränderungen des Niederschlags an Land. Insbesondere wird der Einfluss der brechenden Rossby-Wellen (RWB) an der Tropopause-Ebene auf ”Ridging Highs” über Südafrika und die damit verbundenen Niederschläge untersucht. Zu den neuen Ergebnissen gehört, dass etwa 44% der ”Ridging Highs” von RWB begleitet werden und dass diese ”Ridging Highs” eine andere Entwicklung aufweisen und mehr Niederschlag über Südafrika bringen als solche, die ohne RWB auftreten. Darüber hinaus scheint die RWB die Auswirkung zunehmender THG auf ”Ridging Highs” abzuschwächen: Nur ”Ridging Highs”, die von RWB begleitet werden, unterliegen Veränderungen während des einundzwanzigsten Jahrhunderts.

Ein sekundäres Ziel dieser Arbeit ist es, die Empfindlichkeit der simulierten dynamischen Veränderungen gegenüber der Art und Weise zu untersuchen, wie das Ozonfeld in

den Simulationen berücksichtigt wird. Zu diesem Zweck werden Simulationen, in denen das Ozonfeld interaktiv berechnet wird, mit Simulationen verglichen, in denen das CMIP6-Ozonfeld vorgeschrieben wurde. Sowohl für die Vergangenheit als auch für die Zukunft sind die Auswirkungen von Ozonveränderungen schwächer und die Auswirkungen zunehmender THG dominieren stärker in den Simulationen, in denen das CMIP6-Ozonfeld vorgegeben ist. Die Unterschiede zwischen den simulierten Veränderungen mit interaktivem und mit vorgegebenem Ozon verdeutlichen die Unsicherheiten bei künftigen Projekten im Zusammenhang mit dem Ozonfeld, inbesondere da der Großteil der Modelle in CMIP6 das Ozonfeld vorgibt.

Insgesamt bietet diese Arbeit neue Einblicke in die zukünftigen Veränderungen der atmosphärischen und ozeanischen Zirkulation in der südlichen Hemisphäre während des einundzwanzigsten Jahrhunderts und unterstreicht die Unsicherheiten im Zusammenhang mit dem Ozonfeld.

Motivation

Anthropogenic activities have had a profound effect on our climate system in the last decades. Emissions of greenhouse gases led to a pronounced warming of the troposphere and to significant changes in the atmospheric circulation. At the same time, emissions of ozone depleting substances, some of which also act as greenhouse gases, resulted in a decrease in stratospheric ozone. Nowhere has this decrease been so severe as over Antarctica, where unique meteorological conditions provided an environment in which enhanced depletion could occur, resulting in the formation of the ozone hole. Like the increase in anthropogenic greenhouse gases, the development of the ozone hole has been associated with a number of dynamical changes, extending from the stratosphere to the ocean in the Southern Hemisphere.

As a consequence of the ozone hole formation and of increasing concentrations of greenhouse gases, the polar vortex strengthened and its breakdown in spring was delayed, which in turn altered the propagation of planetary waves into the stratosphere, leading to a strengthening of the polar downwelling and of the meridional circulation in the stratosphere, the Brewer-Dobson circulation. As the Brewer-Dobson circulation transports ozone from its production regions at low latitudes towards mid- and high latitudes, its changes fed back onto the ozone field. This is also one of several ways in which the anthropogenic greenhouse gases that are not also ozone depleting substances impact the stratospheric ozone.

The changes in dynamics were not confined only to the stratosphere. In the troposphere, the westerly winds in the Southern Hemisphere intensified and shifted poleward accompanied by a shift toward the positive phase of the Southern Annular Mode and by a poleward expansion of the Hadley cell. Furthermore, the wind changes affected the oceanic circulation, from the Indo-Atlantic exchange of water, the Agulhas leakage, to the Southern Ocean overturning circulation. Consequently, the northern part of the Southern Ocean has warmed in the past decades, while the waters around Antarctica have cooled.

During the second half of the twentieth century, ozone depletion and increasing greenhouse gases drove dynamical changes in the same direction. However, the ozone hole is expected to recover during the twenty-first century as ozone depleting substances are being phased-out following the Montreal Protocol and its amendments and adjustments, while

greenhouse gas levels continue to increase. The primary aim of this thesis is to study how these two competing factors, namely ozone recovery and the continued increase in greenhouse gases, will affect the atmospheric and oceanic circulation in the Southern Hemisphere during the twenty-first century. A region of particular interest is Southern Africa and its adjacent oceans, a highly-populated region expected to experience important precipitation changes in the future. The Cape Basin at the tip of Africa contributes to the Indo-Atlantic exchange of warm and saline waters feeding the upper limb of the Atlantic Meridional Overturning Circulation, while also representing an important source of moisture for precipitation on land.

Although climate models generally agree that ozone depletion played a major role in past dynamical changes in the Southern Hemisphere, there is a large spread in the magnitude of the simulated changes. This is in part due to the ozone field used, as some models interactively simulate the ozone field, but the majority of the models participating in CMIP6 still prescribe it. For the models in the second category, the prescribed ozone field can be inconsistent with the simulated dynamics and neither feedbacks between ozone, temperature and dynamics nor the influence of greenhouse gases on ozone are simulated. Models in the first category simulate themselves a wide range of depletion magnitudes. A second aim of this thesis is to investigate the impact of the ozone field on the simulated changes by comparing simulations that include interactive ozone chemistry with simulations to which the ozone field used in CMIP6 is prescribed.

Table of contents

Chapter 1

Introduction

1.1 Greenhouse Gases and their Role in the Climate System

In 1856, Eunice Newton Foote discovered that carbon dioxide (CO_2), referred to as carbonic acid at the time, and water vapor warm more strongly than common air when exposed to sunlight. She was the first to prove that gases interact with radiation. As a result of her findings, Foote concluded that an atmosphere containing a higher proportion of CO_2 would be warmer (*Foote*, 1856). Due to her setup, Foote could not distinguish between solar and thermal radiation in her experiments. Three years later, John Tyndall performed a series of laboratory experiments that proved that gases such as water vapor, CO_2 and methane (CH_4) trap thermal radiation (*Tyndall*, 1859, 1861). Tyndall recognized that the atmosphere is more transparent to solar radiation than to the radiation "modified" by the Earth and that this trapping of radiation results in an accumulation of heat at the Earth's surface (*Tyndall*, 1859). He also noted that gases differ in their effect on radiation. The first calculation of the temperature change resulting from variations in atmospheric CO_2 was performed by Svante Arrhenius in 1896. Calculating the warming associated with different levels of increases and decreases in atmospheric CO_2 for each season and every 10° of latitude, he found, for example, a warming of 8 to 9°C in the Arctic for an increase in CO_2 by 2.5 to 3 times (*Arrhenius*, 1896). Arrhenius refined his calculation, stating in his 1908 book "Worlds in the making: the evolution of the universe", that a doubling of CO_2 would lead to a 4°C increase in the temperature of the Earth's surface. Based on the estimate that the atmosphere contains 0.03% CO_2 by volume, Arrhenius wrote that "comparatively unimportant variations in the composition of the air have a very great influence" (*Arrhenius* 1908, p. 52-53). Furthermore, he and his colleague, Arvid Högbom, knew already in 1896 that the industrial use of coal was adding CO_2 into the atmosphere. However, their focus was on explaining the occurrence of glacial periods and they did not recognize the problems associated with this increase

in CO_2. In fact, Arrhenius thought that this increase might be beneficial (*Fleming*, 1998). In addition, they thought that, taking industrial advances into account, the rate at which CO_2 is emitted would lead to a noticeable change in atmospheric CO_2 on timescales of a few centuries (*Arrhenius*, 1908). The first observations confirming that atmospheric CO_2 is indeed rising were performed by Charles David Keeling (*Keeling*, 1960). Since 1958, the record of atmospheric CO_2 measurements at the Mauna Loa Observatory in Hawaii started by Keeling is maintained by the Scrips Institution of Oceanography and bears the name "Keeling Curve" (Fig. 1.1).

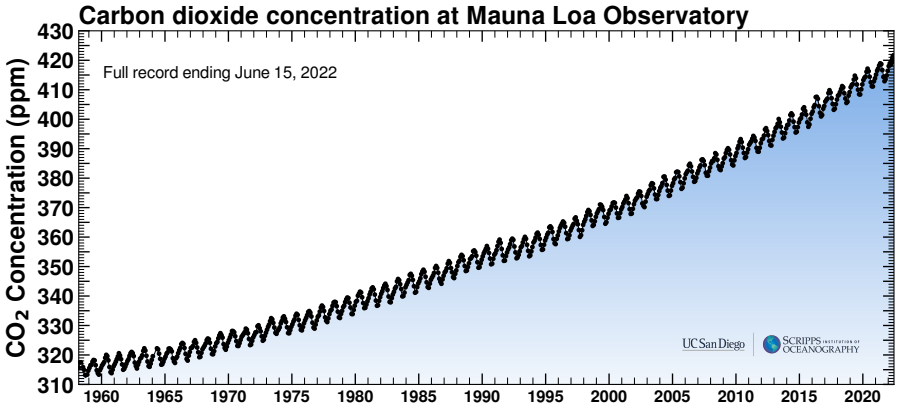

Fig. 1.1 The Keeling Curve showing CO_2 concentrations (ppm) at the Mauna Loa Observatory. Figure from the Scripps Institution of Oceanography.

It has been over a century and a half since Foote's observation that certain gases interact with radiation and have a warming effect. Nowadays, climate models and observations alike show the extent of the impact that the increase in such gases had on our climate system. This impact is limited not only to temperature changes, but encompasses a variety of changes in the atmospheric and oceanic dynamics (e.g., *IPCC*, 2013). The interaction between certain atmospheric constituents and radiation, resulting in warming, is now well understood and referred to as the greenhouse effect. It can be described as follows: the Earth receives its energy from the Sun in the form of solar radiation, also referred to as shortwave radiation due to the range of wavelengths that it covers, between 0.1 and 4 μm (*Petty*, 2006). 30% of the solar radiation is reflected back into space by the atmosphere and the Earth's surface, while the remaining 70% is absorbed (e.g. *Liou*, 2002). The Earth-atmosphere system emits, in turn, terrestrial or thermal radiation, also known as longwave radiation as it covers wavelengths in the infrared band, between 4 and 100 μm, that are longer than the wavelengths of solar radiation (*Petty*, 2006). Radiatively active gases in the atmosphere absorb thermal radiation and warm the atmosphere as a result. These gases are collectively referred to as greenhouse gases (GHGs).

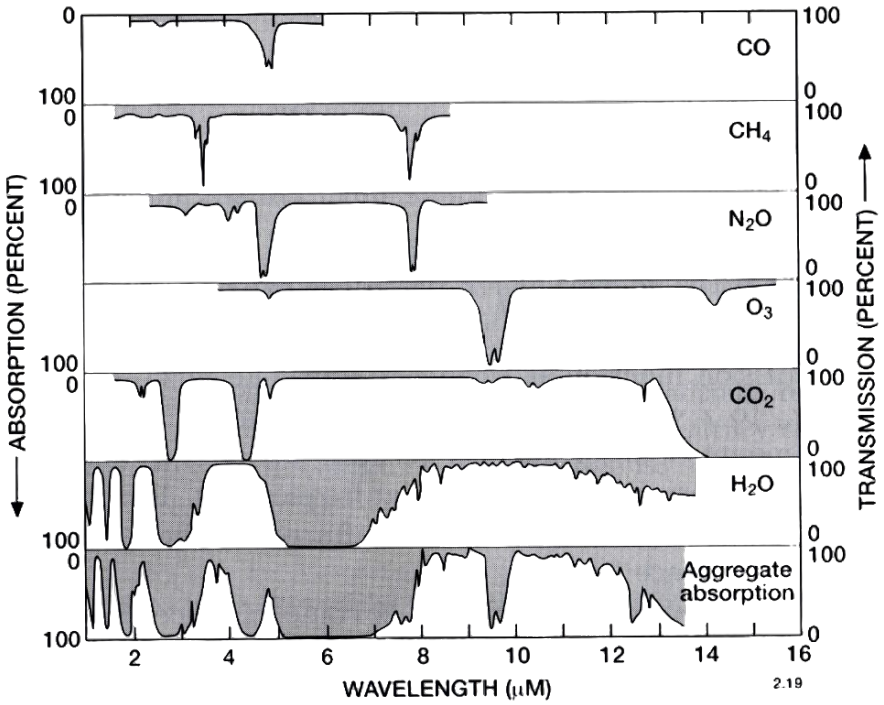

Fig. 1.2 Spectral distribution of the absorption bands for different greenhouse gases. The total absorption is shown in the lowermost panel. Figure from *Brasseur and Solomon* (2005).

The greenhouse effect is a naturally-occurring process that enables the existence of life on Earth by sustaining a surface temperature of 15°C. In the absence of greenhouse gases, the Earth's temperature would be much colder, -18°C (e.g., *Liou*, 2002). The most important natural GHG is water vapor, whose main absorption band in the infrared part of the spectrum is a broad band centered at 6.25 μm (Fig. 1.2) (*Liou*, 2002). Since the industrial revolution anthropogenic emissions of CO_2, CH_4 and other GHGs have led to a human-induced warming of the Earth's surface. This represents the anthropogenic greenhouse effect. Since the nineteenth century, the total surface temperature increase was estimated to be between 0.8°C and 1.3°C (*IPCC*, 2021). The largest contributor to this warming is CO_2. CO_2 exhibits two main absorption bands in the infrared part of the spectrum, centered at 4.3 and 15 μm (Fig. 1.2). While the 4.3 μm band is stronger, it contributes less to the anthropogenic greenhouse effect because it is located at the edge of the terrestrial band (*Petty*, 2006). In contrast, the 15 μm band is located near the wavelength of the maximum intensity of the terrestrial radiation (*Liou*, 2002) and is therefore very important. This band is particularly strong rendering the atmosphere opaque with respect to terrestrial radiation between 14 and 16 μm, as depicted in Fig. 1.2.

Although CO_2 has a net warming effect in the troposphere, in the stratosphere it has a net cooling effect instead (Fig. 1.3). As mentioned above, the CO_2 absorption band centered

at 15 μm is very effective, such that most of the radiation emitted at the Earth's surface is absorbed in the troposphere. This not only warms the troposphere, but it also implies that the radiation absorbed by CO_2 in the stratosphere originates from the upper levels of the troposphere, where temperatures are lower than at the surface. In the stratosphere, the temperature increases with altitude. As CO_2 also emits thermal radiation and as the emitted radiation depends on temperature according to the Plank function, the radiation emitted by CO_2 in the stratosphere will not be balanced by the absorbed radiation, resulting in net cooling. The cooling effect is strongest in the upper stratosphere, where the temperature is the highest (*World Meteorological Organization*, 2018). Longwave cooling due to CO_2 is the most important cooling term in the stratosphere (*Brasseur and Solomon*, 2005), as depicted in Fig. 1.3. Similarly, other GHGs also have a cooling effect in the upper stratosphere and their increase due to anthropogenic activities results in a cooling trend in the stratosphere. Due to the meridional variation in the height of the tropopause, the warming of the troposphere and the cooling of the stratosphere due to GHGs alters the meridional temperature gradient at tropopause levels. This, in turn, affects the strength of the westerly jet (e.g. *Barnes and Polvani*, 2013) and, as a result, the propagation of planetary waves from the troposphere into the stratosphere. These changes have a multitude of consequences for the atmospheric and oceanic circulation.

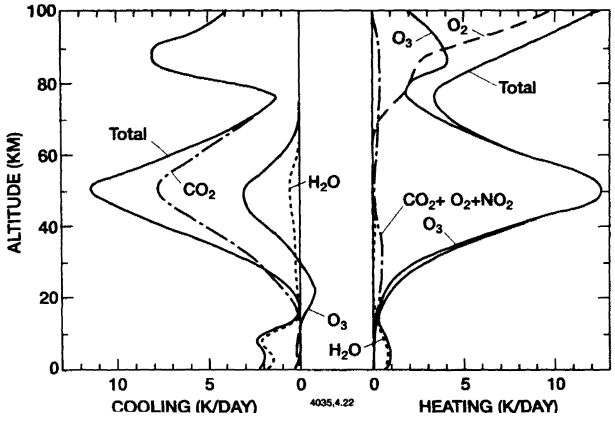

Fig. 1.3 Vertical profile of longwave cooling rates and shortwave heating rates. In the stratosphere, CO_2 has an important cooling effect, while ozone accounts for most of the heating. Figure from *Brasseur and Solomon* (2005).

In this thesis the effects of increasing levels of anthropogenic GHGs on the atmospheric and oceanic circulation in the Southern Hemisphere are investigated in a coupled climate model, both for the second half of the twentieth century and for the twenty-first century. These effects are compared to the effects of changes in stratospheric ozone concentrations and their contribution to the total circulation changes are assessed. For the twenty-first century,

the high emission scenario SSP5-8.5 is used. In this scenario, CO_2 concentrations equal 1135 *ppm* and the radiative forcing is 8.5 $W\ m^{-2}$ in 2100 relative to 1750 (*Meinshausen et al.*, 2020). For comparisson, in 2019 the CO_2 concentrations equaled 410 *ppm* and the radiative forcing was 3.3 $W\ m^{-2}$ relative to 1750 (*IPCC* 2021, see also Fig. 1.1).

1.2 Ozone and its Role in the Climate System

Ozone is an important atmospheric constituent as it is both chemically and radiatively active. 90% of all ozone is found in the stratosphere, with only 10% of total ozone found in the troposphere (Fig. 1.4), where it is a trace gas (*World Meteorological Organization*, 2018). In the troposphere, ozone acts as a pollutant, having a detrimental influence on human health and plants (*Brasseur et al.*, 1999). It is also a GHG, absorbing terrestrial infrared radiation in a band centered at 9.6 μm (Fig. 1.2) within the atmospheric window (*Fishman et al.*, 1979; *Brasseur et al.*, 1999). As variations in stratospheric ozone concentrations have wide-ranging consequences, not only for the atmospheric, but also for the oceanic dynamics (e.g., *Li et al.*, 2016; *Seviour et al.*, 2016), this thesis deals with the effects of stratospheric ozone changes, while tropospheric ozone is not discussed any further.

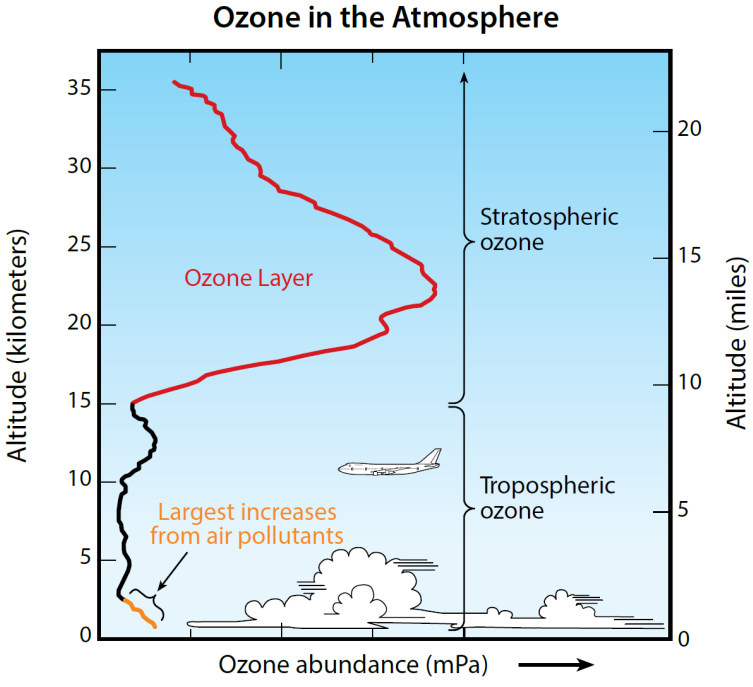

Fig. 1.4 Vertical profile of ozone, with the majority of ozone residing in the stratosphere in the ”ozone layer”. Ozone in the troposphere acts as a greenhouse gas and is increased by anthropogenic activities. Figure from *World Meteorological Organization* (2018).

In the stratosphere, ozone peaks at heights between 15 km and 35 km (Fig. 1.4). This is where the so-called "ozone layer" is located, although ozone is not residing in a single layer, but rather in a broad altitude range. Ozone in the stratosphere absorbs solar shortwave radiation in three main spectral regions: the Hartley band (200-310 nm), the Huggings bands (310-350 nm), both corresponding to the ultraviolet (UV) part of the spectrum, and in the Chappuis bands (410 and 750 nm), corresponding to the visible part of the spectrum (*Brasseur and Solomon*, 2005). Therefore, the stratospheric ozone protects life on Earth from harmful UV radiation. Through its absorption of shortwave radiation, ozone radiatively heats the stratosphere, representing the primary source of heat for the stratosphere (Fig. 1.3). The stratospheres owes its thermal structure, characterized by increasing temperature with height, and its resulting stability to the presence of ozone and its radiative heating (e.g., *Andrews et al.*, 1987).

Ozone is produced in the stratosphere in the presence of sunlight through the Chapman cycle, named after Sidney Chapman who was the first to propose a theory for the photochemical production and destruction of ozone. UV radiation is required for the photodissociation of oxygen molecules into oxygen atoms that subsequently react with molecular oxygen to form ozone. Ozone is destroyed through gas phase catalytic cycles involving chlorine, bromine, iodine, hydrogen and nitrogen (*Solomon* 1999 and references therein) and through heterogeneous chemical reactions occurring in polar regions, as described in Sect. 1.2.1. Because the formation of ozone requires sunlight, ozone is primarily formed at low latitudes in the stratosphere. However, the largest ozone abundance occurs at mid- to high latitudes. This latitudinal distribution of ozone, which varies seasonally, is owed to the transport of ozone by the Brewer-Dobson circulation (BDC, Sect. 1.3.1). This meridional circulation, consisting of an ascending branch in the tropics and a descending branch at mid- to high latitudes, transports ozone from its production regions in the tropics to high latitudes (e.g., *Butchart*, 2014). In fact, it was first discovered based on observations of ozone by *Dobson et al.* (1929) and of water vapor by *Brewer* (1949). The BDC is strongest in the winter hemisphere, therefore the largest amount of ozone is found at mid-latitudes in the Southern Hemisphere and at mid- and high latitudes in the Northern Hemisphere in spring, as ozone transported from the tropics accumulates there (Fig. 1.5). Despite the enhanced transport, Southern Hemisphere polar ozone exhibits a minimum in spring due to the formation of the ozone hole, which is discussed in the next section (Sect. 1.2.1).

1.2.1 The Ozone Hole

The ozone hole was discovered in 1985 by Joseph Farman, Brian Gardiner and Jonathan Shanklin, who observed a strong decline in total column ozone above the British Antarctic

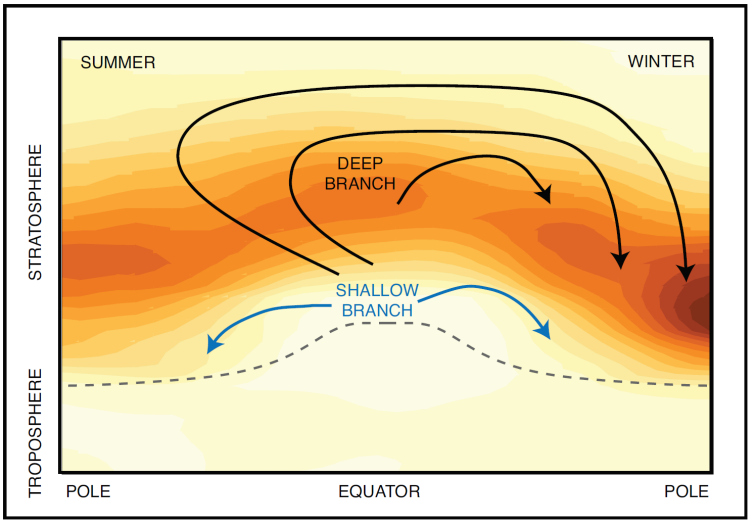

Fig. 1.5 Latitudinal distribution of ozone density (color shading, darker colors indicate higher values) and the branches of the Brewer-Dobson circulation at the solstices. The Brewer-Dobson circulation is strongest in winter, so the largest ozone values are found in the mid- and high latitudes in the winter hemisphere. Figure from *World Meteorological Organization* (2014).

Survey station at Halley Bay during spring (*Farman et al.*, 1985). The ozone hole is now a recurrent feature of the Antarctic stratosphere, forming every spring with the return of sunlight to the polar region (Fig. 1.6). *Farman et al.* (1985) suggested that chlorine chemistry in the cold Antarctic winter is responsible for the observed ozone decline. Subsequent laboratory, modeling and observational studies investigating the formation of the ozone hole (e.g., *Solomon et al.*, 1986), confirmed the results of *Farman et al.* (1985) and provided important insights into the processes responsible for ozone depletion over Antarctica.

The wintertime Antarctic stratosphere is characterized by unique conditions, with extremely low temperatures and a strong polar vortex that isolates polar air from the surrounding midlatitudes. These extremely low temperatures during winter precondition the Antarctic lower stratosphere for the formation of polar stratospheric clouds (*McCormick et al.*, 1982). Heterogeneous chlorine chemistry on the surface of these clouds results in more severe ozone depletion compared to that caused by homogeneous gas phase chemistry. The polar stratospheric clouds provide a reaction site for the reactions that release chlorine from its reservoir species. As the sunlight returns to the polar region in early spring, the activated chlorine depletes ozone, explaining the occurrence of the ozone hole over Antarctica in spring (*Solomon et al.*, 1986; *Solomon*, 1999).

Although severe ozone depletion events have been also observed in the Arctic during years characterized by a strong and persistent polar vortex (e.g., *Manney et al.*, 2011), ozone

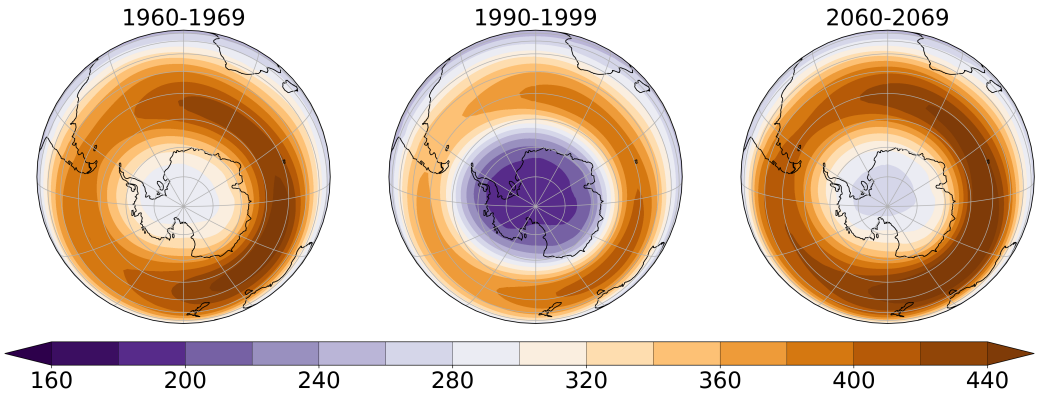

Fig. 1.6 Evolution of the ozone hole in the coupled climate model with ozone chemistry FOCI, depicted by the total column ozone (DU) in September for the 1960s, before depletion occurred, the 1990s, when depletion reached its maximum and the 2060s, when the ozone hole is predicted to recover.

depletion in this region is milder than in the Antarctic and there is no yearly recurrent ozone hole. The difference between the Arctic and the Antarctic occurs because more land masses are present in the Northern Hemisphere, leading to stronger topographic and thermal wave forcing. The wintertime Arctic stratosphere experiences more wave activity propagating from the troposphere, disturbing the polar vortex and enhancing polar downwelling. Consequently, temperatures within the Arctic polar vortex are higher than in the Antarctic and polar stratospheric clouds are less frequent (*McCormick et al.*, 1982). In addition, the exchange of polar and midlatitude air as the polar vortex is perturbed inhibits the accumulation of chlorine, in contrast to the Antarctic, and brings ozone-rich air to the polar region.

While ozone depletion is most pronounced within the Antarctic ozone hole, it is a global phenomenon of the last decades. It is caused by anthropogenic emissions of ozone depleting substances (ODSs, Box. 1.1), which are source gases of chlorine and bromine involved in the destruction of ozone. The emissions of ODSs increased sharply in the second half of the twentieth century triggering ozone depletion. Figure 1.6 shows the evolution of Antarctic total column ozone, which gives the vertically integrated ozone amount. In the 1960s, before ozone depletion began, the total column ozone was above 280 DU. By the 1990s, when the ozone hole reached its peak, total column ozone values dropped below 200 DU. The decline in ozone cooled the stratosphere and led to a variety of dynamical changes by altering the meridional temperature gradient in the lower stratosphere (e.g., *Gillett and Thompson*, 2003; *McLandress et al.*, 2010). These changes caused by ozone depletion are investigated in this thesis and compared to the changes induced by the increase in anthropogenic GHGs.

Box 1.1: Ozone Depleting Substances

Mario J. Molina and F. Sherwood Rowland were the first to recognize in 1974 that chlorofluorocarbons (CFCs), used as aerosol propellants and refrigerants, produce chlorine in the stratosphere and lead to the destruction of ozone (*Molina and Rowland*, 1974). Subsequently, more compounds were added to the list of ozone depleting substances (ODSs). ODSs are compounds containing chlorine and bromine that are broken up by UV radiation in the stratosphere releasing chemically active chlorine and bromine species that destroy ozone (*Solomon*, 1999). The substances currently controlled under the Montreal Protocol fall into the following groups: CFCs, methyl chloroform, carbon tetrachloride, hydrochlorofluorocarbons, halons and methylbromide. Additionally, hydrofluorocarbons (HFCs) were included on the list of controlled substances through the 2016 Kigali Amendment. HFCs are used as a replacement for CFCs as they do not lead to ozone destruction, but they are powerful GHGs (*World Meteorological Organization*, 2018).

ODSs have long atmospheric lifetimes, typically decades or even centuries, implying that they persist in the atmosphere and deplete ozone for a long time after emissions have ceased. There is a second category of chlorine- and bromine-containing substances harmful to ozone that is not regulated by the Montreal Protocol, termed very short lived substances (VSLS) due to their short atmospheric lifetimes, below 0.5 years. VSLS have both natural and anthropogenic sources and have increased in the past decades, contributing to abundances of stratospheric chlorine and bromine (*World Meteorological Organization*, 2018).

As the role played by ODSs in destroying the ozone layer gained recognition and concern was raised over the negative impacts of ozone depletion on human health and the environment, the Montreal Protocol (Box 1.2) was adopted. As a consequence of the Montreal Protocol and its amendments and adjustments, ODSs are being phased out and the ozone in the stratosphere is expected to recover to pre-depletion levels within the twenty-first century. The most recent Scientific Assessment of Ozone Depletion declared for the first time that the ozone hole has diminished in size and depth since 2000 (*World Meteorological Organization*, 2018). Model simulations with chemistry-climate models can be used to estimate when the stratospheric ozone concentrations will increase to pre-depletion values, known as the return date of stratospheric ozone from depletion. The Chemistry-Climate Model Initiative (CCMI) ensemble predicts that the Antarctic total column ozone will return to 1980 values in 2060, with a 1σ spread of 2055-2066 (*Dhomse et al.*, 2018). The latest estimate of ozone return date from the same ensemble uses a weighted multi-model mean that accounts for model

independence and performance and places the return of the Antarctic total column ozone to 1980 values in 2056, with a 95% confidence interval of 2052-2060 (*Amos et al.*, 2020).

Like ozone depletion, ozone recovery is expected to alter the thermal structure of the stratosphere and to drive dynamical changes. These changes are superimposed on the changes driven by increasing concentrations of GHGs that will become more pronounced as GHG concentrations continue to increase in the future. The effects of ozone recovery and increased GHGs on the Southern Hemisphere dynamics in the twenty-first century are separated and compared in this thesis.

1.2.2 Ozone Feedbacks

As a gas that is both chemically and radiatively active, ozone is involved in a series of feedbacks with the stratospheric temperature and dynamics, schematically shown in Fig. 1.7. Ozone has a net radiative warming effect in the stratosphere (e.g., *Gille and Lyjak*, 1986) and declining ozone levels lead to a cooling trend that maximizes at the stratopause (*Langematz et al.*, 2003). The gas phase chemical reactions that destroy ozone are temperature dependent and become less efficient at lower temperatures (*Haigh and Pyle*, 1982; *Jonsson et al.*, 2004). Consequently, the ozone-induced cooling slows down ozone depletion in a negative feedback. This feedback occurs in the middle and upper stratosphere. On the other hand, cooling in the lower stratosphere can bring temperatures below the threshold for polar stratospheric cloud formation, which leads to more ozone depletion in a positive feedback (*Austin et al.*, 1992).

In spring, the cooling of the polar lower stratosphere due to the formation of the ozone hole enhances the meridional temperature gradient between the cold high latitudes and the relatively warmer midlatitudes. According to the thermal wind balance this accelerates the westerly winds in the stratosphere, the polar night jet (Sect. 1.3.2), altering the propagation and dissipation of planetary waves from the troposphere. The background strength of the polar night jet controls whether planetary wave propagation is enhanced or inhibited (*Charney and Drazin*, 1961). For weak background westerlies, the propagation of planetary waves is enhanced, resulting in a stronger BDC and polar downwelling. A stronger BDC implies enhanced ozone transport to the polar region (e.g., *Li et al.*, 2009), while the stronger downwelling dynamically warms the polar cap (*Mahlman et al.*, 1994; *Manzini et al.*, 2003; *Keeble et al.*, 2014). Both of these effects lead to an increase in polar ozone, completing a negative feedback loop. Additionally, the cooling due to the ozone hole extends the lifetime of the polar vortex (*Waugh et al.*, 1999; *McLandress et al.*, 2010; *Keeble et al.*, 2014), which also promotes the propagation of planetary waves and ultimately increases ozone levels in a similar negative feedback (*Lin et al.*, 2017; *Haase et al.*, 2020). Instead, if the background westerlies are strong, the feedback is positive as the acceleration of the westerlies inhibits

planetary wave activity. The BDC is decelerated, transporting less ozone to the polar region, and the downwelling is weakened, dynamically cooling the polar cap.

Box 1.2: The Montreal Protocol

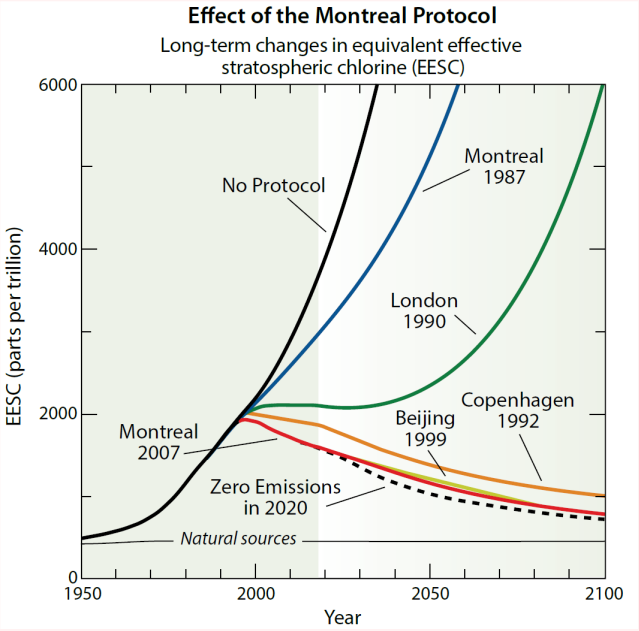

In 1985, by singing of the Vienna Convention for the Protection of the Ozone Layer, the states of the United Nations acknowledged the threat posed by the depletion of stratospheric ozone to human health and the environment and agreed to take protective measures against the harmful effects caused by ozone loss. However, the signatory states of the Vienna Convention were not obliged to pass regulation controlling the use of substances harmful for the ozone layer. The Montreal Protocol on Substances that Deplete the Ozone Layer, which was signed in 1987 and entered into force in 1989, and its subsequent amendments and adjustments control the total global emissions of anthropogenic substances that deplete the ozone layer with the ultimate goal of phasing them out. It is a landmark agreement whose objectives have been successfully met. The figure included in this box, taken from the *World Meteorological Organization* (2018), shows the projected effect of the Montreal Protocol and its amendments and adjustments in reducing ODSs, given as the change in equivalent effective stratospheric chlorine (EESC). Observations agree with these projections and show that EESC is declining, with values in the mid-latitudes having decreased by 18% in 2018 compared to their peak in 1996 (*World Meteorological Organization*, 2018). Consequently, the loss of ozone has leveled off and there are signs that a reversal in ozone trends has started to occur since the year 2000 in certain regions and seasons (*Solomon et al.*, 2016, 2017; *Banerjee et al.*, 2020). This contrasts estimates of the ”world avoided” by the Montreal Protocol obtained using chemistry-climate models that show that, in the absence of the Montreal Protocol, 67% of the 1980 global mean column ozone would be depleted by 2065 (*Newman et al.*, 2009), with values dropping to 100 DU or below in all regions (*Garcia et al.*, 2012).

1.2.3 Influence of Greenhouse Gases on Ozone

Anthropogenic activities affect the ozone in the stratosphere not only through ODSs, but also through the increase in GHGs. The effects of GHGs on ozone can be chemical, radiative or dynamical in nature and vary with latitude, altitude and season. They are schematically summarized in Fig. 1.7. As discussed in Sect. 1.1, CO_2 radiatively cools the stratosphere. Since the catalytic cycles involved in ozone depletion are less efficient at lower temperature (*Haigh and Pyle*, 1982; *Jonsson et al.*, 2004) this cooling slows down ozone depletion and accelerates ozone recovery (*Rosenfield et al.*, 2002; *Revell et al.*, 2012). This effect is important in the middle and upper stratosphere.

In the tropical lower stratosphere, the dynamical effects of increased GHGs influence ozone abundances. GHGs accelerate the BDC and tropical upwelling and therefore the transport of ozone out of the tropical lower stratosphere, leading to a decrease in ozone there (*Li et al.*, 2009; *Waugh et al.*, 2009a; *Chiodo et al.*, 2018). At the same time, the higher ozone abundances in middle and upper tropical stratosphere due to GHGs lead to less UV radiation penetrating to the lower stratosphere, which reduces ozone production and further decreases ozone abundances. This is known as the "reversed self healing" property of ozone (*Haigh and Pyle*, 1982; *Rosenfield et al.*, 2002; *Jonsson et al.*, 2004; *Portmann and Solomon*, 2007). These effects cause ozone abundances in this region to remain low even in the second half of the twenty-first century (*Li et al.*, 2009; *Waugh et al.*, 2009a; *Dhomse et al.*, 2018). The acceleration of the BDC due to GHGs additionally transports more ozone to the extratropics, where there is a general increase in ozone due to GHGs (*Li et al.*, 2009).

Methane and nitrous oxide (N_2O) increases cause ozone changes by affecting ozone chemistry. The increase in methane leads to increased water vapor content in the stratosphere, which results in more hydrogen oxide radicals that cause ozone depletion (*Portmann and Solomon*, 2007), on one hand, and cools the middle stratosphere slowing down ozone loss, on the other hand (*Fleming et al.*, 2011; *Revell et al.*, 2012). Methane also results in the conversion of chlorine from active to reservoir species, leading to an increase in ozone (*Fleming et al.*, 2011; *Revell et al.*, 2012). The net effect of increased methane is an increase in total column ozone (*Fleming et al.*, 2011; *Morgenstern et al.*, 2018). Nitrous oxide decays into nitrogen oxides in the stratosphere and therefore enhances ozone depletion through the catalytic ozone loss cycle involving nitrogen (*Portmann and Solomon*, 2007; *Revell et al.*, 2012).

These effects imply that the rate of increase in GHGs will influence the ozone return date (e.g., *Dhomse et al.*, 2018). At the same time, the effect of GHGs on ozone influences the response of the atmospheric circulation to the increase in GHGs, as the ozone changes induced by GHGs have thermal and dynamical effects that can offset some of the direct (i.e.

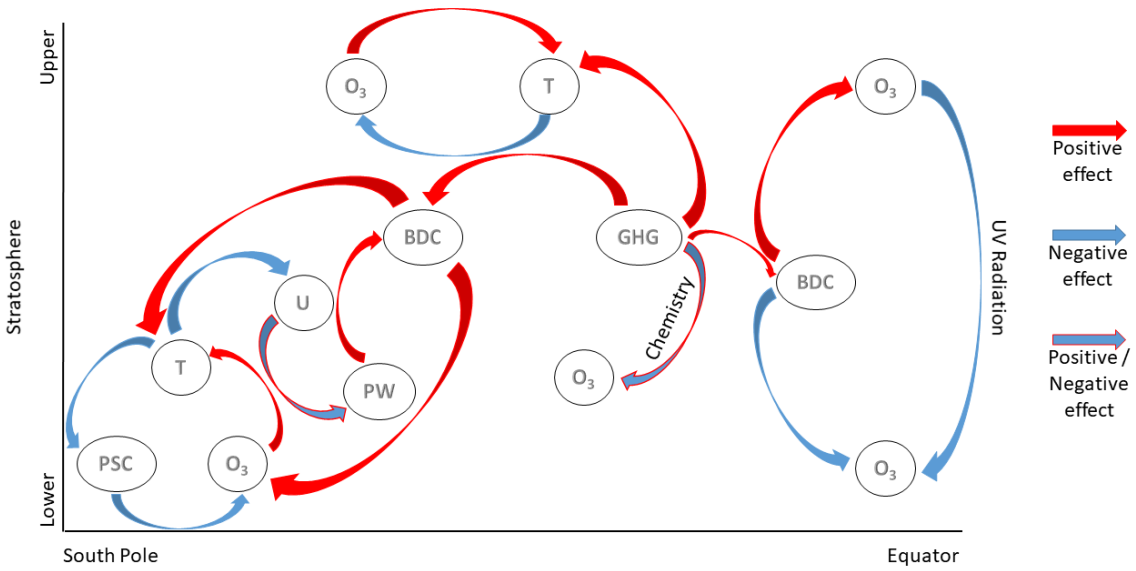

Fig. 1.7 Schematic of the chemical, thermal and dynamical effects and feedbacks that influence the stratospheric ozone and their approximate latitude and height. Note that greenhouse gases are present throughout the stratosphere and are placed in the middle for simplicity. The abbreviations are as follows: O_3 for ozone, GHG for greenhouse gases, T for temperature, U for zonal wind, PSC for polar stratospheric clouds, PW for planetary waves and BDC for Brewer-Dobson circulation. Red arrows depict positive effects, where an increase in one factor leads to an increase in another, blue arrows depict negative effects, where an increase in one factor leads to a decrease in another and blue arrows with red edges depict effects that can be both positive and negative. The effects are described in detail in Sections 1.2.2 and 1.2.3.

not mediated by ozone) effects of the increase in GHGs (*Morgenstern et al.*, 2014; *Chiodo and Polvani*, 2016). These factors need to be taken into account when the impacts of GHGs and ozone changes on the circulation are studied, as it is aimed in this thesis. As detailed in Chapter 2, the coupled climate model used in this thesis is capable of accounting for the connection between GHGs and ozone changes through the use of a module that computes the ozone chemistry interactively.

1.2.4 Ozone in Climate Models

The ozone field can be either prescribed or calculated interactively in climate models. The models that calculate the ozone field and other chemical constituents interactively are referred to as chemistry climate models (CCMs) and can be coupled to an ocean or not. Interactively

calculating the ozone field is computationally expensive, particularly for century-long climate model simulations, hence many models prescribe the ozone field instead. The details of how the ozone field is prescribed differs between climate centers and model generations. During Phase 3 of the Coupled Model Intercomparison Project (CMIP3) half of the models did not account for changes in stratospheric ozone at all, while the other half used prescribed ozone fields whose temporal and spatial structures were not documented (*Cordero and Forster*, 2006; *Son et al.*, 2008).

Following a series of studies that emphasized the large differences between models that do not take ozone changes into account and either models that do (*Perlwitz et al.*, 2008; *Son et al.*, 2008, 2010) or observations (*Cordero and Forster*, 2006), all the models participating in CMIP5 included time-varying ozone. While some CMIP5 models calculated the ozone chemistry interactively, others prescribed the International Global Atmospheric Chemistry (IGAC) and Stratosphere-Troposphere Processes and Their Role in Climate (SPARC) zonal mean, monthly mean ozone field (*Cionni et al.*, 2011) that did not vary according to the future GHG scenario used (*Eyring et al.*, 2013). Although it represented a clear improvement to the previous CMIP phase, this ozone dataset still presented several issues. The monthly averaging meant that the ozone field was linearly interpolated to the time step of the model to which it was prescribed. Several studies showed that this interpolation misses the extremes during the time of strong ozone changes, resulting in weaker ozone depletion and associated effects (*Sassi et al.*, 2005; *Neely et al.*, 2014; *Seviour et al.*, 2016). As the ozone hole is not centered over the polar cap (*Grytsai et al.*, 2007), the ozone field exhibits asymmetries in both zonal and meridional directions in reality. Prescribing a zonal mean ozone field excludes the zonal asymmetries. This was shown to affect both the mean state (*Crook et al.*, 2008; *Gillett et al.*, 2009) and the trends in the Southern Hemisphere atmospheric and oceanic circulation (*Waugh et al.*, 2009b; *Li et al.*, 2016; *Haase et al.*, 2020). Furthermore, as the chemical, thermal and dynamical effects of the increasing GHGs impact the ozone field as discussed in Sect. 1.2.3, using the same ozone field for all future emission scenarios is problematic. A part of the effect of the increased GHGs on the Southern Hemisphere dynamics is mediated by changes in ozone induced by the increased GHGs (*Morgenstern et al.*, 2014; *Morgenstern*, 2021; *Chiodo and Polvani*, 2016). If the ozone field is not sensitive to the amount of increase in GHGs, this indirect effect cannot be accurately captured. For example, in the study by *Chiodo and Polvani* (2016), the magnitude of the strengthening and poleward shift in the mid-latitude jet due to a quadrupling of CO_2 was smaller by 20% when the effect of the CO_2 change on the ozone field was considered compared to when it was ignored.

In CMIP6, the current phase of CMIP, there are still many models that prescribe the ozone field. The recommended ozone field for CMIP6 (*Hegglin et al.*, 2016) now includes

zonal ozone asymmetries and depends on the GHG emission scenarios. However, the increase in GHG used to generate this ozone field is not consistent with the SSPs used in CMIP6 (*Revell et al.*, 2022). Furthermore, it is still a monthly-mean field, implying that the temporal interpolation issues are still present. All the models that prescribe the ozone field are additionally not capable of capturing the feedbacks that occur between ozone, on one hand, and temperature and dynamics, on the other hand (Sect. 1.2.2). The lack of these feedbacks was shown to lead to differences in dynamics in both hemispheres between simulations with prescribed and simulations with interactive ozone (*Haase and Matthes*, 2019; *Haase et al.*, 2020). The 1969 - 1998 Antarctic lower stratospheric ozone-induced cooling was found to be weaker by about 1 K if these feedbacks are ignored (*Haase et al.*, 2020). Furthermore, an ozone field generated by CCMs and prescribed to other models, as performed in CMIP6, is neither spatially nor temporally consistent with the dynamics of these models, possibly also leading to differences between CMIP6 models with prescribed and with interactive ozone.

In light of the persistent issues with prescribing the ozone field in climate models, one of the aspects addressed by this thesis is whether there are substantial differences in the Southern Hemisphere climate simulated by a coupled climate model with interactive ozone chemistry and the same model to which the CMIP6 ozone field is prescribed.

1.3 Stratosphere, Troposphere and Ocean Dynamics and Interactions

This section introduces the aspects of the Southern Hemisphere circulation whose behavior under GHG and ozone forcing is studied in this thesis. The Brewer-Dobson circulation (BDC) in the stratosphere, the westerly winds in both stratosphere and troposphere and the Southern Ocean circulation are presented. These circulations are not independent of each other, with changes in one impacting the other. For example, the strength of the stratospheric westerlies affects the propagation of waves into the stratosphere (e.g., *Charney and Drazin*, 1961), whose dissipation drives the BDC (e.g., *Holton et al.*, 1995). Changes in the BDC also impact the westerly winds by altering the meridional temperature gradient, either directly via dynamical heating or indirectly through the transport of ozone (e.g., *Butchart*, 2014). The stratospheric and tropospheric westerlies are linked, with changes in the former extending down to the latter. The surface winds, in turn, affect the exchange of momentum, heat and freshwater between the atmosphere and the ocean. The Southern Ocean and the Agulhas Current System are responding to changes in the surface westerly winds (e.g., *Biastoch et al.*,

2009; *Seviour et al.*, 2016). The Agulhas System will be introduced in Sect. 1.4, which is dedicated to the Southern African region.

1.3.1 The Brewer-Dobson Circulation

The Brewer-Dobson circulation is the meridional overturning circulation in the stratosphere, characterized by ascending motion in the tropics, poleward transport and descending motion at mid- and high latitudes (Fig. 1.8). It is named after Alan Brewer and Gordon Dobson who were the first to infer such a circulation in the stratosphere from the distribution of water vapor and ozone, respectively (*Dobson et al.*, 1929; *Dobson*, 1956; *Brewer*, 1949). As seen in Fig. 1.8, the BDC consists of a shallow branch, which extends to the mid-latitudes in both hemispheres, and a deep branch, which reaches into the upper stratosphere and mesosphere and which extends to high latitudes (e.g., *Birner and Bönisch*, 2011).

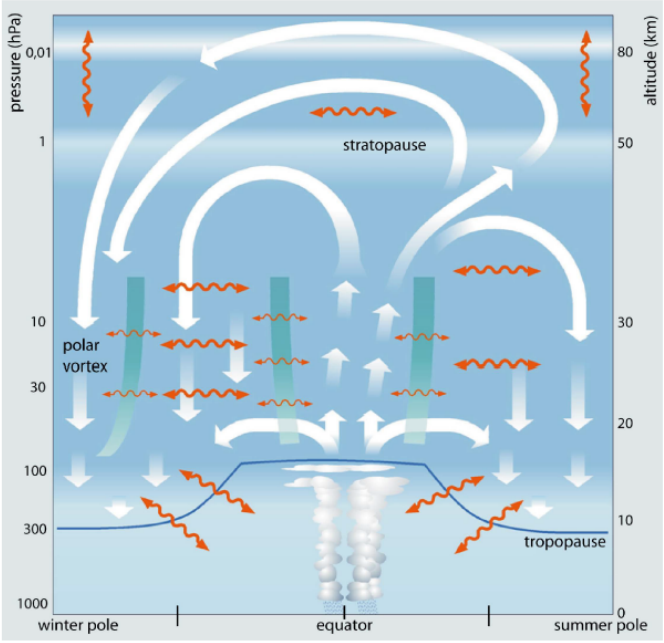

Fig. 1.8 Schematic of the Brewer-Dobson circulation comprising the residual-mean circulation (white arrows) and two-way mixing (red arrows). The green vertical lines depict transport barriers and the blue line depicts the tropopause. The shallow branches of the circulation are present in both hemispheres, while the deep branch occurs in the winter hemisphere. Figure from *Bönisch et al.* (2011).

The BDC is responsible for transport of trace chemical species within the stratosphere and between the troposphere and the stratosphere. This is achieved via a residual-mean circulation (white arrows in Fig. 1.8) and via two-way isentropic mixing (wavy red arrows in Fig. 1.8) (*Plumb*, 2007). Both of these processes are driven by atmospheric waves. Atmospheric

waves propagate upward from the troposphere into the stratosphere and break within their critical layers in a mid-latitude region known as the ”surf zone”, a process that implies the irreversible deformation of material contours (*McIntyre and Palmer*, 1983, 1984). In the stratosphere, the dominant waves are planetary-scale Rossby waves, with gravity waves also being important and dominating in the mesosphere (e.g., *McLandress and Shepherd*, 2009; *Oberländer et al.*, 2013). Planetary-scale wave breaking stirs air parcels along isentropic surfaces within the ”surf zone” (*Plumb*, 2002). Additionally, stirring due to synoptic-scale waves occurs in the subtropical lower stratosphere and above the subtropical jet (*Butchart*, 2014). Planetary wave breaking exerts a drag on the zonal mean circulation, which can be quantified via the Eliassen-Palm (EP) flux divergence (Box. 1.3). For Rossby waves, the drag resulting from their breaking is westward and the divergence of the EP flux is negative. This induces a meridional circulation by pumping air poleward, in a mechanism known as the ”Rossby-wave pump” (e.g., *Holton et al.*, 1995; *Plumb*, 2002). The resulting circulation is the residual-mean circulation, which transports air upward in the tropics, poleward and downward in the mid- and high latitudes. The residual circulation can be diagnosed in the transformed Eulerian-mean formulation (Box. 1.3). As Rossby waves can only propagate in westerly background flow, the processes associated with Rossby wave propagation and breaking in the middle stratosphere are confined to the winter hemisphere. Therefore, the deep branch of the BDC is present in the winter hemisphere. The lower branch is driven by planetary and synoptic-scale waves that break just above the subtropical jet and, as such, it is present in both hemispheres throughout the year (*Plumb*, 2002; *Birner and Bönisch*, 2011).

The BDC responds to changing concentrations of both GHGs and stratospheric ozone. Modeling studies all agree that increasing GHGs and the formation of the Antarctic ozone hole drive a strengthening of the BDC by altering the stratospheric wave drag (*Rind et al.*, 1990; *Butchart and Scaife*, 2001; *Li et al.*, 2008, 2018; *Garcia and Randel*, 2008; *Calvo and Garcia*, 2009; *Oman et al.*, 2009; *McLandress and Shepherd*, 2009; *McLandress et al.*, 2011; *Lin and Fu*, 2013; *Oberländer-Hayn et al.*, 2015; *Polvani et al.*, 2019; *Abalos et al.*, 2019, 2021). While changes in wave drag due to ozone depletion appear to be radiatively-driven through circulation changes, changes in tropical sea surface temperature (SST) play an important role in mediating the wave drag changes due to GHGs (*Oman et al.*, 2009; *Oberländer et al.*, 2013; *Chrysanthou et al.*, 2020). The simulated strengthening occurs for all branches of the BDC, but is weaker for the deep branch (e.g., *Lin and Fu*, 2013).

The BDC cannot be measured directly, but changes in its strength can be inferred from measurements of trace chemical species, using the mean age of air concept. The mean age of air represents the mean time that an air parcel has traveled since it entered the stratosphere at the tropical tropopause and it is a measure for the residual-mean circulation and two-way

Box 1.3: The Transformed Eulerian-Mean Formulation

The meridional circulation in the stratosphere is commonly diagnosed using the transformed Eulerian-mean formulation (e.g., *Andrews et al.*, 1987). In this formulation, a residual-mean meridional circulation is defined, whose meridional and vertical velocity components are given by:

$$\overline{v^*} = \overline{v} - \frac{\partial}{\partial p}\left(\frac{\overline{v'\theta'}}{\overline{\theta_p}}\right) \tag{1.1}$$

$$\overline{w^*} = \overline{w} + \frac{1}{a\cos\phi}\frac{\partial}{\partial \phi}\left(\frac{\cos\phi\,\overline{v'\theta'}}{\overline{\theta_p}}\right) \tag{1.2}$$

u and v are the zonal and meridional velocity components, respectively, a is the radius of the Earth, ϕ is the latitude, θ is the potential temperature and θ_p is the partial derivative of θ with respect to pressure. The overbars denote the zonal mean and the primes denote departures from the zonal mean. This circulation is driven by wave dissipation, which exerts a drag on the westerly mean flow. The wave drag can be expressed through the divergence of the Eliassen-Palm (EP) flux:

$$\nabla \cdot F = \frac{1}{a\cos\phi}\frac{\partial(F_\phi \cos\phi)}{\partial\phi} + \frac{\partial F_p}{\partial p} \tag{1.3}$$

whose components are:

$$F_\phi = -a\cos\phi\,\overline{v'u'} \tag{1.4}$$

$$F_p = fa\cos\phi\,\frac{\overline{v'\theta'}}{\overline{\theta_p}} \tag{1.5}$$

This formulation allows for the application of the downward control principle, which states that for steady-state conditions, the zonally average vertical motion across an isentropic surface is determined by the vertical integral of the wave forcing above (*Haynes et al.*, 1991). Therefore, the residual vertical velocity at a certain level can be obtained from the wave dissipation above that level.

mixing combined (e.g., *Butchart*, 2014). A stronger BDC transports air faster and therefore implies a shorter mean age of air. Trends in the strength of the BDC inferred from tracer observations tend to contradict simulated trends at least for the deep branch (*Engel et al.*, 2009, 2017), but such observations are sparse and do not exhibit a robust trend in the mean age of air. For the Northern Hemisphere mid-latitudes, *Engel et al.* (2009) reported that there

is no significant mean age of air trend for the period 1975-2005 and this remained valid when their observational record was update to 2016 (*Engel et al.*, 2017). Global mean age of air trends inferred from only a decade of satellite observations exhibit different signs depending on location and altitude (*Stiller et al.*, 2012). Reanalysis products exhibit a robust decrease in the mean age of air in the lower stratosphere in both hemispheres, implying that the shallow branch of the BDC has strengthened, but they do not agree on the sign of the change in the middle and upper stratosphere of the Northern Hemisphere (*Diallo et al.*, 2012; *Ploeger et al.*, 2019). In contrast, the multi-model mean of both CMIP6 and CCMI ensembles simulate negative mean age of air trends throughout the stratosphere and thus a strengthening in both branches of the BDC (*Abalos et al.*, 2021).

Changes in the advective part of the BDC can be obtained from temperature observations by separating the temperature changes into a radiative and a dynamical component, as performed by *Fu et al.* (2015, 2019). Based on satellite Microwave Sounding Unit observations of the temperature in the lower stratosphere, *Fu et al.* (2015, 2019) found that the annual mean BDC has strengthened, with contributions from both hemispheres. Reanalysis products show an acceleration of the residual circulation, with the exception of the ERA-Interim reanalysis, which instead shows a weakening of the residual circulation over the past decades (*Abalos et al.*, 2015; *Diallo et al.*, 2021). The CMIP6 and CCMI multi-model means also show an acceleration of both branches of the residual circulation (*Abalos et al.*, 2021).

Overall, while there is abundant evidence that the shallow branch of the BDC strengthened in the past decades, there are still uncertainties regarding the changes in the deep branch. In this thesis, both past and future changes in the BDC are investigated in a coupled climate model and the contributions of increasing GHGs and of changes in stratospheric ozone concentrations are separated. As the BDC transports both ozone and ODSs, among other trace species, changes in the BDC will impact ozone recovery. A stronger BDC leads to a decrease in lower stratospheric ozone in the tropics and an increase in the extratropics, as it transports ozone poleward faster (e.g., *Butchart*, 2014). At the same time, a stronger BDC results in a faster removal of CFCs from the atmosphere (e.g., *Butchart and Scaife*, 2001).

1.3.2 Westerly Winds in the Stratosphere and the Troposphere

Westerly jets are present in the atmosphere, from the subtropics to the high latitudes, both in the troposphere and in the stratosphere. Although anomalies in the stratospheric westerly jets descend to the tropospheric jets, with implications for weather and the oceanic circulation, the jets are driven by distinct processes and are characterized by different seasonalities and latitudinal distributions. This section presents a short characterization of the stratospheric

and tropospheric westerly jets (Fig. 1.9), clarifying the distinction between them and their interactions.

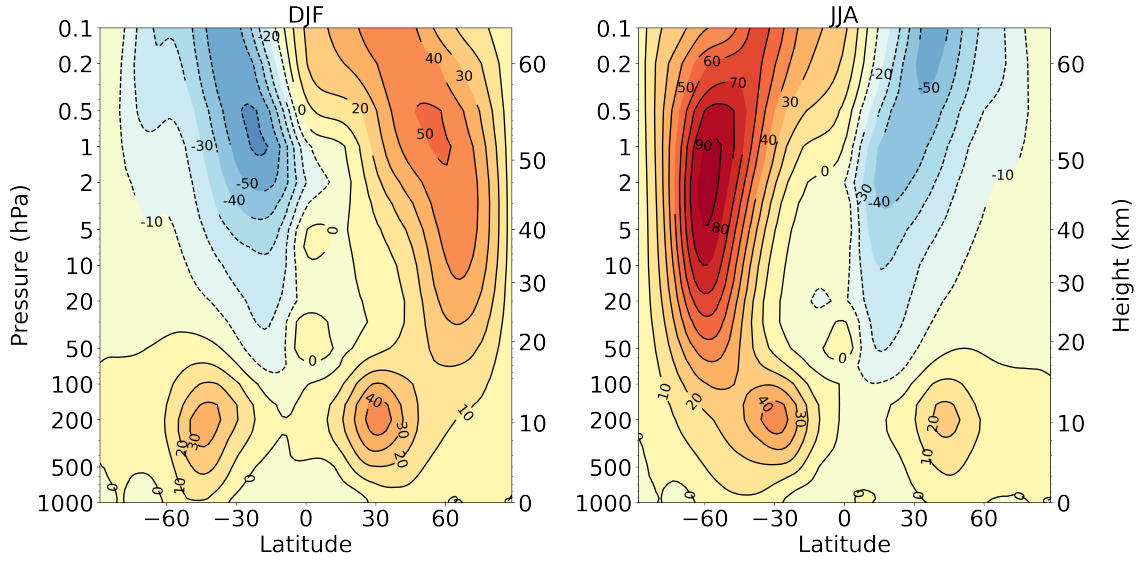

Fig. 1.9 Climatological zonal-mean zonal winds ($m\ s^{-1}$) in the coupled climate model FOCI during December-January-February (DJF) and June-July-August (JJA) for the time period 1958-2013. The polar night jet can be seen in the stratosphere in the winter hemisphere and the subtropical jets can be seen in the troposphere in both hemispheres.

The polar vortex occurs throughout the depth of the stratosphere in each hemisphere during the respective winter (e.g., *Palmer*, 1959). As solar radiation stops reaching the polar regions in autumn, the continuous emission of thermal radiation cools the polar regions resulting in a strong meridional temperature gradient. In accordance with the thermal wind balance, the meridional temperature gradient leads to the formation of a strong circumpolar westerly jet, known as the polar night jet (PNJ) (e.g., *Scherhag*, 1948; *Gutenberg*, 1949; *Schoeberl and Hartmann*, 1991; *Labitzke and van Loon*, 1999; *Waugh and Polvani*, 2010). The PNJ represents the boundary of the polar vortex and is centered around 60° S and N (e.g., *Waugh et al.*, 2017), peaking around the stratopause (e.g., *Schoeberl and Newman*, 2015), as seen in Fig. 1.9. The polar vortex is characterized by high potential vorticity (PV) values and a sharp PV gradient at its edge (e.g., *Waugh et al.*, 2017). This inhibits the mixing of heat and chemical species between the core of the vortex and the mid-latitudes (*Schoeberl and Hartmann*, 1991). The lack of mixing and the very low temperatures at its core make the polar vortex in the Southern Hemisphere an ideal environment for enhanced ozone depletion, leading to the formation of the Antarctic ozone hole, as discussed in Sect. 1.2.1. Ozone depletion is less severe in the Northern Hemisphere polar vortex, which is less stable and warmer.

The polar vortex in either hemisphere is disturbed by planetary-scale Rossby waves that are excited by land-sea thermal contrasts and by topography in the troposphere. These waves propagate upward into the stratosphere and break as they reach their critical layers (*Dickinson*, 1968), depositing their easterly momentum and decelerating the PNJ. The strength of the PNJ affects in turn the propagation of waves into the stratosphere and, consequently, the strength of the BDC. Because more land masses are present in the Northern Hemisphere, and hence stronger topographic forcing and thermal contrasts, the polar vortex there is more disturbed and therefore weaker and warmer than in the Southern Hemisphere (*Labitzke*, 1974; *Schoeberl and Hartmann*, 1991; *Labitzke and van Loon*, 1999; *Waugh and Polvani*, 2010; *Waugh et al.*, 2017). The interannual variability of the Arctic vortex is very large (e.g., *Labitzke*, 1977), much larger than that of the Antarctic vortex (e.g., *Labitzke and van Loon*, 1999; *Waugh and Randel*, 1999). During periods of enhanced wave activity propagation, the disturbances can be strong enough to cause a temporary break down of the polar vortex and a reversal of the meridional temperature gradient. These events, termed Sudden Stratospheric Warmings (SSWs), were discovered by *Scherhag* (1952) and occur with a frequency of about six per decade in the Northern Hemisphere (e.g., *Charlton and Polvani*, 2007), influencing the surface weather (e.g., *Baldwin and Dunkerton*, 2001) as well as upper-ocean variability (e.g., *Haase et al.*, 2018). In contrast, SSWs are rare in the Southern Hemisphere, with only one major SSW having occurred since the beginning of the observational record six decades ago (*Charlton et al.*, 2005; *Roscoe et al.*, 2005). Southern Hemisphere SSWs are predicted to become even rarer due to climate change in the future, as the polar vortex strengthens (*Jucker et al.*, 2021).

Another important difference between hemispheres is the timing of the peak in wave activity. While the Northern Hemisphere is most active and the polar vortex exhibits the largest variability during (boreal) winter (e.g., *Labitzke and van Loon*, 1999; *Waugh and Randel*, 1999), in the Southern Hemisphere the PNJ is too strong in winter to allow the propagation of planetary waves, which can only propagate in weak westerly background winds (*Charney and Drazin*, 1961). Wave activity peaks in (austral) spring instead, when the return of sunlight reduces the meridional temperature gradient and the PNJ weakens. The polar vortex eventually breaks down in spring and easterly winds take its place in summer (Fig. 1.9), as the polar region warms and the meridional temperature gradient reverses (e.g., *Schoeberl and Hartmann*, 1991; *Schoeberl and Newman*, 2015; *Waugh and Polvani*, 2010). The polar vortex in the Southern Hemisphere typically breaks down in November, while that in the Northern Hemisphere typically breaks down in March (*Labitzke and van Loon*, 1999; *Waugh and Randel*, 1999). Seen from the perspective of spring in the respective hemisphere, this represents a difference in the timing of the vortex break down of more than a month.

Ozone depletion during the last decades further delayed the break down of the Antarctic polar vortex by about two weeks (*Previdi and Polvani*, 2014).

In the troposphere, a subtropical and a polar front jet are often distinguished in the literature (e.g., *Lee and Kim*, 2003). The subtropical jet has its core at approximately 200 hPa and is centered around 30° S and N in winter, migrating poleward in summer (*Hartmann*, 2007) (Fig. 1.9). Its location corresponds to the poleward edge of the Hadley cell and it owes its existence to the angular momentum transport from the tropics due to the Hadley circulation (*Held and Hou*, 1980). This is balanced by the divergence of the eddy momentum flux at low latitudes (*Hartmann*, 2007). The polar front jet is driven by the convergence of eddy momentum flux in the mid-latitudes (*Panetta*, 1993). As such, it is also referred to as the eddy-driven jet. The two tropospheric jets cannot always be clearly distinguished from one-another, sometimes appearing as a single jet. While in winter the eddy-driven jet in the Southern Hemisphere reaches 60° S and is clearly separated from the subtropical jet located at 30° S, in summer a single jet appears at about 40° S (*Gallego et al.*, 2005).

The Southern Hemisphere eddy-driven jet experienced a poleward strengthening during the past decades due to the formation of the Antarctic ozone hole (e.g., *Thompson and Solomon*, 2002; *Gillett and Thompson*, 2003; *Polvani et al.*, 2011). This poleward shift manifested as a change towards the positive phase of the Southern Annular Mode (SAM), the leading mode of low-frequency variability in the extratropical Southern Hemisphere (*Thompson and Wallace*, 2000). The change in the tropospheric westerly winds extended to the surface, where it induced changes in ocean circulation. Sections 1.3.3 and 1.4.1 introduce the aspects of the ocean circulation that respond to changes in the Southern Hemisphere westerly winds.

The evolution of the stratospheric and tropospheric westerly jets in the Southern Hemisphere in the future is investigated in Chapter 4 of this thesis. As GHGs continue to increase, they are expected to have a stronger influence on the tropospheric jets and to compete with the influence of the recovering ozone hole. In addition, the effect of different ozone fields used in simulations on the magnitude of past and future changes in the westerly jets is studied in Chapters 3 and 4, respectively.

1.3.3 The Antarctic Circumpolar Current

The Antarctic Circumpolar Current (ACC) is the largest current system in the world (e.g., *Meredith et al.*, 2011) and connects all three major ocean basins, allowing for the existence of a global overturning circulation (e.g., *Rintoul and Naveira Garabato*, 2013). The ACC is driven by the Southern Hemisphere westerly winds, which blow at the surface of the Southern Ocean and input eastward momentum into the ocean, and by surface buoyancy fluxes (e.g.,

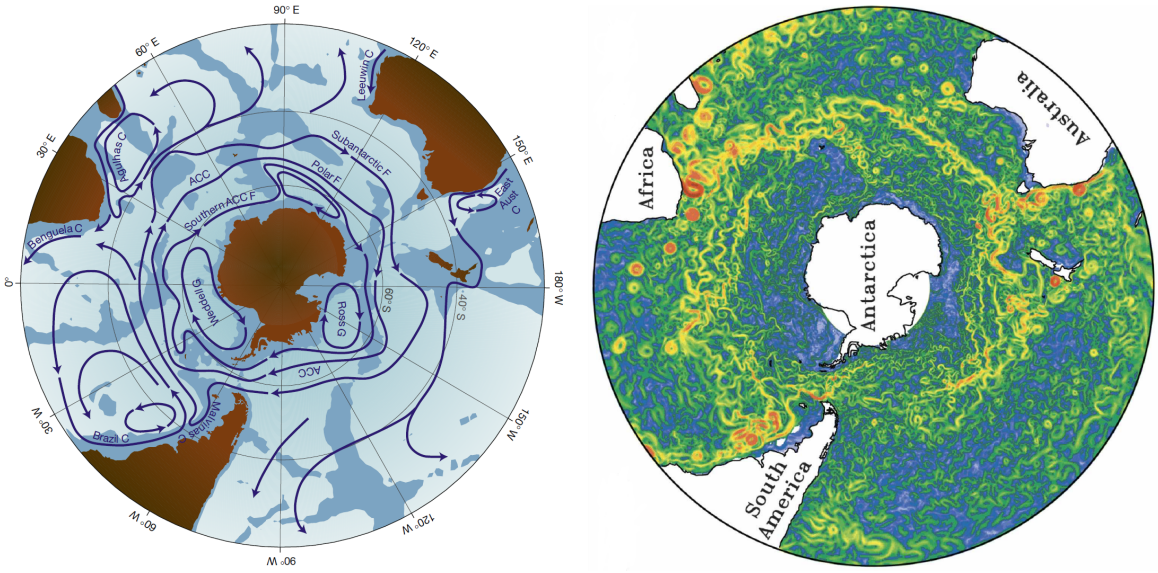

(a) (b)

Fig. 1.10 (a) The classical view of the Southern Ocean circulation with the three fronts of the ACC: the Subantarctic Front, the Polar Front and the Southern ACC Front. Figure from *Rintoul and da Silva* (2019). (b) The ACC surface speed modeled by a high resolution model. Figure from *Hallberg and Gnanadesikan* (2006).

Allison et al., 2010; *Hogg*, 2010; *Rintoul and Naveira Garabato*, 2013). Ocean eddies, which are abundant in the Southern Ocean are an important component of the circulation. They provide the poleward heat transport required to balance the heat loss to the atmosphere near Antarctica and the equatorward heat transport in the Ekman layer (e.g., *Rintoul et al.*, 2001). Eddies additionally transfer momentum from the surface downward. Unlike the other ocean basins, the Southern Ocean lacks a continental boundary in the Drake Passage. For this reason, the momentum imparted by the winds at the surface cannot be balanced by a zonal pressure gradient. In the Southern Ocean, the eastward momentum at the surface is instead balanced by bottom (topographic) form stress, which is related to the pressure difference across topographic ridges (*Munk and Palmén*, 1951). Within the water column, the vertical transfer of momentum from the surface, between different density layers and to the seafloor is achieved through interfacial form stress by standing and transient eddies (*Johnson and Bryden*, 1989; *Olbers et al.*, 2004; *Ward and Hogg*, 2011).

Traditionally, the ACC was thought to comprise three narrow, circumpolar fronts: the Subantarctic Front, the Polar Front and the Southern ACC Front (*Orsi et al.*, 1995), depicted in Fig. 1.10 a. As these fronts represent the boundaries between waters with different temperature and salinity signatures, they are associated with jets that result from the meridional density gradients. Newer observations and high resolution model simulations revealed

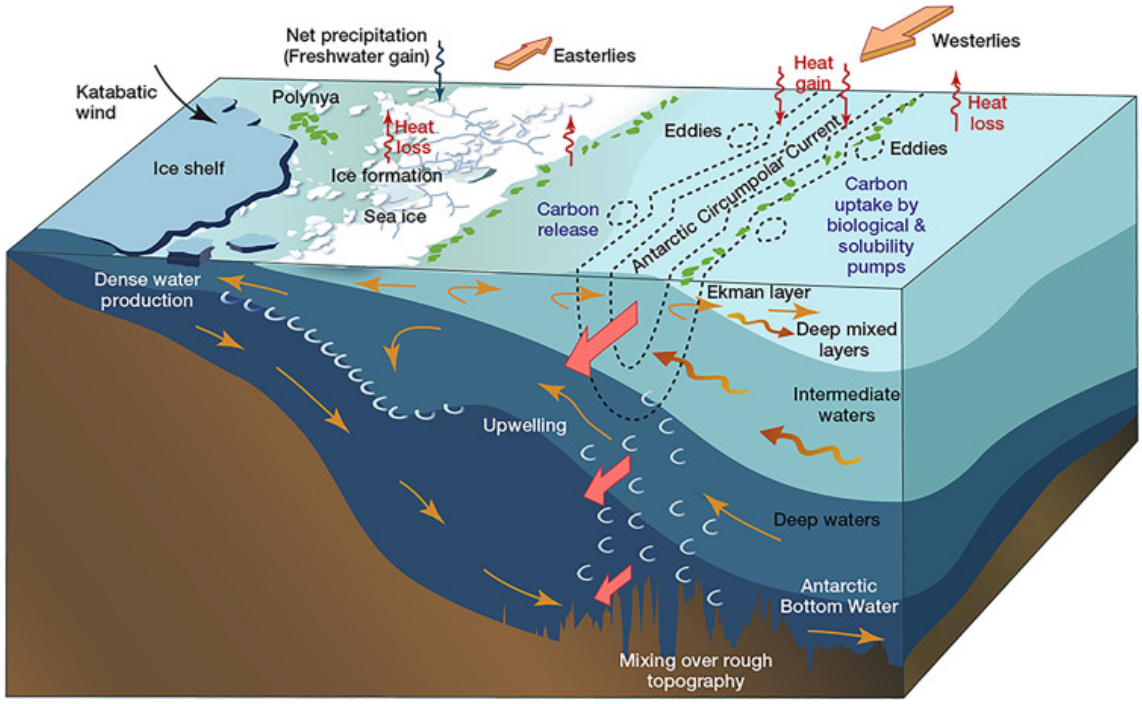

Fig. 1.11 Depth-longitude schematic of the Southern Ocean, with the eastward flowing ACC, upwelling of deep waters and their transformation processes involving heat and freshwater exchange with the atmosphere and brine rejection during sea ice formation (see text for details). The two cells of the Southern Ocean overturning circulation are depicted by the orange arrows. Figure from *Kennicutt et al.* (2019).

instead a complex structure, with the fronts comprising multiple jets that merge and diverge along the way (e.g., *Hughes and Ash*, 2001; *Hallberg and Gnanadesikan*, 2006; *Giglio and Johnson*, 2016), as seen in Fig. 1.10 b. The canonical value of the average absolute ACC transport through the Drake Passage is 133.8 Sv (1 Sv = 10^6 m^3 s^{-1}), with an error of up to 27 Sv (*Whitworth*, 1983; *Whitworth and Peterson*, 1985; *Cunningham et al.*, 2003). The latest absolute transport estimate based on observations with higher horizontal and temporal resolution raised this values by 30% to 173.3 $\pm$ 10.7 Sv (*Donohue et al.*, 2016). This absolute transport is composed of a baroclinic and a barotropic component. The baroclinic transport through the Drake Passage was estimated to be 136.7 $\pm$ 7.8 Sv by *Cunningham et al.* (2003) and 127.7 $\pm$ 1.0 Sv by *Chidichimo et al.* (2014). *Cunningham et al.* (2003) additionally provided the contribution of the three major fronts to this baroclinic transport: the Subantarctic Front transports 53 $\pm$ 10 Sv, the Polar Front transports 57.5 $\pm$ 5.7 Sv and the Southern ACC Front transports 9.3 $\pm$ 2.4 Sv, while a further 16 Sv are transported by the eddy field. The barotropic transport is 45.6$\pm$ 8.9 Sv (*Donohue et al.*, 2016).

Box 1.4: Eddy Saturation and Eddy Compensation

A strengthening of the Southern Hemisphere westerly winds increases the equatorward Ekman transport and the upwelling (downwelling) on the poleward (equatorward) side of the westerlies, leading to a steepening of isopycnals across the Southern Ocean. As the velocity of the ACC is linked to the meridional density gradient through the thermal wind relation, the transport of the ACC should increase in response to strengthened westerlies. Similarly, the intensified northward Ekman transport should strengthen the Southern Ocean overturning circulation. However, the increased tilt of the isopycnals implies an enhanced baroclinicity and therefore a more energetic eddy field, as hypothesized by *Straub* (1993) and confirmed by more recent studies (e.g., *Hallberg and Gnanadesikan*, 2006; *Meredith and Hogg*, 2006; *Meredith et al.*, 2012; *Marshall et al.*, 2017). As a result, the additional energy input from the winds is transferred to the eddy field, rather than acting to strengthen the ACC. The eddies act to flatten the isopycnals and transport heat poleward, opposing the direct effect of the wind strengthening (*Hogg et al.*, 2008; *Farneti et al.*, 2010; *Farneti and Delworth*, 2010; *Meredith et al.*, 2012). Therefore, the strengths of the ACC and of the overturning do not increase proportionally with the strengthening of the winds (*Hallberg and Gnanadesikan*, 2006; *Farneti et al.*, 2010). For the ACC, this effect is termed ”eddy saturation”, as there is little change in the ACC transport in response to wind changes. The overturning circulation exhibits some change, but less than expected from the increase in Ekman transport, so the effect on the overturning circulation is termed ”eddy compensation” (e.g., *Gent*, 2016).

The transport of the ACC may be impacted by remote processes that affect the global pycnocline and therefore the slope of isopycnals across the ACC, such as remote diapycnal mixing (*Munday et al.*, 2011) or the rate of deep water formation in the North Atlantic (*Fučkar and Vallis*, 2007). The flow of the ACC is related via the thermal wind balance to the steep isopycnals in the Southern Ocean, which outcrop on the poleward flank of the current, where upwelling of deep waters occurs (Fig. 1.11). These deep waters are Lower Circumpolar Deep Water (LCDW), a successor of North Atlantic Deep Water (NADW), and Upper Circumpolar Deep Water (UCDW), which forms due to deep mixing within the Indian and Pacific Oceans (*Rintoul and Naveira Garabato*, 2013). Their upwelling is part of the Southern Ocean overturning circulation, which is characterized by two counter-rotating cells (Fig. 1.11) and which is interlinked with the flow of the ACC. Within the lower cell, LCDW spreads southward and upwells close to Antarctica, where heat loss to the cold atmosphere and brine rejection during sea ice formation in the marginal seas of the Southern Ocean, as

well as deep diapycnal mixing, transform it into Antarctic Bottom Water (AABW) (*Lumpkin and Speer*, 2007; *Marshall and Speer*, 2012). AABW then spreads equatorward, closing the lower cell. UCDW upwells within the ACC and, under the influence of surface heat and freshwater fluxes, is transformed into the lighter Antarctic Intermediate Water (AAIW) and Subantarctic Mode Water (SAMW), which spread equatorward (*Speer et al.*, 2000; *Marshall and Speer*, 2012; *Rintoul and Naveira Garabato*, 2013). The circulation arising from the poleward flowing UCDW and equatorward flowing AAIW and SAMW represents the upper cell of the Southern Ocean overturning circulation. Within the Eulerian frame of reference, the westerly winds and the resulting northward Ekman transport drive an overturning cell with upwelling to the south and downwelling to the north of the wind maximum, the Deacon Cell (e.g., *Döös and Webb*, 1994). This circulation is opposed by an eddy-driven circulation, as a result of baroclinic instability in the ACC (e.g., *Marshall and Radko*, 2003). The sum of the Eulerian and the eddy-driven circulation gives the residual circulation, which is characterized by upwelling along isopycnals and gives the net heat transport (*Abernathey et al.*, 2011; *Marshall and Speer*, 2012).

The westerly winds and surface buoyancy fluxes influence the tilt of the isopycnals across the ACC and, at the same time, the rate of water mass transformation, affecting the Southern Ocean overturning circulation. As such, changes in either factor has implications for both the ACC and the overturning circulation. The westerly winds in the Southern Hemisphere have experienced a strengthening and poleward shift in the past decades, driven primarily by the formation of the Antarctic ozone hole, with a secondary contribution from the increase in anthropogenic GHGs (e.g., *Thompson et al.*, 2011). Some studies using coarse resolution models have argued that this led to a strengthening and poleward shift of the ACC, accompanied by enhanced overturning (*Fyfe and Saenko*, 2006; *Ferreira et al.*, 2015; *Solomon et al.*, 2015). However, *Hallberg and Gnanadesikan* (2006) showed that in contrast to coarse resolution models, in models that resolve the mesoscale eddy field, the Southern Ocean is in an "eddy-compensated" state, while the ACC is "eddy-saturated" (Box 1.4). This means that the residual circulation exhibits much smaller changes than expected from the increase in Ekman transport and that the ACC is relatively insensitive to the wind changes. These results have been confirmed by subsequent modeling studies (*Farneti et al.*, 2010; *Farneti and Delworth*, 2010; *Meredith et al.*, 2012; *Morrison and Hogg*, 2013; *Munday et al.*, 2013) and observations (*Böning et al.*, 2008) and imply that changes in the ACC and the overturning circulation in coupled climate models, which do not typically resolve mesoscale eddies, should be interpreted with caution. The representation of "eddy compensation" in such models can be improved if a variable eddy diffusivity coefficient is used in the *Gent and Mcwilliams* (1990) eddy parametrization (*Gent*, 2016). Still, this

class of models, which includes the models used in CMIP6, is inferior to high resolution, mesoscale-resolving models with respect to the representation of the changes in the ACC and the overturning circulation.

The past strengthening of the westerly winds and the associated oceanic circulation changes additionally affected the SST and heat content in the Southern Ocean. Observations show that the waters of the ACC have warmed and freshened since 1960 (*Böning et al.*, 2008). The SST exhibits a two-step response to the strengthening of the westerlies: an initial cooling driven by the enhanced northward Ekman transport as a fast response, followed by large-scale warming as a slow response (*Hogg et al.*, 2008; *Ferreira et al.*, 2015; *Seviour et al.*, 2016, 2019). Studies do not agree, however, on the drivers of the slow response. *Hogg et al.* (2008) attribute the warming to an enhanced southward eddy heat flux as eddy activity increases with a lag of two to three years (*Meredith and Hogg*, 2006). *Ferreira et al.* (2015) and *Seviour et al.* (2016) argue that the warming occurs due to enhanced upwelling of warmer waters from below. *Seviour et al.* (2016) also acknowledges a potential role played by changes in cloud cover and precipitation driven by changes in the storm tracks.

In Chapter 4 of this thesis, the response of the Southern Ocean temperature and of the ACC transport to the recovery of the Antarctic ozone hole and to increasing GHGs during the twenty-first century is investigated. As indicated above, the induced changes in the Southern Hemisphere westerly winds are an important driver of changes in ocean circulation. The coupled climate model employed includes a nest with 0.1° resolution over the South Atlantic and western Indian Ocean. The mesoscale eddies are therefore in part resolved. In addition, the two-way nesting technique (*Debreu et al.*, 2008) used in the model ensures that the rest of the ocean receives information about the fine-scale state of the nest. For the global ocean with a resolution of 0.5°, an eddy parametrization (*Gent and Mcwilliams*, 1990) with a temporally and horizontally varying coefficient is used. For these reasons, the model is expected to simulate the eddy effects more accurately than the CMIP6 class of climate models.

1.4 The Southern African Region

The Southern African region will receive particular attention in this thesis. This highly populated region is among the regions predicted to experience the largest decrease in precipitation during the twenty-first century (*IPCC*, 2021). The ocean around Southern Africa is home to the Agulhas Current, the largest western boundary current in the Southern Hemisphere. Around the southern tip of Africa, the leakage of Agulhas waters transport Indian Ocean waters into the Atlantic Ocean, in the larger of the two routes that supply waters to the upper limb of the Atlantic Meridional Overturning Circulation (AMOC) (e.g., *Rühs et al.*, 2019).

At the same time, the warm waters of the Agulhas System are associated with large heat and moisture fluxes into the atmosphere (e.g., *Lee-Thorp et al.*, 1999), playing an important role for precipitation on land. This section introduces the ocean circulation around Southern Africa and the atmospheric processes relevant for precipitation on land.

1.4.1 The Agulhas Current System

The Agulhas Current flows southwestward along the eastern coast of South Africa and is the western boundary current in the subtropical gyre of the Indian Ocean (Fig. 1.12). As such, it transports warm and saline waters poleward. It draws its waters from the recirculation in the South-West Indian Ocean subgyre, from the Mozambique Channel and from the east of Madagascar (*Stramma and Lutjeharms*, 1997; *De Ruijter et al.*, 1999a; *Lutjeharms*, 2007). The warm Agulhas Current is characterized by high heat and moisture fluxes into the atmosphere (*Lee-Thorp et al.*, 1999), exerting an important influence on rainfall over neighboring South Africa (*Jury et al.*, 1993; *Reason*, 2001; *Nkwinkwa Njouodo et al.*, 2018, 2021), as detailed in Sect. 1.4.2. Three years of observations of the Agulhas Current at 34°S placed its mean transport between 77 ± 5 and 84 ± 11 Sv and revealed that the Agulhas Current exhibits an annual cycle with an amplitude of 10 Sv, being strongest during austral summer (*Beal et al.*, 2015). As such, the Agulhas Current is the strongest western boundary current in the Southern Hemisphere.

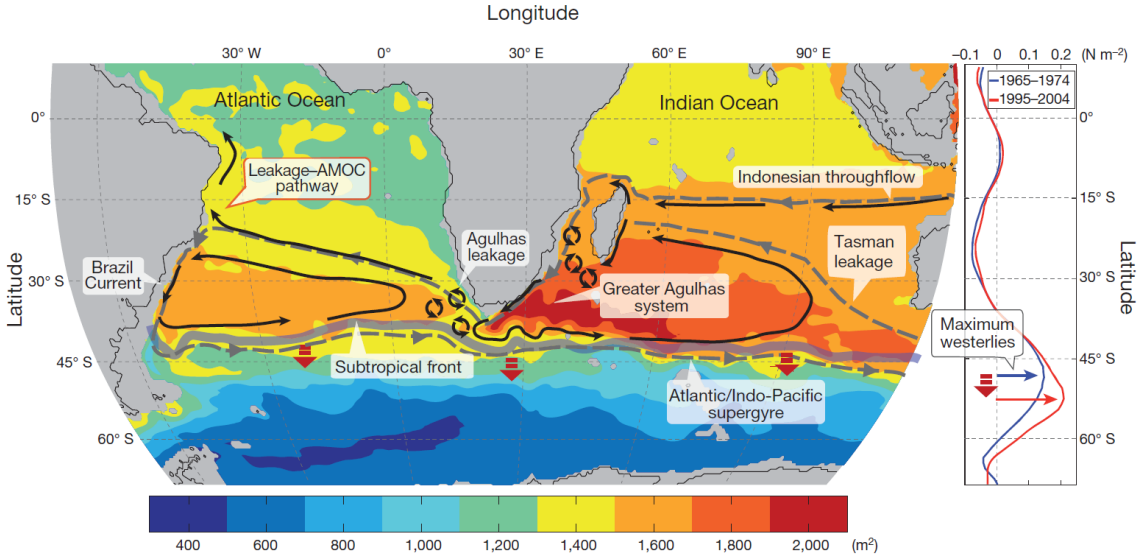

Fig. 1.12 Schematic of the Agulhas Current System linking the South Atlantic and Indian Oceans within the Southern Hemisphere supergyre. The panel on the right side depicts the change in the westerly winds during the second half of the twentieth century. The westerly winds drive variations in Agulhas leakage. Figure from *Beal et al.* (2011).

Upon reaching the end of the African continent, the Agulhas Current continues its southward trajectory, overshooting the tip of the African continental shelf, until it makes a sharp turn eastward (e.g., *Ou and De Ruijter*, 1986) and flows back into the Indian Ocean as the Agulhas Return Current (e.g., *Boebel et al.*, 2003a). This turn is termed the Agulhas retroflection and is the most energetic in the world (*Gordon*, 2003). About 25% of the Agulhas Current waters flow into the Atlantic Ocean as Agulhas leakage. During the retroflection process large anticyclonic rings, several hundreds of km in diameter (e.g., *Biastoch and Krauss*, 1999; *Van Aken et al.*, 2003; *Casanova-Masjoan et al.*, 2017), can detach from the current and propagate into the Atlantic Ocean (*Schouten et al.*, 2000). The average frequency of ring shedding was estimated to be 5 rings per year according to observations (e.g., *Schouten et al.*, 2000). Ring shedding can be triggered by baroclinic instabilities of the circulation in the retroflection region (*Weijer et al.*, 2013), or by the occurrence of Natal Pulses (*van Leeuwen et al.*, 2000), which are large, solitary meanders of the Agulhas Current that propagate downstream and grow in amplitude (*Lutjeharms and Roberts*, 1988; *De Ruijter et al.*, 1999b). Observations show that Natal Pulses occur with an average frequency of 1.6 per year, with about two thirds of the events leading to ring shedding, while most ring shedding occurs independently of Natal Pulses (*Elipot and Beal*, 2015).

Rings shed from the Agulhas retroflection (*Schouten et al.*, 2000), together with eddies (*Boebel et al.*, 2003b), filaments (*Lutjeharms and Cooper*, 1996) and a direct flow constitute the leakage of Agulhas waters into the South Atlantic Ocean (*Lutjeharms*, 2006). The Agulhas leakage connects the Indian and Atlantic subtropical gyres into a supergyre (Fig. 1.12) and transports warm and saline thermocline and intermediate waters from the Indian into the Atlantic Ocean (*Gordon et al.*, 1992). It is the major supplier of waters to the upper limb of the AMOC (*Rühs et al.*, 2019), via the "warm water route" (*Gordon*, 1986), transporting 15 Sv in the upper 1000 *m* (*Richardson*, 2007) and 21.3 ± 4.7 Sv in the upper 2000 *m* (*Daher et al.*, 2020). The upper limb of the AMOC is additionally supplied by cold and fresh waters flowing directly from the Pacific Ocean through the Drake Passage, known as the "cold water route" (e.g., *Speich et al.*, 2001; *Rühs et al.*, 2019).

The waters entering the Atlantic Ocean as Agulhas leakage originate from the marginal seas of the Indian Ocean, from the Pacific Ocean and, to a small degree from the South Atlantic Ocean itself (Fig. 1.13), as shown by an in-depth modeling study using Lagrangian particles to trace the source waters of the Agulhas leakage (*Durgadoo et al.*, 2017). Waters from the Pacific Ocean reach the Agulhas System via the Indonesian Through-Flow, arriving at the tip of Africa predominantly through the Mozambique Channel, and as Tasman leakage south of Australia, arriving mostly via the Southeast Madagascar Current. Waters from the Red Sea and the Persian Gulf are transported on both sides of Madagascar after first taking

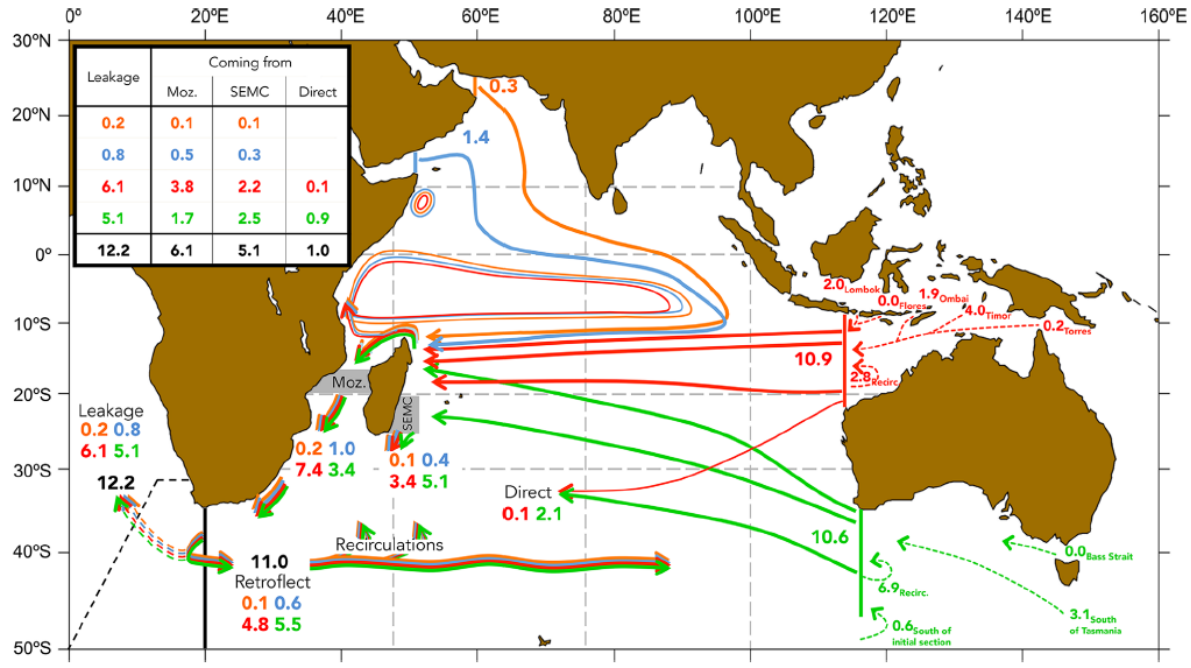

Fig. 1.13 Schematic of the pathways of Agulhas leakage source waters through the Indian Ocean. The numbers represent transports in Sv for Red Sea Water (blue), Persian Gulf Water (orange), Indonesian Through-Flow (red) and Tasman leakage (green). Figure from *Durgadoo et al.* (2017).

a detour to the northeastern Indian Ocean. In addition, waters from the South Atlantic and the Pacific Oceans reach the Agulhas System via recirculations from the frontal regions of the Southern Ocean (*Durgadoo et al.*, 2017). Within the Indian Ocean and the Agulhas Retroflection region, these waters undergo water mass alteration either through mixing or through exchanges of heat and water with the atmosphere. The water masses entering the South Atlantic as Agulhas leakage were identified from hydrographic stations performed in the Cape Basin or from observations of individual rings (*Gordon et al.*, 1987; *Van Aken et al.*, 2003; *Giulivi and Gordon*, 2006). These observations are sparse in time and space, underlining the general difficulty of continuously sampling the ocean for longer periods of time. They show that the thermocline layer is occupied by Subtropical Mode Water formed in the southwestern Indian Ocean, South Indian Ocean Central Water and Subantarctic Mode Water. Antarctic Intermediate Water dominates the intermediate layer below, with remnants of Red Sea Water also present.

During the second half of the twentieth century the leakage of Agulhas waters into the Atlantic Ocean has experienced an increase as a result of changes in the Southern Hemisphere westerly winds (*Biastoch et al.*, 2009, 2015; *Rouault et al.*, 2009; *Loveday et al.*, 2015). This positive trend has leveled off between the 1990s and 2013 (*Le Bars et al.*, 2014). Although

changes in both the strength of the westerlies and the location of their maximum have been proposed as drivers of the increase in Agulhas leakage (*Biastoch et al.*, 2009; *Beal et al.*, 2011; *Loveday et al.*, 2015), an idealized modeling study in which the strength and the location of the westerlies were altered separately clearly revealed that strengthening the winds increases the leakage, while a poleward shift in their location decreases the leakage (*Durgadoo et al.*, 2013). Stronger westerlies result in an increase in the wind stress curl over the southern Indian Ocean, which in turn drives an increase in the equatorward interior Sverdrup transport across the southern part of the supergyre. Consequently, the Agulhas leakage increases in order to balance the meridional mass transport, as required by continuity (*Durgadoo et al.*, 2013).

The mechanism proposed by *Durgadoo et al.* (2013) does not require an increase in the transport of the Agulhas Current for the increase in leakage to occur. In fact, previous studies disagree on the nature of the relationship between the Agulhas Current and leakage. *Rouault et al.* (2009) found that an increase in leakage is related to an increase in Agulhas Current transport, while *van Sebille et al.* (2009) argued that a reduction of the Agulhas Current transport leads to more leakage. More recently, *Loveday et al.* (2014) showed that a relationship between Agulhas Current transport and leakage is only found in lower resolution models, while in mesoscale-resolving models that simulate more accurate leakage values the leakage does not respond to changes in Agulhas Current transport. The decoupling between the Agulhas Current transport and leakage is supported by the lack of a significant trend in an observational-based proxy for the Agulhas Current (*Beal and Elipot*, 2016; *Elipot and Beal*, 2018). However, direct observations of the Agulhas Current are sparse and cover only a few years, with models remaining the primary tool employed to study long term changes in the Agulhas System.

As the Agulhas leakage transports warm and saline waters into the South Atlantic Ocean, changes in leakage can alter the thermohaline properties of the Atlantic Ocean and the stability of the AMOC. *Weijer et al.* (2002) showed that, in a coarse resolution Ocean General Circulation Model with mixed boundary conditions allowing for the development of density anomalies, Agulhas heat and salt anomalies alter the overturning circulation in the Atlantic Ocean. Coupled climate models simulate an advective pathway for salinity anomalies from the Agulhas region into the North Atlantic on timescales of 30-40 years, but their typical low resolution leads to an overestimation of the Agulhas leakage and salinity biases that cause the Agulhas leakage salinity anomalies to be too weak (*Weijer and van Sebille*, 2014). These results are nevertheless consistent with a high resolution ocean simulation in which an increased Agulhas leakage in response to changes in the surface westerlies leads to a salinification of thermocline waters spreading into the North Atlantic on time scales of two

to three decades (*Biastoch and Böning*, 2013). A more recent study with a high resolution ocean model that used a Lagrangian approach estimated the transit time of Agulhas waters to the North Brazil Current at 6°S to be about a decade (*Rühs et al.*, 2019). *Rühs et al.* (2019) additionally found that Agulhas waters undergo a substantial modification of their thermohaline properties during their transit through the South Atlantic, resulting in a net density gain through a net salinity increase. The same study also showed that an increase in Agulhas leakage results in an increased Agulhas contribution to the upper limb transport of the AMOC. The Agulhas leakage was also found to act as a source of decadal AMOC variability (*Biastoch et al.*, 2008) and to be significantly correlated with the Atlantic Multidecadal Oscillation at a lag of 15 years (*Biastoch et al.*, 2015).

A shut down of the Agulhas leakage has been associated with a northward shift of the Intertropical Convergence Zone and consequent changes in precipitation, reduced equatorial upwelling, and a cooling and freshening of the Equatorial Undercurrent in the tropical Atlantic, as part of the initial response simulated in a coupled climate model (*Haarsma et al.*, 2011). Furthermore, paleoclimate studies suggest that the Agulhas leakage was low during glacial and high during inter-glacial periods and that it played an important role in glacial terminations through its influence on the AMOC (*Knorr and Lohmann*, 2003; *Peeters et al.*, 2004). The Agulhas leakage is the main source of central water masses in the Benguela upwelling system, an important primary production region, and it has been hypothesized that a future increase in leakage could increase the contribution of Agulhas waters to the region and lead to changes in the oxygen, CO_2 and nutrient content (*Tim et al.*, 2018). An increased Agulhas leakage was additionally found to contribute to the warming of the tropical Atlantic (*Lübbecke et al.*, 2015) and to the increase in the Atlantic Ocean heat content observed over the last decades (*Lee et al.*, 2011; *Biastoch et al.*, 2015).

Given the importance of the Agulhas leakage in the climate system, it is necessary to understand its future evolution. In Chapter 4 of this thesis, the changes in Agulhas leakage during the twenty-first century are studied in a coupled climate model that has high, mesoscale-resolving resolution in the ocean around the Agulhas System. The relative contributions of the two principle drivers of change in the Agulhas System, increasing GHGs and ozone recovery, are examined. Studying the effects of stratospheric ozone changes on the Agulhas System is made possible by the climate model used in this thesis, which is unique as it not only resolves the oceanic mesoscale features, but it also includes a module for calculating the ozone chemistry interactively. The impacts of the simulated changes in Agulhas leakage on the thermohaline characteristics of the Atlantic Ocean are additionally investigated.

1.4.2 Precipitation over South Africa

The precipitation over semi-arid South Africa exhibits a marked seasonality and large regional variations, with different rain-producing weather systems dominating in different seasons and regions. South Africa can be split into three regions, based on the seasonality of rainfall occurrence. The interior and eastern parts of the country form the summer rainfall zone, which receives the highest amount of rainfall in the country. In contrast, the southwestern Cape region is a winter rainfall zone, while the southern coast receives precipitation throughout the year and is therefore termed the all-year rainfall zone (*Engelbrecht et al.*, 2015; *Roffe et al.*, 2019).

South African precipitation is shaped by both atmospheric and oceanic dynamics. The oceans on each side of the country exhibit distinct and contrasting conditions. Along the eastern and southern coasts, the western boundary current of the Indian Ocean, the Agulhas Current, transports heat poleward and is characterized by warm waters, which give rise to large heat and moisture fluxes (*Lee-Thorp et al.*, 1999; *Rouault et al.*, 2000; *Nkwinkwa Njouodo et al.*, 2018). The latent heat flux was found to be about five times larger over the Agulhas Current than over the neighboring waters (*Rouault et al.*, 2000). In contrast, the waters along the western coast are relatively cold, owing to the presence of one of the four Eastern Boundary Upwelling Systems in the world, the Benguela Upwelling System (*Shannon*, 1985). Due to these contrasting oceanographic conditions, the amount of precipitation over eastern and western South Africa differs greatly, with annual mean rainfall values below 200 *mm* over most of the western coast and above 1000 *mm* over the summer rainfall region in the eastern part of the country (Fig. 1.14). The Agulhas Current System in particular impacts precipitation over large parts of South Africa (*Walker*, 1990; *Reason and Mulenga*, 1999; *Reason*, 2001; *Nkwinkwa Njouodo et al.*, 2021). Positive SST anomalies in the Agulhas Current System are associated with increased precipitation over eastern and central South Africa in summer (*Reason and Mulenga*, 1999; *Reason*, 2001; *Nkwinkwa Njouodo et al.*, 2021) and over the western Cape region in winter (*Reason*, 2001).

Several synoptic-scale rainfall-producing weather systems are responsible for precipitation over South Africa. Tropical-extratropical cloud bands, termed tropical-temperate troughs (TTTs) over Southern Africa, are cloud bands with a northwest-southeast orientation that connect the summertime tropical low over central Africa, the Angola low, with temperate cyclones to the south of the continent (*Harrison*, 1984). TTTs contribute over 30% of the rain days during the wet summer season and are also associated with over half of the extreme precipitation events (*Hart et al.*, 2013). Additionally, mesoscale convective systems are important for the austral summer rainfall over eastern South Africa (*Blamey and Reason*, 2012; *Morake et al.*, 2021). In the winter rainfall zone, the largest proportion of rainfall

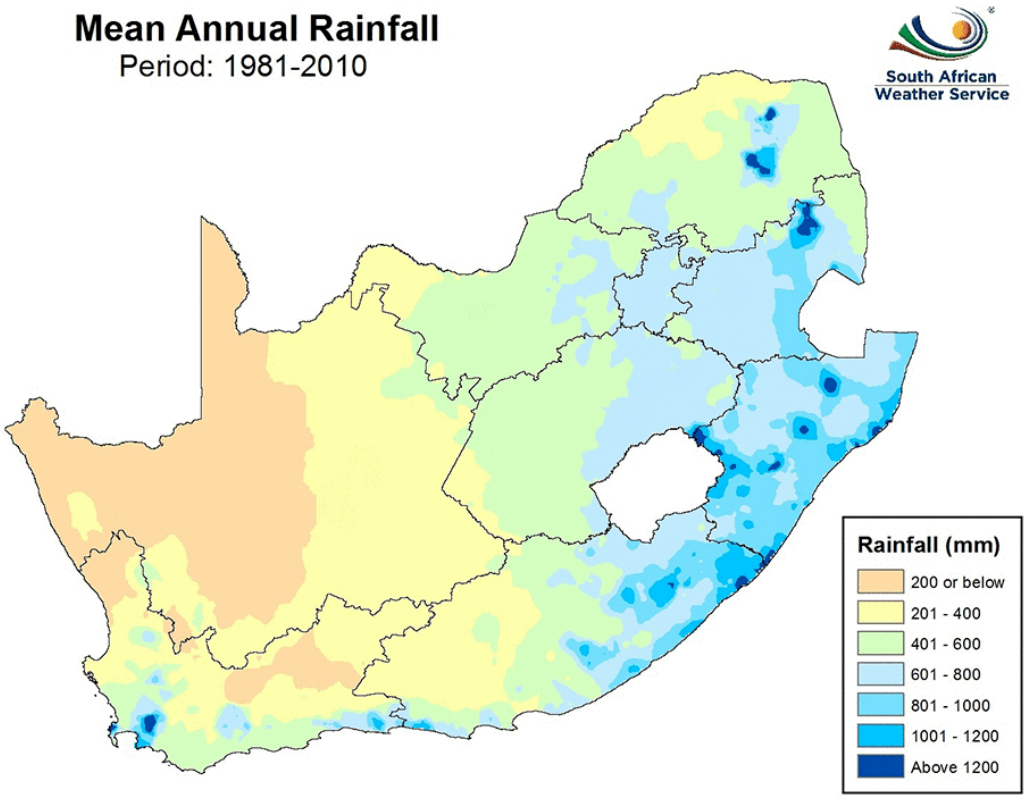

Fig. 1.14 Map of the 1981-2010 annual mean precipitation over South Africa. Figure from the South African National Climate Change Information System.

in contributed by cold fronts (e.g., *Burls et al.*, 2019). Cut-off lows (COLs), which are associated with high potential vorticity anomalies (*Hoskins et al.*, 1985), occur throughout the year, peaking in spring and autumn (*Singleton and Reason*, 2007a), and are known to result in extreme precipitation events and flooding (*Singleton and Reason*, 2006, 2007b). Surface heat and moisture fluxes from the warm Agulhas Current System have been found to play an important role in the development of COLs (*Singleton and Reason*, 2006, 2007b). COLs contribute between 25 to 35% of the annual precipitation over the southern and eastern coasts of South Africa, as well as inland (*Favre et al.*, 2013). In addition, the ridging of the South Atlantic Anticyclone over South Africa contributes 46% of the annual rainfall over the southern coast (*Engelbrecht et al.*, 2015) and 60% of the summer rainfall days in the summer rainfall zone (*Ndarana et al.*, 2021). Due to their important contribution to South African precipitation, these ridging events, referred to as ridging highs, are studied in this thesis. Ridging highs are not convective rainfall-producing systems on their own, but they result in southerly and southeasterly onshore winds that transport moisture from the Southwest

Indian Ocean onto land (*Blamey and Reason*, 2009; *Rapolaki et al.*, 2020; *Ndarana et al.*, 2021). They can result in orographic rainfall when the associated flow encounters the coastal mountains, or they can occur together with COLs (*Singleton and Reason*, 2007b) or TTTs (*Ndarana et al.*, 2021), which provide the dynamical lifting of the moist air necessary for precipitation to occur. When occurring in combination with a tropical low, ridging highs were also found to be involved in extreme precipitation events (*Crimp and Mason*, 1999). Ridging high have been classified as Type-N, when they extend over South Africa, or Type-S, when they extend south of the continent (*Ndarana et al.*, 2022).

The breaking of Rossby waves in the upper troposphere and lower stratosphere appears to also have an influence on precipitation over South Africa. *Hart et al.* (2010) found Rossby wave breaking (RWB) to precede TTTs, while 89% of the COLs identified by *Ndarana and Waugh* (2010) were accompanied by RWB. RWB was additionally associated with the development of ridging highs (*Ndarana et al.*, 2018).

In Chapter 5 of this thesis, the impact that RWB has on ridging highs and on the associated precipitation is studied. This is motivated by the fact that ridging highs contribute more than half of the precipitation in the eastern part of South Africa. Ridging highs are separated for the first time based on whether they occur together with RWB or not and precipitation differences between these two types of ridging highs are analyzed. Furthermore, the predicted future changes in ridging highs and the role played by RWB in these changes are investigated. This analysis is part of the SPACES-II CASISAC project.

1.5 Scientific Questions of this Thesis

From changes in precipitation patterns to changes in the oceanic circulation and temperature that affect both our climate as well as marine ecosystems, the impacts of the increase in anthropogenic GHGs and of changes in stratospheric ozone concentrations have manifold consequences for humans and the society. The main objective of this thesis is to separate the effects that the increase in anthropogenic GHGs and changes in stratospheric ozone concentrations have on the atmospheric and oceanic circulation in the Southern Hemisphere. To this end, an atmosphere-ocean coupled climate model is employed, FOCI (*Matthes et al.*, 2020), with enhanced oceanic resolution in the South Atlantic Ocean and the western Indian Ocean. The simulations either include a module for interactively calculating the ozone chemistry or prescribe the ozone field recommended for CMIP6. The configuration with both interactive ozone chemistry and high resolution ocean is unique to FOCI and render the model more advanced than the standard climate models participating in CMIP6, which have coarse oceanic resolution and typically do not explicitly calculate the ozone field. Therefore,

this thesis provides new aspects of the future projected changes in the Southern Hemisphere that cannot be reliably studied with CMIP6-class models, such as changes in the Agulhas leakage or the role played by ozone recovery.

First, the simulated past (1958-2002) changes in the Southern Hemisphere atmospheric circulation are separated based on whether they were caused by ozone depletion or increasing GHGs. The results are compared to those of previous studies and the total simulated changes are validated against observations and the ERA5 reanalysis to answer the question:

1. **How well does the coupled climate model FOCI simulate the changes caused in the second half of the twentieth century in the Southern Hemisphere by ozone depletion and increasing levels of anthropogenic GHGs?** (Chapter 3)

In the future, GHGs continue to increase, but the ozone hole is expected to recover as a result of the Montreal Protocol and its subsequent amendments and adjustments, which mandate the phasing out of ODSs. Both of these factors are expected to exert an important influence not only on the atmospheric, but also on the oceanic circulation. Therefore, the second question addressed in this thesis is:

2. **How will increasing concentrations of GHGs and the recovery of stratospheric ozone impact the atmospheric and oceanic circulation in the Southern Hemisphere in the twenty-first century? What will the net effect of these changes in atmospheric composition be?** (Chapter 4)

A special focus is set on the Southern African region, a region interesting both from an oceanographic and meteorological point of view. The warm waters from the Agulhas Current System enter the Atlantic Ocean at the southern tip of Africa and feed the upper limb of the AMOC, while also resulting in large heat and moisture fluxes into the atmosphere, affecting precipitation on land. The moisture originating from the Agulhas System can be transported over the continent by southerly and southeasterly winds, which arise during the ridging of the South Atlantic Anticyclone over Africa, among other synoptic-scale systems. This ridging process has been recently associated with Rossby wave breaking aloft. In light of these aspects, the third question addressed in this thesis is:

3. **How are the Southern African region and the adjacent oceans impacted by the increases in GHGs and ozone in the twenty-first century? Do ridging highs over South Africa that are accompanied by Rossby wave breaking at the tropopause bring a different contribution to precipitation in the region than ridging highs that are not?** (Chapters 4 and 5)

As the ozone field, and whether it is calculated interactively or prescribed, can lead to different estimates of the magnitude of the ozone-induced changes, the changes simulated by the coupled climate model with interactive ozone chemistry and with prescribed CMIP6 ozone are compared, to answer the question:

4. **How does the representation of stratospheric ozone in climate models affect the simulated dynamics and what are the implications for future climate model intercomparison projects?** (Chapters 3 and 4)

This thesis is structured as follows. Chapter 2 gives an overview of the coupled climate model simulations used throughout the thesis. In Chapter 3, the simulated changes in the Southern Hemisphere atmospheric dynamics induced by ozone depletion and increasing levels of GHGs during the second half of the twentieth century are investigated and validated against observations. At the same time, the dynamical changes are compared between a version of the model that interactively simulates the ozone field and a version to which the ozone field used in CMIP6 is prescribed, with the aim of assessing the importance of the ozone field for the simulated changes. Chapter 4 investigates the effects that the future increase in GHGs according to the high emission scenario SSP5-8.5 and the expected recovery of the ozone hole have in the Southern Hemisphere. These effects are systematically studied, starting from the stratosphere, through the troposphere and towards a detailed analysis of the resulting ocean changes. In addition, the role of the ozone field for future predictions is assessed. Chapter 5 focuses on the Southern African region, studying the relationship between the ridging of the South Atlantic Anticyclone over South Africa and Rossby wave breaking at tropopause levels and its implications for precipitation. After describing this relationship, its evolution during the twenty-first century under increasing levels of GHGs and ozone recovery is studied. Finally, the conclusions of the thesis and their implication for future research are presented in Chapter 6.

Chapter 2

Model simulations

2.1 The Coupled Climate Model FOCI

The simulations analyzed in this thesis were performed with the state-of-the-art coupled ocean-atmosphere climate model FOCI (Flexible Ocean Climate Infrastructure, *Matthes et al.*, 2020), whose components are depicted in Fig. 2.1. The atmospheric component of FOCI is ECHAM6.3 (*Stevens et al.*, 2013) in the T63L95 setting, corresponding to approximately 1.8° by 1.8° horizontal resolution or 200 km and laying within the range of CMIP6 model resolutions of 100 km to 250 km. The 95 vertical hybrid sigma-pressure levels extend up to the model top located well above the stratopause at 0.01 hPa and lay at the high end of the number of vertical levels used in CMIP6, between 30 and 95. The stratosphere is thus fully included in FOCI and the model is adequate for simulating stratospheric processes. The vertical levels are distributed every 1 to 2 km in the stratosphere. The quasi-biennial oscillation (QBO) is internally generated. The radiative transfer calculation uses 16 bands in the longwave and 14 bands in the shortwave spectrum. Variations in solar activity are included in FOCI following the recommendations for CMIP6 (*Matthes et al.*, 2017) and are treated independently for each of the 14 shortwave radiation bands. FOCI optionally includes a module for interactively simulating chemical processes in the atmosphere, MOZART3 (Model for Ozone and Related Chemical Tracers, *Kinnison et al.*, 2007), implemented in ECHAM6 (*Schultz et al.*, 2018). This allows for a total of 182 chemical reactions involving 52 chemical constituents to be simulated, with a focus on stratospheric chemistry. The chemical reactions relevant for the formation and destruction of stratospheric ozone are all simulated. As such, in this configuration, FOCI is suitable for the study of past and future stratospheric ozone changes and their impacts.

The oceanic component of FOCI is NEMO3.6 (Nucleus for European Modeling of the Ocean, *Madec and the NEMO team*, 2016) in the ORCA05 configuration, corresponding

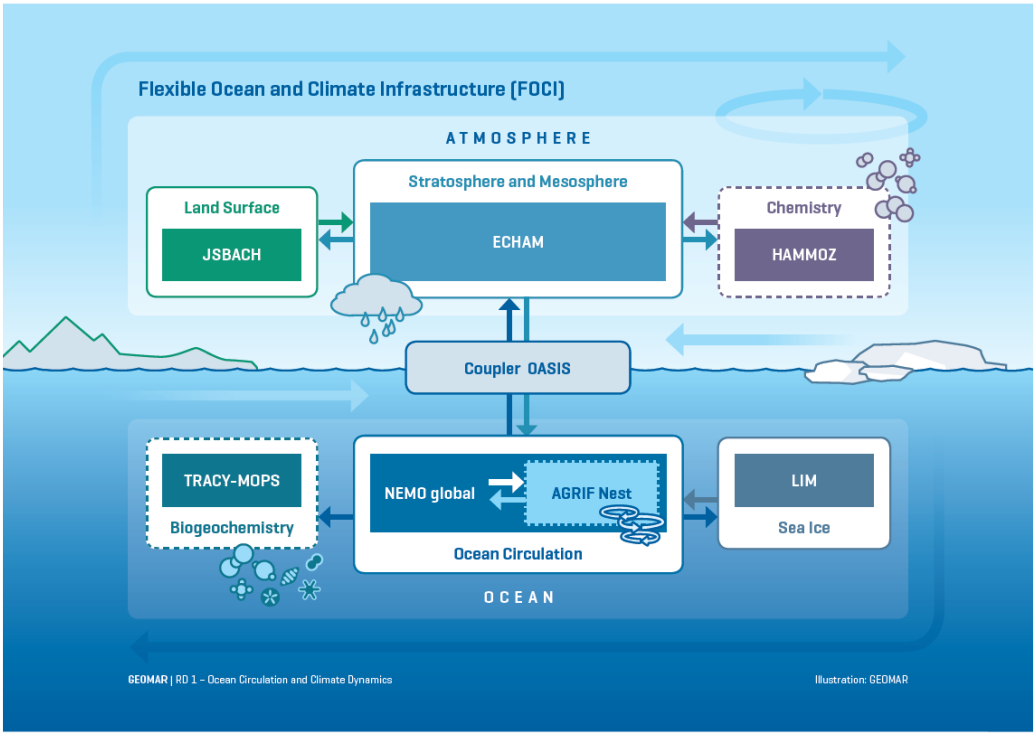

Fig. 2.1 The components of the coupled climate model FOCI. Optional components are depicted by dashed boxes. Figure from *Matthes et al.* (2020).

to a global nominal resolution of 0.5° and 46 z levels, whose spacing ranges from every 6 m at the surface to every 250 m in the deep ocean. The horizontal resolution translates to approximately 39 km in the global average. A special feature of FOCI is the ability to include a high-resolution ocean nest, increasing the oceanic resolution to 0.1° in an area of interest. In this thesis, the INALT10X high-resolution nest (*Schwarzkopf et al.*, 2019) is used for the South Atlantic Ocean and the western part of the Indian Ocean. INALT10X extends from 63°S to 10°N and from 70°W to 70°E (Fig. 2.2), also covering parts of the Southern Ocean. The enhanced resolution, about 8 km at 45°S, allows for mesoscale processes to be resolved in the nesting domain. As mesoscale processes form an important part of the Agulhas Current System, the enhanced resolution allows for the realistic study of changes in the Agulhas Current System. As shown by *Schwarzkopf et al.* (2019), the Agulhas leakage in INALT10X is more realistic than that simulated at lower resolution. The impact of the high-resolution nest is also felt outside of the nesting domain, owing to a two-way nesting technique (*Debreu et al.*, 2008). The nest not only receives information at its boundary from the ORCA05 host, but it also feeds back its fine scale state to the host. Outside of the nesting domain, where mesoscale processes are not resolved, an eddy parametrization scheme (*Gent and Mcwilliams*, 1990) is employed, with an eddy diffusivity coefficient that

varies temporally and horizontally with the growth of baroclinic instability, up to 2000 m^2 s^{-1} (*Treguier et al.*, 1997). Allowing the eddy parametrization coefficient to vary allows for a better representation of Southern Ocean processes (*Gent*, 2016).

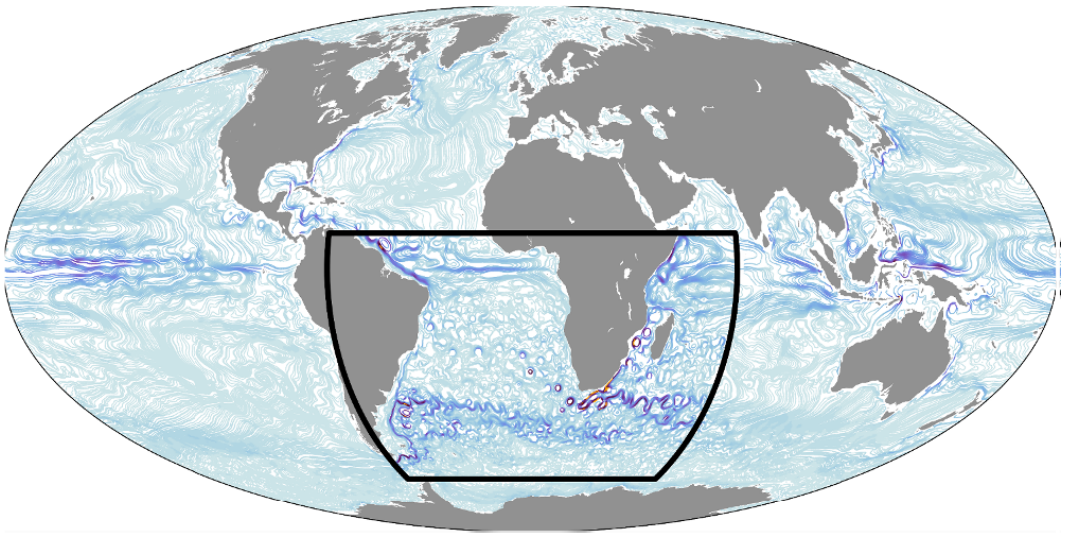

Fig. 2.2 The INALT10X high resolution (0.1°) ocean nest, with boundaries depicted in black, embedded into the global ocean. Figure from *Matthes et al.* (2020).

Finally, sea-ice processes are simulated by the LIM2 (*Fichefet and Maqueda*, 1997) module and land surface processes are simulated by the JSBACH (*Brovkin et al.*, 2009; *Reick et al.*, 2013) module.

2.2 The Ensembles of Simulations

A total of nine ensembles of three simulations each are carried out and analyzed in this thesis. The simulations within an ensemble were initialized using different initial conditions. The simulations are summarized in Table 2.1 and an overview of the ensembles is provided in Table 2.2. Three of these ensembles are used in Chapter 3 to separate the effects of increasing GHGs and of ozone depletion on the Southern Hemisphere circulation and to check the ability of the model to simulate the past changes driven by these two factors. These ensembles cover the historical period 1958-2013 and are all performed with the configuration of FOCI that includes both the module for interactive ozone chemistry and the high-resolution INALT10X nest. One ensemble is used as a reference of the total changes that occurred due to both increasing GHGs and ozone depletion. This ensemble is further used in Chapter 5 to investigate the influence of RWB on ridging highs over South Africa and their associated precipitation. The other two ensembles also cover the period 1958-2013, but they include

either only the increase in GHGs or the increase in ODSs that lead to ozone depletion. More specifically, either the GHGs CO_2 and CH_4 or the ODSs follow a perpetual seasonal cycle representative of the 1960 conditions, obtained for each chemical constituent by averaging over the period 1955 to 1965.

Two further ensembles are used in Chapter 3 to assess if the simulated past changes in circulation are sensitive to whether the ozone field is calculated interactively or the CMIP6 ozone field (*Hegglin et al.*, 2016) is prescribed. These ensembles do not include the high-resolution ocean nest, which is computationally expensive. The configuration of FOCI with interactive ozone chemistry is about 6 times more computationally expensive than the standard version of the model, while including both the INALT10X high resolution nest and interactive ozone chemistry is 10 times more expensive than the standard.

Four ensembles were performed using the high-emission scenario SSP5-8.5 for the future period 2013-2099. This scenario is characterized by CO_2 concentrations reaching 1135 ppm by the end of the century, with the radiative forcing reaching 8.5 $W\ m^{-2}$ (*Meinshausen et al.*, 2020). The simulations in all of these ensembles include the high-resolution INALT10X nest. Two ensembles are used in Chapter 4 to study the differences in future dynamical changes between the model configuration with interactive ozone chemistry and the model configuration with prescribed CMIP6 ozone. The ensemble with interactive ozone chemistry is further used as the reference ensemble in Chapters 4 and 5. This ensemble gives the dynamical changes occurring due to both the increase in GHGs and the recovery of the ozone hole and is compared to the last two ensembles, in which either GHGs or ODSs follow a repeated seasonal cycle representative of 1995 conditions obtained by averaging over the period 1991-2000. These latter ensembles enable the separation of the effects of increasing GHGs and of the recovery of the Antarctic ozone hole on the atmospheric and oceanic circulation in the Southern Hemisphere during the twenty-first century.

Table 2.1 Simulations used in this thesis.

Simulation	Time Span	Ozone Field	High-Resolution Nest	GHGs	ODSs
II005	1958-2013	interactive	INALT10X	historical CMIP6	historical CMIP6
II006	1958-2013	interactive	INALT10X	historical CMIP6	historical CMIP6
II007	1958-2013	interactive	INALT10X	historical CMIP6	historical CMIP6
II008	1958-2013	interactive	INALT10X	historical CMIP6	fixed at 1960 levels
SW112	1958-2013	interactive	INALT10X	historical CMIP6	fixed at 1960 levels
SW114	1958-2013	interactive	INALT10X	historical CMIP6	fixed at 1960 levels
II009	1958-2013	interactive	INALT10X	fixed at 1960 levels	historical CMIP6
SW113	1958-2013	interactive	INALT10X	fixed at 1960 levels	historical CMIP6
SW115	1958-2013	interactive	INALT10X	fixed at 1960 levels	historical CMIP6
SW060	1958-2013	prescribed CMIP6	-	historical CMIP6	historical CMIP6
SW061	1958-2013	prescribed CMIP6	-	historical CMIP6	historical CMIP6
JH019	1958-2013	prescribed CMIP6	-	historical CMIP6	historical CMIP6
SW054	1958-2013	interactive	-	historical CMIP6	historical CMIP6
SW064	1958-2013	interactive	-	historical CMIP6	historical CMIP6
SW065	1958-2013	interactive	-	historical CMIP6	historical CMIP6
II010	2014-2099	interactive	INALT10X	SSP5-8.5	SSP5-8.5
II011	2014-2099	interactive	INALT10X	SSP5-8.5	SSP5-8.5
SW128	2014-2099	interactive	INALT10X	SSP5-8.5	SSP5-8.5
II012	2014-2099	interactive	INALT10X	SSP5-8.5	fixed at 1995 levels
II014	2014-2099	interactive	INALT10X	SSP5-8.5	fixed at 1995 levels
II016	2014-2099	interactive	INALT10X	SSP5-8.5	fixed at 1995 levels
II013	2014-2099	interactive	INALT10X	fixed at 1995 levels	SSP5-8.5
II015	2014-2099	interactive	INALT10X	fixed at 1995 levels	SSP5-8.5
II017	2014-2099	interactive	INALT10X	fixed at 1995 levels	SSP5-8.5
JH027	2011-2099	prescribed CMIP6	INALT10X	SSP5-8.5	SSP5-8.5
JH037	2011-2099	prescribed CMIP6	INALT10X	SSP5-8.5	SSP5-8.5
JH039	2011-2099	prescribed CMIP6	INALT10X	SSP5-8.5	SSP5-8.5

Table 2.2 Overview of the ensembles used in this thesis. Note that the ensembles were given different names in different chapters and these names are provided in the fourth column.

Simulations	Description	Chapter	Name in Chapter
II005, II006, II007	Historical ensemble with interactive ozone and high resolution ocean	3, 5	REF, PAST
II008, SW112, SW114	Historical ensemble with interactive ozone and high resolution ocean in which ODSs are fixed at 1960 levels	3	NoODS
II009, SW113, SW115	Historical ensemble with interactive ozone and high resolution ocean in which GHGs are fixed at 1960 levels	3	NoGHG
SW060, SW061, JH019	Historical ensemble with prescribed ozone	3	Fixed O_3
SW054, SW064, SW065	Historical ensemble with interactive ozone	3	INTERACT O_3
II010, II011, SW128	Future ensemble with interactive ozone and high resolution ocean	4, 5	INTERACT_O_3, FUTURE
II012, II014, II016	Future ensemble with interactive ozone and high resolution ocean in which ODSs are fixed at 1995 levels	4, 5	FixODS, GHG
II013, II015, II017	Future ensemble with interactive ozone and high resolution ocean in which GHGs are fixed at 1995 levels	4, 5	FixGHG, OZONE
JH027, JH037, JH039	Future ensemble with prescribed ozone and high resolution ocean	4	CMIP6_O_3

Chapter 3

Effects of prescribed CMIP6 ozone on simulating the Southern Hemisphere atmospheric circulation response to ozone depletion

This chapter separates the effects of the increase in anthropogenic GHGs and of ozone depletion on the Southern Hemisphere atmospheric circulation during the second half of the twentieth century and assess the ability of the coupled climate model FOCI to simulate these effects through a comparison with observations and previous studies. FOCI correctly simulates all the known past atmospheric circulation changes and identifies ozone depletion as their primary driver, in agreement with other studies.

Furthermore, this chapter investigates how the representation of stratospheric ozone affects the simulated past changes and shows that prescribing the CMIP6 ozone field results in weaker changes compared to calculating the ozone field interactively. This highlights the importance of using a consistent ozone field in climate simulations.

Citation: Ivanciu, I. , Matthes, K. , Wahl, S. , Harlaß, J. and Biastoch, A.: Effects of prescribed CMIP6 ozone on simulating the Southern Hemisphere atmospheric circulation response to ozone depletion, Atmospheric Chemistry and Physics, 21 (8), 5777-5806, doi: 10.5194/acp-21-5777-2021, 2021.

Candidate's contributions to this publication:

- She designed the experimental set-up and performed five of the simulations.
- She performed all of the analyses.
- She produced all the figures.
- She wrote the manuscript, from the first draft to the final version.

Atmos. Chem. Phys., 21, 5777–5806, 2021
https://doi.org/10.5194/acp-21-5777-2021

Atmospheric Chemistry and Physics
Open Access
EGU

Effects of prescribed CMIP6 ozone on simulating the Southern Hemisphere atmospheric circulation response to ozone depletion

Ioana Ivanciu[1], **Katja Matthes**[1,2], **Sebastian Wahl**[1], **Jan Harlaß**[1], **and Arne Biastoch**[1,2]

[1]GEOMAR Helmholtz Centre for Ocean Research Kiel, Kiel, Germany
[2]Faculty of Mathematics and Natural Sciences, Christian-Albrechts Universität zu Kiel, Kiel, Germany

Correspondence: Ioana Ivanciu (iivanciu@geomar.de)

Received: 11 July 2020 – Discussion started: 5 October 2020
Revised: 31 January 2021 – Accepted: 5 March 2021 – Published: 19 April 2021

Abstract. The Antarctic ozone hole has led to substantial changes in the Southern Hemisphere atmospheric circulation, such as the strengthening and poleward shift of the midlatitude westerly jet. Ozone recovery during the twenty-first century is expected to continue to affect the jet's strength and position, leading to changes in the opposite direction compared to the twentieth century and competing with the effect of increasing greenhouse gases. Simulations of the Earth's past and future climate, such as those performed for the Coupled Model Intercomparison Project Phase 6 (CMIP6), require an accurate representation of these ozone effects. Climate models that use prescribed ozone fields lack the important feedbacks between ozone chemistry, radiative heating, dynamics, and transport. In addition, when the prescribed ozone field was not generated by the same model to which it is prescribed, the imposed ozone hole is inconsistent with the simulated dynamics. These limitations ultimately affect the climate response to ozone depletion. This study investigates the impact of prescribing the ozone field recommended for CMIP6 on the simulated effects of ozone depletion in the Southern Hemisphere. We employ a new state-of-the-art coupled climate model, Flexible Ocean Climate Infrastructure (FOCI), to compare simulations in which the CMIP6 ozone is prescribed with simulations in which the ozone chemistry is calculated interactively. At the same time, we compare the roles played by ozone depletion and by increasing concentrations of greenhouse gases in driving changes in the Southern Hemisphere atmospheric circulation using a series of historical sensitivity simulations. FOCI captures the known effects of ozone depletion, simulating an austral spring and summer intensification of the midlatitude westerly winds and of the Brewer–Dobson circulation in the Southern Hemisphere. Ozone depletion is the primary driver of these historical circulation changes in FOCI. The austral spring cooling of the polar cap in the lower stratosphere in response to ozone depletion is weaker in the simulations that prescribe the CMIP6 ozone field. We attribute this weaker response to a prescribed ozone hole that is different to the model dynamics and is not collocated with the simulated polar vortex, altering the strength and position of the planetary wavenumber one. As a result, the dynamical contribution to the ozone-induced austral spring lower-stratospheric cooling is suppressed, leading to a weaker cooling trend. Consequently, the intensification of the polar night jet is also weaker in the simulations with prescribed CMIP6 ozone. In contrast, the differences in the tropospheric westerly jet response to ozone depletion fall within the internal variability present in the model. The persistence of the Southern Annular Mode is shorter in the prescribed ozone chemistry simulations. The results obtained with the FOCI model suggest that climate models that prescribe the CMIP6 ozone field still simulate a weaker Southern Hemisphere stratospheric response to ozone depletion compared to models that calculate the ozone chemistry interactively.

1 Introduction

Anthropogenic emissions of ozone-depleting substances (ODSs), in particular chlorofluorocarbons (CFCs), have led to a steep decline in stratospheric ozone concentrations since the 1980s. The strongest ozone depletion occurred in austral spring above Antarctica. There, the particularly low temperatures inside the winter polar vortex enable the forma-

tion of polar stratospheric clouds (PSCs). Upon the arrival of sunlight in spring, heterogeneous chlorine photochemistry on the surface of PSCs makes chlorine particularly effective at destroying ozone (e.g., Solomon, 1999). As a result, the ozone hole develops every spring in the Antarctic stratosphere, with profound impacts for the Southern Hemisphere (SH) climate. Observations (e.g., Randel and Wu, 1999; Thompson and Solomon, 2002; Randel et al., 2009; Young et al., 2013) and model simulations (Mahlman et al., 1994; Arblaster and Meehl, 2006; Gillett and Thompson, 2003; Stolarski et al., 2010; Perlwitz et al., 2008; Son et al., 2010; McLandress et al., 2010; Polvani et al., 2011; Young et al., 2013; Eyring et al., 2013; Keeble et al., 2014) consistently show a cooling of the Antarctic lower stratosphere in austral spring and summer during the last decades of the twentieth century due to decreased radiative heating as a result of ozone depletion. This cooling has led to important changes in the dynamics of the SH. Lower polar cap temperatures resulted in an increased meridional temperature gradient between the cold polar cap and the relatively warmer midlatitudes. Consequently, the spring stratospheric polar vortex strengthened (Thompson and Solomon, 2002; Gillett and Thompson, 2003; Arblaster and Meehl, 2006; McLandress et al., 2010; Thompson et al., 2011; Keeble et al., 2014), and its breakdown was delayed by about 2 weeks (Waugh et al., 1999; Langematz et al., 2003; McLandress et al., 2010; Previdi and Polvani, 2014; Keeble et al., 2014). This enabled an intensification of the planetary wave activity propagating into the stratosphere, resulting in an enhancement of the Brewer–Dobson circulation (BDC) in austral summer (Li et al., 2008, 2010; Oberländer-Hayn et al., 2015; Polvani et al., 2018; Abalos et al., 2019).

At the same time, the strengthening of the stratospheric westerlies extended downward, affecting the tropospheric jet, which intensified with a lag of 1 to 2 months in austral summer (Thompson and Solomon, 2002; Gillett and Thompson, 2003; Perlwitz et al., 2008; Son et al., 2010; Eyring et al., 2013). The intensification of the stratospheric and tropospheric jets was accompanied by a concurrent positive trend in the Southern Annular Mode (SAM; Thompson and Solomon, 2002; Gillett and Thompson, 2003; Marshall, 2003; Perlwitz et al., 2008; Fogt et al., 2009; Thompson et al., 2011). The surface westerlies strengthened on their poleward side and weakened on their equatorward side, therefore shifting towards higher latitudes during the austral summer (Polvani et al., 2011). This resulted in the poleward displacement of the SH storm track and led to changes in cloud cover (Grise et al., 2013) and precipitation, not only at the high latitudes and midlatitudes (Polvani et al., 2011; Previdi and Polvani, 2014), but also in the subtropics (Kang et al., 2011). The formation of the ozone hole also affected the Antarctic surface temperatures, with large regional variations in the temperature trend over the continent. Significant warming over the Antarctic Peninsula and Patagonia was reported by Thompson and Solomon (2002). Other consequences of ozone hole formation include the elevation of the SH polar tropopause (Son et al., 2009; Polvani et al., 2011) and the poleward expansion of the Hadley cell (Garfinkel et al., 2015; Waugh et al., 2015; Polvani et al., 2011; Min and Son, 2013; Previdi and Polvani, 2014) in austral summer. The wind stress over the Southern Ocean, associated with the westerlies, has also experienced a significant strengthening and poleward shift (Yang et al., 2007; Swart and Fyfe, 2012), with implications for the SH ocean circulation. Ocean circulation changes due to the formation of the Antarctic ozone hole include the intensification and poleward shift of the SH supergyre, which connects the subtropical Pacific, Atlantic, and Indian Ocean (Cai, 2006), an increase in the transport of salty and warm waters from the Indian into the Atlantic Ocean, known as the Agulhas leakage (Biastoch et al., 2009, 2015; Durgadoo et al., 2013), and changes in the Ekman transport and upwelling in the Southern Ocean (Thompson et al., 2011, and references therein).

As ozone depletion had such profound implications for the SH climate, accurate model simulations of past and future climate change require a correct representation of stratospheric ozone changes and their associated impacts. Multiple lines of evidence suggest that the method used to specify stratospheric ozone in models affects their response to ozone depletion (Gabriel et al., 2007; Crook et al., 2008; Gillett et al., 2009; Waugh et al., 2009; Haase and Matthes, 2019). Ozone concentrations can be calculated interactively (e.g., Haase and Matthes, 2019), as is the case in chemistry climate models (CCMs), or they can be prescribed either as zonal means, three-dimensionally (3D; e.g., Crook et al., 2008), as monthly means, or at daily resolution. Ozone asymmetries, the temporal resolution of the prescribed ozone field, and feedbacks between ozone, temperature, dynamics, and transport all impact the way in which changes driven by decreasing ozone concentrations are simulated. This paper investigates how prescribing the ozone field recommended for the Coupled Model Intercomparison Project Phase 6 (CMIP6) affects the atmospheric circulation response to ozone depletion by drawing a comparison with simulations that calculate the ozone chemistry interactively.

The position of the Antarctic ozone hole is not centered above the South Pole but varies with that of the polar vortex, being displaced towards the Atlantic sector in the climatological mean (e.g., Grytsai et al., 2007). As a result, the ozone field is characterized by asymmetries in the zonal direction, henceforth referred to as zonal asymmetries in ozone or ozone waves. The effect of zonal asymmetries in ozone was previously investigated for both hemispheres (e.g., Gabriel et al., 2007; Crook et al., 2008). In the Northern Hemisphere winter, zonally asymmetric ozone alters the structure of the stationary wave one, resulting in temperature changes in the stratosphere and mesosphere (Gabriel et al., 2007; Gillett et al., 2009). Ozone waves were also found to affect the number of sudden stratospheric warmings (SSWs), but studies disagree about the sign of the change (Peters et al., 2015;

Haase and Matthes, 2019). Peters et al. (2015) reported an increased number of SSWs and a weakening of the Arctic Oscillation between the mid-1980s and mid-1990s in a simulation with specified zonal asymmetries in ozone compared to one in which zonal mean ozone was prescribed. In contrast, Haase and Matthes (2019) found that fewer SSWs occurred between 1955 and 2019 when zonal asymmetries in ozone were prescribed, and even fewer SSWs occurred when the ozone chemistry was calculated interactively. In a recent study, Oehrlein et al. (2020) found no significant difference in the number of midwinter SSWs between their 200-year time-slice simulations with interactive and with prescribed zonally symmetric ozone.

In the SH, the largest zonal asymmetries in ozone occur in spring (Gillett et al., 2009; Waugh et al., 2009), when the stratospheric polar vortex is disturbed by the flux of wave activity from the troposphere and when the ozone hole develops. Model simulations that do not include zonal asymmetries in ozone exhibit a warmer lower stratosphere above Antarctica in austral spring and weaker westerly winds during the decades characterized by strong ozone depletion (Crook et al., 2008; Gillett et al., 2009). The effect of zonal asymmetries in ozone on stratospheric temperature, and hence on the polar vortex, is mediated through changes in stratospheric dynamics and cannot be explained solely by changes in radiative heating associated with the ozone field (Crook et al., 2008; Li et al., 2016). In addition to differences in the mean state, trends in temperature and in the strength of the stratospheric and tropospheric westerly jets are underestimated in both past (Waugh et al., 2009; Li et al., 2016; Haase et al., 2020) and future (Waugh et al., 2009) simulations that do not include zonal asymmetries in ozone. Furthermore, as the ocean circulation is sensitive to changes in the surface wind stress, it is also affected by the stratospheric zonal asymmetries in ozone. Weaker spring and summer surface westerlies trends in simulations that prescribe zonal mean monthly mean ozone therefore translate into weaker changes in the SH Ekman transport and in the Meridional Overturning Circulation (Li et al., 2016).

Besides zonal asymmetries in ozone, prescribing monthly mean ozone values that are then linearly interpolated to obtain a higher temporal resolution also leads to differences in atmospheric dynamics compared to simulations using interactive chemistry (Sassi et al., 2005; Neely et al., 2014). Linearly interpolating between prescribed monthly ozone values results in an underestimation of ozone depletion compared to interactive chemistry simulations, as the rapid ozone changes during austral spring cannot be fully captured. The weaker ozone hole, in turn, leads to a warmer lower stratosphere and smaller changes in both the stratospheric and the tropospheric westerly winds. Neely et al. (2014) found that these differences are greatly diminished if daily ozone is prescribed instead of monthly mean ozone and concluded that the coarse temporal resolution of the prescribed ozone accounts for the majority of the difference in the austral spring stratospheric temperature and the austral summer stratospheric westerly jet between simulations with prescribed and interactive ozone.

Feedbacks between stratospheric ozone, temperature, and dynamics can only occur in models that calculate the ozone chemistry interactively, i.e., in CCMs. The importance of such feedbacks in both hemispheres was previously shown in studies by Haase and Matthes (2019), Haase et al. (2020), and Oehrlein et al. (2020). Changes in temperature caused by ozone depletion, either directly through radiative cooling or indirectly through changes in dynamics, feed back onto ozone concentrations by altering the rate of the catalytic ozone destruction reactions. At the same time, cooling of the polar caps due to ozone loss enhances the meridional temperature gradient in the stratosphere and, as dictated by the thermal wind balance, strengthens the polar vortices. The stronger westerlies, in turn, impact the upward propagation of planetary waves from the troposphere and therefore lead to changes in the BDC, which transports ozone to high latitudes. Changes in stratospheric dynamics due to ozone depletion thus also feed back onto the ozone concentrations. Haase and Matthes (2019) described one such feedback in the Northern Hemisphere spring during the breakup of the polar vortex. At this time of the year the westerlies are weak and decreasing ozone levels lead to increased planetary wave forcing. This results in dynamical heating and enhanced ozone transport from the low latitudes, both of which lead to an increase in the ozone concentrations, forming a negative feedback loop. This feedback only occurred in the model simulation in which interactive chemistry was used and not in the simulations in which either zonal mean or three-dimensional ozone was prescribed, showing the importance of calculating the ozone chemistry interactively. A similar feedback also operates in the SH (Lin et al., 2017; Haase et al., 2020). In addition, a positive feedback was reported in the lower stratosphere for the SH by Haase et al. (2020). A new study investigating historical SAM trends in the CMIP6 models and their drivers found that an indirect effect of increasing greenhouse gases (GHGs) on the SAM due to GHG-induced changes in ozone offsets the direct effect of GHGs on the SAM (Morgenstern, 2021). The study showed that models that do not use interactive chemistry therefore overestimate the contribution of GHGs to the historical SAM strengthening.

Previous research conducted using the same model to test the sensitivity of simulations to the method used to represent ozone thus points to climate models that include interactively calculated ozone chemistry as the preferred choice for studies of past and future climate. In contrast, the tropospheric jet's response to ozone depletion is not significantly different between models with and without ozone chemistry in studies that used different models to assess the sensitivity of the response to how the ozone is imposed (Eyring et al., 2013; Seviour et al., 2017; Son et al., 2018). In the study of Eyring et al. (2013), however, some of the models categorized as in-

cluding ozone chemistry actually prescribed the ozone field. The difference to the models without chemistry was, in the case of several models, that the ozone field was produced by the interactive chemistry version of the same model. In addition, using different models to evaluate the impact of the method used to impose ozone changes makes it difficult to assess how other differences between those models, such as the strength of the stratosphere–troposphere coupling, affect the results.

The computational cost of coupled climate models with interactive chemistry is still very high, especially when long climate simulations are needed, as for CMIP6. Therefore, not all climate models participating in CMIP6 use interactive chemistry (Keeble et al., 2020) but instead use atmospheric chemistry datasets obtained from simulations with CCMs. The new atmospheric ozone field recommended for use in CMIP6 (Hegglin et al., 2016) is 3D and has monthly temporal resolution. The issue of smoothing ozone extremes by linearly interpolating from monthly values to the model time step still remains in CMIP6. Additionally, the prescribed ozone field, which was generated by averaging the output of two different CCMs (Keeble et al., 2020), is not consistent with the dynamics of the models to which it is prescribed, and, furthermore, feedbacks between ozone, temperature, and dynamics cannot occur. Moreover, Hardiman et al. (2019) showed that a mismatch between the tropopause height present in the prescribed ozone dataset and the tropopause height in the climate model that uses the prescribed ozone dataset can cause erroneous heating rates around the tropopause. These limitations suggest that there are still differences in atmospheric dynamics between climate models using the prescribed CMIP6 ozone and fully interactive CCMs. In this study, we test this hypothesis for the first time by comparing two ensembles of simulations with the new coupled climate model FOCI (Flexible Ocean Climate Infrastructure; Matthes et al., 2020): one ensemble in which the model uses interactive ozone chemistry and one ensemble in which the CMIP6 ozone is prescribed. We investigate differences in atmospheric dynamics with respect to both the mean state and multi-decadal trends over the second half of the twentieth century. Details about the climate model FOCI and our methodology can be found in Sect. 2. As the increase in anthropogenic GHGs was also reported to lead to changes in the SH circulation (Fyfe et al., 1999; Kushner et al., 2001), we first assess the extent to which the formation of the ozone hole and the increase in GHGs contribute to the changes simulated in FOCI in Sect. 3, and we verify the model's ability to simulate the effects of ozone depletion. We then compare the two ensemble simulations and evaluate the performance of the model with prescribed CMIP6 ozone against the interactive chemistry version of the model in Sect. 4. Finally, Sect. 5 presents the discussion of the results, together with our conclusion.

2 Model description and methodology

2.1 Model description and experimental design

The coupled climate model employed in this study is the new Flexible Ocean Climate Infrastructure (FOCI; Matthes et al., 2020). FOCI consists of the high-top atmospheric model ECHAM6.3 (Stevens et al., 2013) coupled to the NEMO3.6 ocean model (Madec and the NEMO team, 2016). Land surface processes and sea ice are simulated by the JSBACH (Brovkin et al., 2009; Reick et al., 2013) and LIM2 (Fichefet and Maqueda, 1997) modules, respectively. We use the T63L95 setting of ECHAM6, corresponding to 95 vertical hybrid sigma-pressure levels up to the model top at 0.01 hPa and approximately 1.8° by 1.8° horizontal resolution in the atmosphere. The ocean model, in the ORCA05 configuration (Biastoch et al., 2008), has a nominal global resolution of $1/2°$ and 46 z levels in the vertical. FOCI has an internally generated quasi-biennial oscillation (QBO) and includes variations in solar activity according to the recommendations of the SOLARIS-HEPPA project (Matthes et al., 2017) for CMIP6. For the interactive chemistry simulations used in this study, chemical processes were simulated using the Model for Ozone and Related Chemical Tracers (MOZART3; Kinnison et al., 2007), implemented in ECHAM6 (ECHAM6-HAMMOZ; Schultz et al., 2018). A detailed description of FOCI, including the configuration of ECHAM6-HAMMOZ and its chemical mechanism, can be found in the paper by Matthes et al. (2020). A 1500-year-long pre-industrial control simulation with FOCI, allowing for the proper spin-up of the model, serves as the starting point for the simulations described below.

Table 1 gives an overview of the simulations used in this study. Three ensembles, each consisting of three simulations differing only in their initial conditions, were conducted in order to distinguish between the effects of ozone depletion and those of increasing GHG concentrations on the SH climate. The first ensemble (REF) comprises transient simulations in which surface volume mixing ratios of both GHGs and ODSs are prescribed and vary as a function of time according to the historical CMIP6 forcing dataset (Meinshausen et al., 2017). Therefore, this ensemble captures the combined effects of ozone depletion and GHG increase. In the second ensemble (NoODS), CO_2 and CH_4 surface volume mixing ratios are prescribed and vary according to the historical forcing, but the ODSs follow a perpetual seasonal cycle representative of 1960 conditions, computed for each ODS by taking the mean annual cycle between 1955 and 1965. This ensemble was designed to simulate the effects of increasing GHGs in the absence of ozone depletion. Here, we use GHGs to refer to CO_2 and CH_4 only, while the other anthropogenic GHGs, including N_2O, fall under the ODS category. In the third ensemble (NoGHG), the ODSs vary according to the historical forcing, while GHGs follow a perpetual 1960 seasonal cycle, meaning that there is no increase

Table 1. Overview of the FOCI ensembles used in this study. Each ensemble consists of three simulations that vary in their initial conditions.

Ensemble	Ozone chemistry	GHGs	ODSs	Analysis period
FIXED O_3	prescribed CMIP6	historical CMIP6	historical CMIP6	1958–2002
INTERACT O_3	interactive	historical CMIP6	historical CMIP6	1958–2002
REF	interactive	historical CMIP6	historical CMIP6	1978–2002
NoODS	interactive	historical CMIP6	fixed at 1960s level	1978–2002
NoGHG	interactive	fixed at 1960s level	historical CMIP6	1978–2002

in GHGs past this date. This experimental design allows us to quantify the impact of the formation of the ozone hole by taking the difference between REF and NoODS and that of climate change by taking the difference between REF and NoGHG. All of these sensitivity simulations use the FOCI configuration that includes interactive chemistry such that the chemical–radiative–dynamical feedbacks are captured and the ozone field is consistent with the simulated dynamics. Additionally, the high-resolution ocean nest INALT10X (Schwarzkopf et al., 2019) was used for these simulations. Therefore, the REF ensemble differs from the INTERACT O_3 ensemble discussed below. The INALT10X nest enhances the ocean resolution to $1/10°$ over the South Atlantic Ocean, the western part of the Indian Ocean, and the corresponding Southern Ocean sectors, resolving the mesoscale eddies found in these regions and allowing us to assess, in a follow-up study, the influence of climate change and ozone depletion on the ocean circulation around the tip of South Africa.

In order to analyze the differences between simulations with interactive ozone chemistry and simulations with prescribed CMIP6 ozone, two further ensembles were performed, each consisting of three simulations differing only in their initial conditions. For the INTERACT O_3 ensemble, FOCI was run in the configuration with interactive chemistry such that the chemical reactions that are necessary to represent stratospheric chemical processes were included. Therefore, the feedbacks between the stratospheric ozone, temperature, and dynamics occur in INTERACT O_3 and the simulated ozone field is consistent with the dynamics. A comparison of the ozone field simulated in INTERACT O_3 with observations can be found in the work of Matthes et al. (2020). For the FIXED O_3 ensemble, the ozone field recommended for CMIP6 (Hegglin et al., 2016) was prescribed. The CMIP6 ozone field was generated by two CCMs and includes solar variations from the SOLARIS-HEPPA project (Matthes et al., 2017). It is a monthly mean three-dimensional field and therefore includes zonal asymmetries in ozone. The monthly mean values were linearly interpolated and prescribed at each model time step. The comparison of the INTERACT O_3 and FIXED O_3 ensembles sheds light on the impact of prescribing the CMIP6 chemistry on the climate simulated by the coupled climate model FOCI.

2.2 Observational data

The Integrated Global Radiosonde Archive (IGRA) version 2 (Durre et al., 2006) temperature was used in order to compare the temperature trends simulated by the FOCI ensembles with observational estimates. Data from 11 Antarctic stations located south of 65° S offering sufficient coverage for the period 1958–2002 were averaged for each day and pressure level up to 30 hPa. As only the South Pole station is located south of 80° S, a trend computed for the entire polar cap is biased towards the lower latitudes, and only the trend derived from the spatial average over the 65–80° S latitude band is shown in Fig. 10. The full polar cap IGRA temperature trend is sown in the Supplement in Fig. S5. In addition, the temperature and wind from the ERA5 reanalysis (Hersbach et al., 2020) were used to further verify the trends obtained from our model.

2.3 Methodology

We used the transformed Eulerian mean framework (Andrews et al., 1987) to calculate the residual circulation and its forcing. According to the downward control principle of Haynes et al. (1991), the residual downward velocity $\overline{w^*}$ at a certain level is driven by the wave dissipation at the levels above. The divergence of the Eliassen–Palm (EP) flux, $(a\cos\phi)^{-1}\nabla\cdot F$, gives a measure of the dissipation of resolved waves, where

$$\nabla\cdot F = \frac{1}{a\cos\phi}\frac{\partial(F_\phi\cos\phi)}{\partial\phi} + \frac{\partial F_\mathrm{p}}{\partial p}. \tag{1}$$

The components of the EP flux are given by

$$F_\phi = -a\cos\phi\overline{v'u'}, \tag{2}$$

$$F_\mathrm{p} = fa\cos\phi\frac{\overline{v'\theta'}}{\overline{\theta_\mathrm{p}}}. \tag{3}$$

The notation is the same as in Andrews et al. (1987): the overbars denote the zonal mean and the primes denote departures from the zonal mean, a is the radius of the Earth, ϕ is the latitude, u and v are the zonal and meridional velocity components, respectively, f is the Coriolis parameter, θ is the potential temperature, and θ_p is the partial derivative of θ with respect to pressure. The residual vertical velocity

was calculated from the streamfunction, as in McLandress and Shepherd (2009):

$$\overline{w^*} = \frac{gH}{pa\cos\phi}\frac{\partial\Psi}{\partial\phi}, \tag{4}$$

where the streamfunction is given by

$$\Psi = -\frac{\cos\phi}{g}\int_{\mathrm{p}}^{0}\overline{v^*}(\phi, p)\mathrm{d}p, \tag{5}$$

and the meridional residual velocity is given by

$$\overline{v^*} = \overline{v} - \frac{\partial}{\partial p}\left(\frac{\overline{v'\theta'}}{\overline{\theta_{\mathrm{p}}}}\right), \tag{6}$$

with g being the gravitational acceleration and H the scale height taken as 7000 m. The shortwave (SW) and longwave (LW) heating rates are part of the standard FOCI output, and the total radiative heating rate was obtained by taking the sum of the two. The dynamical heating rate was calculated as the difference between the temperature tendency at daily resolution and the total radiative heating rate.

The SAM was computed as the first empirical orthogonal function (EOF) of the daily zonal mean geopotential height anomalies at each pressure level following the method outlined in Gerber et al. (2010). To obtain the geopotential height anomalies, the weighted global mean geopotential height was first subtracted for each day and at each level and latitude. A slowly varying climatology was then removed to ensure that the resulting SAM index does not exhibit any long-term trend driven by external climate forcing such that it only reflects internal variability. The slowly varying climatology was obtained by applying a 60 d low-pass filter to the geopotential height anomalies from the global mean. Then, time series were created for each day of the year and at each location from the filtered anomalies, and each time series was smoothed using a 30-year low-pass filter. The smoothed time series were subtracted from the anomalies with respect to the global mean for each respective day and location. The anomalies thus obtained were multiplied by the square root of the cosine of latitude in order to account for the convergence of the meridians towards the poles (North et al., 1982), and only the anomalies for the SH were retained. The first EOF of these anomalies was calculated at each pressure level, and the expansion coefficients (principle component time series) were obtained by projecting the anomalies onto the first EOF pattern. The expansion coefficients give the SAM index, normalized to have zero mean and unit variance.

The SAM e-folding timescale was computed for each day of the year at each pressure level using the method of Simpson et al. (2011). The autocorrelation function (ACF) was obtained by correlating the time series for a particular day of the year with the time series for the days lagging and leading it. The ACF was smoothed at each lag and pressure level by applying a Gaussian filter with a full width at half-maximum of 42 d over a 181 d window. An exponential function was then fitted to the smoothed ACF up to a lag of 50 d using the least squares method, and the SAM timescale was obtained by taking the lag at which the exponential function drops to $1/e$.

Linear trends were calculated over the 1958–2002 period for the analyzed fields at each level and location, and the significance of the trends was assessed based on a Mann–Kendall test. Where differences between simulations are shown, a two-sided t test was used to test for significance. The significance is always given at the 95 % confidence interval. The differences between the REF and the NoODS or NoGHG ensembles were computed over the 1978–2002 period, as this is the period characterized by the strongest ozone depletion.

3 Impacts of ozone depletion and climate change on Southern Hemisphere dynamics

The radiative effects of increasing GHG concentrations lead to cooling of the stratosphere and warming of the troposphere, enhancing the meridional temperature gradient at the tropopause levels in a similar manner to ozone depletion. While some older studies argued that rising levels of GHGs are the driver of the historical dynamical changes in the SH (Fyfe et al., 1999; Kushner et al., 2001; Marshall et al., 2004), at present the general consensus is that the formation of the Antarctic ozone hole is the main cause of these dynamical changes in austral spring and summer and that increasing GHGs played only a secondary role (Arblaster and Meehl, 2006; McLandress et al., 2011; Polvani et al., 2011; Keeble et al., 2014; Previdi and Polvani, 2014; World Meteorological Organization, 2018). In this section, we separate the effects of ozone depletion from those of increasing GHGs in FOCI, and we verify the ability of the model to correctly simulate the dynamical response to ozone loss.

Figure 1 shows the reduction in ozone above the Antarctic polar cap caused by ODSs (panel a) together with the accompanying changes in the SW heating rate (panel b). There is a strong decrease in the ozone volume mixing ratio in the lower stratosphere in austral spring, peaking in October, in agreement with previous studies (Perlwitz et al., 2008; Son et al., 2010; Polvani et al., 2011; Eyring et al., 2013). This leads to a significant radiative cooling due to decreased absorption of SW radiation (Fig. 1b). An even stronger SW cooling can be seen above 5 hPa between September and April, in line with the results of Langematz et al. (2003), who found a reduction of the SW heating rate in the upper stratosphere in response to decreasing ozone concentrations. A significant SW warming appears in December and January between 50 and 10 hPa, related to an increased ozone mixing ratio. As will be shown later in this section, these latter changes are attributed to a dynamical response to the spring ozone loss.

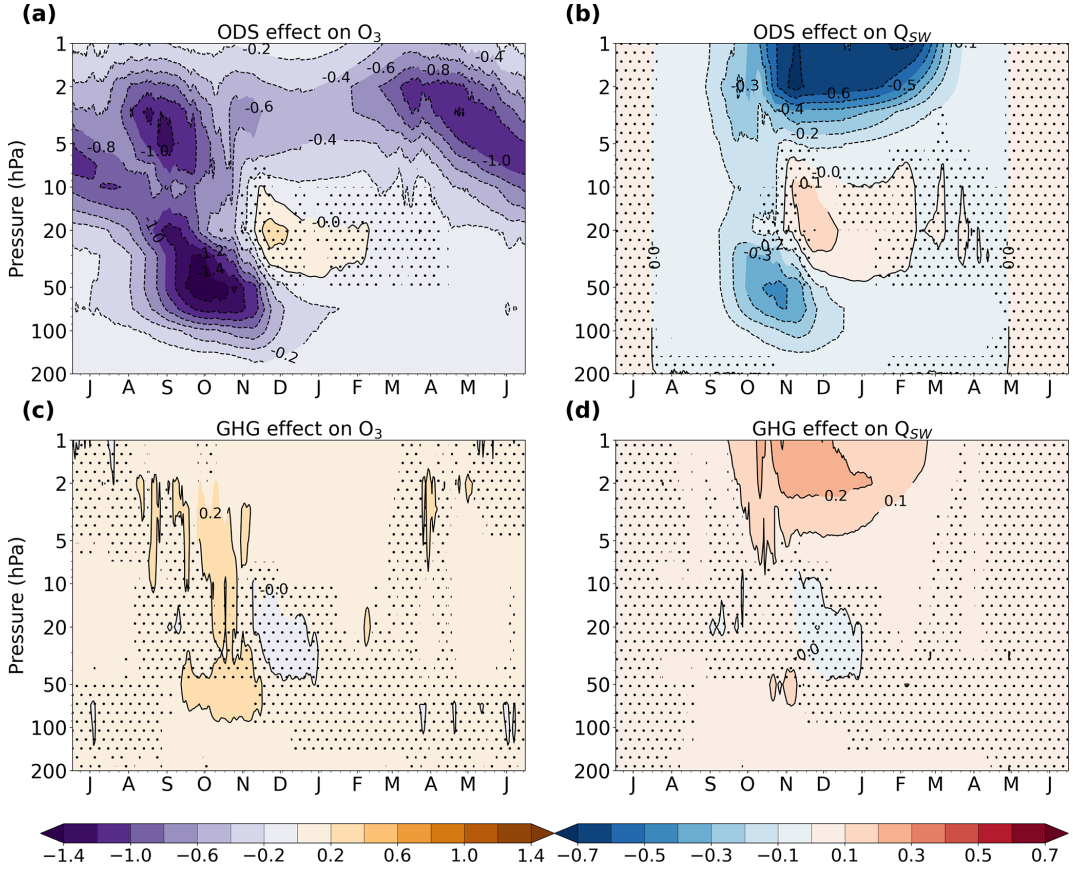

Figure 1. Seasonal cycle of the difference between REF and NoODS **(a, b)** and between REF and NoGHG **(c, d)** in the ozone volume mixing ratio (**a, c**; ppmv) and the SW heating rate (**b, d**; $\mathrm{K\,d^{-1}}$) averaged over the polar cap (70–90° S) for the period 1978–2002. Stippling masks values that are not significant at the 95 % confidence interval. The letter corresponding to each month marks the middle of that month.

Figure 1c shows the ozone changes caused by increasing GHGs. There are two regions of statistically significant ozone increase: the upper stratosphere in austral spring and summer and the region of the ozone hole. The SW heating rate (Fig. 1d) exhibits warming in response to increased GHGs in the same two regions. As the direct effect of GHGs on the SW heating rate is small (Langematz et al., 2003), this warming is likely caused by the higher ozone levels arising in response to the GHG increase, and not directly by the GHGs themselves. Higher levels of GHGs lead to increased emissions of LW radiation (not shown) and have a net cooling effect in the stratosphere. In the upper stratosphere, lower temperatures slow down ozone depletion (Haigh and Pyle, 1982; Jonsson et al., 2004; Stolarski et al., 2010; Chiodo et al., 2018), explaining the simulated increase in ozone. The ozone increase in the lower stratosphere is more surprising. Here, colder conditions facilitate the formation of PSCs and are therefore expected to enhance ozone loss. Solomon et al. (2015) showed that a cooling of 2 K results in 30 DU more total column ozone loss over Antarctica. Therefore, it does not seem likely that the elevated ozone levels are caused by the radiative effects of GHGs. Instead, we find a small but significant enhancement of the downwelling over the polar cap between 50 and 200 hPa in the second half of October, which is associated with increased wave forcing between 20 and 100 hPa (not shown). This suggests that changes in dynamics are responsible for transporting more ozone into the polar lower stratosphere, in agreement with previous studies that linked a GHG-induced acceleration of the BDC to a decrease in lower-stratospheric ozone in the tropics and an increase at high latitudes (Dietmüller et al., 2014; Nowack et al., 2015; Chiodo et al., 2018). As a result, the stratospheric ozone depletion is stronger in the absence of increased GHGs (NoGHG experiments) than in their presence (REF experiments). The ozone increase related to GHGs of about 0.2 ppmv, however, is small compared to the ozone loss due to ODSs, which exceeds 1.4 ppmv in the region of strongest depletion.

The polar cap temperature response to ozone depletion (Fig. 2a) is closely related to the changes in the SW heating rate shown in Fig. 1b. A statistically significant cooling occurs in the lower stratosphere in austral spring and in the upper stratosphere in summer. Additionally, there is a warming above the ozone hole in late spring. It should be noted

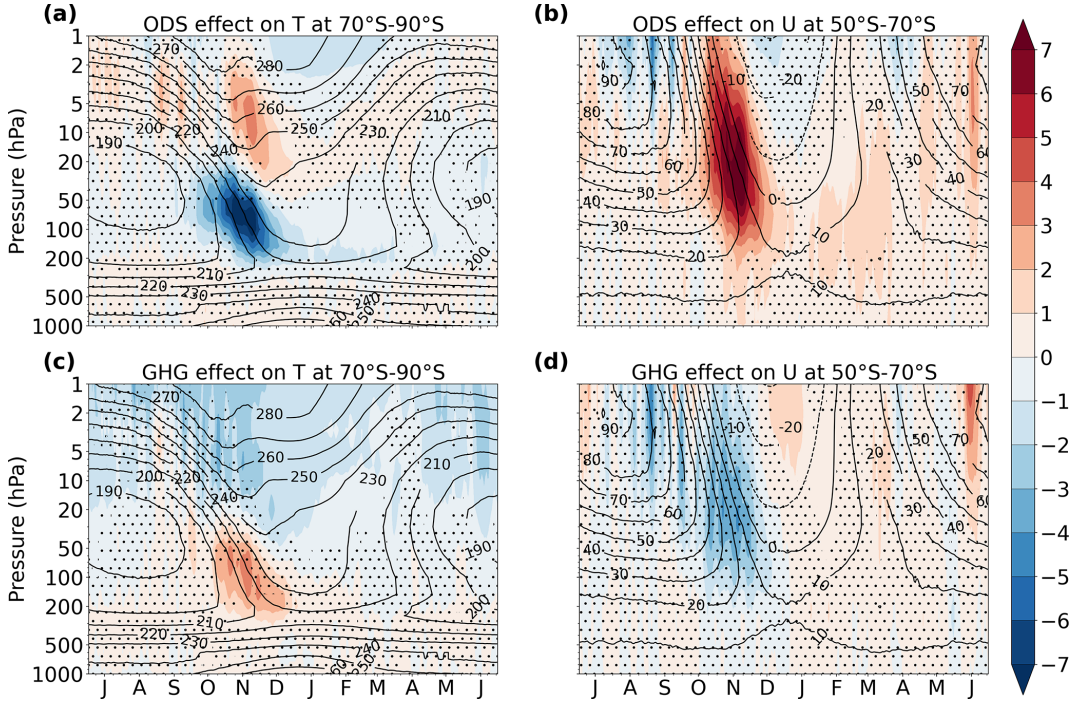

Figure 2. Seasonal cycle of the difference between REF and NoODS **(a, b)** and between REF and NoGHG **(c, d)** in the polar cap (70–90° S) temperature (**a, c**; K) and in the midlatitude (50–70° S) zonal wind (**b, d**; $\mathrm{m\,s^{-1}}$) for the period 1978–2002 (color shading). Stippling masks values that are not significant at the 95 % confidence interval. Contours show the corresponding climatological temperature and zonal wind from REF. The letter corresponding to each month marks the middle of that month.

that the maximum temperature increase above the ozone hole occurs about 1 month earlier than the maximum shortwave warming, hinting at the fact that it is not a direct radiative effect of the increase in ozone. The temperature decreases are a direct response to ozone depletion. The spring cooling in the lower stratosphere represents the well-known signature of the ozone hole. In contrast to the impact of the ozone hole, there is no significant cooling in the polar lower stratosphere due to increased GHGs (Fig. 2c). The cooling resulting from enhanced LW emissions is confined to the upper levels of the stratosphere. The lower stratosphere warms in November in response to GHGs. At these levels the SW warming (Fig. 1d) due to the elevated ozone concentrations dominates the LW cooling (not shown) due to GHGs, resulting in a net radiative warming.

The zonal wind changes associated with ozone depletion (Fig. 2b) and increasing GHGs (Fig. 2d) obey the thermal wind balance. The polar night jet accelerates from October onwards as a consequence of the enhanced meridional temperature gradient caused by ozone loss. The maximum acceleration occurs between November and December (Fig. 2b), concomitant with the strongest cooling (Fig. 2a). This westerly acceleration propagates downwards to the tropospheric eddy-driven jet and reaches the surface in November and December. Figure 3a shows the ozone-induced change in the surface zonal wind for these months. The surface westerlies strengthen on their poleward side and weaken on their equatorward side, shifting poleward. This shift is accompanied by changes in sea level pressure (SLP). The pressure over Antarctica drops significantly and the midlatitude SLP increases in response to ozone depletion (Fig. 3c), signaling a change towards the positive phase of the SAM. All these changes in the SH dynamics simulated in FOCI in response to ozone depletion, both in the stratosphere and in the troposphere, are in good agreement with the results of previous studies that isolated the impacts of ozone loss from those of the increase in GHGs (Arblaster and Meehl, 2006; McLandress et al., 2010, 2011; Polvani et al., 2011; Keeble et al., 2014), as well as with the trends from observations and the ERA5 reanalysis presented in Sect. 4. This demonstrates that FOCI is able to capture the effects of ozone depletion and is therefore suited to studying how prescribing the CMIP6 ozone affects the simulated climate response to ozone loss.

The response of the stratospheric westerlies to higher GHG concentrations is markedly different from that to ozone depletion (Fig. 2b, d). Driven by the warming over the polar cap, the polar night jet weakens in November south of 60° S (Fig. S1 in the Supplement). This change is much weaker compared to that resulting from ozone loss and is confined to the stratosphere. While GHGs do not cause an acceleration of the polar night jet in FOCI, there is a significant positive change in the zonal wind strength centered around

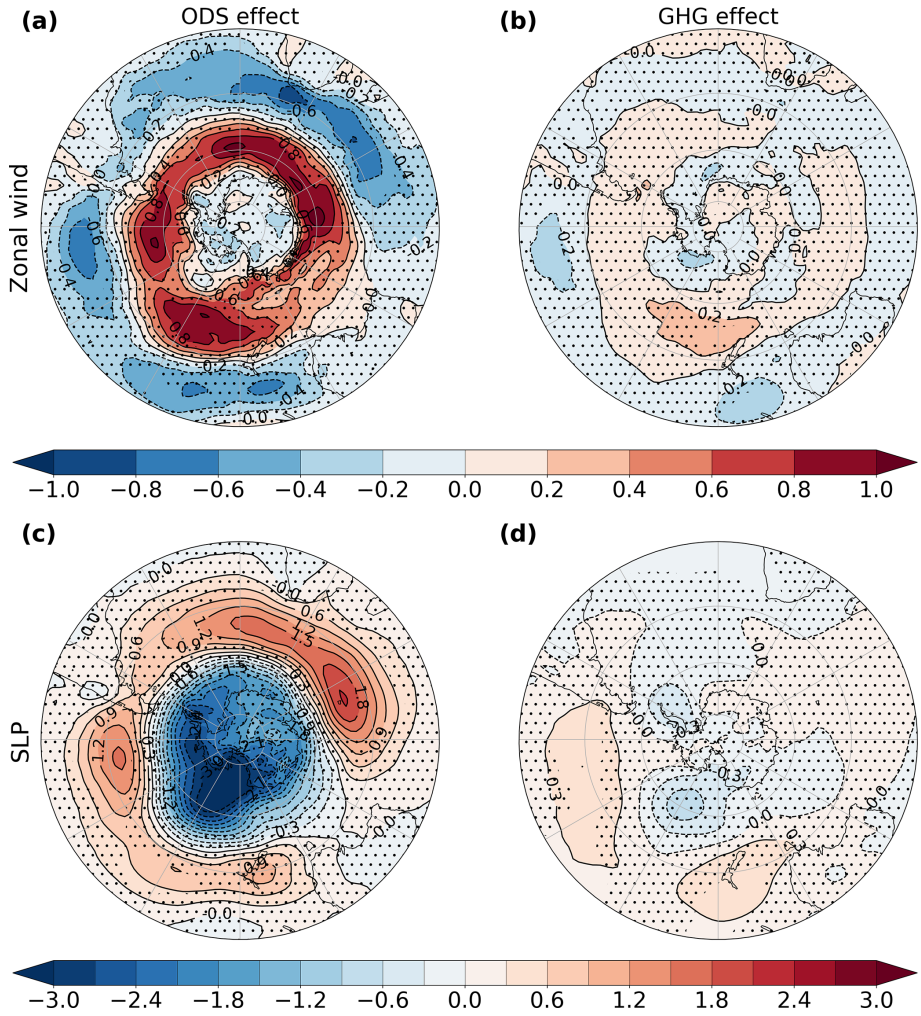

Figure 3. Polar stereographic maps of the November–December difference between REF and NoODS **(a, c)** and the annual mean difference between REF and NoGHG **(b, d)** in the surface zonal wind (**a, b**; $\mathrm{m\,s^{-1}}$) and in sea level pressure (**c, d**; hPa) for the period 1978–2002. Stippling masks values that are not significant at the 95 % confidence interval.

30° S, extending from the top of the eddy-driven jet into the middle stratosphere (Fig. S1). This westerly change implies a strengthening of the upper flank of the tropospheric jet, in agreement with the findings of McLandress et al. (2010). Figure 3b shows a map of the annual mean GHG-induced changes in the surface zonal winds. We show the annual mean change due to GHGs and not the November–December change as for the case of ozone depletion because, unlike the effects of ozone loss, the effects of increasing GHGs do not exhibit any seasonality. Although the GHG-induced pattern of zonal wind change is similar to that caused by ozone depletion, the changes are much weaker and mostly insignificant. This indicates that the magnitude of GHG increase was not large enough to induce a strong strengthening or poleward shift of the surface westerly winds. The SLP response to increasing GHGs exhibits a significant increase in the mid-latitudes over the South Pacific Ocean, but the magnitude of this increase is less than a quarter of that due to ozone loss and there is no significant SLP decrease over the polar cap.

Our sensitivity experiments confirm that the changes in the SH polar night jet (Fig. 2b, d) and eddy-driven jet (Fig. 3a, b) during the later part of the twentieth century were mainly driven by ozone depletion. Increasing GHGs have played only a minor role, acting to enhance the effect of the ozone hole in the troposphere and to partially counteract the impact of ozone loss on the polar night jet. In addition, we found that the upper stratosphere has cooled significantly and the troposphere has warmed significantly in response to increasing concentrations of GHGs.

Having distinguished the contributions of ozone loss and rising GHG levels to the changes in the westerly winds, we now turn our attention to the impacts of ozone depletion on the BDC. Figure 4 shows the November ozone-induced changes in the residual circulation, which is commonly used as a proxy for the BDC. The residual circulation is primarily

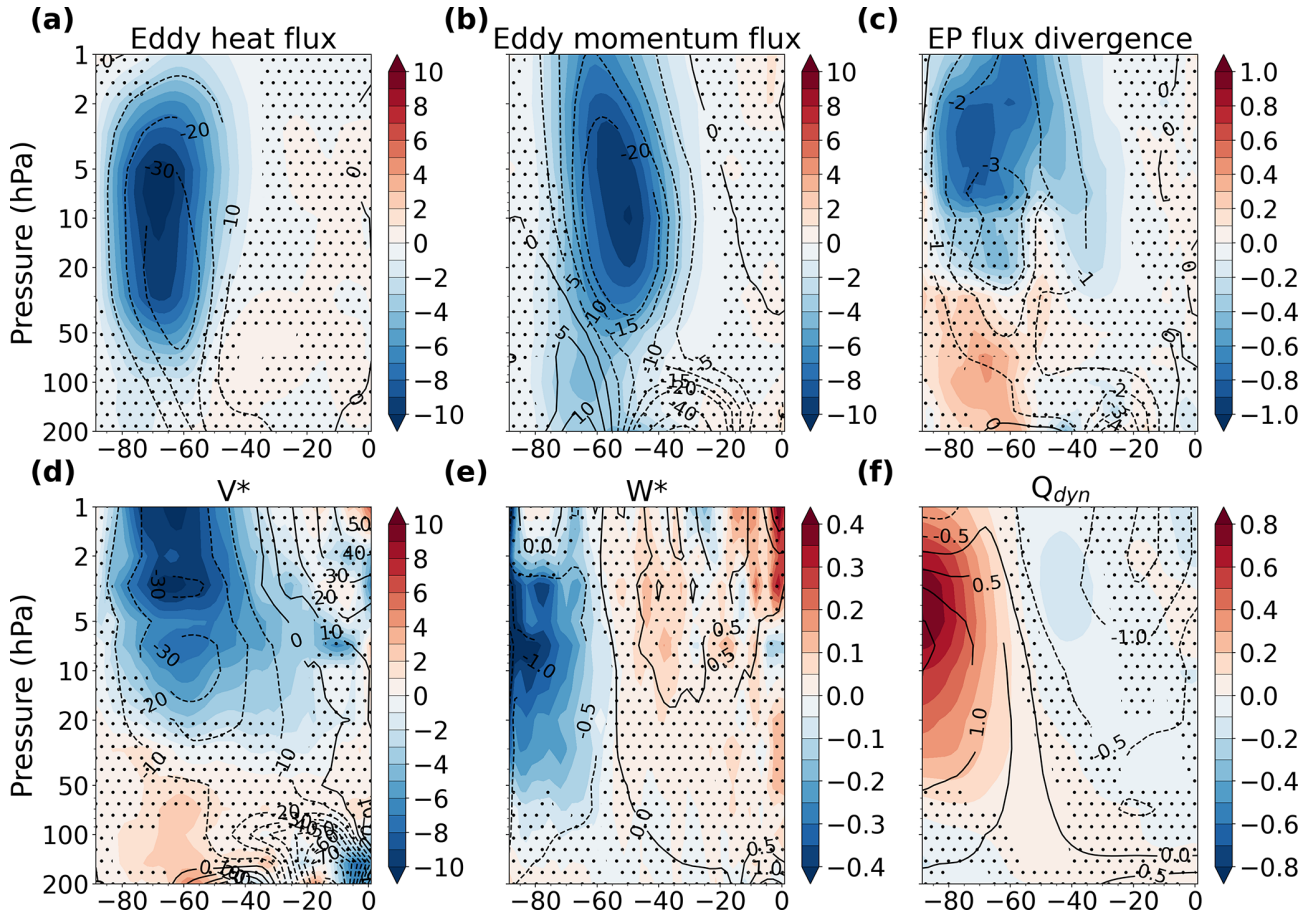

Figure 4. November latitude–height difference between REF and NoODS in the eddy heat flux (**a**; $\mathrm{K\,m\,s^{-1}}$), the eddy momentum flux (**b**; $\mathrm{m^2\,s^{-2}}$), the divergence of the EP flux (**c**; $\mathrm{m\,s^{-1}\,d^{-1}}$), the meridional residual velocity (**d**; $\mathrm{cm\,s^{-1}}$), the vertical residual velocity (**e**; $\mathrm{mm\,s^{-1}}$), and the dynamical heating rate (**f**; $\mathrm{K\,d^{-1}}$) for the period 1978–2002 (color shading). Contours in each panel show the corresponding climatology from REF. Stippling masks values that are not significant at the 95 % confidence interval.

forced by the dissipation of vertically propagating planetary waves from the troposphere. Therefore, we also present in Fig. 4 the changes in eddy heat and momentum fluxes, which reveal the direction of wave propagation, and the changes in the divergence of the EP flux, which measures the wave forcing. The EP flux divergence (Fig. 4c) is characterized by a significant negative change above 10 hPa (stronger convergence) and a significant positive change (weaker convergence) in the lower stratosphere below 50 hPa. This implies a reduction of wave dissipation in the lower stratosphere and an increase above, suggesting that atmospheric waves propagating from the troposphere reach higher into the stratosphere. This is confirmed by the strengthening of the eddy heat flux above 50 hPa (Fig. 4a). The eddy heat flux is equivalent to the vertical component of the EP flux and gives a measure of the vertical propagation of resolved waves. This strengthening entails increased wave propagation in the middle and upper stratosphere. Similarly, the eddy momentum flux exhibits a negative change, implying increased equatorward wave propagation (Fig. 4b). The ability of the waves to propagate deeper into the stratosphere is related to the strengthening of the polar night jet in response to ozone depletion. Enhanced westerly velocities in November lead to a delay in the breakdown of the polar vortex (e.g., Waugh et al., 1999; Langematz et al., 2003) and sustain wave activity. McLandress et al. (2010) showed that, as a result of ozone depletion, (1) the height of the transition between westerly and easterly velocities has increased, implying that waves can propagate higher at the end of spring, and (2) the date of this transition has been delayed by 10 to 15 d, implying that the period during which waves can penetrate into the stratosphere has been prolonged. As a result, the wave drag due to the dissipation of resolved waves increased in the upper stratosphere and decreased in the lower stratosphere in November (Fig. 4c), while it increased in the middle stratosphere in December (Fig. S2), driving similar changes in the residual circulation. In November, the residual meridional velocity (Fig. 4d) shows a significant poleward intensification above 20 hPa and a significant weakening below 50 hPa, in good agreement with the changes in the EP flux

divergence. The downwelling over the polar cap is enhanced above 50 hPa (Fig. 4e). Associated with this intensification is a large dynamical warming (Fig. 4f) that increases the temperature above the ozone hole, as shown in Fig. 2a, consistent with the results of Mahlman et al. (1994), Li et al. (2008), Stolarski et al. (2010), Keeble et al. (2014), and Ivy et al. (2016). At the same time, the strengthening of the residual circulation transports more ozone to the polar regions, leading to the increase in ozone seen in December between 50 and 10 hPa in Fig. 1a. The residual vertical velocity in the lower stratosphere is expected to weaken in response to the decreased wave drag seen in Fig. 4c below 50 hPa. Such a weakening is simulated in FOCI at 200 hPa (Fig. 4e), accompanied by a decrease in dynamical heating (Fig. 4f). However, the lower-stratospheric change in downwelling is not significant at the 95 % confidence interval, and the change in the dynamical heating is only partly significant. The decrease in austral spring lower stratosphere downwelling was previously reported by Li et al. (2008), McLandress et al. (2010), and Lubis et al. (2016), while the decrease in dynamical heating was shown by Keeley et al. (2007), Orr et al. (2013), and Lubis et al. (2016). Consistent with our results, McLandress et al. (2010) also attributed their weaker downwelling to reduced wave drag in the austral spring. We note that Fig. 4 displays changes averaged for the entire month of November. However, the analysis of Orr et al. (2012, 2013) using 15 d averages showed that, at this time of the year, changes in the lower stratosphere wave driving and dynamical heating due to ozone depletion occur over a shorter time. Therefore, it is likely that our November averaging is applied over periods exhibiting changes of different sign, consequently diminishing the magnitude of the change and rendering it insignificant. At the same time, the large internal variability in FOCI makes it hard to discern this change using fields with higher temporal resolution, and more ensemble members would be needed to clearly detect the weakening in downwelling.

The temporal evolution of the ozone-driven changes in wave forcing and, as a result, in the residual circulation can be seen by comparing Fig. 4 with Fig. S2, which shows the same quantities but for December. It is clear that there is a downward propagation of the changes in all quantities from November to December. As the polar vortex breaks down at the upper levels, the zonal velocities remain westerly below 50 hPa (contours in Fig. 2b) and are still able to support the remnant wave propagation. Stronger westerlies in the lower stratosphere in December imply enhanced wave dissipation. As a result, the downwelling is accelerated in the lower stratosphere, driving dynamical warming there. These results are consistent with those of McLandress et al. (2010) and explain the reason behind the change in the sign of the residual vertical velocity trends in the lower stratosphere between spring and summer.

Our results clearly show that ozone depletion had a significant influence on the SH BDC in austral spring and summer. FOCI simulates little significant residual circulation change in the SH due to increasing GHGs. Therefore, we conclude that the historical changes in the SH residual circulation over the period of ozone depletion are a consequence of the formation of the ozone hole, in line with the findings of Keeble et al. (2014), Oberländer-Hayn et al. (2015), Polvani et al. (2018), Li et al. (2018), Abalos et al. (2019), and the most recent Scientific Assessment of Ozone Depletion (World Meteorological Organization, 2018). Consistent with these studies, FOCI simulates a strengthening of the SH residual circulation in response to enhanced wave forcing at the end of the spring and the beginning of summer. At the same time, a weakening of the spring lower stratosphere residual circulation is simulated, as found by the few studies that investigated springtime changes in the BDC (Li et al., 2008; McLandress et al., 2010; Lubis et al., 2016). The good agreement with previous studies demonstrates that the interactive chemistry configuration of FOCI adequately simulates the impact of ozone depletion on the residual circulation.

4 Effects of prescribing the CMIP6 ozone field

We aim to understand how prescribing the ozone field recommended for CMIP6 affects the SH atmospheric circulation response to ozone depletion. To this end, we compare an ensemble of simulations using prescribed CMIP6 ozone with an ensemble of simulations that use fully interactive chemistry. The use of an ozone field that differs from that internally simulated by the model and that is not consistent with the model dynamics, the lack of chemical–radiative–dynamical feedbacks, and the temporal interpolation from the monthly prescribed values to the model time step can all lead to differences between the two ensembles. With a view on these deficiencies, we begin by analyzing the differences in the mean state in Sect. 4.1, and we then compare the simulated SH variability in Sect. 4.2 and the persistence of the SAM in Sect. 4.3.

4.1 Effects on the mean state

Figure 5 shows the difference between INTERACT O_3 and FIXED O_3 in October average ozone and November average temperature, geopotential height, and zonal wind at 70 hPa. The CMIP6 ozone field was used for FIXED O_3. FOCI simulates significantly lower ozone levels above the Antarctic Peninsula and the Bellingshausen Sea in October compared to the CMIP6 ozone (Fig. 5a). As a consequence, the November temperature (Fig. 5b) and the geopotential height (Fig. 5c) are also lower in this region in INTERACT O_3 compared to FIXED O_3. We note that the pattern of the temperature difference between INTERACT O_3 and FIXED O_3 is markedly different to the pattern reported by Crook et al. (2008) and Gillett et al. (2009), which arises due to zonal asymmetries in ozone. The CMIP6 ozone field prescribed in FIXED O_3 includes ozone asymmetries, and their effects are

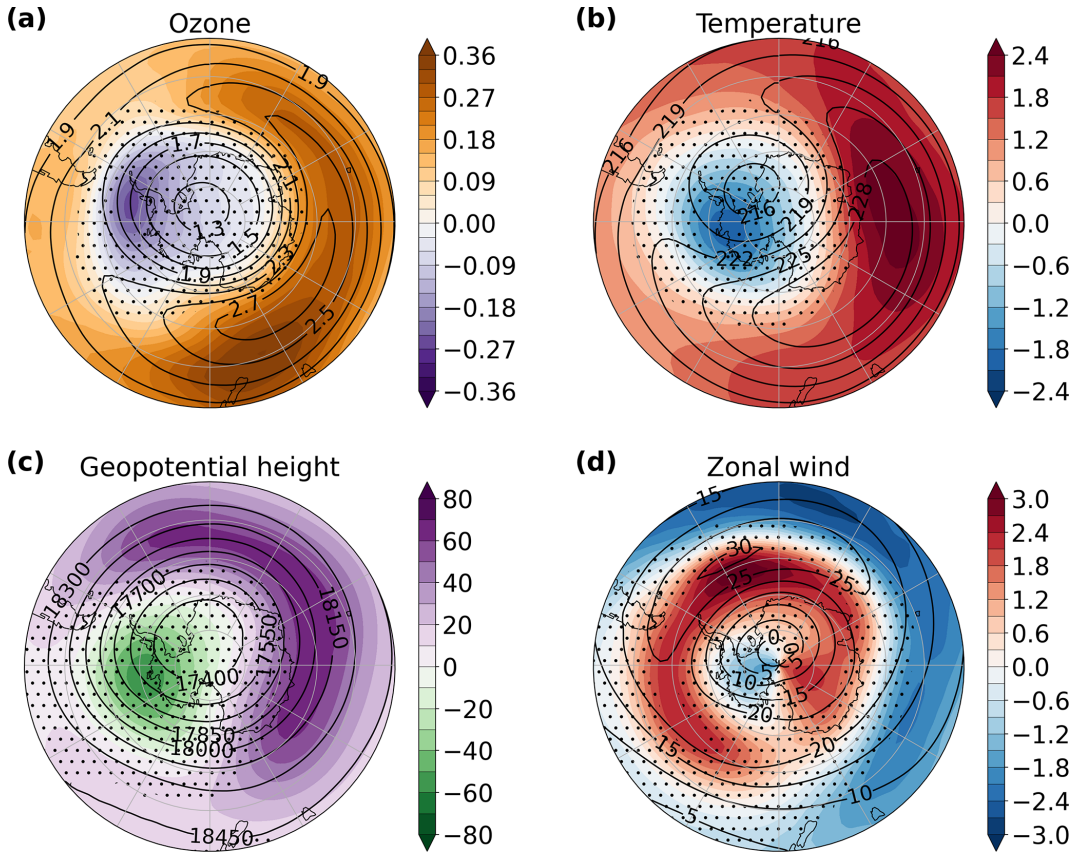

Figure 5. Polar stereographic maps of the difference between INTERACT O_3 and FIXED O_3 in the October mean ozone (**a**; ppmv) and the November mean temperature (**b**; K), geopotential height (**c**; m), and zonal wind (**d**; $m\,s^{-1}$) at 70 hPa (color shading). The stippling masks regions that are not significant at the 95 % confidence interval. The overlaying contours mark the 1958–2013 INTERACT O_3 climatology of each respective variable and month.

therefore captured in FIXED O_3. Despite this, spatial temperature and geopotential height differences still remain between simulations with prescribed ozone asymmetries and simulations with fully interactive ozone chemistry because the prescribed ozone field differs from the simulated one and is not consistent with the simulated dynamics.

The differences between the FOCI and CMIP6 ozone fields are not confined just to the ozone hole itself. Outside the polar vortex, INTERACT O_3 exhibits significantly higher ozone levels at all longitudes. The difference in ozone maximizes in the eastern hemisphere, as the polar vortex, and hence the ozone hole, is not centered over the pole but displaced towards the Atlantic Ocean and South America (contours in Fig. 5a). This significant positive difference was found in the middle to high latitudes of both hemispheres and in all seasons (not shown). We hypothesize that it is the result of a stronger BDC in FOCI compared to the models used to generate the CMIP6 ozone field, leading to increased ozone transport from the tropics. Associated with the higher ozone levels, the November midlatitude temperature and geopotential height are also elevated in INTERACT O_3 compared to FIXED O_3. In the Atlantic and Indian sectors, the higher temperature outside the polar vortex in INTERACT O_3 enhances the meridional pressure gradient between the polar low and the midlatitude high. In the Pacific sector, the meridional pressure gradient is stronger in INTERACT O_3 due to the lower temperature above West Antarctica and the Bellingshausen Sea. As a result, the November polar night jet is circumpolarly stronger in INTERACT O_3 compared to FIXED O_3 (Fig. 5d).

To better understand the cause of the lower ozone levels above the Antarctic Peninsula and the Bellingshausen Sea in INTERACT O_3, Fig. 6c shows the October average ozone anomalies from the zonal mean in INTERACT O_3 at 70 hPa and the difference to FIXED O_3. A zonal wavenumber one pattern is clearly visible, with the ridge at the edge of Antarctica towards New Zealand and the trough over the tip of the Antarctic Peninsula. The ozone wave simulated in FOCI is consistent with that inferred from satellite observations by Lin et al. (2009) and Grytsai et al. (2007), from reanalyses by Crook et al. (2008), and with that simulated by Gillett et al. (2009). This wave pattern confirms that the simulated ozone hole is not centered on the South Pole. While the CMIP6 ozone hole is also displaced from the pole, its location and

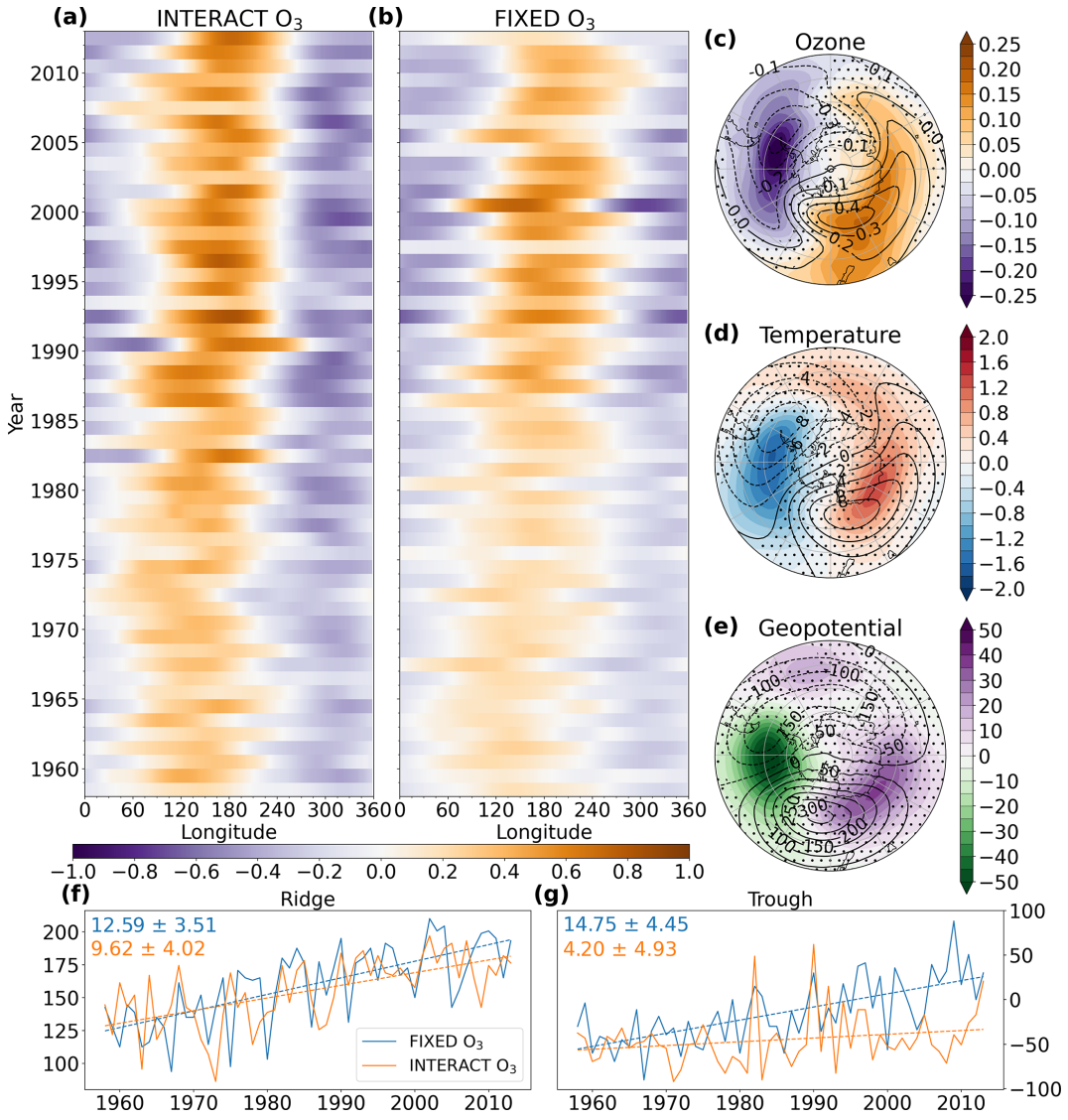

Figure 6. Hovmöller diagram of the October anomalies from the zonal mean ozone volume mixing ratio (ppmv) in INTERACT O_3 **(a)** and FIXED O_3 **(b)** averaged over 60–70° S and maps of the October difference between INTERACT O_3 and FIXED O_3 in the anomalies from the zonal mean ozone volume mixing ratio (**c**; ppmv), temperature (**d**; K), and geopotential height (**e**; m) at 70 hPa for the period 1958-2013 (color shading). The stippling in panels **(c)**–**(e)** masks regions that are not significant at the 95 % confidence interval. The overlaying contours mark the INTERACT O_3 1958–2013 average anomalies from the zonal mean for each respective variable. Time series of the longitude of the ozone ridge maximum **(f)** and of the ozone trough minimum **(g)** for INTERACT O_3 (solid orange lines) and FIXED O_3 (solid blue lines), together with their corresponding trends for the period 1958–2013 (dashed lines). The values of the trends are in degrees of longitude per decade, and their 95 % confidence interval according to a two-tailed t test is given in the upper left corner of each panel.

extent are not the same as those simulated by FOCI (compare contours in Fig. 7a and d). The difference shown in Fig. 6c reveals that, on the one hand, the trough of the wave is shifted towards South America and reaches deeper into the Pacific sector in INTERACT O_3. On the other hand, the amplitude of the wave is significantly greater in INTERACT O_3 (also compare contours in Fig. 8a and b). Figure 6c thus demonstrates that the prescribed CMIP6 ozone field is not spatially consistent with the polar vortex simulated in FOCI.

Figure 6a and b show the time evolution of the ozone wave averaged between 60 and 70° S for the month of October for INTERACT O_3 and FIXED O_3, respectively. Despite considerable interannual variability, the westward shift of the wave in INTERACT O_3 compared to that in FIXED O_3 is clearly discernable. This can be attributed to different evolutions of the wave trough in the two ensembles. Figure 6f and g show the time series of the longitudes at which the ozone maximum occurs within the ridge of the wave and at which the ozone minimum occurs within the trough of the wave, re-

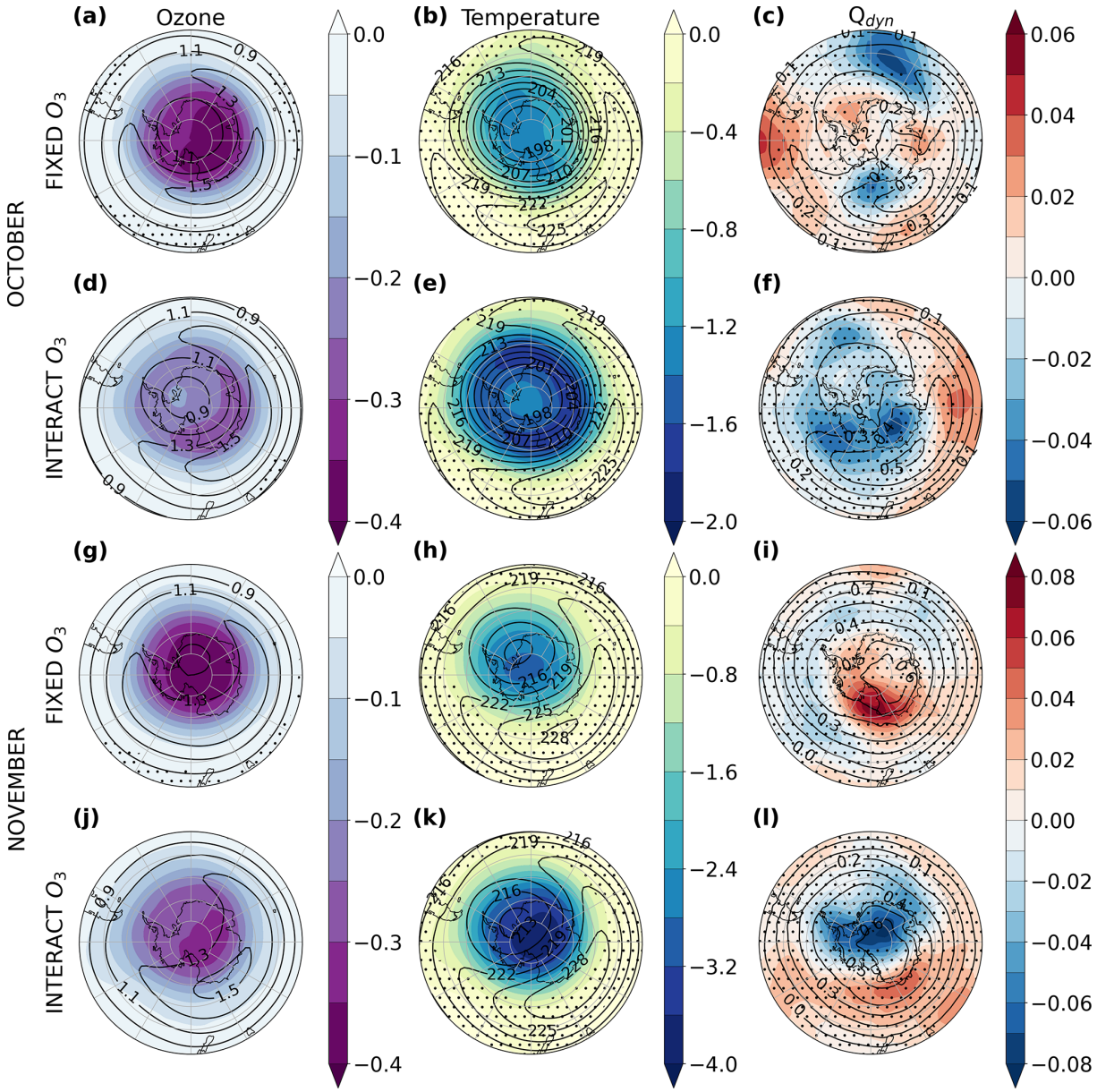

Figure 7. Polar stereographic maps of the October **(a–f)** and November **(g–l)** trends in ozone (**a, d, g, j**; ppmv per decade), temperature (**b, e, h, k**; K per decade), and dynamical heating rate (**c, f, i, l**; $K\,d^{-1}$ per decade) at 100 hPa for FIXED O_3 **(a–c, g–i)** and INTERACT O_3 **(d–f, j–l)** over 1958–2002 (color shading). Stippling masks regions where the trends are not significant at the 95 % confidence level. The overlaying contours show the respective climatologies for 1958–2002.

spectively, together with their corresponding trends. While the FIXED O_3 trough exhibits a significant eastward shift of $14.75 \pm 4.45\,^\circ$ per decade, the INTERACT O_3 trough does not exhibit a significant shift. In the time mean, this results in the INTERACT O_3 ozone trough being located more to the west than the FIXED O_3 trough. The ridge of the wave shifts eastwards in both ensembles (Fig. 6f). Although the magnitude of the shift is stronger in FIXED O_3, the trends are not significantly different, as they fall within each other's 95 % confidence intervals. Both ozone fields exhibit a deepening of the wave pattern over time, in particular in the 1980s, as the ozone hole becomes stronger, in agreement with the increase in the ozone wave amplitude reported by Grytsai et al. (2007) and Crook et al. (2008). In addition, the slow eastward shift of the wave with time is consistent with the phase shift based on temperature observations reported by Lin et al. (2009). An eastward shift of the ozone zonal wave one was also inferred from satellite observations by Grytsai et al. (2007), accompanied by a westward-shifting zonal wavenumber two. Due to the superposition of the two wavenumbers, only the

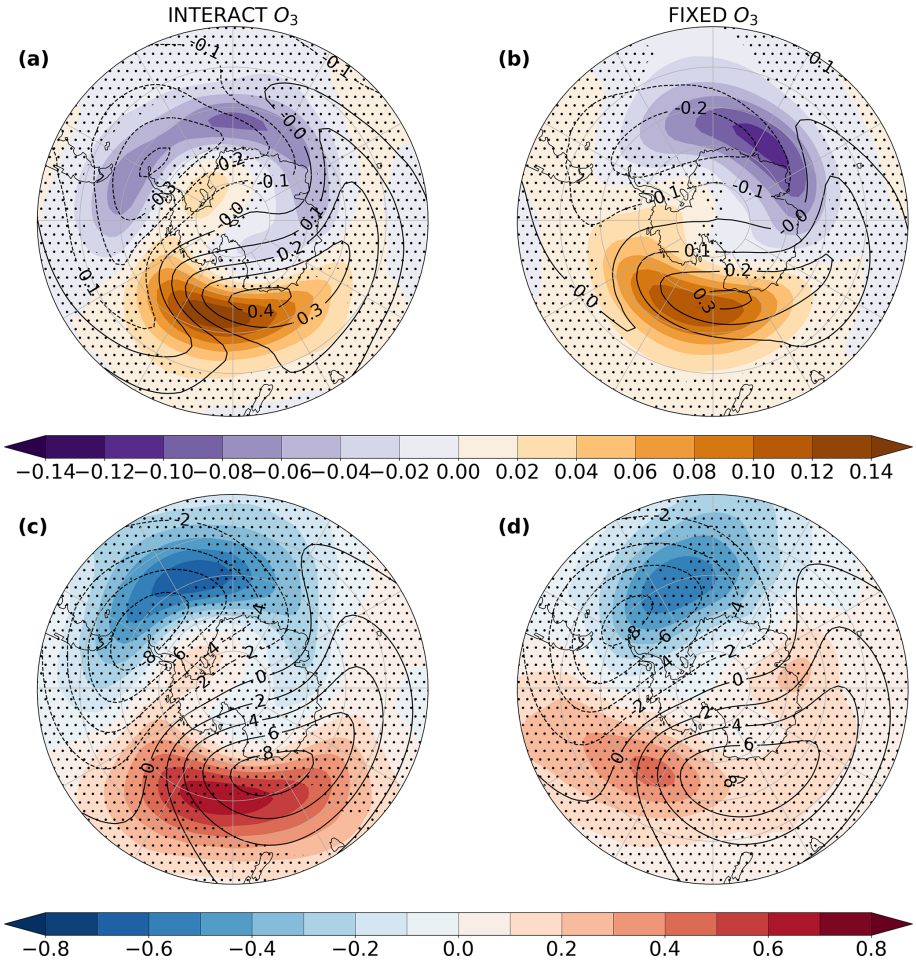

Figure 8. Polar stereographic maps of the October 70 hPa trends in INTERACT O_3 **(a, c)** and FIXED O_3 **(b, d)** ozone (**a, b**; ppmv per decade) and temperature (**c, d**; K per decade) anomalies from the zonal mean for the period 1958–2002 (color shading). Stippling masks regions where the trends are not significant at the 95 % confidence level. The overlaying contours show the corresponding October climatologies.

through of the wave sum shifted eastward, while the ridge remained stationary. Dennison et al. (2017) fitted an ellipse to the ozone hole and showed that the central longitude of the ellipse moves westward as the ozone is depleted. Due to the use of different methods, it is not straightforward to compare the results of Dennison et al. (2017) with the results presented here or in the studies of Lin et al. (2009) and Grytsai et al. (2007). In our analysis, both the through and the peak exhibit a phase shift in FIXED O_3, but only the ridge exhibits an eastward shift in INTERACT O_3. This results in the shift being stronger in FIXED O_3 (Fig. 6b) and less evident in INTERACT O_3 (Fig. 6a).

The consequences of prescribing an ozone field that is not consistent with the model dynamics are depicted in Fig. 6d and e. The wave one pattern can be seen in both temperature and geopotential height anomalies from the zonal means in October. In both fields there are significant differences between INTERACT O_3 and FIXED O_3. Consistent with the ozone anomalies, the temperature trough is shifted westward in INTERACT O_3 and the amplitude of the wave is stronger. The radiative effects of a prescribed ozone hole that is not collocated with the polar vortex appear to alter the location of the wave, while the weaker amplitude of the prescribed ozone wave affects the amplitude of the temperature response. The westward shift of the INTERACT O_3 wave is also seen in the geopotential height field (Fig. 6e). We thus conclude that prescribing the CMIP6 ozone field, which is not consistent with the model dynamics in general and with the simulated stratospheric polar vortex in particular, gives rise to significant differences in the spatial structure and the amplitude of the springtime lower stratospheric wave one, as well as to significant differences in the springtime climatological strength of the polar night jet. Although we presented evidence for the 70 hPa level here, the results hold true for levels throughout the lower and middle stratosphere.

4.2 Effects on the simulated Southern Hemisphere variability

4.2.1 Temperature

We now turn our attention to the differences in the trends simulated by the two ensembles in response to ozone depletion. First, we compare the October and November 100 hPa ozone trends between INTERACT O_3 and FIXED O_3 (Fig. 7a, d, g, j), as they are at the root of the polar stratospheric temperature changes. We also examine the eddy contribution to the October trends, i.e., the trends in the anomalies from the zonal mean (Fig. 8a, b). The FIXED O_3 ozone is given by the prescribed CMIP6 ozone field.

The total spatial extent of ozone depletion is greater in INTERACT O_3 compared to FIXED O_3, but in both cases, in October, the ozone trend maximizes over East Antarctica (Fig. 7a, d). In contrast, in November the FIXED O_3 trend maximum covers most of the Antarctic continent, while the INTERACT O_3 trend maximum is located over East Antarctica (Fig. 7g, j). The maximum ozone depletion is stronger in FIXED O_3 than in INTERACT O_3 during both October and November (Fig. 7a, d, g, j). The trends in ozone anomalies from the zonal mean exhibit a wave one structure, but the wave is shifted eastwards compared to its climatological position in both ensembles (Fig. 8a, b). This implies a progressive eastward migration of the wave structure over time and an increase in the amplitude of the wave, in agreement with Fig. 6. The locations of the October trend minimum over the Atlantic sector and of the trend maximum over the Pacific sector are consistent with observations (Lin et al., 2009).

There are notable differences between the eddy component of the ozone trends in INTERACT O_3 and FIXED O_3. The position of the trough is farther east in FIXED O_3, while the ridge extends more towards the Drake Passage. In INTERACT O_3, the trend trough is strong and significant over the Drake Passage, but in FIXED O_3 it has the opposite sign and is not significant. The pattern of the trend trough in INTERACT O_3, which extends into the Pacific to the west of the time mean trough, explains the lack of an eastward shift of the ozone wave trough in this ensemble, as shown in Fig. 6g. In addition, the ridge of the trend wave is stronger in INTERACT O_3 than in FIXED O_3. These differences in the trends of the ozone fields passed to the radiation scheme in the two ensembles translate into differences in temperature trends between them. Similarly to the trend in ozone, the eddy component of the temperature trend exhibits a wave one structure that is shifted eastward in FIXED O_3 compared to INTERACT O_3, although it is less than in the case of ozone (Fig. 8c, d). In agreement with the stronger ozone trend ridge in INTERACT O_3, the temperature trend ridge is also stronger than in FIXED O_3, with the latter not being statistically significant. The eastward displacement of the temperature trend pattern in FIXED O_3 shows that prescribing an ozone field inconsistent with the dynamics of the model to which it is prescribed alters the spatial structure of the temperature trend. We also note that the ozone and temperature trend wave patterns are not properly collocated in FIXED O_3, as is the case in INTERACT O_3, further highlighting the discrepancies between the prescribed ozone field and the simulated dynamics.

Even larger differences appear when the full polar temperature trends are compared (Fig. 7b, e, h, k). Despite its stronger ozone trend (Fig. 7a, d, g, j), FIXED O_3 displays a considerably weaker temperature trend over the entire Antarctic continent. This is true for each of the individual ensemble members in FIXED O_3 and INTERACT O_3 (Figs. 10c and S3), indicating that the spring lower-stratospheric temperature trends are significantly different in simulations with prescribed CMIP6 ozone and with interactive ozone chemistry. The trend in the SW heating rate (Figs. 10b and S4) is stronger in FIXED O_3 than in INTERACT O_3, consistent with the trends in the respective ozone fields (Fig. 7a, d, g, j). The net radiative contribution to the temperature trend is weaker in both experiments due to the partial cancelation of the SW cooling and LW warming trends (not shown). Nevertheless, the stronger SW heating trend in FIXED O_3 demonstrates that the temperature trend differences between INTERACT O_3 and FIXED O_3 cannot be explained by the differences in the trends of the imposed ozone fields, nor can they be explained by the linear interpolation of the monthly CMIP6 ozone field to the model time step, as was the case in the studies by Sassi et al. (2005) and Neely et al. (2014). If that were the case, the smaller ozone extremes resulting from the interpolation would also reduce the FIXED O_3 SW heating rate trend, not just the temperature trend. Anomalies from the daily climatology of the polar cap SW heating rate (Fig. S7) show more strong positive extremes in the 1960s and 1970s and more strong negative extremes after 1990 in FIXED O_3 than in INTERACT O_3, further confirming that differences in the SW heating rate variations cannot explain the stronger temperature trend in INTERACT O_3. The key to the different temperature trends in INTERACT O_3 and FIXED O_3 lies instead in the dynamical heating rate trends (Fig. 7c, f, i, l). In INTERACT O_3, there is a strong and significant dynamical cooling trend in October over the majority of the Antarctic continent, peaking and becoming significant over East Antarctica (Fig. 7f). This dynamical cooling trend becomes stronger in November (Fig. 7l) and moves away from the Pacific, while a dynamical warming trend appears south of Australia and New Zealand. The dynamical cooling trend greatly amplifies the lower-stratospheric temperature trend due to the radiative heating rate in INTERACT O_3. In FIXED O_3, the October dynamical cooling trend over East Antarctica is much weaker and is not significant, while a warming trend is visible over parts of the continent (Fig. 7c). A strong and significant warming trend appears over the Ross Sea during November in FIXED O_3. Consequently, the dynamical heating rate in FIXED O_3 brings a negligible contribution to the tempera-

ture trend in October and acts to offset the radiative cooling trend in November, explaining the considerably weaker cooling in this ensemble. The strongest dynamical cooling trend in FIXED O_3 occurs over the Atlantic sector of the Southern Ocean during October. The dynamical heating rate is closely related to the polar downwelling, which is, in turn, controlled by the wave dissipation above. Therefore, the different October and November dynamical cooling trend patterns in Fig. 7c and i and Fig. 7f and l have two implications: (1) wave dissipation is suppressed, and (2) the downwelling weakens in completely different regions in the two ensembles. The cause of these spatial discrepancies is the spatial inconsistency between the prescribed ozone hole and the simulated polar vortex in FIXED O_3. The stronger temperature trend in INTERACT O_3 compared to FIXED O_3 can be explained by the different lower-stratospheric dynamical responses to ozone depletion in the two ensembles.

The temperature trends are weaker in FIXED O_3 throughout the lower stratosphere (Fig. 9a, b). The spread among the individual ensemble members is shown is Fig. S5, and all three INTERACT O_3 members exhibit stronger cooling in the lower stratosphere during spring compared to all three FIXED O_3 members, confirming that the difference between the ensemble mean trends is significant. Figure 9c shows the seasonal evolution of the temperature trends from the ERA5 reanalysis. Like INTERACT O_3 and FIXED O_3, ERA5 exhibits maximum cooling in November at 100 hPa. The maximum cooling is stronger in ERA5 than in FIXED O_3, and it is closer in magnitude to the INTERACT O_3 cooling, but its vertical extent and duration are reduced compared to INTERACT O_3. Figure 10c shows the November 100 hPa temperature trend for the individual members of INTERACT O_3 and FIXED O_3, as well as the trends from the ERA5 reanalysis and the IGRA radiosonde observations. As the IGRA temperature data contain only one station located south of 80° S, the temperature trend in Fig. 10c is given for 65–80° S in order not to bias the IGRA trend towards the lower latitudes. The trends for the entire polar cap can be compared in Figs. 9 and S5. Despite considerable spread among the individual ensemble members, all INTERACT O_3 members exhibit stronger temperature trends compared to the FIXED O_3 members. This contrasts with the trends in ozone (Fig. 10a) and SW heating rate (Fig. 10b), which are stronger in FIXED O_3, in agreement with Figs. 7 and S4. The lack of spread in the SW heating rate trend among the FIXED O_3 members seen in Fig. 10b is a consequence of imposing the same ozone field in each of these members. The ERA5 and IGRA temperature trends fall in the lower end of the INTERACT O_3 trend range but are stronger than the trends in all of the FIXED O_3 members (Fig. 10c). The apparent disagreement between the weaker ozone and SW heating rate trends (Fig. 10a, b) and the stronger temperature trend (Fig. 10c) in INTERACT O_3 compared to FIXED O_3 can be explained by the dynamical cooling trend present in the first ensemble (Fig. 13e). Comparing the spring lower-stratospheric temperature trends in INTERACT O_3 and FIXED O_3 with trends from the ERA5 reanalysis and from the observations shows that FIXED O_3 tends to underestimate the ozone-induced cooling, while INTERACT O_3 tends to overestimate it, although individual ensemble members can simulate trends that are close to those observed.

The lack of observations in the middle and upper stratosphere, particularly before the satellite era, cast doubt on the reliability of the ERA5 temperature trends at these levels (Fig. 9c). The very strong cooling seen between April and September above 20 hPa is likely spurious. A significant warming trend can be seen between 50 and 10 hPa above the ozone hole during November and December, in agreement with the FOCI simulations. This warming is weaker in FIXED O_3 and ERA5 than in INTERACT O_3. As shown in Sect. 3, this warming is attributed to changes in the strength of the BDC. Its different magnitude between INTERACT O_3 and FIXED O_3 thus points to the role played by the dynamics in setting the different responses to ozone depletion in the two model configurations. In contrast, the magnitude of the cooling at the stratopause levels in winter and fall is similar between INTERACT O_3 and FIXED O_3, as this cooling is a purely radiative effect of ozone loss and increased GHGs (Sect. 3).

4.2.2 Zonal winds

The magnitude of the stratospheric circumpolar westerly winds trend in INTERACT O_3 and FIXED O_3 is consistent with the magnitude of the temperature trends. A stronger lower stratosphere cooling in INTERACT O_3 implies a more pronounced enhancement of the meridional temperature gradient and hence a stronger acceleration of the westerly winds (Fig. 9d, e). All INTERACT O_3 members simulate a stronger acceleration of the stratospheric westerlies compared to all FIXED O_3 members (Figs. 10d and S6), confirming that the trends are significantly different between the two ensembles. Similar to the temperature trends, the magnitude of the maximum stratospheric acceleration of the westerlies in ERA5 lies between that in the INTERACT O_3 and the FIXED O_3 ensemble means (Figs. 9d, e, f). However, unlike the temperature trends, the ERA5 wind trend falls within the range of the FIXED O_3 trends and is smaller than all the INTERACT O_3 trends (Fig. 10d). The zonal wind trend in INTERACT O_3 is not only stronger, but it also occurs about half a month earlier than in FIXED O_3 and ERA5, from the end of September onwards. Although there are pronounced differences between the ERA5 and both the INTERACT O_3 and the FIXED O_3 upper-stratospheric wind trends, the reliability of the ERA5 trends is questionable due to a lack of observations at these levels.

The timing of the downward propagation of the zonal wind trends to the troposphere also differs between the two ensembles. Figure 11 shows the seasonal cycle of the 850 hPa zonal wind trends as a function of latitude. A significant

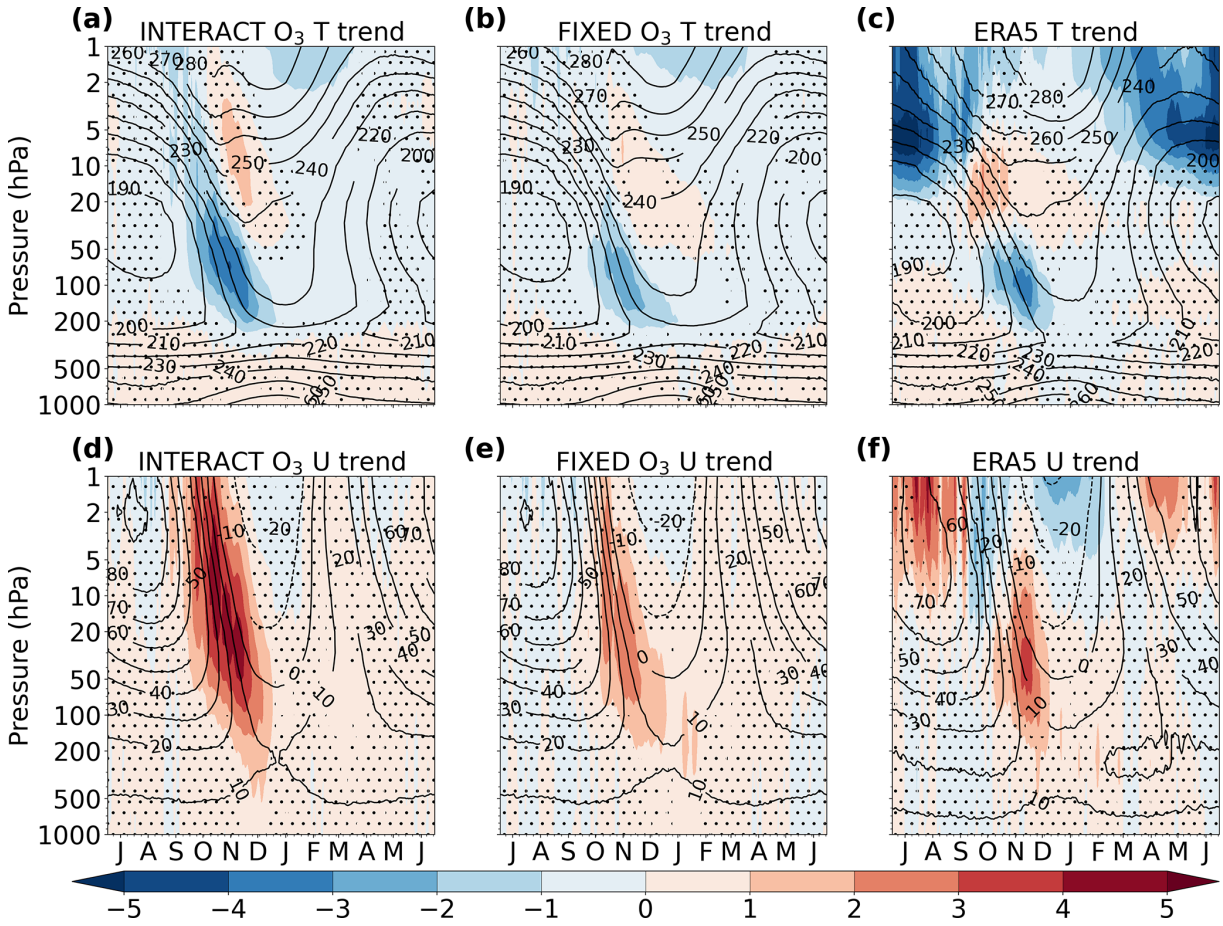

Figure 9. Seasonal cycle of the INTERACT O_3 **(a, d)**, FIXED O_3 **(b, e)**, and ERA5 **(c, f)** trends in polar cap (65–90° S) temperature (**a–c**; K per decade) and in the midlatitude (50–70° S) zonal wind (**d–f**; $m\,s^{-1}$ per decade) for the period 1958–2002 (color shading). Stippling masks regions where the trends are not significant at the 95 % confidence level. The overlaying contours show the corresponding climatological seasonal cycle for 1958–2002. The letter corresponding to each month marks the middle of that month.

poleward intensification of the tropospheric westerlies can be seen from late November through January in INTERACT O_3, accompanied by a deceleration on the equatorward side. In contrast, the westerly winds in FIXED O_3 exhibit significant trends on both flanks only starting in late December, and the trends remain significant throughout February. The timing of the strengthening of the ERA5 850 hPa westerlies agrees better with FIXED O_3, although there is a large number of days with insignificant trends between December and February (Fig. 11e). The weakening of the westerlies on their equatorward side is not significant in the zonal mean in ERA5. Figure 11 also shows maps of the zonal wind trends at 850 hPa averaged over December and January, the two months in which both ensembles exhibit significant trends in the troposphere. The trends are a circumpolar feature and are characterized by strengthening on the poleward side and a weakening on the equatorward side of the tropospheric jet, implying that the jet has shifted poleward in both ensembles. The maximum magnitude of the poleward strengthening is similar in INTERACT O_3 and FIXED O_3, but there are clear spatial differences between the two ensembles. Figure 10e shows the shift in the latitude of the zonal mean jet maximum for December and January separately. The poleward shift in the ensemble mean westerlies is significant in December for INTERACT O_3 and in both December and January for FIXED O_3, although not all ensemble members exhibit a significant shift. ERA5 exhibits a significant poleward shift of the westerlies only in January. The positive and negative wind trends in ERA5 are less zonal than in FOCI (Fig. 11f), with the positive trend reaching equatorward of 40° S in the Pacific sector. This could partly explain the lack of a significant equatorward weakening of the westerlies when the zonal mean trends are considered (Fig. 11e), as trends of opposite sign cancel each other out in the zonal mean.

Figure 10f shows the December and January westerly wind trends for the latitude band in which the trend is positive (45–70° S). We chose to average the winds over this latitude band as opposed to taking the trends at the latitude at which

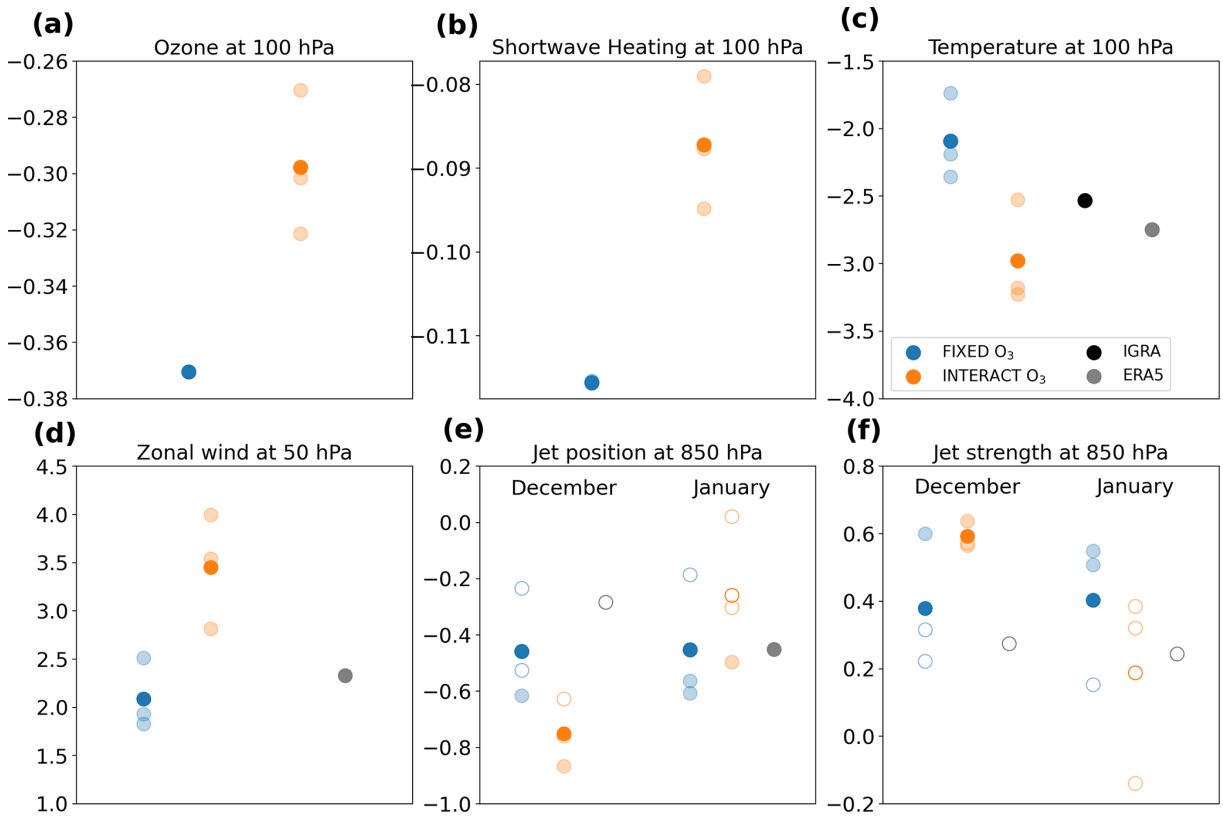

Figure 10. Trends in November 100 hPa ozone (**a**; ppmv per decade), SW heating rate (**b**; $\mathrm{K\,d^{-1}}$ per decade), temperature (**c**; K per decade), 50 hPa zonal wind (**d**; $\mathrm{m\,s^{-1}}$ per decade), and December and January 850 hPa jet position (**e**; ° per decade) and strength (**f**; $\mathrm{m\,s^{-1}}$ per decade). The ozone and SW heating rate are averaged over 65–90° S, the temperature is averaged over 65–80° S, the zonal wind is averaged over 50–70° S, and the jet's position is given as the latitude at which the zonal mean maximum occurs. FIXED O_3 trends are shown in blue, INTERACT O_3 trends are shown in orange, ERA5 trends are shown in grey, and the IGRA temperature trend is shown in black. Ensemble mean trends are depicted by the dark-colored circles, while the individual member trends are depicted in faded colors. Trends that are significant at the 95 % confidence level are marked by filled circles.

the westerlies maximize because the maximum of the westerlies is located in the transition zone between positive and negative trends and therefore exhibits weak trends that are not significant (Fig. 11). FIXED O_3 exhibits trends of comparable magnitude in both months. Although the FIXED O_3 ensemble mean trend is significant, only one member shows a significant trend in December, while two members show significant trends in January. The ensemble mean exhibits significant trends when the individual members do not because the ensemble averaging reduces the interannual variability, which is large in the individual members. All INTERACT O_3 members exhibit a significant strengthening of the westerlies in December, but this ensemble does not show a significant zonal mean trend in January. The zonal mean ERA5 strengthening of the westerlies is not significant in either December or January, although certain regions show significant trends, as seen in Fig. 11f.

The tropospheric westerly jet trends in INTERACT O_3 and FIXED O_3 cannot be clearly differentiated, as is the case for the stratospheric jet. Both the poleward shift of the jet and its strengthening appear stronger in INTERACT O_3 in December, but the ranges of the trends given by the individual ensemble members overlap. In contrast, in January the INTERACT O_3 trends tend to be weaker than the FIXED O_3 trends and are not significant, with one member showing trends in the opposite direction. However, there is a large overlap between the range of the trends in the two ensembles. The maps of the December–January averaged trends (Fig. 11b, d) show maxima of similar magnitude, albeit at different locations. Therefore, we conclude that the differences in the tropospheric westerly jet trends in INTERACT O_3 and FIXED O_3 are within the range of internal variability, in agreement with the results of Eyring et al. (2013), Seviour et al. (2017), and Son et al. (2018).

4.2.3 Mechanisms for the different responses to ozone depletion

To obtain a clear understanding of the dynamical mechanisms responsible for the temperature and zonal wind trend

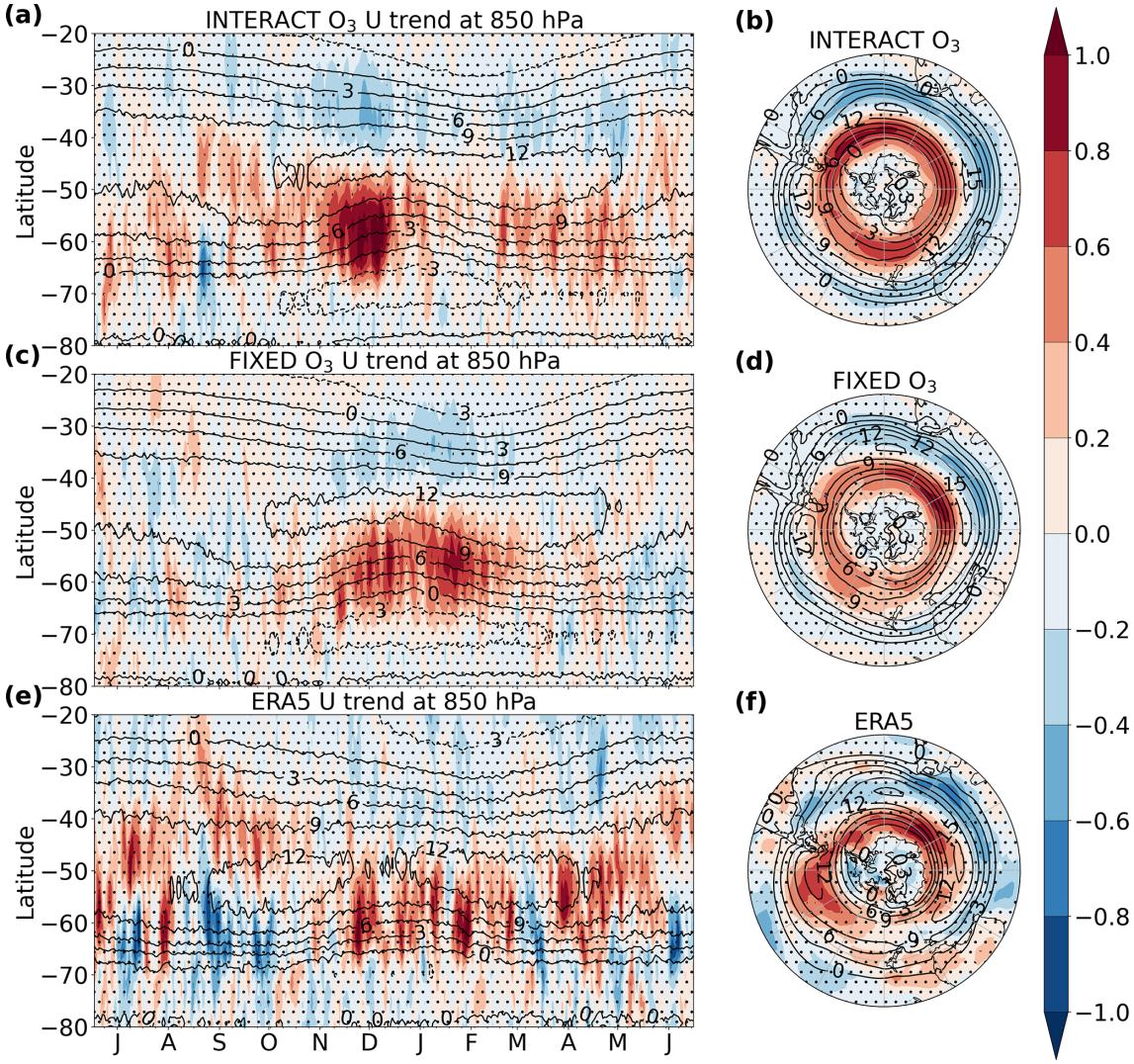

Figure 11. Seasonal cycle **(a, c, e)** and December–January polar stereographic maps **(b, d, f)** of the 850 hPa zonal wind trend ($m\,s^{-1}$ per decade) in INTERACT O_3 **(a, b)**, FIXED O_3 **(c, d)**, and ERA5 **(e, f)** for the period 1958–2002 (color shading). Stippling masks regions where the trends are not significant at the 95 % confidence level. The overlaying contours show the corresponding climatologies for 1958–2002. The letter corresponding to each month marks the middle of that month.

differences between INTERACT O_3 and FIXED O_3, we investigate the trends in the residual circulation and its drivers. Figure 12 shows vertical profiles of the November trend in the eddy heat flux, the divergence of the EP flux, and the vertical and meridional components of the residual circulation. Trends for October and December have additionally been examined but are not shown. The October and November dynamical heating rate trends are illustrated in Fig. S8. Figure 13 shows the spread of the November trends in these fields between the individual ensemble members. We selected the pressure levels at which the trends tend to maximize. In choosing the pressure levels, we took care that the trends in the divergence of the EP flux and in the meridional residual velocity are given at a height above the trends in the vertical residual velocity, as the downward control principle (Haynes et al., 1991) states that the vertical residual velocity is driven by wave dissipation above. In the lower stratosphere, we show dynamical heating and vertical meridional velocity trends at 100 hPa, where the temperature trends maximize.

We first focus on the different onset dates of the westerly wind trends. A significant positive trend can already be seen in the middle and upper stratosphere in INTERACT O_3 at the beginning of October (Fig. 9d), but it only appears in the second half of October in FIXED O_3 (Fig. 9e). There is also a significant cooling visible in the polar cap middle stratosphere at the beginning of October in INTERACT O_3 (Fig. 9a). As this trend occurs above the ozone hole, it is likely the result of dynamical rather than radiative changes. At the beginning of October, the westerly velocities in the

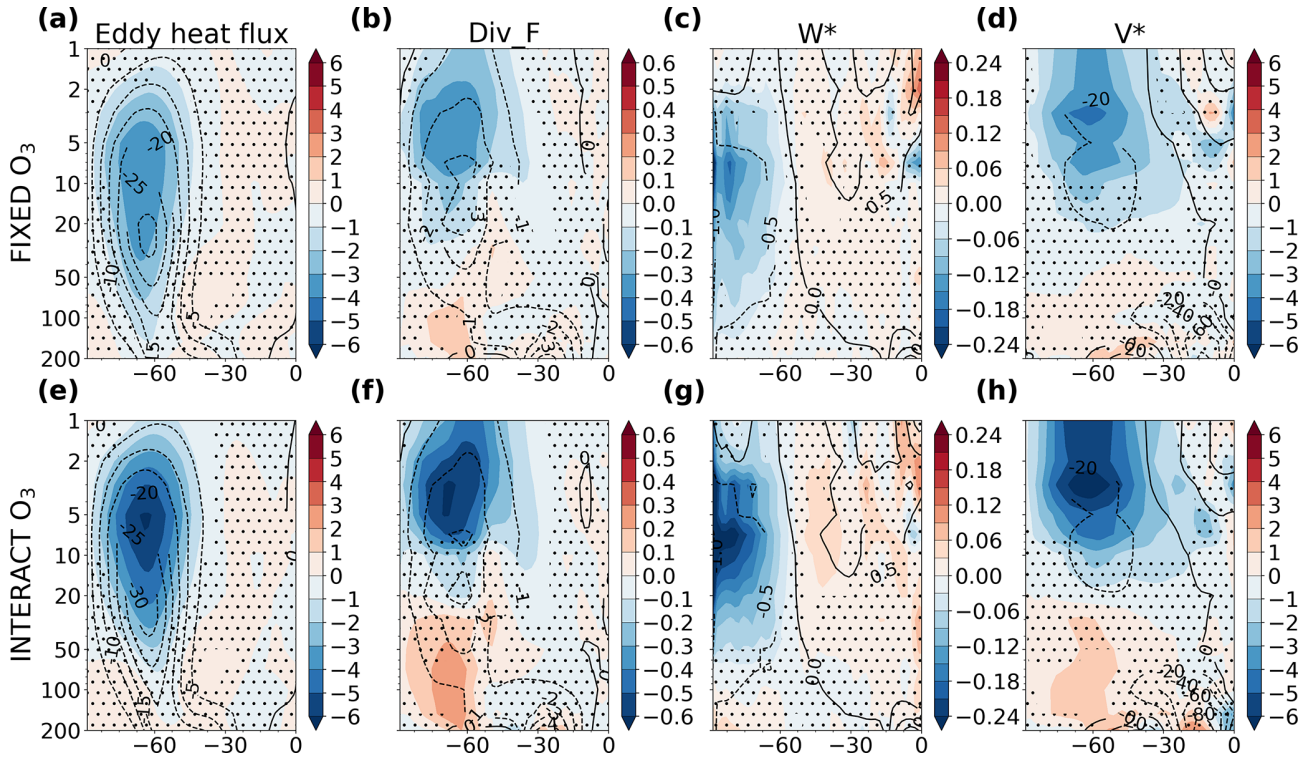

Figure 12. November latitude–height trends in the eddy heat flux (**a, e**; K m s^{-1} per decade), the divergence of the EP flux (**b, f**; m s^{-1} d^{-1} per decade), the vertical residual velocity (**c, g**; mm s^{-1} per decade), and the meridional residual velocity (**d, h**; cm s^{-1} per decade) for the period 1958–2002 in FIXED O_3 (**a–d**) and INTERACT O_3 (**e–h**). The overlaying contours in each panel show the corresponding climatologies. Stippling masks the trends that are not significant at the 95 % confidence interval.

polar night jet (contours in Fig. 9d, e) are close to the critical velocity for Rossby wave propagation (Charney and Drazin, 1961). The positive trend (Fig. 9d) enhances the winds past this critical velocity and inhibits wave propagation in INTERACT O_3. A significant decrease in wave dissipation in the lower and middle stratosphere occurs in October in INTERACT O_3 but not in FIXED O_3 (not shown). This October reduction in wave forcing in INTERACT O_3 is consistent with the findings of McLandress et al. (2010), who also used a CCM in their study. The reduced wave forcing has two effects: first, less easterly momentum is deposited through wave dissipation, further enhancing the westerly winds. Second, the polar cap downwelling in the lower stratosphere is weakened due to the decreased wave forcing above, leading to a significant dynamical cooling. A significant October polar cap dynamical cooling trend occurs in the lower stratosphere only in INTERACT O_3, and it is absent in FIXED O_3 (Figs. 7c, f and S8a, b). The lack of a dynamical cooling trend in FIXED O_3 is explained by a prescribed ozone hole that is not consistent with the dynamics, which alters the propagation of planetary waves, as demonstrated above. The dynamical cooling in INTERACT O_3 reinforces the negative temperature trend due to the radiative effects of ozone loss and further strengthens the westerly winds via the thermal wind balance, resulting in stronger temperature and zonal wind trends compared to FIXED O_3.

In November, the polar vortex breaks down and climatological easterly winds occur in the upper and middle stratosphere (contours in Fig. 9d, e). The positive zonal wind trend prolongs the life of the polar vortex, delaying its breakdown (e.g., McLandress et al., 2010) and allowing planetary waves to propagate higher into the stratosphere, as shown by the negative trend in the eddy heat flux (Fig. 12a, e). Wave dissipation is enhanced in the middle and upper stratosphere and decreased in the lower stratosphere in both FIXED O_3 and INTERACT O_3 (Fig. 12b, f), but the magnitude of the INTERACT O_3 trends is larger. As shown in Fig. 13a and b, the upper-stratospheric negative trends in both the eddy heat flux and the divergence of the EP flux are stronger in all the INTERACT O_3 simulations than in all the FIXED O_3 simulations. The positive EP flux divergence trends in the lower stratosphere are not as clearly separated between the two ensembles, but two of the INTERACT O_3 simulations exhibit significant trends, while the FIXED O_3 simulations and the ensemble mean do not. The region of enhanced wave dissipation extends farther down in FIXED O_3, confining the region of reduced wave dissipation to the levels below 100 hPa. This has important implications for the residual circulation trends. In FIXED O_3, the negative trend in the polar cap

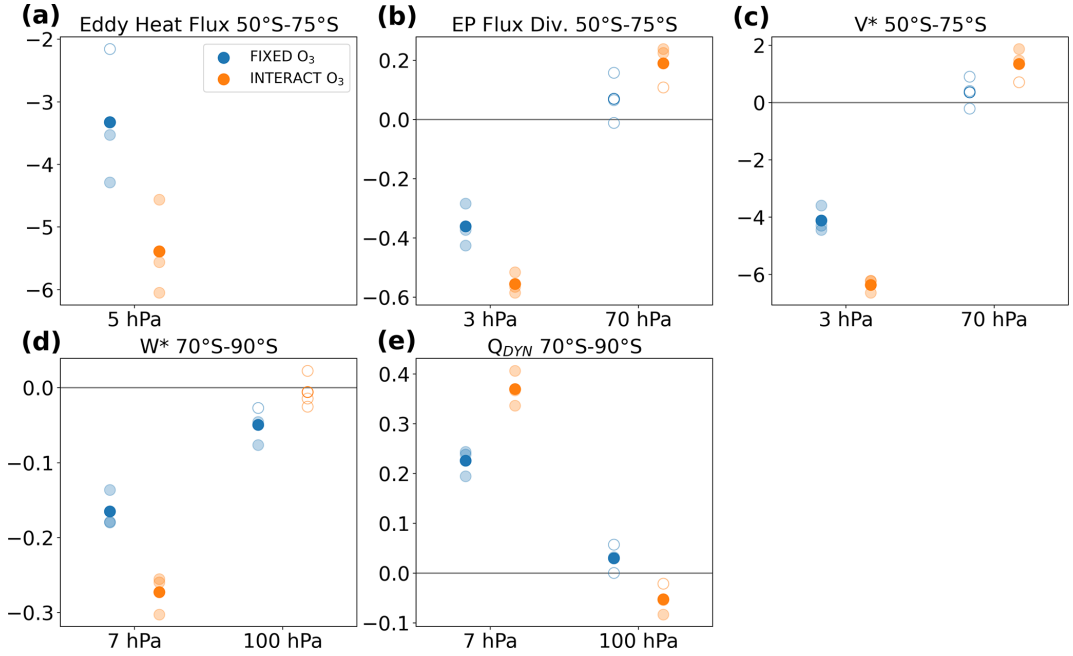

Figure 13. Trends in November eddy heat flux (**a**; $\mathrm{K\,m\,s^{-1}}$ per decade), EP flux divergence (**b**; $\mathrm{m\,s^{-1}\,d^{-1}}$ per decade), meridional residual velocity (**c**; $\mathrm{cm\,s^{-1}}$ per decade), vertical residual velocity (**d**; $\mathrm{mm\,s^{-1}}$ per decade), and dynamical heating rate (**e**; $\mathrm{K\,d^{-1}}$ per decade). The eddy heat flux, EP flux divergence, and meridional residual velocity are averaged over 50–75° S, and the vertical residual velocity and the dynamical heating rate are averaged over 70–90° S. FIXED O_3 trends are shown in blue, and INTERACT O_3 trends are shown in orange. Ensemble mean trends are depicted by the dark-colored circles, while the individual member trends are depicted in faded colors. Trends that are significant at the 95 % confidence level are marked by filled circles.

downwelling reaches all the way into the lower stratosphere (Fig. 12c). The accompanying polar cap dynamical warming trend (Figs. 7i and S8d) partly offsets the radiative cooling trend due to ozone depletion, resulting in the weaker temperature trend seen in Fig. 9b. In contrast, the polar downwelling in INTERACT O_3 strengthens only above 50 hPa and exhibits an insignificant weakening below (Fig. 12g). The meridional residual velocity follows a similar pattern, strengthening in the upper stratosphere and weakening in the lower stratosphere (Fig. 12h). There is a clear distinction between the INTERACT O_3 and FIXED O_3 ensembles regarding the magnitude of the residual circulation and dynamical heating trends in the middle and upper stratosphere, with INTERACT O_3 exhibiting a stronger intensification of the residual circulation (Fig. 13c, d, e). In the lower stratosphere, only the dynamical heating trends can be separated. Two out of three INTERACT O_3 members simulate a significant cooling, while the FIXED O_3 ensemble mean simulates a significant warming, despite the fact that the warming in the individual members is not significant (Fig. 13e). This warming is consistent with the enhanced polar cap downwelling simulated by the FIXED O_3 simulations (Fig. 13d). In contrast to the weakening of the meridional residual velocity and to the dynamical warming simulated by INTERACT O_3, this ensemble does not exhibit a weakening of the polar cap downwelling in the lower stratosphere. While this is surprising, it is possible that the zonally asymmetric nature of the polar downwelling results in trends of opposite signs canceling each other out when averaged over the polar cap. The constraints of the zonal mean fields obtained trough the transformed Eulerian mean framework do not allow us to investigate this issue. Nevertheless, the dynamical changes in the lower stratosphere drive a dynamical cooling trend over the polar cap (Figs. 7l, 13e and S8c) that, as in October, adds to the radiative cooling trend due to ozone depletion to produce a stronger negative temperature trend in INTERACT O_3. The dynamical warming in the middle and upper polar stratosphere is also stronger in INTERACT O_3, explaining the stronger warming trend in Fig. 9a.

The residual circulation in the lower stratosphere thus exhibits a different response to the formation of the ozone hole in FIXED O_3 compared to INTERACT O_3. These different residual circulation changes are a consequence of the fact that the prescribed ozone hole is not consistent with the simulated dynamics. They are at the core of the stratospheric temperature and westerly wind differences between the two ensembles, as they drive the dynamical heating contribution to the temperature changes.

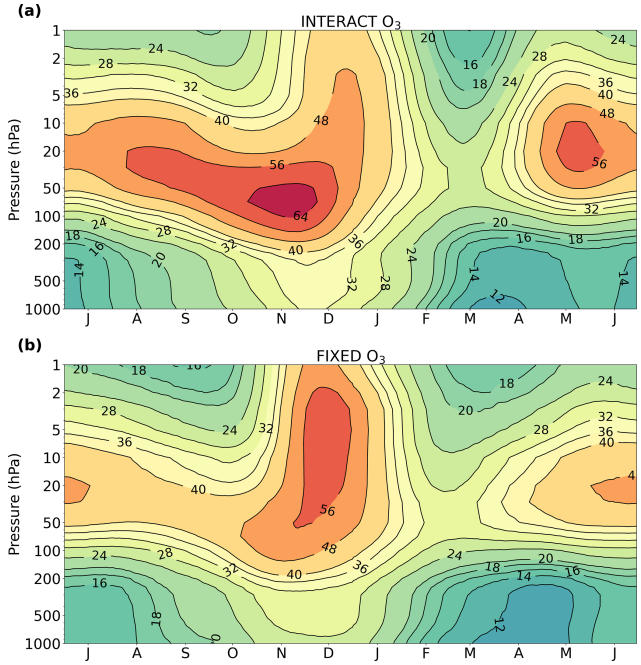

Figure 14. Seasonal cycle of the SAM timescale in INTERACT O_3 **(a)** and FIXED O_3 **(b)**. Note that the contour interval is nonlinear.

4.3 Effects on the SAM timescale

Dennison et al. (2015) showed that ozone depletion increases the persistence of the SAM in the stratosphere. This raises the question of whether prescribing the CMIP6 ozone affects the impact of the ozone hole on the SAM persistence. Figure 14 shows the seasonal evolution of the ensemble mean SAM timescale for INTERACT O_3 and FIXED O_3. The SAM timescale was first computed for the individual ensemble members and then averaged to obtain the ensemble means. While both INTERACT O_3 and FIXED O_3 capture the peak SAM persistence in austral spring and summer (Gerber et al., 2008, 2010), there are marked differences between the timescales in the two ensembles. The middle stratosphere SAM is more persistent in INTERACT O_3 between August and January, bringing the amplitude and the seasonal structure of the SAM timescale in INTERACT O_3 closer to those exhibited in reanalyses (compare Fig. 14 with Fig. 8b in the study by Gerber et al., 2010). In contrast, FIXED O_3 is characterized by a more vertical structure of the maximum persistence focused in December and overall by a shorter timescale. The inconsistent evolution of the ozone hole and the polar vortex in FIXED O_3 dampens the dynamical response to ozone depletion and reduces the SAM timescale. At the same time, the chemical–dynamical feedbacks present only in INTERACT O_3 reinforce the ozone-induced anomalies and lead to more persistent polar vortex anomalies, reflected in the longer SAM timescale in this ensemble. In a parallel study conducted with a different CCM by Haase et al. (2020), an ensemble of experiments with prescribed daily zonally asymmetric ozone consistent with the dynamics still exhibits shorter SAM timescales compared to the interactive chemistry experiment. This highlights the role of the feedbacks with the ozone chemistry in prolonging the SAM persistence. The same study additionally shows that the effect of zonal asymmetries in ozone is also to enhance the SAM timescale.

In the troposphere, both INTERACT O_3 and FIXED O_3 overestimate the SAM timescale and exhibit a peak persistence that is too broad when compared to the SAM timescale derived from reanalyses by Gerber et al. (2010) and Simpson et al. (2011). This is a common problem of climate models reported by Gerber et al. (2008) for the CMIP3 models and by Gerber et al. (2010) for CCMs, and it appears to persist in the current generation of climate models. Simpson et al. (2011) attempted to identify the sources of the exaggerated tropospheric SAM persistence and found that the stratospheric SAM persistence contributes about half of the bias, while the other half is of tropospheric origin. The authors cite an equatorward-biased position of the tropospheric jet as a possible reason for the tropospheric contribution to the overestimation of the SAM timescale. This also holds true in our model, since the tropospheric jet in FOCI is located closer to the Equator compared to observations, as is common in climate models (Swart and Fyfe, 2012). Overall, the use of interactive chemistry improves the representation of the stratospheric SAM timescale in FOCI, but the tropospheric issues common to climate models still remain.

5 Discussion and conclusion

The ocean–atmosphere coupled climate model FOCI was used in this study to (1) separate the effects of ozone depletion on the SH temperature and dynamics from those arising from increasing concentrations of GHGs and (2) compare these effects between an ensemble of simulations wherein the CMIP6 ozone field is prescribed and an ensemble of simulations that use interactive chemistry. We found the following.

- The formation of the Antarctic ozone hole is the primary driver of the dynamical changes in the atmosphere that have occurred in the SH spring and summer during the last decades. These changes comprise an acceleration of the polar night jet, which propagated to the surface where the surface westerlies shifted poleward and the SAM shifted toward its high index polarity.

- The increase in anthropogenic GHGs partly offset the November polar night jet response to ozone depletion in the stratosphere. At the surface, it resulted in a similar response of the westerlies and of the SAM, but this response was much weaker compared to that driven by ozone loss and is generally not statistically significant.

- Ozone depletion drove an intensification of the SH BDC in the middle stratosphere in November and in the lower stratosphere in December. In contrast, a decrease in wave dissipation driven by ozone loss led to the weakening of the residual circulation in the lower stratosphere in November.
- The CMIP6 ozone field is not consistent with the dynamics simulated by FOCI, and the ozone hole is not collocated with the polar vortex. Consequently, the austral spring zonal wavenumber one is weaker in FIXED O_3 and shifted eastwards compared to INTERACT O_3. The austral spring climatological polar night jet is weaker in FIXED O_3 than in INTERACT O_3.
- The dynamical response to ozone depletion enhanced the radiatively driven austral spring lower-stratospheric cooling. A novel result of this study is that this effect only occurs in INTERACT O_3 and is suppressed in FIXED O_3. Furthermore, the November lower stratosphere was dynamically warmed in FIXED O_3, which partly offset the radiative cooling effect of ozone depletion.
- Prescribing the CMIP6 ozone field, which is not consistent with the dynamics in FOCI, alters the propagation of planetary waves from the troposphere and changes the location of suppressed wave breaking induced by the ozone hole.
- The ozone-induced austral spring polar cap cooling in the lower stratosphere is weaker in FIXED O_3 than in INTERACT O_3. The cooling trends estimated from the IGRA radiosonde observations and from the ERA5 reanalysis are stronger than those obtained from the FIXED O_3 simulations and fall at the lower end of the range of trends simulated by INTERACT O_3.
- The acceleration of the stratospheric jet in response to ozone depletion is also weaker in FIXED O_3 than in INTERACT O_3, and it agrees better with the estimate from the ERA5 reanalysis. In contrast, the tropospheric jet trend differences between FIXED O_3 and INTERACT O_3 fall within the range of internal variability.
- The persistence of the SAM is reduced in FIXED O_3 due to the dynamically inconsistent prescribed ozone field, which represents another new result.

The temperature and dynamical response to ozone depletion simulated by FOCI is in good agreement with previous studies. The austral spring lower-stratospheric cooling is the signature of the formation of the Antarctic ozone hole, a direct radiative effect also reported by Mahlman et al. (1994), Li et al. (2008), Stolarski et al. (2010), Keeble et al. (2014), Ivy et al. (2016), and Lubis et al. (2016). The November–December warming above the ozone hole represents a dynamical response to ozone loss and is in agreement with the findings of Mahlman et al. (1994), Li et al. (2008), Stolarski et al. (2010), Keeble et al. (2014), and Ivy et al. (2016). This confirms the ability of the model to accurately capture the stratospheric temperature response to ozone depletion. The strong and significant intensification of the polar night jet in austral spring and that of the surface westerlies in austral summer simulated by FOCI as a result of Antarctic ozone loss, combined with the weak and insignificant response of the surface westerlies to the increase in GHGs, bring robustness to the conclusions of previous studies (Arblaster and Meehl, 2006; McLandress et al., 2010; Polvani et al., 2011; Previdi and Polvani, 2014; World Meteorological Organization, 2018) that ozone depletion is the main driver of SH stratospheric and tropospheric dynamical changes over the later part of the twentieth century. This is likely to change in the twenty-first century, as even higher GHG levels will increase the GHG impact on the atmospheric circulation, while the ban on CFC emissions following the Montreal protocol is expected to result in a recovery of the ozone hole, driving circulation changes in the opposite direction to those that occurred over the historical period (Perlwitz et al., 2008; Son et al., 2008; McLandress et al., 2010; Eyring et al., 2013).

The strengthening of the westerly winds in response to ozone depletion delayed the breakdown of the polar vortex, which allowed planetary waves to propagate higher into the stratosphere in November and for a longer period of time in December. This resulted in stronger wave dissipation in the upper stratosphere in November and in the middle stratosphere in December, leading to the concomitant intensification of the residual circulation, in agreement with the findings of previous studies that used CCMs (Li et al., 2008; McLandress et al., 2010; Li et al., 2010; Keeble et al., 2014; Oberländer-Hayn et al., 2015; Polvani et al., 2018; Abalos et al., 2019). A new result of this study is that the intensification of the residual circulation is weaker when the CMIP6 ozone field is prescribed, and, furthermore, it extends farther down in the lower stratosphere in November. FIXED O_3 is not able to reproduce the November lower stratosphere residual circulation weakening found in INTERACT O_3, in agreement with other CCMs (Li et al., 2008; McLandress et al., 2010; Lubis et al., 2016). This is an essential aspect of explaining the weaker lower-stratospheric cooling in response to ozone depletion in FIXED O_3. The enhanced lower-stratospheric polar cap downwelling results in dynamical warming, which reduces the radiative cooling due to ozone loss in November. The consequence is that FIXED O_3 exhibits a weaker spring lower-stratospheric cooling compared to INTERACT O_3.

The performance of simulations prescribing the CMIP6 ozone field was tested here for the first time against simulations using the same model, but in the version that includes interactive ozone chemistry. We found significant differences in the response of the stratospheric temperature and dynamics to ozone depletion in INTERACT O_3 and FIXED O_3 by comparing the spread of the individual ensemble mem-

ber trends. Each ensemble member represents one realization of the impacts of ozone depletion using the two methods of imposing ozone changes. Their spread gives an estimate of the range of trends that can be expected from each ensemble, taking into account the internal variability in the model. The caveat of this approach is that we are restricted to only three simulations per ensemble due to the large computational costs of such simulations. In contrast to the trends in the stratospheric westerly jet, the difference in the tropospheric jet trends between FIXED O_3 and INTERACT O_3 falls within the internal variability of the model.

Several factors can potentially explain the differences in the ozone-induced stratospheric temperature and circulation trends between INTERACT O_3 and FIXED O_3. (1) The CMIP6 and FOCI ozone fields exhibit different climatologies, as discussed in Sect. 4.1. Neither the climatological CMIP6 ozone hole nor its variability is consistent with FOCI's dynamics. The fact that the prescribed ozone hole is displaced in relation to the simulated polar vortex alters the propagation of planetary waves from the troposphere to the stratosphere and therefore leads to changes in the dynamical response to ozone depletion. This results in different dynamical heating rate trends in FIXED O_3 and INTERACT O_3. (2) The CMIP6 and FOCI ozone fields exhibit different trends. The austral spring polar cap ozone and, consequently, the SW heating rate trends are stronger in FIXED O_3 than in INTERACT O_3. In contrast, the temperature trends are weaker in FIXED O_3 than in INTERACT O_3. We therefore conclude that the difference in the imposed ozone trends cannot explain the difference in the temperature trends. (3) The CMIP6 ozone field is interpolated from monthly values to the model time step, and the studies of Sassi et al. (2005) and Neely et al. (2014) showed that this can lead to lower temperature trends when monthly ozone fields are prescribed. In this case, the SW heating rate trend would also be weaker in FIXED O_3 than in INTERACT O_3. However, the FIXED O_3 SW heating rate trend is stronger in our study, in line with the stronger ozone trend. Therefore, the monthly resolution of the prescribed CMIP6 ozone field cannot explain the weaker temperature trend in FIXED O_3. (4) Feedbacks between ozone, radiation, and dynamics cannot occur in FIXED O_3. In a recent study with a different model, Haase et al. (2020) used the daily three-dimensional ozone from the interactive chemistry version and prescribed it to the version without interactive chemistry. Despite the fact that the ozone and SW heating rates were the same in their two ensembles, they still found differences between the SH polar cap lower-stratospheric temperature and dynamical heating rate trends and attributed these differences to the missing ozone-related feedbacks when ozone is prescribed. These ozone–radiative–dynamical feedbacks are also missing in our FIXED O_3 ensemble and might therefore contribute to the differences in the stratospheric temperature and dynamics trends between FIXED O_3 and INTERACT O_3.

Although the results presented here were obtained using a single model, FOCI, they suggest that prescribing the CMIP6 ozone field leads to weaker simulated effects of ozone depletion in the Southern Hemisphere stratosphere compared to computing the ozone chemistry interactively. This is because the features of the prescribed ozone field are likely to differ in position and variability from the simulated dynamics, particularly in models that were not involved in the generation of the CMIP6 ozone field. While the effects of prescribing the CMIP6 ozone field on the tropospheric westerly jet cannot be distinguished from internal variability in the current study, they might become more important in the twenty-first century when ozone recovery occurs.

Code availability. The code used to obtain the figures presented in this study can be found at https://doi.org/10.5281/zenodo.4680722 (Ivanciu, 2021).

Data availability. The model data used in this study can be found at https://doi.org/10.5281/zenodo.3931507 (Ivanciu, 2020). The CMIP6 ozone field prescribed to the simulations that do not calculate the ozone chemistry interactively is publicly available at http://esgf-node.llnl.gov/search/input4mips/?mip_era=CMIP6&activity_id=input4MIPs&institution_id=UReading&target_mip=CMIP&source_id=UReading-CCMI-1-0 (last access: April 2021, Hegglin et al., 2016). The IGRA radiosonde observations are publicly available at ftp://ftp.ncdc.noaa.gov/pub/data/igra/data/data-por/ (last access: April 2021, Durre et al., 2006). The ERA5 dataset is available for public use at https://cds.climate.copernicus.eu/cdsapp#!/dataset/reanalysis-era5-pressure-levels-monthly-means?tab=overview (last access: April 2021, Hersbach et al., 2020).

Supplement. The supplement related to this article is available online at: https://doi.org/10.5194/acp-21-5777-2021-supplement.

Author contributions. II, KM, and AB designed the study and the experimental setup. SW, II, and JH carried out the model simulations. II carried out the analysis, and all authors discussed the results. II wrote the paper with contributions from all co-authors.

Competing interests. The authors declare that they have no conflict of interest.

Acknowledgements. The model simulations used in this study were performed with resources provided by the North-German Supercomputing Alliance (HLRN). The authors thank Isla Simpson for her help in the calculation of the Southern Annular Mode timescale.

Financial support. This research has been supported by the German Federal Ministry of Education and Research (grant no. 03F0796A).

The article processing charges for this open-access publication were covered by a Research Centre of the Helmholtz Association.

Review statement. This paper was edited by Martin Dameris and reviewed by Gabriel Chiodo and two anonymous referees.

References

Abalos, M., Polvani, L., Calvo, N., Kinnison, D., Ploeger, F., Randel, W., and Solomon, S.: New Insights on the Impact of Ozone-Depleting Substances on the Brewer-Dobson Circulation, J. Geophys. Res.-Atmos., 124, 2435–2451, https://doi.org/10.1029/2018JD029301, 2019.

Andrews, D. G., Holton, J. R., and Leovy, C. B.: Middle Atmosphere Dynamics, vol. 40 of International Geophysics Series, Academic Press, San Diego, 1987.

Arblaster, J. M. and Meehl, G. A.: Contributions of External Forcings to Southern Annular Mode Trends, J. Climate, 19, 2896–2905, https://doi.org/10.1175/JCLI3774.1, 2006.

Biastoch, A., Böning, C. W., Getzlaff, J., Molines, J.-M., and Madec, G.: Causes of Interannual–Decadal Variability in the Meridional Overturning Circulation of the Midlatitude North Atlantic Ocean, J. Climate, 21, 6599–6615, https://doi.org/10.1175/2008JCLI2404.1, 2008.

Biastoch, A., Böning, C. W., Schwarzkopf, F. U., and Lutjeharms, J. R. E.: Increase in Agulhas leakage due to poleward shift of Southern Hemisphere westerlies, Nature, 462, 495–498, https://doi.org/10.1038/nature08519, 2009.

Biastoch, A., Durgadoo, J. V., Morrison, A. K., van Sebille, E., Weijer, W., and Griffies, S. M.: Atlantic multi-decadal oscillation covaries with Agulhas leakage, Nat. Commun., 6, 10082, https://doi.org/10.1038/ncomms10082, 2015.

Brovkin, V., Raddatz, T., Reick, C. H., Claussen, M., and Gayler, V.: Global biogeophysical interactions between forest and climate, Geophys. Res. Lett., 36, L07405, https://doi.org/10.1029/2009GL037543, 2009.

Cai, W.: Antarctic ozone depletion causes an intensification of the Southern Ocean super-gyre circulation, Geophys. Res. Lett., 33, L03712, https://doi.org/10.1029/2005GL024911, 2006.

Charney, J. G. and Drazin, P. G.: Propagation of planetary-scale disturbances from the lower into the upper atmosphere, J. Geophys. Res., 66, 83–109, 1961.

Chiodo, G., Polvani, L. M., Marsh, D. R., Stenke, A., Ball, W., Rozanov, E., Muthers, S., and Tsigaridis, K.: The Response of the Ozone Layer to Quadrupled CO2 Concentrations, J. Climate, 31, 3893–3907, https://doi.org/10.1175/JCLI-D-17-0492.1, 2018.

Crook, J. A., Gillett, N. P., and Keeley, S. P. E.: Sensitivity of Southern Hemisphere climate to zonal asymmetry in ozone, Geophys. Res. Lett., 35, L07806, https://doi.org/10.1029/2007GL032698, 2008.

Dennison, F., McDonald, A., and Morgenstern, O.: The evolution of zonally asymmetric austral ozone in a chemistry–climate model, Atmos. Chem. Phys., 17, 14075–14084, https://doi.org/10.5194/acp-17-14075-2017, 2017.

Dennison, F. W., McDonald, A. J., and Morgenstern, O.: The effect of ozone depletion on the Southern Annular Mode and stratosphere-troposphere coupling, J. Geophys. Res.-Atmos., 120, 6305–6312, https://doi.org/10.1002/2014JD023009, 2015.

Dietmüller, S., Ponater, M., and Sausen, R.: Interactive ozone induces a negative feedback in CO2-driven climate change simulations, J. Geophys. Res.-Atmos., 119, 1796–1805, https://doi.org/10.1002/2013JD020575, 2014.

Durgadoo, J. V., Loveday, B. R., Reason, C. J. C., Penven, P., and Biastoch, A.: Agulhas Leakage Predominantly Responds to the Southern Hemisphere Westerlies, J. Phys. Oceanogr., 43, 2113–2131, https://doi.org/10.1175/JPO-D-13-047.1, 2013.

Durre, I., Vose, R. S., and Wuertz, D. B.: Overview of the Integrated Global Radiosonde Archive, J. Climate, 19, 53–68, https://doi.org/10.1175/JCLI3594.1, 2006.

Eyring, V., Arblaster, J. M., Cionni, I., Sedláček, J., Perlwitz, J., Young, P. J., Bekki, S., Bergmann, D., Cameron-Smith, P., Collins, W. J., Faluvegi, G., Gottschaldt, K.-D., Horowitz, L. W., Kinnison, D. E., Lamarque, J.-F., Marsh, D. R., Saint-Martin, D., Shindell, D. T., Sudo, K., Szopa, S., and Watanabe, S.: Long-term ozone changes and associated climate impacts in CMIP5 simulations, J. Geophys. Res.-Atmos., 118, 5029–5060, https://doi.org/10.1002/jgrd.50316, 2013.

Fichefet, T. and Maqueda, M. A. M.: Sensitivity of a global sea ice model to the treatment of ice thermodynamics and dynamics, J. Geophys. Res.-Oceans, 102, 12609–12646, https://doi.org/10.1029/97JC00480, 1997.

Fogt, R. L., Perlwitz, J., Monaghan, A. J., Bromwich, D. H., Jones, J. M., and Marshall, G. J.: Historical SAM Variability. Part II: Twentieth-Century Variability and Trends from Reconstructions, Observations, and the IPCC AR4 Models, J. Climate, 22, 5346–5365, https://doi.org/10.1175/2009JCLI2786.1, 2009.

Fyfe, J. C., Boer, G. J., and Flato, G. M.: The Arctic and Antarctic oscillations and their projected changes under global warming, Geophys. Res. Lett., 26, 1601–1604, https://doi.org/10.1029/1999GL900317, 1999.

Gabriel, A., Peters, D., Kirchner, I., and Graf, H.-F.: Effect of zonally asymmetric ozone on stratospheric temperature and planetary wave propagation, Geophys. Res. Lett., 34, L06807, https://doi.org/10.1029/2006GL028998, 2007.

Garfinkel, C. I., Waugh, D. W., and Polvani, L. M.: Recent Hadley cell expansion: The role of internal atmospheric variability in reconciling modeled and observed trends, Geophys. Res. Lett., 42, 10824–10831, https://doi.org/10.1002/2015GL066942, 2015.

Gerber, E. P., Polvani, L. M., and Ancukiewicz, D.: Annular mode time scales in the Intergovernmental Panel on Climate Change Fourth Assessment Report models, Geophys. Res. Lett., 35, L22707, https://doi.org/10.1029/2008GL035712, 2008.

Gerber, E. P., Baldwin, M. P., Akiyoshi, H., Austin, J., Bekki, S., Braesicke, P., Butchart, N., Chipperfield, M., Dameris, M., Dhomse, S., Frith, S. M., Garcia, R. R., Garny, H., Gettelman, A., Hardiman, S. C., Karpechko, A., Marchand, M., Morgenstern, O., Nielsen, J. E., Pawson, S., Peter, T., Plummer, D. A., Pyle, J. A., Rozanov, E., Scinocca, J. F., Shepherd, T. G., and Smale, D.: Stratosphere-troposphere coupling and annular mode vari-

ability in chemistry-climate models, J. Geophys. Res.-Atmos., 115, D00M06, https://doi.org/10.1029/2009JD013770, 2010.

Gillett, N. P. and Thompson, D. W. J.: Simulation of Recent Southern Hemisphere Climate Change, Science, 302, 273–275, https://doi.org/10.1126/science.1087440, 2003.

Gillett, N. P., Scinocca, J. F., Plummer, D. A., and Reader, M. C.: Sensitivity of climate to dynamically-consistent zonal asymmetries in ozone, Geophys. Res. Lett., 36, L10809, https://doi.org/10.1029/2009GL037246, 2009.

Grise, K. M., Polvani, L. M., Tselioudis, G., Wu, Y., and Zelinka, M. D.: The ozone hole indirect effect: Cloud-radiative anomalies accompanying the poleward shift of the eddy-driven jet in the Southern Hemisphere, Geophys. Res. Lett., 40, 3688–3692, https://doi.org/10.1002/grl.50675, 2013.

Grytsai, A. V., Evtushevsky, O. M., Agapitov, O. V., Klekociuk, A. R., and Milinevsky, G. P.: Structure and long-term change in the zonal asymmetry in Antarctic total ozone during spring, Ann. Geophys., 25, 361–374, https://doi.org/10.5194/angeo-25-361-2007, 2007.

Haase, S. and Matthes, K.: The importance of interactive chemistry for stratosphere–troposphere coupling, Atmos. Chem. Phys., 19, 3417–3432, https://doi.org/10.5194/acp-19-3417-2019, 2019.

Haase, S., Fricke, J., Kruschke, T., Wahl, S., and Matthes, K.: Sensitivity of the Southern Hemisphere circumpolar jet response to Antarctic ozone depletion: prescribed versus interactive chemistry, Atmos. Chem. Phys., 20, 14043–14061, https://doi.org/10.5194/acp-20-14043-2020, 2020.

Haigh, J. D. and Pyle, J. A.: Ozone perturbation experiments in a two-dimensional circulation model, Q. J. Roy. Meteor. Soc., 108, 551–574, https://doi.org/10.1002/qj.49710845705, 1982.

Hardiman, S. C., Andrews, M. B., Andrews, T., Bushell, A. C., Dunstone, N. J., Dyson, H., Jones, G. S., Knight, J. R., Neininger, E., O'Connor, F. M., Ridley, J. K., Ringer, M. A., Scaife, A. A., Senior, C. A., and Wood, R. A.: The Impact of Prescribed Ozone in Climate Projections Run With HadGEM3-GC3.1, J. Adv. Model. Earth Sy., 11, 3443–3453, https://doi.org/10.1029/2019MS001714, 2019.

Haynes, P. H., McIntyre, M. E., Shepherd, T. G., Marks, C. J., and Shine, K. P.: On the "Downward Control" of Extratropical Diabatic Circulations by Eddy-Induced Mean Zonal Forces, J. Atmos. Sci., 48, 651–678, https://doi.org/10.1175/1520-0469(1991)048<0651:OTCOED>2.0.CO;2, 1991.

Hegglin, M., Kinnison, D., Lamarque, J.-F., and Plummer, D.: CCMI ozone in support of CMIP6 – version 1.0, Earth System Grid Federation, https://doi.org/10.22033/ESGF/input4MIPs.1115, 2016.

Hersbach, H., Bell, B., Berrisford, P., Hirahara, S., Horányi, A., Muñoz-Sabater, J., Nicolas, J., Peubey, C., Radu, R., Schepers, D., Simmons, A., Soci, C., Abdalla, S., Abellan, X., Balsamo, G., Bechtold, P., Biavati, G., Bidlot, J., Bonavita, M., De Chiara, G., Dahlgren, P., Dee, D., Diamantakis, M., Dragani, R., Flemming, J., Forbes, R., Fuentes, M., Geer, A., Haimberger, L., Healy, S., Hogan, R. J., Hólm, E., Janisková, M., Keeley, S., Laloyaux, P., Lopez, P., Lupu, C., Radnoti, G., de Rosnay, P., Rozum, I., Vamborg, F., Villaume, S., and Thépaut, J.-N.: The ERA5 global reanalysis, Q. J. Roy. Meteor. Soc., 146, 1999–2049, https://doi.org/10.1002/qj.3803, 2020.

Ivanciu, I.: Ivanciu et al., 2020 – Effects of prescribed CMIP6 ozone on simulating the Southern Hemisphere atmospheric circulation response to ozone depletion [Data set], Zenodo, https://doi.org/10.5281/zenodo.3931507, 2020.

Ivanciu, I.: Code used in Ivanciu et al., 2021 – Effects of prescribed CMIP6 ozone on simulating the Southern Hemisphere atmospheric circulation response to ozone depletion, Zenodo, https://doi.org/10.5281/zenodo.4680722, 2021.

Ivy, D. J., Solomon, S., and Rieder, H. E.: Radiative and Dynamical Influences on Polar Stratospheric Temperature Trends, J. Climate, 29, 4927–4938, https://doi.org/10.1175/JCLI-D-15-0503.1, 2016.

Jonsson, A. I., de Grandpré, J., Fomichev, V. I., McConnell, J. C., and Beagley, S. R.: Doubled CO2-induced cooling in the middle atmosphere: Photochemical analysis of the ozone radiative feedback, J. Geophys. Res.-Atmos., 109, D24103, https://doi.org/10.1029/2004JD005093, 2004.

Kang, S. M., Polvani, L. M., Fyfe, J. C., and Sigmond, M.: Impact of Polar Ozone Depletion on Subtropical Precipitation, Science, 332, 951–954, https://doi.org/10.1126/science.1202131, 2011.

Keeble, J., Braesicke, P., Abraham, N. L., Roscoe, H. K., and Pyle, J. A.: The impact of polar stratospheric ozone loss on Southern Hemisphere stratospheric circulation and climate, Atmos. Chem. Phys., 14, 13705–13717, https://doi.org/10.5194/acp-14-13705-2014, 2014.

Keeble, J., Hassler, B., Banerjee, A., Checa-Garcia, R., Chiodo, G., Davis, S., Eyring, V., Griffiths, P. T., Morgenstern, O., Nowack, P., Zeng, G., Zhang, J., Bodeker, G., Cugnet, D., Danabasoglu, G., Deushi, M., Horowitz, L. W., Li, L., Michou, M., Mills, M. J., Nabat, P., Park, S., and Wu, T.: Evaluating stratospheric ozone and water vapor changes in CMIP6 models from 1850–2100, Atmos. Chem. Phys. Discuss. [preprint], https://doi.org/10.5194/acp-2019-1202, in review, 2020.

Keeley, S. P. E., Gillett, N. P., Thompson, D. W. J., Solomon, S., and Forster, P. M.: Is Antarctic climate most sensitive to ozone depletion in the middle or lower stratosphere?, Geophys. Res. Lett., 34, L22812, https://doi.org/10.1029/2007GL031238, 2007.

Kinnison, D. E., Brasseur, G. P., Walters, S., Garcia, R. R., Marsh, D. R., Sassi, F., Harvey, V. L., Randall, C. E., Emmons, L., Lamarque, J. F., Hess, P., Orlando, J. J., Tie, X. X., Randel, W., Pan, L. L., Gettelman, A., Granier, C., Diehl, T., Niemeier, U., and Simmons, A. J.: Sensitivity of chemical tracers to meteorological parameters in the MOZART-3 chemical transport model, J. Geophys. Res.-Atmos., 112, D20302, https://doi.org/10.1029/2006JD007879, 2007.

Kushner, P. J., Held, I. M., and Delworth, T. L.: Southern Hemisphere Atmospheric Circulation Response to Global Warming, J. Climate, 14, 2238–2249, https://doi.org/10.1175/1520-0442(2001)014<0001:SHACRT>2.0.CO;2, 2001.

Langematz, U., Kunze, M., Krüger, K., Labitzke, K., and Roff, G. L.: Thermal and dynamical changes of the stratosphere since 1979 and their link to ozone and CO2 changes, J. Geophys. Res.-Atmos., 108, ACL 9-1–ACL 9-13, https://doi.org/10.1029/2002JD002069, 2003.

Li, F., Austin, J., and Wilson, J.: The Strength of the Brewer-Dobson Circulation in a Changing Climate: Coupled Chemistry-Climate Model Simulations, J. Climate, 21, 40–57, https://doi.org/10.1175/2007JCLI1663.1, 2008.

Li, F., Newman, P. A., and Stolarski, R. S.: Relationships between the Brewer-Dobson circulation and the southern annular mode during austral summer in coupled chemistry-climate

model simulations, J. Geophys. Res.-Atmos., 115, D15106, https://doi.org/10.1029/2009JD012876, 2010.

Li, F., Vikhliaev, Y. V., Newman, P. A., Pawson, S., Perlwitz, J., Waugh, D. W., and Douglass, A. R.: Impacts of Interactive Stratospheric Chemistry on Antarctic and Southern Ocean Climate Change in the Goddard Earth Observing System, Version 5 (GEOS-5), J. Climate, 29, 3199–3218, https://doi.org/10.1175/JCLI-D-15-0572.1, 2016.

Li, F., Newman, P., Pawson, S., and Perlwitz, J.: Effects of Greenhouse Gas Increase and Stratospheric Ozone Depletion on Stratospheric Mean Age of Air in 1960-2010, J. Geophys. Res.-Atmos., 123, 2098–2110, https://doi.org/10.1002/2017JD027562, 2018.

Lin, P., Fu, Q., Solomon, S., and Wallace, J. M.: Temperature Trend Patterns in Southern Hemisphere High Latitudes: Novel Indicators of Stratospheric Change, J. Climate, 22, 6325–6341, https://doi.org/10.1175/2009JCLI2971.1, 2009.

Lin, P., Paynter, D., Polvani, L., Correa, G. J. P., Ming, Y., and Ramaswamy, V.: Dependence of model-simulated response to ozone depletion on stratospheric polar vortex climatology, Geophys. Res. Lett., 44, 6391–6398, https://doi.org/10.1002/2017GL073862, 2017.

Lubis, S. W., Omrani, N.-E., Matthes, K., and Wahl, S.: Impact of the Antarctic Ozone Hole on the Vertical Coupling of the Stratosphere–Mesosphere–Lower Thermosphere System, J. Atmos. Sci., 73, 2509–2528, https://doi.org/10.1175/JAS-D-15-0189.1, 2016.

Madec, G. and the NEMO team: NEMO ocean engine – version 3.6, Note du Pôle de modélisation, Institut Pierre-Simon Laplace (IPSL), France, 406, 2016.

Mahlman, J. D., Umscheid, L. J., and Pinto, J. P.: Transport, Radiative, and Dynamical Effects of the Antarctic Ozone Hole: A GFDL "SKYHI" Model Experiment, J. Atmos. Sci., 51, 489–508, https://doi.org/10.1175/1520-0469(1994)051<0489:TRADEO>2.0.CO;2, 1994.

Marshall, G. J.: Trends in the Southern Annular Mode from Observations and Reanalyses, J. Climate, 16, 4134–4143, https://doi.org/10.1175/1520-0442(2003)016<4134:TITSAM>2.0.CO;2, 2003.

Marshall, G. J., Stott, P. A., Turner, J., Connolley, W. M., King, J. C., and Lachlan-Cope, T. A.: Causes of exceptional atmospheric circulation changes in the Southern Hemisphere, Geophys. Res. Lett., 31, L14205, https://doi.org/10.1029/2004GL019952, 2004.

Matthes, K., Funke, B., Andersson, M. E., Barnard, L., Beer, J., Charbonneau, P., Clilverd, M. A., Dudok de Wit, T., Haberreiter, M., Hendry, A., Jackman, C. H., Kretzschmar, M., Kruschke, T., Kunze, M., Langematz, U., Marsh, D. R., Maycock, A. C., Misios, S., Rodger, C. J., Scaife, A. A., Seppälä, A., Shangguan, M., Sinnhuber, M., Tourpali, K., Usoskin, I., van de Kamp, M., Verronen, P. T., and Versick, S.: Solar forcing for CMIP6 (v3.2), Geosci. Model Dev., 10, 2247–2302, https://doi.org/10.5194/gmd-10-2247-2017, 2017.

Matthes, K., Biastoch, A., Wahl, S., Harlaß, J., Martin, T., Brücher, T., Drews, A., Ehlert, D., Getzlaff, K., Krüger, F., Rath, W., Scheinert, M., Schwarzkopf, F. U., Bayr, T., Schmidt, H., and Park, W.: The Flexible Ocean and Climate Infrastructure version 1 (FOCI1): mean state and variability, Geosci. Model Dev., 13, 2533–2568, https://doi.org/10.5194/gmd-13-2533-2020, 2020.

McLandress, C. and Shepherd, T. G.: Simulated Anthropogenic Changes in the Brewer–Dobson Circulation, Including Its Extension to High Latitudes, J. Climate, 22, 1516–1540, https://doi.org/10.1175/2008JCLI2679.1, 2009.

McLandress, C., Jonsson, A. I., Plummer, D. A., Reader, M. C., Scinocca, J. F., and Shepherd, T. G.: Separating the Dynamical Effects of Climate Change and Ozone Depletion. Part I: Southern Hemisphere Stratosphere, J. Climate, 23, 5002–5020, https://doi.org/10.1175/2010JCLI3586.1, 2010.

McLandress, C., Shepherd, T. G., Scinocca, J. F., Plummer, D. A., Sigmond, M., Jonsson, A. I., and Reader, M. C.: Separating the Dynamical Effects of Climate Change and Ozone Depletion. Part II: Southern Hemisphere Troposphere, J. Climate, 24, 1850–1868, https://doi.org/10.1175/2010JCLI3958.1, 2011.

Meinshausen, M., Vogel, E., Nauels, A., Lorbacher, K., Meinshausen, N., Etheridge, D. M., Fraser, P. J., Montzka, S. A., Rayner, P. J., Trudinger, C. M., Krummel, P. B., Beyerle, U., Canadell, J. G., Daniel, J. S., Enting, I. G., Law, R. M., Lunder, C. R., O'Doherty, S., Prinn, R. G., Reimann, S., Rubino, M., Velders, G. J. M., Vollmer, M. K., Wang, R. H. J., and Weiss, R.: Historical greenhouse gas concentrations for climate modelling (CMIP6), Geosci. Model Dev., 10, 2057–2116, https://doi.org/10.5194/gmd-10-2057-2017, 2017.

Min, S.-K. and Son, S.-W.: Multimodel attribution of the Southern Hemisphere Hadley cell widening: Major role of ozone depletion, J. Geophys. Res.-Atmos., 118, 3007–3015, https://doi.org/10.1002/jgrd.50232, 2013.

Morgenstern, O.: The Southern Annular Mode in 6th Coupled Model Intercomparison Project Models, J. Geophys. Res.-Atmos., 126, e2020JD034161, https://doi.org/10.1029/2020JD034161, 2021.

Neely, R. R., Marsh, D. R., Smith, K. L., Davis, S. M., and Polvani, L. M.: Biases in southern hemisphere climate trends induced by coarsely specifying the temporal resolution of stratospheric ozone, Geophys. Res. Lett., 41, 8602–8610, https://doi.org/10.1002/2014GL061627, 2014.

North, G. R., Bell, T. L., Cahalan, R. F., and Moeng, F. J.: Sampling Errors in the Estimation of Empirical Orthogonal Functions, Mon. Weather Rev., 110, 699–706, https://doi.org/10.1175/1520-0493(1982)110<0699:SEITEO>2.0.CO;2, 1982.

Nowack, P. J., Luke Abraham, N., Maycock, A. C., Braesicke, P., Gregory, J. M., Joshi, M. M., Osprey, A., and Pyle, J. A.: A large ozone-circulation feedback and its implications for global warming assessments, Nat. Clim. Change, 5, 41–45, https://doi.org/10.1038/nclimate2451, 2015.

Oberländer-Hayn, S., Meul, S., Langematz, U., Abalichin, J., and Haenel, F.: A chemistry-climate model study of past changes in the Brewer-Dobson circulation, J. Geophys. Res.-Atmos., 120, 6742–6757, https://doi.org/10.1002/2014JD022843, 2015.

Oehrlein, J., Chiodo, G., and Polvani, L. M.: The effect of interactive ozone chemistry on weak and strong stratospheric polar vortex events, Atmos. Chem. Phys., 20, 10531–10544, https://doi.org/10.5194/acp-20-10531-2020, 2020.

Orr, A., Bracegirdle, T. J., Hosking, J. S., Jung, T., Haigh, J. D., Phillips, T., and Feng, W.: Possible Dynamical Mechanisms for Southern Hemisphere Climate Change due to the Ozone Hole, J. Atmos. Sci., 69, 2917–2932, https://doi.org/10.1175/JAS-D-11-0210.1, 2012.

Orr, A., Bracegirdle, T. J., Hosking, J. S., Feng, W., Roscoe, H. K., and Haigh, J. D.: Strong Dynamical Modulation of the Cooling of the Polar Stratosphere Associated with the Antarctic Ozone

Hole, J. Climate, 26, 662–668, https://doi.org/10.1175/JCLI-D-12-00480.1, 2013.

Perlwitz, J., Pawson, S., Fogt, R. L., Nielsen, J. E., and Neff, W. D.: Impact of stratospheric ozone hole recovery on Antarctic climate, Geophys. Res. Lett., 35, L08714, https://doi.org/10.1029/2008GL033317, 2008.

Peters, D. H. W., Schneidereit, A., Bügelmayer, M., Zülicke, C., and Kirchner, I.: Atmospheric Circulation Changes in Response to an Observed Stratospheric Zonal Ozone Anomaly, Atmosphere-Ocean, 53, 74–88, https://doi.org/10.1080/07055900.2013.878833, 2015.

Polvani, L. M., Waugh, D. W., Correa, G. J. P., and Son, S.-W.: Stratospheric Ozone Depletion: The Main Driver of Twentieth-Century Atmospheric Circulation Changes in the Southern Hemisphere, J. Climate, 24, 795–812, https://doi.org/10.1175/2010JCLI3772.1, 2011.

Polvani, L. M., Abalos, M., Garcia, R., Kinnison, D., and Randel, W. J.: Significant Weakening of Brewer-Dobson Circulation Trends Over the 21st Century as a Consequence of the Montreal Protocol, Geophys. Res. Lett., 45, 401–409, https://doi.org/10.1002/2017GL075345, 2018.

Previdi, M. and Polvani, L. M.: Climate system response to stratospheric ozone depletion and recovery, Q. J. Roy. Meteor. Soc., 140, 2401–2419, https://doi.org/10.1002/qj.2330, 2014.

Randel, W. J. and Wu, F.: Cooling of the Arctic and Antarctic Polar Stratospheres due to Ozone Depletion, J. Climate, 12, 1467–1479, https://doi.org/10.1175/1520-0442(1999)012<1467:COTAAA>2.0.CO;2, 1999.

Randel, W. J., Shine, K. P., Austin, J., Barnett, J., Claud, C., Gillett, N. P., Keckhut, P., Langematz, U., Lin, R., Long, C., Mears, C., Miller, A., Nash, J., Seidel, D. J., Thompson, D. W. J., Wu, F., and Yoden, S.: An update of observed stratospheric temperature trends, J. Geophys. Res.-Atmos., 114, D02107, https://doi.org/10.1029/2008JD010421, 2009.

Reick, C. H., Raddatz, T., Brovkin, V., and Gayler, V.: Representation of natural and anthropogenic land cover change in MPI-ESM, J. Adv. Model. Earth Sy., 5, 459–482, https://doi.org/10.1002/jame.20022, 2013.

Sassi, F., Boville, B. A., Kinnison, D., and Garcia, R. R.: The effects of interactive ozone chemistry on simulations of the middle atmosphere, Geophys. Res. Lett., 32, L07811, https://doi.org/10.1029/2004GL022131, 2005.

Schultz, M. G., Stadtler, S., Schröder, S., Taraborrelli, D., Franco, B., Krefting, J., Henrot, A., Ferrachat, S., Lohmann, U., Neubauer, D., Siegenthaler-Le Drian, C., Wahl, S., Kokkola, H., Kühn, T., Rast, S., Schmidt, H., Stier, P., Kinnison, D., Tyndall, G. S., Orlando, J. J., and Wespes, C.: The chemistry–climate model ECHAM6.3-HAM2.3-MOZ1.0, Geosci. Model Dev., 11, 1695–1723, https://doi.org/10.5194/gmd-11-1695-2018, 2018.

Schwarzkopf, F. U., Biastoch, A., Böning, C. W., Chanut, J., Durgadoo, J. V., Getzlaff, K., Harlaß, J., Rieck, J. K., Roth, C., Scheinert, M. M., and Schubert, R.: The INALT family – a set of high-resolution nests for the Agulhas Current system within global NEMO ocean/sea-ice configurations, Geosci. Model Dev., 12, 3329–3355, https://doi.org/10.5194/gmd-12-3329-2019, 2019.

Seviour, W. J. M., Waugh, D. W., Polvani, L. M., Correa, G. J. P., and Garfinkel, C. I.: Robustness of the Simulated Tropospheric Response to Ozone Depletion, J. Climate, 30, 2577–2585, https://doi.org/10.1175/JCLI-D-16-0817.1, 2017.

Simpson, I. R., Hitchcock, P., Shepherd, T. G., and Scinocca, J. F.: Stratospheric variability and tropospheric annular-mode timescales, Geophys. Res. Lett., 38, L20806, https://doi.org/10.1029/2011GL049304, 2011.

Solomon, S.: Stratospheric ozone depletion: A review of concepts and history, Rev. Geophys., 37, 275–316, https://doi.org/10.1029/1999RG900008, 1999.

Solomon, S., Kinnison, D., Bandoro, J., and Garcia, R.: Simulation of polar ozone depletion: An update, J. Geophys. Res.-Atmos., 120, 7958–7974, https://doi.org/10.1002/2015JD023365, 2015.

Son, S.-W., Polvani, L. M., Waugh, D. W., Akiyoshi, H., Garcia, R., Kinnison, D., Pawson, S., Rozanov, E., Shepherd, T. G., and Shibata, K.: The Impact of Stratospheric Ozone Recovery on the Southern Hemisphere Westerly Jet, Science, 320, 1486–1489, https://doi.org/10.1126/science.1155939, 2008.

Son, S.-W., Polvani, L. M., Waugh, D. W., Birner, T., Akiyoshi, H., Garcia, R. R., Gettelman, A., Plummer, D. A., and Rozanov, E.: The Impact of Stratospheric Ozone Recovery on Tropopause Height Trends, J. Climate, 22, 429–445, https://doi.org/10.1175/2008JCLI2215.1, 2009.

Son, S.-W., Gerber, E. P., Perlwitz, J., Polvani, L. M., Gillett, N. P., Seo, K.-H., Eyring, V., Shepherd, T. G., Waugh, D., Akiyoshi, H., Austin, J., Baumgaertner, A., Bekki, S., Braesicke, P., Brühl, C., Butchart, N., Chipperfield, M. P., Cugnet, D., Dameris, M., Dhomse, S., Frith, S., Garny, H., Garcia, R., Hardiman, S. C., Jöckel, P., Lamarque, J. F., Mancini, E., Marchand, M., Michou, M., Nakamura, T., Morgenstern, O., Pitari, G., Plummer, D. A., Pyle, J., Rozanov, E., Scinocca, J. F., Shibata, K., Smale, D., Teyssèdre, H., Tian, W., and Yamashita, Y.: Impact of stratospheric ozone on Southern Hemisphere circulation change: A multimodel assessment, J. Geophys. Res.-Atmos., 115, D00M07, https://doi.org/10.1029/2010JD014271, 2010.

Son, S.-W., Han, B.-R., Garfinkel, C. I., Kim, S.-Y., Park, R., Abraham, N. L., Akiyoshi, H., Archibald, A. T., Butchart, N., Chipperfield, M. P., Dameris, M., Deushi, M., Dhomse, S. S., Hardiman, S. C., Jöckel, P., Kinnison, D., Michou, M., Morgenstern, O., O'Connor, F. M., Oman, L. D., Plummer, D. A., Pozzer, A., Revell, L. E., Rozanov, E., Stenke, A., Stone, K., Tilmes, S., Yamashita, Y., and Zeng, G.: Tropospheric jet response to Antarctic ozone depletion: An update with Chemistry-Climate Model Initiative (CCMI) models, Environ. Res. Lett., 13, 054024, https://doi.org/10.1088/1748-9326/aabf21, 2018.

Stevens, B., Giorgetta, M., Esch, M., Mauritsen, T., Crueger, T., Rast, S., Salzmann, M., Schmidt, H., Bader, J., Block, K., Brokopf, R., Fast, I., Kinne, S., Kornblueh, L., Lohmann, U., Pincus, R., Reichler, T., and Roeckner, E.: Atmospheric component of the MPI-M Earth System Model: ECHAM6, J. Adv. Model. Earth Sy., 5, 146–172, https://doi.org/10.1002/jame.20015, 2013.

Stolarski, R. S., Douglass, A. R., Newman, P. A., Pawson, S., and Schoeberl, M. R.: Relative Contribution of Greenhouse Gases and Ozone-Depleting Substances to Temperature Trends in the Stratosphere: A Chemistry–Climate Model Study, J. Climate, 23, 28–42, https://doi.org/10.1175/2009JCLI2955.1, 2010.

Swart, N. C. and Fyfe, J. C.: Observed and simulated changes in the Southern Hemisphere surface westerly wind-stress, Geophys. Res. Lett., 39, L16711, https://doi.org/10.1029/2012GL052810, 2012.

Thompson, D. W. J. and Solomon, S.: Interpretation of Recent Southern Hemisphere Climate Change, Science, 296, 895–899, https://doi.org/10.1126/science.1069270, 2002.

Thompson, D. W. J., Solomon, S., Kushner, P. J., England, M. H., Grise, K. M., and Karoly, D. J.: Signatures of the Antarctic ozone hole in Southern Hemisphere surface climate change, Nat. Geosci., 4, 741–749, https://doi.org/10.1038/ngeo1296, 2011.

Waugh, D. W., Randel, W. J., Pawson, S., Newman, P. A., and Nash, E. R.: Persistence of the lower stratospheric polar vortices, J. Geophys. Res.-Atmos., 104, 27191–27201, https://doi.org/10.1029/1999JD900795, 1999.

Waugh, D. W., Oman, L., Newman, P. A., Stolarski, R. S., Pawson, S., Nielsen, J. E., and Perlwitz, J.: Effect of zonal asymmetries in stratospheric ozone on simulated Southern Hemisphere climate trends, Geophys. Res. Lett., 36, L18701, https://doi.org/10.1029/2009GL040419, 2009.

Waugh, D. W., Garfinkel, C. I., and Polvani, L. M.: Drivers of the Recent Tropical Expansion in the Southern Hemisphere: Changing SSTs or Ozone Depletion?, J. Climate, 28, 6581–6586, https://doi.org/10.1175/JCLI-D-15-0138.1, 2015.

World Meteorological Organization: Scientific Assessment of Ozone Depletion: 2018, Global Ozone Research and Monitoring Project-Report No. 58, Geneva, Switzerland, 2018.

Yang, X.-Y., Huang, R. X., and Wang, D. X.: Decadal Changes of Wind Stress over the Southern Ocean Associated with Antarctic Ozone Depletion, J. Climate, 20, 3395–3410, https://doi.org/10.1175/JCLI4195.1, 2007.

Young, P. J., Butler, A. H., Calvo, N., Haimberger, L., Kushner, P. J., Marsh, D. R., Randel, W. J., and Rosenlof, K. H.: Agreement in late twentieth century Southern Hemisphere stratospheric temperature trends in observations and CCMVal-2, CMIP3, and CMIP5 models, J. Geophys. Res.-Atmos., 118, 605–613, https://doi.org/10.1002/jgrd.50126, 2013.

Supplement of Atmos. Chem. Phys., 21, 5777–5806, 2021
https://doi.org/10.5194/acp-21-5777-2021-supplement

Atmospheric Chemistry and Physics Open Access

Supplement of

Effects of prescribed CMIP6 ozone on simulating the Southern Hemisphere atmospheric circulation response to ozone depletion

Ioana Ivanciu et al.

Correspondence to: Ioana Ivanciu (iivanciu@geomar.de)

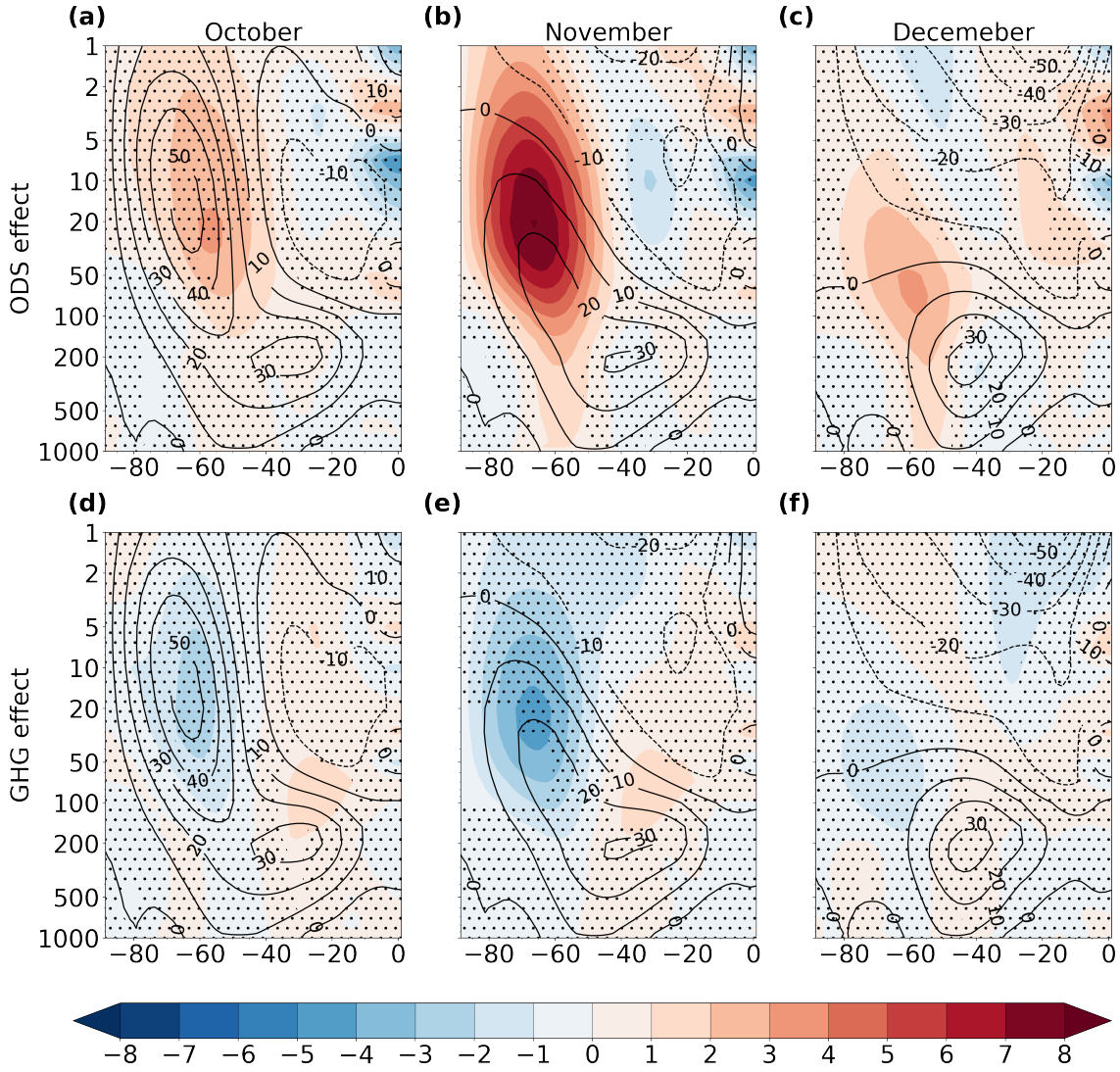

Figure S1. Latitude-height zonal wind difference between REF and NoODS (a, b and c) and between REF and NoGHG (d, e and f) for October (a and d), November (b and e) and December (c and f) in $\mathrm{m\ s^{-1}}$ (color shading). Stippling masks values that are not significant at the 95% confidence interval. The overlaying contours mark the 1978-2002 climatology of each respective month from REF.

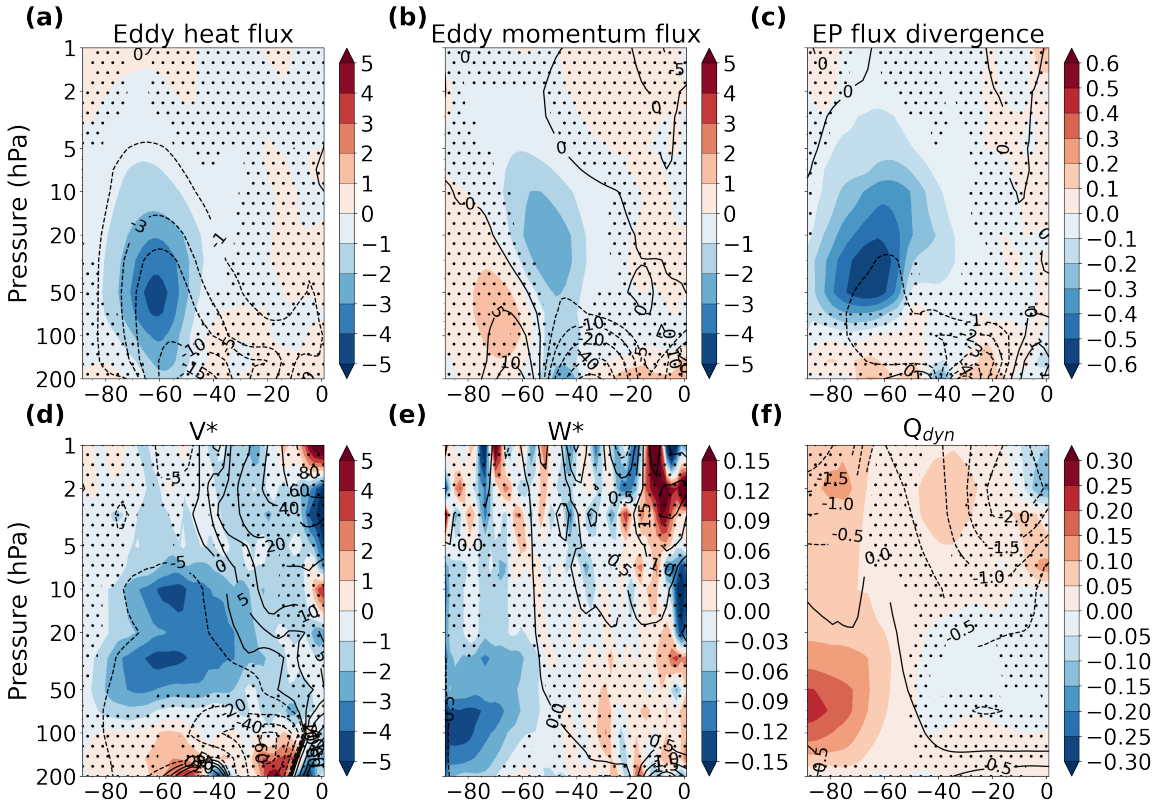

Figure S2. Latitude-height December difference between REF and NoODS in the eddy heat flux (a, in K $\mathrm{m\ s^{-1}}$), the eddy momentum flux (b, in $\mathrm{m^2 s^{-2}}$), the divergence of the EP flux (c, in $\mathrm{m\ s^{-1}\ day^{-1}}$), the meridional residual velocity (d, in $\mathrm{cm\ s^{-1}}$), the vertical residual velocity (e, in $\mathrm{mm\ s^{-1}}$) and in the dynamical heating rate (f, in K $\mathrm{day^{-1}}$) for the period 1978-2002 (color shading). Contours in each panel show the corresponding climatology from REF. Stippling masks values that are not significant at the 95% confidence interval.

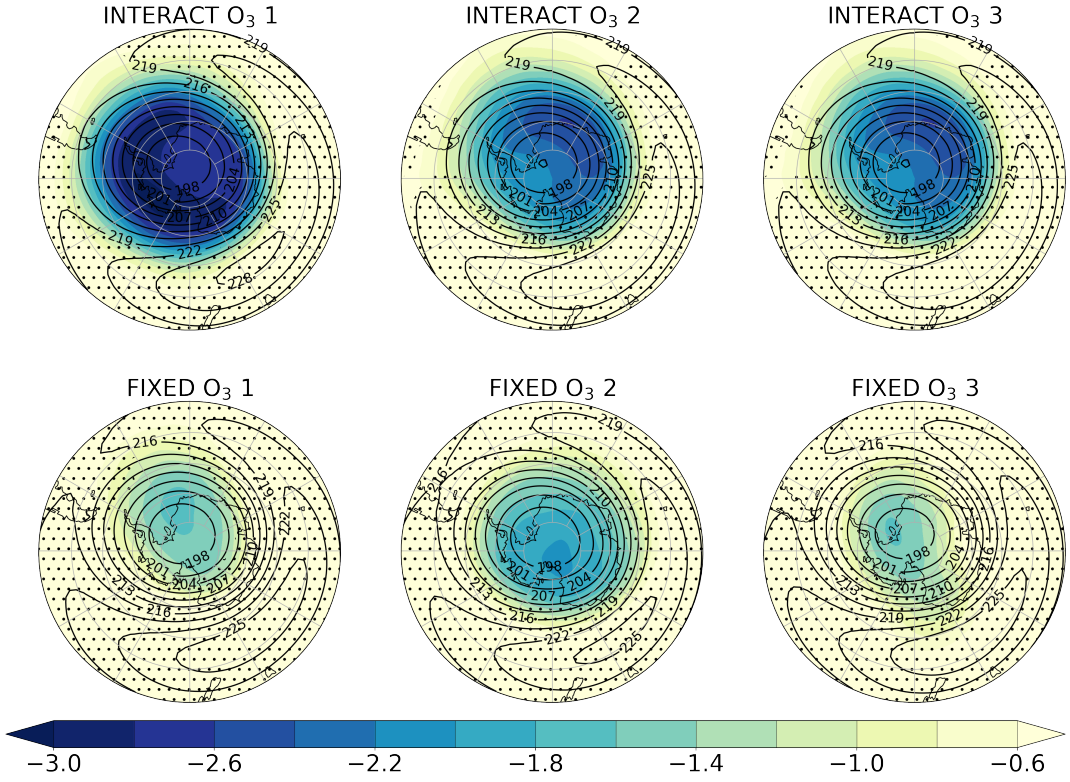

Figure S3. Polar stereographic maps of the October 70 hPa temperature trends for the individual members of INTERACT O_3 (a-c) and FIXED O_3 (d-f) in K dec^{-1} for the period 1958-2002 (color shading). The contours show the October climatological temperature in each simulations. Stippling masks regions where the trends are not significant at the 95% confidence level.

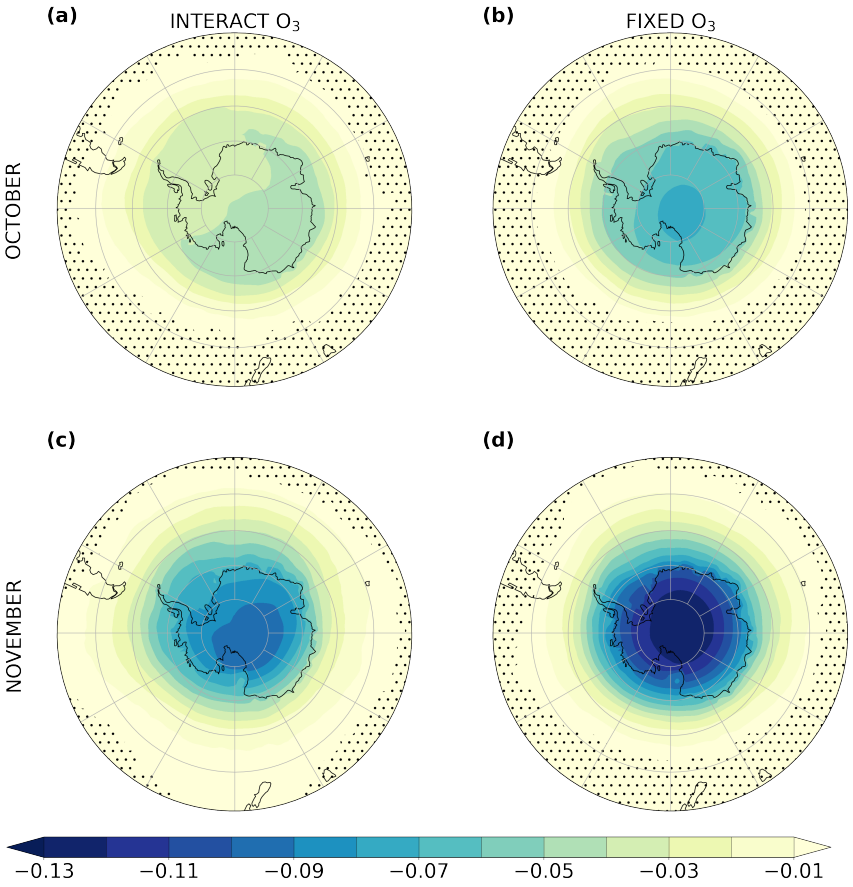

Figure S4. Polar stereographic maps of the October (a and b) and November (c and d) 100 hPa trends in SW heating rate for INTERACT O_3 (a and c) and FIXED O_3 (b and d) in K day^{-1} dec^{-1} for the period 1958-2002. Stippling masks regions where the trends are not significant at the 95% confidence level.

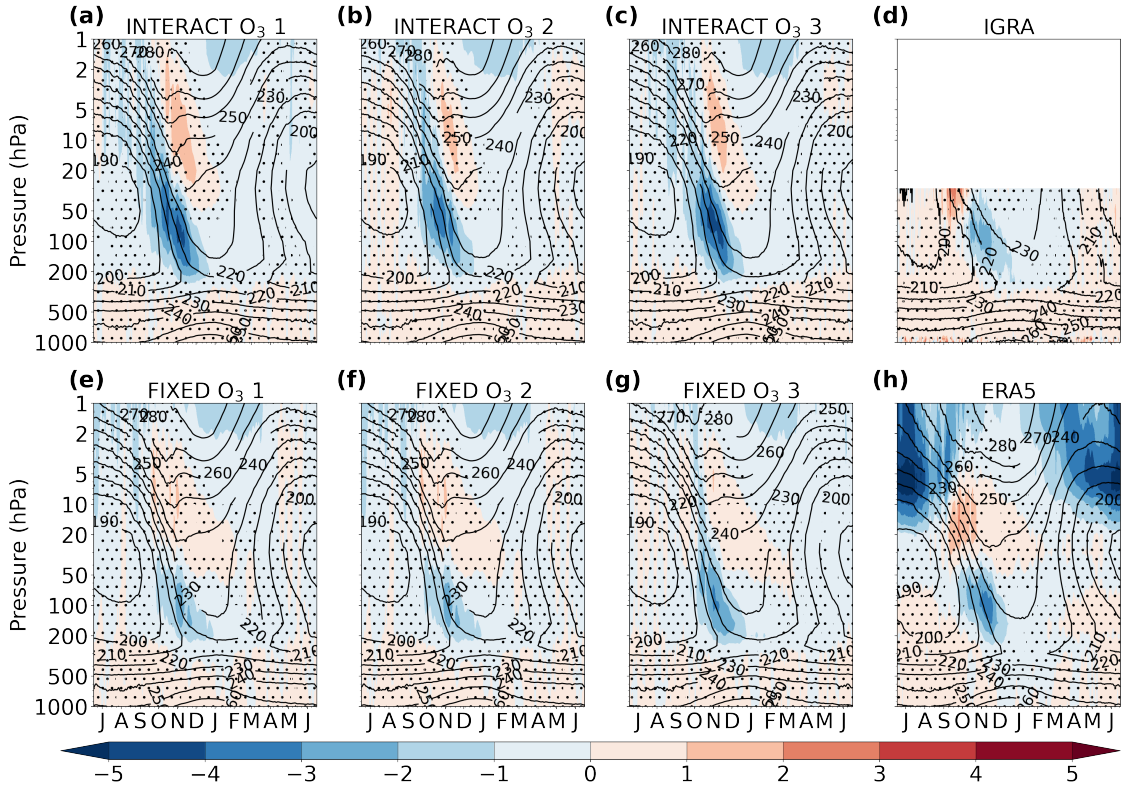

Figure S5. Seasonal cycle of the polar cap (65°S-90°S) temperature trend for the individual members of INTERACT O_3 (a-c) and FIXED O_3 (e-g) and for IGRA (d) and ERA5 (h) for the period 1958-2002 in K dec^{-1} (color shading). Stippling masks regions where the trends are not significant at the 95% confidence level. The overlaying contours show the corresponding climatological seasonal cycle. The letter corresponding to each month marks the middle of that month.

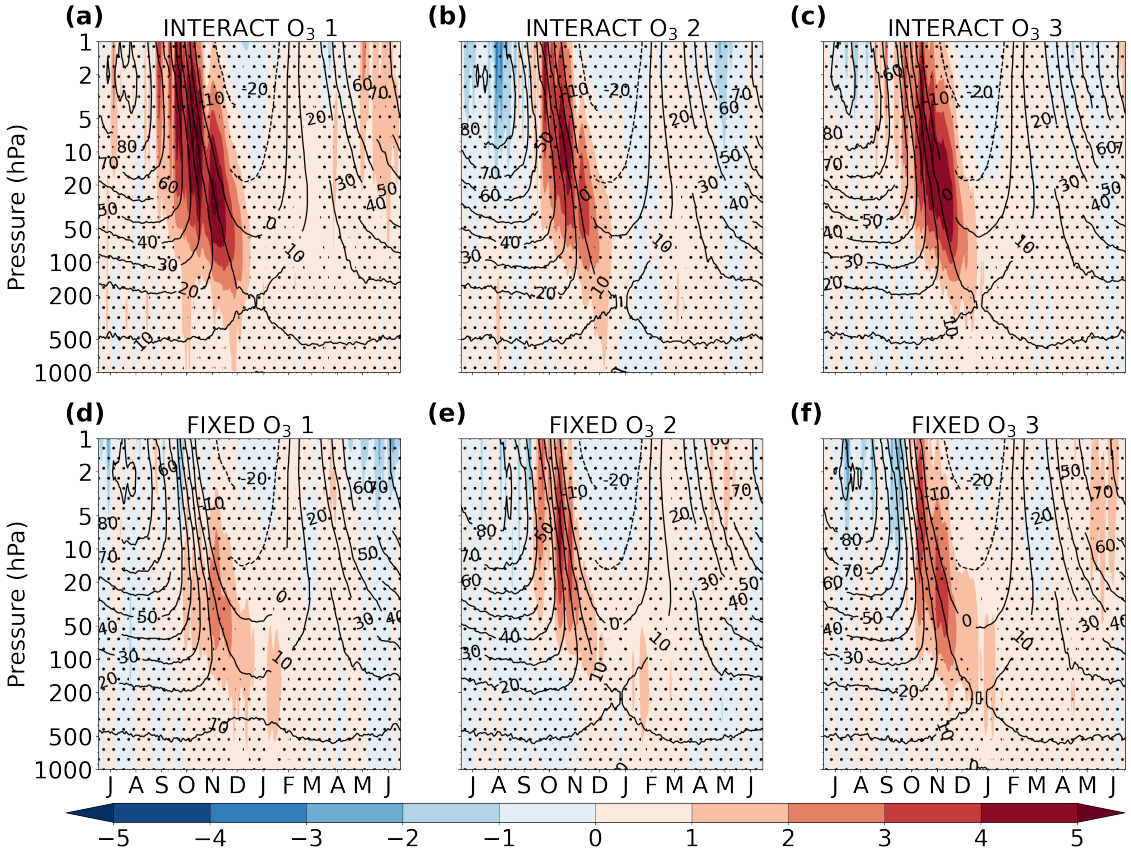

Figure S6. Seasonal cycle of the 50°S-70°S zonal wind trend for the individual members of INTERACT O_3 (a-c) and FIXED O_3 (d-f) for the period 1958-2002 in $\mathrm{m\ s^{-1}\ dec^{-1}}$ (color shading). Stippling masks regions where the trends are not significant at the 95% confidence level. The overlaying contours show the corresponding climatological seasonal cycle. The letter corresponding to each month marks the middle of that month.

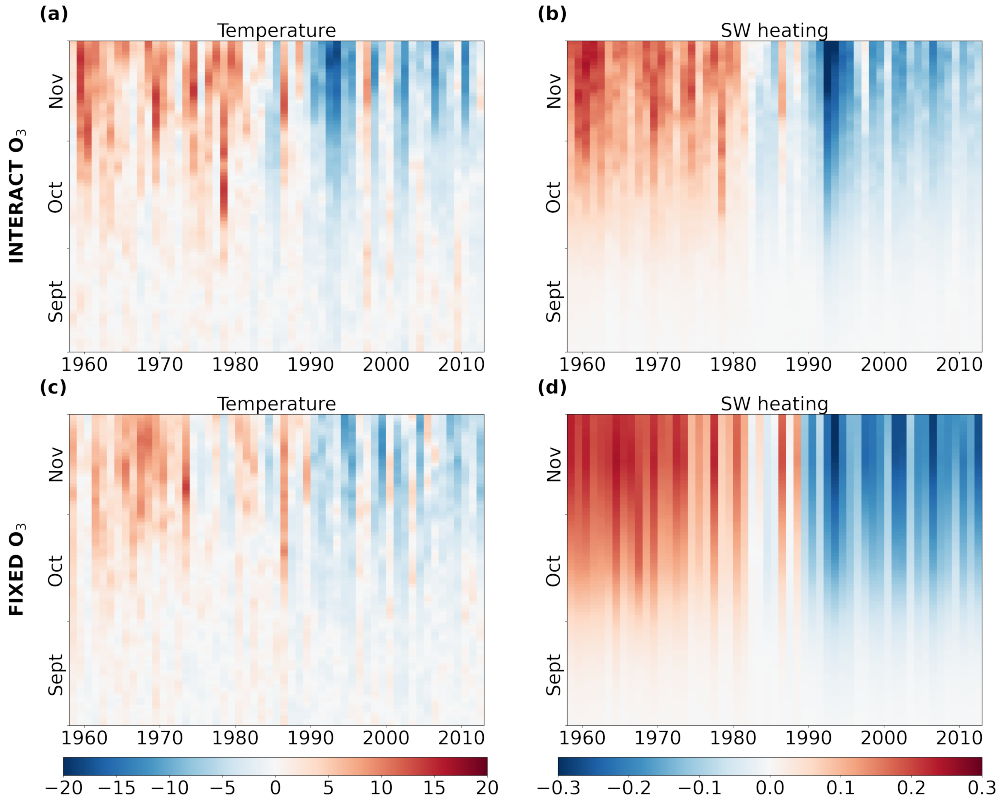

Figure S7. Timeseries of INTERACT O_3 (a, b) and FIXED O_3 (c, d) 100 hPa polar cap (70°S-90°S) temperature (a, c, in K) and SW heating rate (b, d, in K day^{-1}) anomalies with respect to the 1958-2013 climatology for each austral spring day.

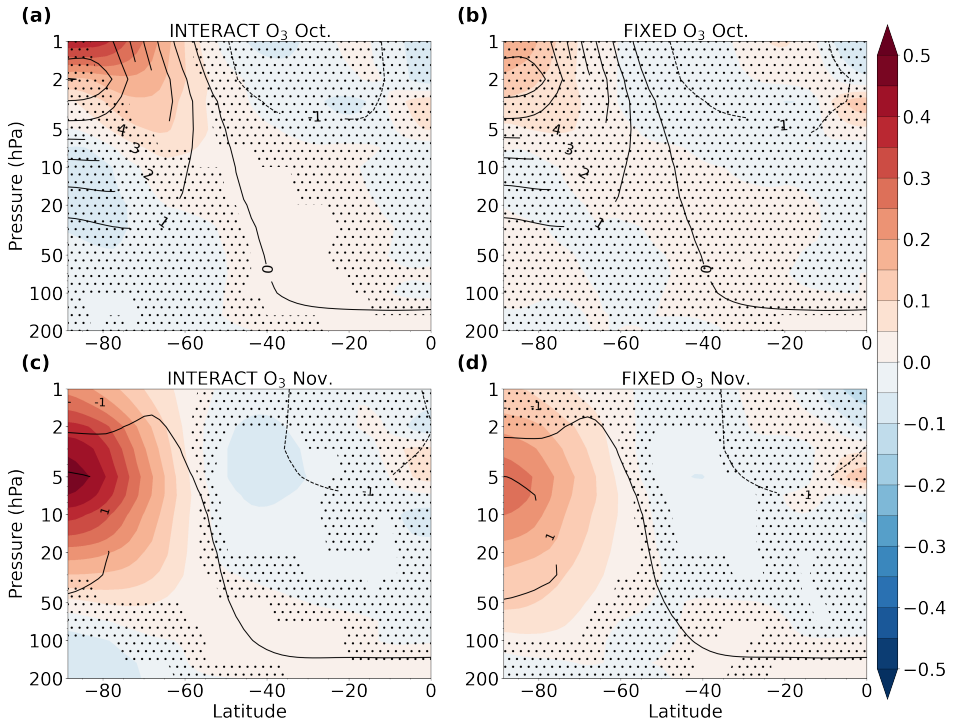

Figure S8. Latitude-height trends in October (a and b) and November (c and d) dynamical heating rate (in $\mathrm{K\ day^{-1}\ dec^{-1}}$) in INTERACT O_3 (a and c) and FIXED O_3 (b and d) for the period 1958-2002 (color shading). Stippling masks the trends that are not significant at the 95% confidence interval. The overlaying contours in each panel show the corresponding climatologies.

Chapter 4

Twenty-first-century Southern Hemisphere impacts of ozone recovery and climate change from the stratosphere to the ocean

This chapter investigates the changes in the Southern Hemisphere atmospheric and oceanic circulation that are predicted to occur during the twenty-first century under the SSP5-8.5 high emission scenario. The contributions of the increase in anthropogenic GHGs and of ozone recovery to these changes are quantified and it is shown that in the stratosphere both forcings are of similar importance, but in the troposphere and in the ocean the increase in GHGs is the dominant driver of changes, while ozone recovery plays an important mitigating role. This chapter presents several novel results, such as a planetary wavenumber 1 structure of the springtime stratospheric GHG effect. Particular attention is given to the future changes experienced by the Agulhas Current System, which are studied for the first time, and an increase in Agulhas leakage is predicted during the twenty-first century.

The effect on the future projections of using different ozone fields is additionally investigated. Using interactively calculated ozone yields stronger ozone effects and a higher degree of mitigation of the GHG impacts compared to when the CMIP6 ozone field is prescribed. The recovery of the CMIP6 ozone lies at the slower end of projections from chemistry climate models and the effect of this slow recovery is in certain fields as large as the ozone-driven change. This underlines the high uncertainties in future projections associated with the ozone field.

Citation: Ivanciu, I. , Matthes, K. , Biastoch, A. , Wahl, S. and Harlaß, J.: Twenty-first century Southern Hemisphere impacts of ozone recovery and climate change from the stratosphere to the ocean, Weather and Climate Dynamics, 3, 139-171, doi:10.5194/wcd-3-139-2022, 2022.

Candidate's contributions to this publication:

- She designed the experimental set-up and performed eight of the simulations.
- She performed all of the analyses.
- She produced all the figures.
- She wrote the manuscript, from the first draft to the final version.

Weather Clim. Dynam., 3, 139–171, 2022
https://doi.org/10.5194/wcd-3-139-2022

Twenty-first-century Southern Hemisphere impacts of ozone recovery and climate change from the stratosphere to the ocean

Ioana Ivanciu[1], **Katja Matthes**[1], **Arne Biastoch**[1,2], **Sebastian Wahl**[1], **and Jan Harlaß**[1]

[1]GEOMAR Helmholtz Centre for Ocean Research Kiel, Kiel, Germany
[2]Faculty of Mathematics and Natural Sciences, Christian-Albrechts Universität zu Kiel, Kiel, Germany

Correspondence: Ioana Ivanciu (iivanciu@geomar.de)

Received: 2 July 2021 – Discussion started: 21 July 2021
Revised: 16 December 2021 – Accepted: 21 December 2021 – Published: 1 February 2022

Abstract. Changes in stratospheric ozone concentrations and increasing concentrations of greenhouse gases (GHGs) alter the temperature structure of the atmosphere and drive changes in the atmospheric and oceanic circulation. We systematically investigate the impacts of ozone recovery and increasing GHGs on the atmospheric and oceanic circulation in the Southern Hemisphere during the twenty-first century using a unique coupled ocean–atmosphere climate model with interactive ozone chemistry and enhanced oceanic resolution. We use the high-emission scenario SSP5-8.5 for GHGs under which the springtime Antarctic total column ozone returns to 1980s levels by 2048 in our model, warming the lower stratosphere and strengthening the stratospheric westerly winds. We perform a spatial analysis and show for the first time that the austral spring stratospheric response to GHGs exhibits a marked planetary wavenumber 1 (PW1) pattern, which reinforces the response to ozone recovery over the Western Hemisphere and weakens it over the Eastern Hemisphere. These changes, which imply an eastward phase shift in the PW1, largely cancel out in the zonal mean. The Southern Hemisphere residual circulation strengthens during most of the year due to the increase in GHGs and weakens in spring due to ozone recovery. However, we find that in November the GHGs also drive a weakening of the residual circulation, reinforcing the effect of ozone recovery, which represents another novel result. At the surface, the westerly winds weaken and shift equatorward due to ozone recovery, driving a weak decrease in the transport of the Antarctic Circumpolar Current and in the Agulhas leakage and a cooling of the upper ocean, which is most pronounced in the latitudinal band 35–45° S. The increasing GHGs drive changes in the opposite direction that overwhelm the ozone effect. The total changes at the surface and in the oceanic circulation are nevertheless weaker in the presence of ozone recovery than those induced by GHGs alone, highlighting the importance of the Montreal Protocol in mitigating some of the impacts of climate change. We additionally compare the combined effect of interactively calculated ozone recovery and increasing GHGs with their combined effect in an ensemble in which we prescribe the CMIP6 ozone field. This second ensemble simulates a weaker ozone effect in all the examined fields, consistent with its weaker increase in ozone. The magnitude of the difference between the simulated changes at the surface and in the oceanic circulation in the two ensembles is as large as the ozone effect itself. This shows the large uncertainty that is associated with the choice of the ozone field and how the ozone is treated.

1 Introduction

Ozone depletion has been the major driver of change in the Southern Hemisphere (SH) atmospheric circulation during the last decades of the twentieth century (e.g., Polvani et al., 2011b). The effects of ozone depletion extend from the stratosphere (e.g., McLandress et al., 2010; Keeble et al., 2014), where the ozone hole is located, down to the surface and to the ocean circulation (e.g., Thompson et al., 2011; Previdi and Polvani, 2014; Ferreira et al., 2015). A decline in the absorption of shortwave (SW) radiation associated with ozone depletion in the past led to the cooling of the Antarctic lower stratosphere in austral spring, which in turn resulted in the acceleration of the stratospheric westerly winds (Thompson and Solomon, 2002; Gillett and Thompson, 2003) and

a delay in the breakdown of the polar vortex (e.g., Waugh et al., 1999; Langematz et al., 2003; McLandress et al., 2010; Keeble et al., 2014). At the same time, the summer Brewer–Dobson circulation (BDC) in the SH has strengthened in response to changes in wave activity associated with the delayed breakdown of the polar vortex (Li et al., 2008, 2010; Oberländer-Hayn et al., 2015; Abalos et al., 2019). The impact of ozone depletion on the westerlies extends to the surface, where the midlatitude jet strengthens and shifts poleward during the austral summer, and the Southern Annular Mode (SAM) experiences a shift towards more positive values (Gillett and Thompson, 2003; Thompson and Solomon, 2002; Son et al., 2010; Thompson et al., 2011). The associated shift in the southern storm track resulted in precipitation changes (Polvani et al., 2011b), extending to the subtropics (Kang et al., 2011). In addition, the edge of the Hadley cell shifted poleward (Son et al., 2010; Polvani et al., 2011b; Min and Son, 2013; Waugh et al., 2015), causing an expansion of the subtropical dry zones in the SH.

The impacts of ozone depletion are also felt by the ocean as the wind stress over the Southern Ocean increases. In response, the northward Ekman transport across the Southern Ocean increased, leading to enhanced divergence (convergence) and upwelling (downwelling) to the south (north) of the maximum westerly wind stress, therefore enhancing the ventilation of the Southern Ocean (e.g., Waugh et al., 2013). These changes in ocean circulation, possibly in combination with changes in surface heat fluxes, led to changes in surface and subsurface temperatures (Ferreira et al., 2015; A. Solomon et al., 2015; Li et al., 2016, 2021; Seviour et al., 2016). Coupled climate models simulate a two-stage response to a sudden stratospheric ozone loss: cold (warm) sea surface temperature (SST) anomalies occur south (north) of 50° S in a fast response caused by advection due to anomalous Ekman transport, followed by a widespread warming of the Southern Ocean, in a slow response caused by anomalous upwelling (Ferreira et al., 2015; Seviour et al., 2016). There are, however, large intermodel differences in the magnitude and timescale of these responses (Seviour et al., 2019). Studies using low-resolution models showed that the subpolar meridional overturning cell and the Antarctic Circumpolar Current (ACC) strengthen and shift poleward (e.g., Oke and England, 2004; Fyfe and Saenko, 2006; Sigmond et al., 2011; Ferreira et al., 2015; A. Solomon et al., 2015) in response to the poleward intensification of the wind stress over the Southern Ocean. However, another important consequence of the westerly wind stress strengthening is the intensification of eddy activity in the Southern Ocean (e.g., Morrison and Hogg, 2013; Hogg et al., 2015; Patara et al., 2016), which cannot be properly simulated in models that do not have a sufficiently high resolution. In high-resolution models that resolve the oceanic mesoscale eddies, the enhanced eddy activity offsets the effects of the enhanced Ekman transport on the meridional overturning circulation and the ACC. These effects are known as "eddy compensation" (e.g., Farneti et al., 2010; Viebahn and Eden, 2010) and "eddy saturation" (e.g., Farneti et al., 2010; Morrison and Hogg, 2013), respectively, and result in weaker overturning and ACC changes than expected from the increase in the wind stress. Observations seem to support the eddy saturation mechanism as past changes in temperature and salinity within the ACC resulted only in a deepening of the isopycnals, consistent with a poleward shift in the ACC but not in a change in the meridional tilt of the isopycnals, implying that the ACC transport has not changed (Böning et al., 2008). This highlights the importance of using climate models that are capable of capturing the effects of eddies for studying the future changes in the Southern Ocean circulation, as is the case of the model used in this study.

The strengthening of the westerlies due to ozone depletion also resulted in an increase in the wind stress curl over the southern part of the Indian Ocean, which drives decadal changes in the Agulhas leakage (Rouault et al., 2009; Durgadoo et al., 2013). The Agulhas leakage transports warm and saline Indian Ocean waters into the South Atlantic at the southern tip of Africa, in the form of rings, eddies, and filaments. Ocean simulations driven by observation-based reanalysis at the surface and an observation-based reconstruction of the Agulhas leakage exhibit an increase in the second half of the twentieth century as a result of the changes in the westerly winds (Biastoch et al., 2009, 2015; Rouault et al., 2009; Schwarzkopf et al., 2019). According to an estimate of leakage from satellite altimetry, this positive trend appears to have ceased since the late twentieth century (Le Bars et al., 2014), likely related to the pause in surface westerly wind trends reported by Banerjee et al. (2020). Once in the Atlantic, the Agulhas waters enter the upper limb of the Atlantic Meridional Overturning Circulation (AMOC) and are transported northwards (Gordon et al., 1992; Donners and Drijfhout, 2004; Rühs et al., 2019). Variations in the Agulhas leakage have been linked to changes in the thermohaline properties of the Atlantic Ocean and to variations in the strength of the AMOC (Weijer et al., 2002; Biastoch et al., 2008; Biastoch and Böning, 2013; Biastoch et al., 2015; Lübbecke et al., 2015). Therefore, it is important to understand how the leakage will change in the twenty-first century under the influence of ozone recovery and increasing greenhouse gases (GHGs). The future behavior of the Agulhas leakage is investigated here for the first time in a coupled climate model, as part of a broader analysis of the effects of ozone recovery and climate change.

Ozone depletion occurred during the last decades of the twentieth century as a result of anthropogenic emissions of ozone-depleting substances (ODSs). The 1987 Montreal Protocol on Substances that Deplete the Ozone Layer and its subsequent amendments and adjustments regulated the production of ODSs and mandated their phasing-out. As a result, the ozone in the stratosphere is expected to recover during the twenty-first century. The most recent estimates of Antarctic total column ozone (TCO) recovery obtained from

the Chemistry–Climate Model Initiative (CCMI) ensemble indicate a return to 1980 levels in 2060, with a 1σ spread of 2055–2066, when the multi-model mean is considered (Dhomse et al., 2018). When a weighted multi-model mean accounting for model independence and performance is used, the recovery is projected to occur in 2056, with a 95 % confidence interval of 2052–2060 (Amos et al., 2020). Detecting ozone recovery in observations is complicated by large year-to-year variability (Chipperfield et al., 2017) and by the short record since the ODSs peaked in the 1990s. Trends in ozone since the year 2000 vary considerably with region and height (Chipperfield et al., 2017). Over Antarctica, observations show that ozone loss has leveled off and started to reverse since the beginning of the century (Solomon et al., 2016, 2017; Banerjee et al., 2020).

The recovery of the ozone hole is expected to largely reverse the effects of ozone loss. However, increasing levels of GHGs due to anthropogenic activities also affect the atmospheric circulation (e.g., Kushner et al., 2001) as well as ozone recovery itself (Rosenfield et al., 2002; Waugh et al., 2009a; Eyring et al., 2010; Revell et al., 2012). Their influence is expected to oppose that of ozone recovery in the twenty-first century. This complicates projections of future changes in the SH circulation. The current study aims to investigate the future impacts of ozone recovery and of increasing GHGs on the SH climate during the twenty-first century under a high-GHG-emission scenario. We systematically separate the effects of the two drivers starting in the SH stratosphere and ending with the circulation in the South Atlantic Ocean and its corresponding Southern Ocean sector.

Although a number of previous studies employed single-forcing model simulations to explicitly separate the effects of ozone recovery and increasing GHGs on various aspects of the SH climate during the twenty-first century (Shindell and Schmidt, 2004; Perlwitz et al., 2008; Oman et al., 2009; Karpechko et al., 2010; McLandress et al., 2010, 2011; Polvani et al., 2011a; Oberländer et al., 2013; Polvani et al., 2018, 2019), this is the first time that these effects are studied in a state-of-the-art coupled ocean–atmosphere chemistry climate model that includes both interactive ozone chemistry and an ocean that contains a high-resolution, mesoscale-resolving nest in the South Atlantic and the western Indian Ocean. This allows us to clearly link stratospheric ozone changes to changes in mesoscale-dominated oceanic features, such as the Agulhas leakage, for the first time in the same model. We therefore revisit the results of the above-mentioned studies using the up-to-date Shared Socioeconomic Pathway (SSP) 5-8.5 used in the Coupled Model Intercomparison Project (CMIP) phase 6, and we expand these results in three ways. (1) We analyze spatial patterns of changes in several stratospheric fields in addition to the zonal-mean analysis customary in previous studies, and we show that the response of the austral spring SH stratospheric dynamics to increasing GHGs exhibits a marked planetary wavenumber 1 (PW1) structure that has not been reported before. (2) We make use of a high-resolution (0.1°) ocean nest that resolves the mesoscale features characteristic of the Southern Ocean and the Agulhas system, and we separate for the first time the impacts of ozone recovery and of increasing GHGs on the ocean circulation in these regions. (3) We compare our future SH climate projections from the interactive chemistry version of the model with projections from the same model, but in the configuration that prescribes the CMIP6 ozone field. This comparison is relevant as not all the models participating in the current CMIP phase include interactive chemistry and therefore have to prescribe this ozone field. Prescribing the ozone field has been shown to alter the response of the SH circulation to ozone changes because of the temporal interpolation from monthly mean values to the model's time step (Neely et al., 2014; Seviour et al., 2016), the missing ozone asymmetries (Waugh et al., 2009b; Li et al., 2016), and ozone-radiative-dynamical feedbacks (Haase et al., 2020) and spatial inconsistencies between the prescribed ozone and the polar vortex (Ivanciu et al., 2021). The CMIP6 ozone field includes zonal variations, but the rest of the abovementioned issues, together with a different magnitude of ozone changes than simulated by the model, are expected to lead to differences in the effects of ozone recovery between the version of the model with interactive ozone and with prescribed CMIP6 ozone. Unlike the ozone field prescribed in CMIP5, the CMIP6 ozone field is dependent on the GHG emission scenario used, such that the effect of GHGs on ozone is captured. As shown in the analyses by Morgenstern et al. (2014) and Chiodo and Polvani (2016), the effect of GHGs on ozone is important as it offsets part of the direct influence of GHGs on the SH dynamics.

The study is structured as follows: Sect. 2 presents our model simulations and methodology, Sect. 3 gives an estimate of ozone recovery in our model, Sect. 4 examines the impacts of ozone recovery and increasing GHGs on the atmospheric and oceanic circulation in the SH and compares the combined impact in simulations with prescribed and interactive ozone, and Sect. 5 provides our summary and discussion.

2 Data and methodology

2.1 Model description and experimental design

We employ the state-of-the-art coupled climate model Flexible Ocean Climate Infrastructure (FOCI; Matthes et al., 2020). The atmospheric component of FOCI is ECHAM6.3 (Stevens et al., 2013) in the T63L95 setting, corresponding to a horizontal resolution of approximately 1.8° by 1.8° and 95 vertical hybrid sigma pressure levels. The 95 vertical levels are chosen to achieve a high vertical resolution, mainly in the stratosphere, to allow for a proper representation of the quasi-biennial oscillation (Matthes et al., 2020). The model top at 0.01 hPa is located well above the stratopause, such that processes throughout the entire strato-

sphere are simulated. Solar activity variations are included in FOCI following the recommendations of the SOLARIS-HEPPA project (Matthes et al., 2017) for CMIP6. ECHAM6 is coupled to the Model for Ozone and Related Chemical Tracers (MOZART3; Kinnison et al., 2007), which simulates chemical processes in the atmosphere. A total of 182 chemical reactions with 52 chemical tracers focusing on stratospheric chemistry are simulated, including all relevant catalytic ozone loss cycles. The ozone chemistry is therefore interactively simulated, and the ozone field responds to changes in temperature, dynamics, and other chemical constituents such as GHGs. Land surface biogeophysical and biogeochemical processes are simulated using the JSBACH land model version 3 (Brovkin et al., 2009; Reick et al., 2013).

The oceanic component of FOCI is the Nucleus for European Modeling of the Ocean version 3.6 (NEMO3.6; Madec and the NEMO team, 2016), coupled to the LIM2 sea ice component (Fichefet and Maqueda, 1997). We use the ORCA05 configuration of NEMO, which has a global nominal resolution of $1/2°$ and 46 z levels. Additionally, we take advantage of the special nesting capabilities of FOCI to enhance the oceanic resolution in the South Atlantic and western Indian Ocean to $1/10°$ using the INALT10X nest described by Schwarzkopf et al. (2019). The nesting domain extends from 63° S to 10° N and from 70° W to 70° E (boundaries of Fig. 17, also depicted in Fig. 2 of Schwarzkopf et al., 2019). A two-way nesting approach is used (Debreu et al., 2008), whereby the nest receives information at its boundaries about the global ocean state from the ORCA05 host, and it feeds back its fine-scale state to the host at regular time intervals prior to each coupling time step. Therefore, the impact of the nest is also felt outside of the nest area. INALT10X resolves mesoscale features such as eddies in the Agulhas system region and, in part, also in the Southern Ocean. The Agulhas leakage in INALT10X is therefore more realistic than that simulated in ORCA05 (Schwarzkopf et al., 2019). Outside of the nesting region, where the resolution does not allow for the eddies to be resolved, an eddy parametrization scheme (Gent and Mcwilliams, 1990) is used, varying temporally and horizontally with the growth of the baroclinic instability up to a maximum of 2000 $m^2\ s^{-1}$ (Treguier et al., 1997).

FOCI was described in detail and was validated against observations by Matthes et al. (2020). The impacts of ozone depletion and increasing GHGs on the atmospheric circulation in FOCI over the last decades of the twentieth century were investigated by Ivanciu et al. (2021) and are in good agreement with those reported in previous studies.

Four ensembles were performed with FOCI for the twenty-first century (Table 1). Each ensemble comprises three members that differ only in their initial conditions. The first ensemble, INTERACT_O_3, is forced using ODSs and GHGs according to the SSP5-8.5, characterized by high GHG emissions. The CO_2 concentrations reach 1135 ppm, and the radiative forcing reaches 8.5 $W\ m^{-2}$ by 2100 in this scenario (Meinshausen et al., 2020). This ensemble is used to assess the combined effect of the increase in GHGs and of ozone recovery by taking the difference between the conditions at the end of the century (2080–2099) and current-day conditions (2011–2030). The second ensemble, FixODS, is forced only by GHGs (CO_2, CH_4, and N_2O) following SSP5-8.5, while ODSs are kept fixed at their 1995 climatological annual cycle, obtained by taking the average over 1991–2000. The majority of the ODSs peaked during this period, and therefore this ensemble simulates a world in which the ozone hole does not recover but persists at its maximum extent. By taking the difference between INTERACT_O_3 and FixODS over 2075–2099, we can extract the influence exerted by ozone recovery until the end of the century. In contrast, the third ensemble, FixGHG, is forced only by ODSs that decrease following SSP5-8.5, and GHGs are kept fixed at their 1995 climatological annual cycle. We take the difference between INTERACT_O_3 and FixGHG over 2075–2099 to extract the effect that climate change has during the twenty-first century. Finally, the fourth ensemble, CMIP6_O_3, is identical to INTERACT_O_3, with the exception that the CMIP6 ozone field (Hegglin et al., 2016) is prescribed instead of calculating the ozone interactively. The combined effect of the increase in GHGs and ozone recovery during the twenty-first century is assessed for the case when the CMIP6 ozone is prescribed by taking the difference between the conditions at the end of the century (2080–2099) and current-day conditions (2011–2030) in this ensemble. This total effect is then compared to that obtained from INTERACT_O_3 to investigate the dependency of our results on the ozone field used. Unlike in the previous CMIP phases, the CMIP6 ozone field includes zonal variations and differs for each future GHG scenario. Therefore, the prescribed ozone field is consistent with the increase in GHGs in SSP5-8.5, which is important as GHGs are known to affect ozone concentrations (Rosenfield et al., 2002; Waugh et al., 2009a; Eyring et al., 2010; Revell et al., 2012). We note that the total effect in CMIP6_O_3 should only be compared with the total effect in INTERACT_O_3 and not with the individual effects of ozone recovery and increasing GHGs because the individual effects are likely to be different when the ozone field is prescribed. The separation of the different effects using the four ensembles described above is summarized in Table 2.

Table 1. Simulations analyzed in this study.

Simulation	Ozone	ODSs	GHGs
FixODS	Interactive	1995 levels	SSP5-8.5
FixGHG	Interactive	SSP5-8.5	1995 levels
INTERACT_O_3	Interactive	SSP5-8.5	SSP5-8.5
CMIP6_O_3	Prescribed CMIP6	SSP5-8.5	SSP5-8.5

Table 2. Separation of the different effects investigated in this study. The first column gives the effect that is extracted, the second column lists the ensembles that are subtracted to extract an effect, and the third column gives the periods over which the differences are taken.

Effect	Simulations	Period
ODS	INTERACT_O_3 – FixODS	2075–2099
GHG	INTERACT_O_3 – FixGHG	2075–2099
Total interactive chemistry	2090 INTERACT_O_3 – 2020 INTERACT_O_3	2080–2099 vs. 2011–2030
Total prescribed chemistry	2090 CMIP6_O_3 – 2020 CMIP6_O_3	2080–2099 vs. 2011–2030

2.2 Residual circulation and wave diagnostics

We examine changes in the zonal-mean residual circulation and its drivers within the transformed Eulerian mean (TEM; Andrews et al., 1987) framework. The quasi-geostrophic Eliassen–Palm (EP) flux of wave activity, equivalent to the zonal mean of the vertical and meridional components of the Plumb flux (Plumb, 1985), is defined as

$$F_\phi = -a\cos\phi\overline{v'u'} \tag{1}$$

$$F_\mathrm{p} = fa\cos\phi\frac{\overline{v'\theta'}}{\overline{\theta_\mathrm{p}}}, \tag{2}$$

and its divergence, $(a\cos\phi)^{-1}\nabla\cdot F$, which is a measure for wave-mean flow interaction, is defined as

$$\nabla\cdot F = \frac{1}{a\cos\phi}\frac{\partial\left(F_\phi\cos\phi\right)}{\partial\phi} + \frac{\partial F_\mathrm{p}}{\partial p}. \tag{3}$$

The zonal and meridional velocity components are represented by u and v, respectively; f is the Coriolis parameter; a is the radius of the Earth; ϕ is the latitude; p is the pressure; θ is the potential temperature; and θ_p is the partial derivative of θ with respect to pressure. The overbars denote the zonal mean, and the primes denote departures from the zonal mean. The downward residual velocity, $\overline{w^*}$, was calculated from the residual stream function, Ψ^*, as

$$\overline{w^*} = \frac{gH}{pa\cos\phi}\frac{\partial\Psi^*}{\partial\phi}, \tag{4}$$

where

$$\Psi^* = -\frac{\cos\phi}{g}\int_\mathrm{p}^0 \overline{v^*}(\phi, p)\mathrm{d}p. \tag{5}$$

The meridional residual velocity is defined as

$$\overline{v^*} = \overline{v} - \frac{\partial}{\partial p}\left(\frac{\overline{v'\theta'}}{\overline{\theta_\mathrm{p}}}\right). \tag{6}$$

The scale height, H, was taken as 7000 m, and g denotes the gravitational acceleration.

2.3 Agulhas leakage calculation

As the Agulhas leakage consists of rings, eddies, and filaments, it is characterized by strong spatiotemporal variability and therefore cannot be properly measured using an Eulerian approach. Instead, the Agulhas leakage is commonly quantified using Lagrangian particle tracking (Biastoch et al., 2008, 2009; van Sebille et al., 2009; Durgadoo et al., 2013; Weijer and van Sebille, 2014; Cheng et al., 2016, 2018). Here, we follow the method of Durgadoo et al. (2013), and we use the offline ARIANE software (Blanke and Raynaud, 1997; Blanke et al., 1999) to track Lagrangian particles originating in the Agulhas Current. The virtual particles are seeded in a zonal section across the Agulhas Current at 32° S over the full depth for southward velocities and are advected for a maximum period of 5 years based on the 5 d three-dimensional velocity field obtained from FOCI. Each particle has a fraction of the total instantaneous Agulhas Current volume transport assigned to it that remains constant as the particle is advected forward. An annual time series of Agulhas leakage is obtained by summing up the volume transport associated with the particles that have exited the Cape Basin through the Good Hope section, marked by the black line in Fig. 16a, within 5 years. This gives the fraction of the Agulhas Current volume transport that enters the Atlantic Ocean. The Agulhas leakage is computed for each ensemble member of FixODS, FixGHG, INTERACT_O_3, and CMIP6_O_3 before the ensemble averaging is performed. Because of the 5-year period granted for the particles to be advected, the Agulhas leakage time series ends in 2094, although the FOCI simulations were performed until 2099. Therefore, we calculated the Agulhas leakage differences between INTERACT_O_3 and FixODS or FixGHG based on the 2075–2094 period, and we estimate the total change in the Agulhas leakage by taking the difference between the 2080–2094 and 2014–2028 periods.

3 Projected ozone recovery in FOCI

Decreasing levels of ODSs and increasing levels of GHGs both lead to changes in the stratospheric ozone. Figure 1 shows the vertical and seasonal distribution of the twenty-first-century changes in Antarctic polar cap ozone due to ODSs, GHGs, and their combined effect. Austral spring

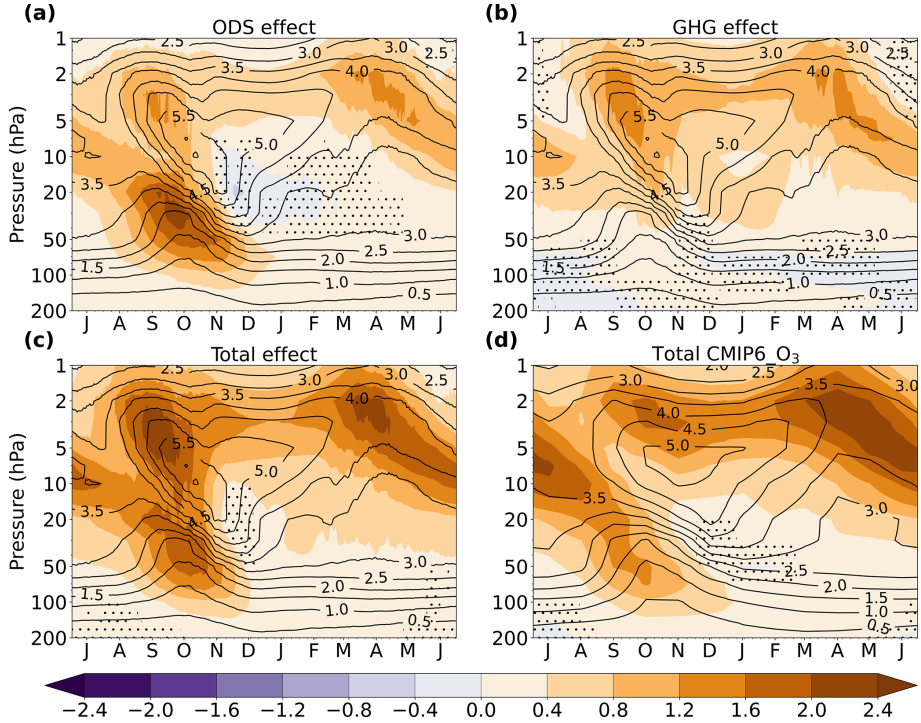

Figure 1. Changes in the polar cap (70–90° S) ozone (ppmv) for each day of the year and pressure level (color shading): effect of ODSs **(a)**, effect of GHGs **(b)**, total effect when ozone is interactive **(c)**, and total effect prescribed in CMIP6_O_3 **(d)**. The contours depict the current-day (2011–2030) climatology from INTERACT_O_3 in **(a)**–**(c)** and the climatology prescribed in CMIP6_O_3 in **(d)**. The stippling masks regions where the changes are not significant at the 95 % confidence interval based on a two-tailed *t* test.

lower- and middle-stratospheric ozone levels exhibit a strong increase in response to declining ODSs (Fig. 1a), peaking in October, in agreement with results from other chemistry–climate models (CCMs) (Perlwitz et al., 2008; Son et al., 2008). This is the month during which the strongest ozone depletion occurred in FOCI in the second half of the twentieth century (Ivanciu et al., 2021). In addition, there is a significant increase in ozone throughout the whole year in the upper stratosphere and a small decrease between 30 and 10 hPa in December and January.

GHGs also influence the stratospheric ozone through their chemical, radiative, and dynamical effects (Haigh and Pyle, 1982; Rosenfield et al., 2002; Revell et al., 2012; Chiodo et al., 2018; Morgenstern et al., 2018). In the upper stratosphere, GHGs lead to an increase in ozone of similar magnitude to the ODSs effect (Fig. 1b). At these levels, GHGs have a strong cooling effect (Fig. 3b) owing to their emission of longwave (LW) radiation. This cooling slows down the temperature-dependent ozone-depleting reactions in the upper stratosphere, resulting in an increase in ozone (Haigh and Pyle, 1982; Jonsson et al., 2004; Rosenfield et al., 2002; Revell et al., 2012; Morgenstern et al., 2018). In addition, an increase in CH_4 causes an overall ozone increase, and an increase in N_2O causes an overall ozone loss through chemical processes. The influences of individual GHGs on ozone levels have been discussed in previous studies (Portmann and Solomon, 2007; Revell et al., 2012; Dhomse et al., 2018; Morgenstern et al., 2018) and are not distinguished here. We show instead the combined influence of CO_2, CH_4, and N_2O on ozone (Fig. 1b) to illustrate that the increase in GHGs drives important changes in ozone. Therefore, the GHG-induced dynamical changes discussed in the following sections include not only the direct effects of GHGs, driven by radiation changes, but also indirect effects mediated through changes in ozone. The studies by Morgenstern et al. (2014) and Chiodo and Polvani (2016) showed that these indirect effects are substantial, and they offset part of the direct GHG impacts on the tropospheric circulation.

Figure 1 shows that increasing GHGs and decreasing ODSs each contribute about half of the total ozone increase in the upper stratosphere (Fig. 1c). This is consistent with the findings of the latest Scientific Assessment of Ozone Depletion (World Meteorological Organization, 2018). In the lower and middle stratosphere in austral spring, the effect of declining ODSs dominates the total ozone change. GHGs also contribute a small increase in ozone at these levels in spring (Fig. 1b) by enhancing the residual circulation, which transports ozone-rich air to the polar cap, as discussed in Sect. 4.1.2.

In FOCI, the INTERACT_O_3 ensemble mean projects that the October Antarctic TCO will return to 1980s values in 2048 under the SSP5-8.5 pathway, with the spread of the

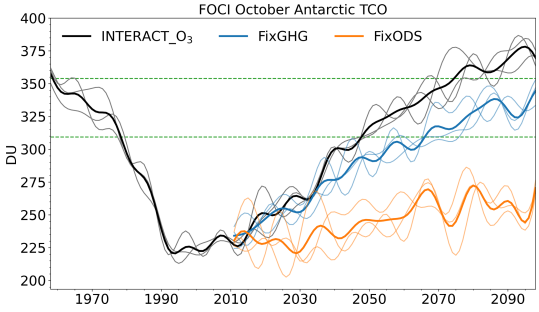

Figure 2. Time series of polar cap (60–90° S) total column ozone for October (DU) from INTERACT_O_3 in black, FixGHG in blue, and FixODS in orange. The ensemble means are depicted by thick lines and the individual members by thin lines. The dashed horizontal green lines mark the 1980 and 1960 ozone levels, computed from the ensemble mean given as the 1979–1981 and 1959–1961 averages, respectively. The time series were filtered using a 10-point boxcar filter.

individual members ranging from 2048 to 2050 (Fig. 2). This is earlier than the CCMI ensemble mean estimate of 2060, with a 1σ uncertainty of 2055–2066 (Dhomse et al., 2018), or the CCMI weighted-mean estimate of 2056, with a 95 % confidence interval of 2052–2060 (Amos et al., 2020), both of which are obtained using RCP6.0. The discrepancy to the CCMI-projected recovery date arises most likely due to higher GHG levels in SSP5-8.5, which accelerate ozone recovery. A positive trend in the October Antarctic TCO can be observed even when ODSs do not decline (FixODS ensemble), demonstrating that GHGs alone can be responsible for a substantial increase in ozone in this region (Fig. 2). In the absence of future increase in GHGs (FixGHG ensemble), the October Antarctic TCO returns to 1980 levels in FOCI only in 2067, with individual members simulating a recovery between 2066 and 2076 (Fig. 2). Our simulations therefore suggest that increasing GHGs following the SSP5-8.5 pathway accelerate Antarctic ozone recovery by at least 2 decades.

Figure 1 offers a comparison between the total ozone change simulated by FOCI and that in the CMIP6 ozone field prescribed to the CMIP6_O_3 ensemble (Fig. 1c and d). Both fields show the recovery of the stratospheric ozone, exhibiting a maximum increase in ozone in the upper stratosphere and, during austral spring, between 100 and 20 hPa. However, there are differences in the magnitude of the ozone increase. The recovery of the ozone hole is stronger in FOCI than in the CMIP6 field. In addition, the increase in the upper stratosphere is stronger in FOCI during spring and weaker during March–June. These differences in ozone recovery between the FOCI and CMIP6 fields contribute to the different changes in temperature and atmospheric circulation in INTERACT_O_3 and CMIP6_O_3 discussed in the following sections.

4 Impacts of ozone recovery and GHG increase in the Southern Hemisphere

4.1 Atmospheric circulation changes

4.1.1 Temperature and zonal wind

Figure 3 shows the effects of ozone recovery and of increasing GHGs on the Antarctic polar cap temperature as well as their combined effects in the presence of interactive ozone (INTERACT_O_3) and of prescribed ozone (CMIP6_O_3). A significant warming occurs between 200 and 20 hPa in austral spring and summer in response to ozone recovery (Fig. 3a), in agreement with previous studies (Perlwitz et al., 2008; Son et al., 2009; Karpechko et al., 2010; McLandress et al., 2010). The warming reaches its maximum in November. Above this warming, a significant cooling occurs in November and December due to the dynamical response to ozone recovery, as discussed below. Increasing GHGs lead to a cooling of the stratosphere throughout the year, which is strongest in the upper stratosphere (Fig. 3b), in line with the findings of McLandress et al. (2010). We note that stratospheric temperature changes due to GHGs inferred from Fig. 3b include the warming caused by the GHG-driven ozone increase in the middle and upper stratosphere (Fig. 1b) and that the direct radiative effect of GHGs is likely larger. An exception to the GHG-induced stratospheric cooling occurs below 20 hPa in austral spring, when the temperature increases as a result of increasing GHGs, but this increase is not significant when the polar cap mean is considered. We show below that this is caused by a change in the PW1 in response to GHGs leading to contrasting dynamical heating over different sectors of the Southern Ocean that compensate each other in the zonal mean. In the troposphere, there is a significant warming due to GHGs throughout the entire year, reaching 4.4 K at the surface.

The combined effect of ozone recovery and GHGs (Fig. 3c and d) is dominated by the GHG-induced cooling (warming) in the stratosphere (troposphere) and by the ozone-induced warming in the lower stratosphere during spring. There is little difference between the temperature changes in the ensemble with interactive ozone, INTERACT_O_3, and the ensemble with prescribed CMIP6 ozone, CMIP6_O_3, during the months when the GHG effect dominates. In contrast, during austral spring, when the stratospheric temperature changes are dictated by changes in ozone, there is a clear difference between the two ensembles. CMIP6_O_3 simulates a spring lower-stratospheric maximum warming that is about half of that simulated by INTERACT_O_3 in the polar cap mean. In addition, the November upper-stratospheric cooling is also weaker in CMIP6_O_3 than in INTERACT_O_3.

Changes in the polar cap temperature are closely related to changes in zonal wind through the thermal wind balance. Figure 4 shows the vertical profile of the zonal-mean zonal

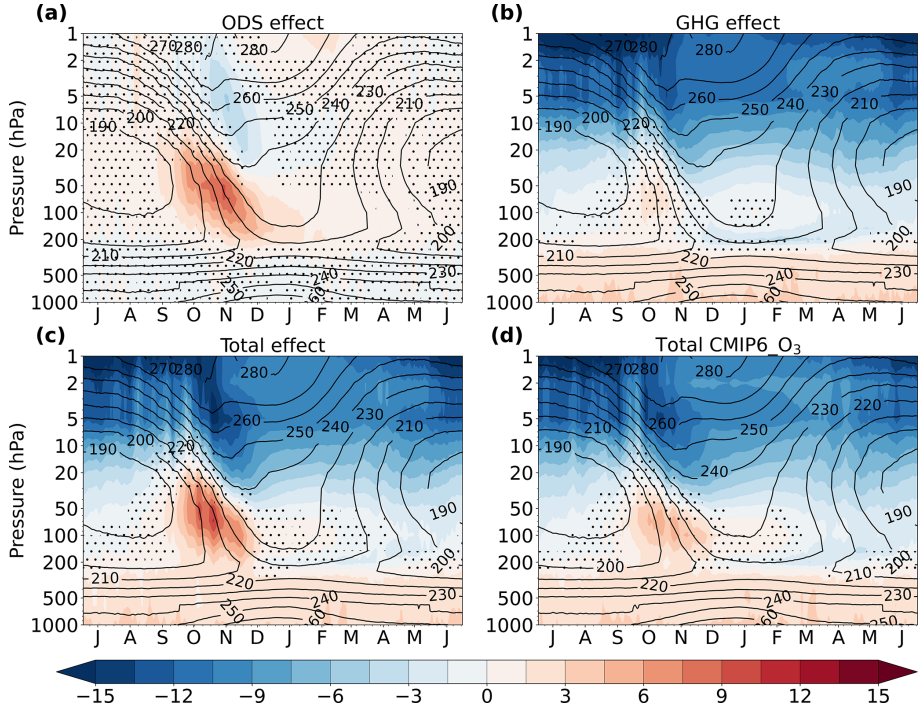

Figure 3. Changes in the polar cap (70–90° S) temperature (K) for each day of the year and pressure level (color shading): effect of ozone recovery **(a)**, effect of GHGs **(b)**, total effect in INTERACT_O_3 **(c)**, and total effect in CMIP6_O_3 **(d)**. The contours depict the current-day (2011–2030) climatology from INTERACT_O_3 in **(a)**–**(c)** and from CMIP6_O_3 in **(d)**. The stippling masks regions where the changes are not significant at the 95 % confidence interval based on a two-tailed *t* test.

wind changes averaged over November and December, when the largest temperature signal in the lower stratosphere occurs (Fig. 3). The ozone-induced polar cap warming is associated with a weakening of the stratospheric westerlies that extends to the troposphere and the surface (Fig. 4a). In contrast, the increasing GHGs result in a positive (westerly) wind change extending from the top of the stratosphere to the surface in the midlatitudes (Fig. 4b). The GHG effect peaks at the upper flank of the subtropical jet around 25° S and occurs throughout the year, unlike the ozone effect, which occurs only during spring in the stratosphere and summer in the troposphere. The combined ozone and GHG effect consists of a weakening of the stratospheric westerlies south of 60° S, where the ozone effect dominates, and a strengthening at the top of the tropospheric jet and on its poleward flank, where the GHG effect dominates (Fig. 4c and d). The stratospheric westerly wind weakening has a much lower magnitude in CMIP6_O_3 than in INTERACT_O_3, in agreement with the lower magnitude of the total spring temperature change. At the same time, the positive change in the midlatitudes is stronger and exhibits a larger latitudinal extent in CMIP6_O_3 in both the stratosphere and the troposphere as the GHG westerly effect is offset to a lesser degree by the weaker ozone easterly effect in this ensemble.

The Antarctic ozone hole is not centered over the polar cap (e.g., Grytsai et al., 2007), and therefore the ozone recovery also occurs displaced from the South Pole. In addition, the dynamical effects of both ozone recovery and increasing GHGs exhibit strong zonal variations. Therefore, it is interesting to investigate the horizontal structure of the stratospheric changes. Figures 5 and 6 show maps of the October ozone and temperature changes at 50 hPa and of the zonal wind changes at 20 hPa. The region of large ozone recovery in response to declining ODS is slightly displaced towards the Atlantic sector (Fig. 5a), causing the warming response to also extend towards the Atlantic (Fig. 5b). This displacement coincides with the displacement of the ozone hole simulated by FOCI for the latter part of the twentieth century (Ivanciu et al., 2021). There is a significant ozone increase due to GHGs focused over the Pacific sector (Fig. 5d), which occurs due to changes in dynamics, as discussed below. This agrees with the zonally asymmetric ozone response to a quadrupling of CO_2 reported from four CCMs by Chiodo et al. (2018), characterized by a positive change over the Pacific and a negative one over the Indian Ocean.

Even more interesting is the temperature response to increasing GHGs (Fig. 5e), which is characterized by a PW1 pattern, with cooling occurring towards South Africa and warming occurring towards the Pacific, in the same region as the strongest ozone increase. To better understand these changes, Fig. 7 illustrates the temperature signature of the current-day PW1 overlaid onto its changes at the end of

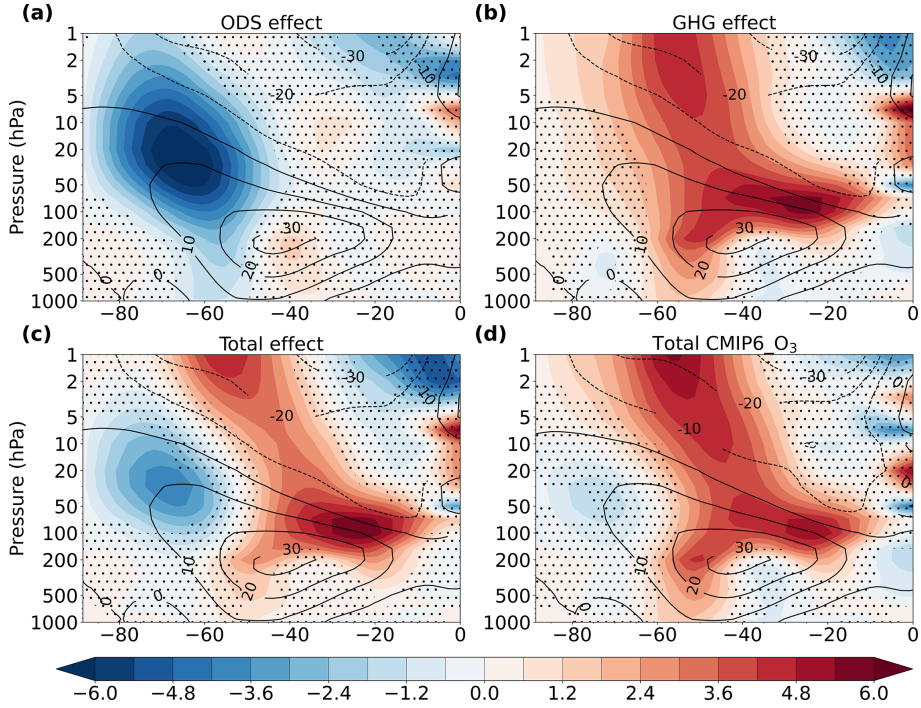

Figure 4. Changes in the November–December zonal-mean zonal wind ($m\,s^{-1}$) for each latitude and pressure level (color shading): effect of ozone recovery **(a)**, effect of GHGs **(b)**, total effect in INTERACT_O_3 **(c)**, and total effect in CMIP6_O_3 **(d)**. The contours depict the current-day (2011–2030) climatology from INTERACT_O_3 in **(a)**–**(c)** and from CMIP6_O_3 in **(d)**. The stippling masks regions where the changes are not significant at the 95 % confidence interval based on a two-tailed t test.

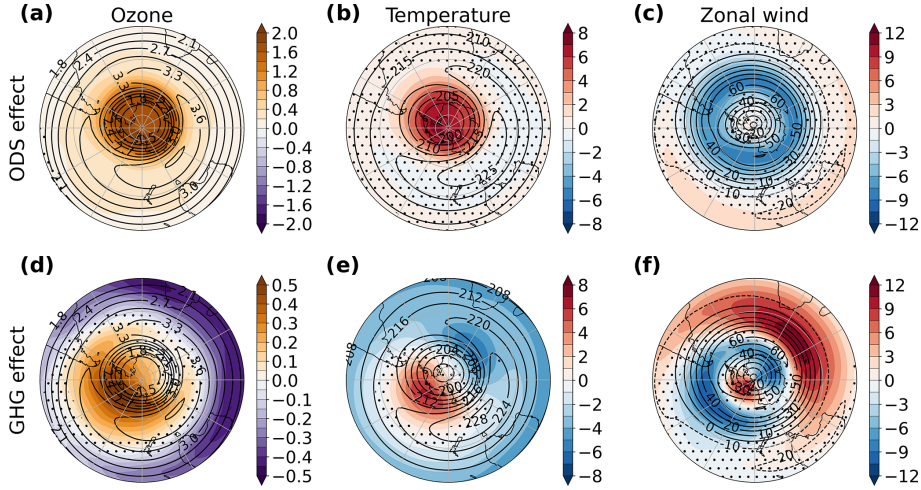

Figure 5. Changes in ozone (**a**, **d**; ppmv) and temperature (**b**, **e**; K) at 50 hPa and in zonal wind (**c**, **f**; $m\,s^{-1}$) at 20 hPa during October due to ODSs **(a–c)** and GHGs **(d–f)**. The contours depict the current-day (2011–2030) climatology from INTERACT_O_3. The stippling masks regions where the changes are not significant at the 95 % confidence interval based on a two-tailed t test.

the century. The PW1 dominates the current-day temperature anomaly from the zonal mean, depicted by the contours in Fig. 8c and f. Comparing the current-day structure with the changes caused by GHGs (Fig. 7b), it becomes clear that the increase in GHGs leads to an eastward phase shift in the PW1. This is further confirmed by the GHG-induced changes in the dynamical heating rate depicted in Fig. 8f, which exhibit the same PW1 pattern and demonstrate that the temperature changes caused in the lower stratosphere during spring by the increase in GHGs are mediated by dynamical changes. An additional contribution is brought by the increase in the SW heating rate over the Pacific sector

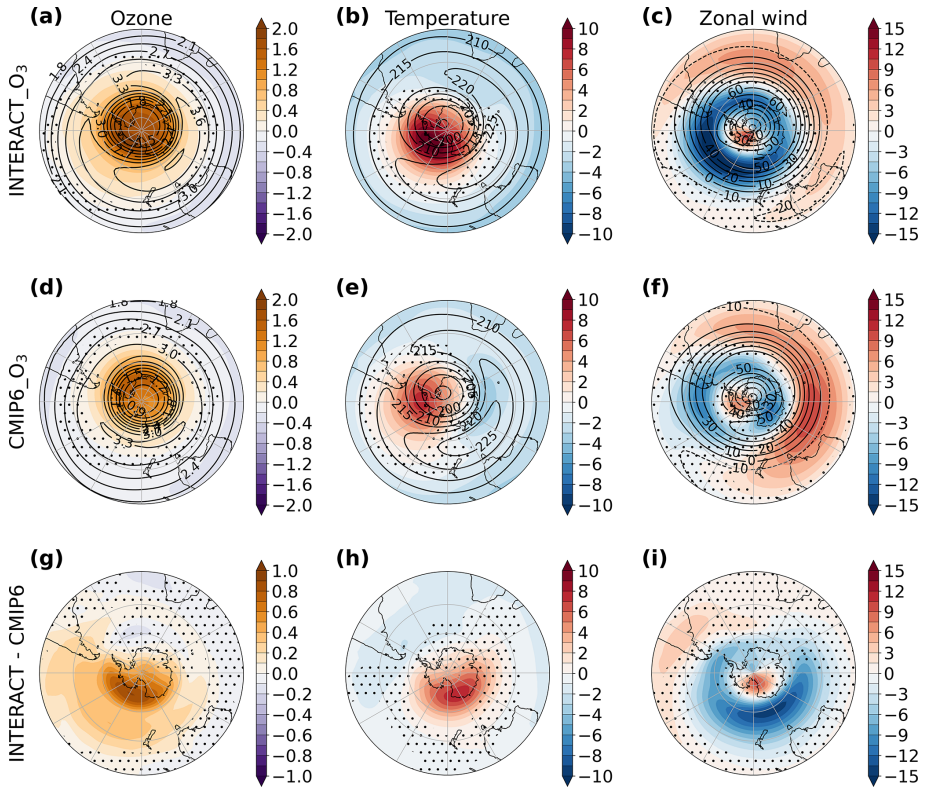

Figure 6. Changes in ozone (**a**, **d**; ppmv) and temperature (**b**, **e**; K) at 50 hPa and in zonal wind (**c**, **f**; $\mathrm{m\,s^{-1}}$) at 20 hPa due to ODSs and GHGs combined, in INTERACT_O_3 **(a–c)** and in CMIP6_O_3 **(d–f)**, and the difference between the INTERACT_O_3 and the CMIP6_O_3 changes **(g–i)**. The stippling in **(a)**–**(f)** masks regions where the changes are not significant at the 95 % confidence interval based on a two-tailed t test, and the stippling in **(g)**–**(i)** masks regions where the difference is lower than 2σ inferred from the spread of the individual ensemble members. The contours in **(a)**–**(f)** show the current-day (2011–2030) climatologies in the respective fields.

(Fig. 8d) caused by the dynamically induced ozone increase in response to increasing GHGs (Fig. 5). This contribution is, however, small in comparison to the contribution of the dynamical heating rate.

Ozone recovery also alters the PW1 (Fig. 7a), dampening its amplitude and slightly altering its phase, but its impact is smaller than that of the GHGs. Unlike the GHG effect, the ozone effect is radiative in nature. The increase in ozone results in more SW radiation being absorbed, warming the lower stratosphere in spring, as shown by the change in the SW heating rate (Fig. 8a). The change in the PW1 depicted in Fig. 7a is a consequence of the fact that the polar vortex, the ozone hole, and consequently its recovery are not centered on the South Pole, being displaced towards the Atlantic Ocean (Figs. 5 and 6).

We note that the magnitude of the total GHG-induced October warming reaches 7 K, only 1 K lower than the maximum warming associated with ozone recovery of 8 K, while the maximum GHG-induced cooling reaches −6 K (Fig. 5b and e). This indicates that the increase in GHGs results in important temperature changes in the lower stratosphere during spring, substantially contributing to the total temperature change in Fig. 6b. However, although the temperature changes resulting from ozone recovery and increasing GHGs have similar magnitudes, the mechanisms behind these changes are different. As shown above, while the temperature changes caused by ozone recovery (Fig. 5b) result primarily from radiative processes, the changes occurring in the springtime lower stratosphere due to GHGs (Fig. 5e) are a result of dynamical processes. The GHG-induced springtime lower-stratospheric temperature changes are largely underestimated if zonally averaged fields are investigated (Fig. 3b) as the PW1 anomalies cancel out to a large degree.

The total October lower-stratospheric temperature change (Fig. 6b) illustrates the combination of the ozone and GHG effects well. The ozone-induced warming persists over Antarctica, but it is extended towards the Pacific by the superposition of the GHG-induced warming. The cooling due to GHGs dominates over the Southern Ocean towards South Africa and at lower latitudes. Consistent with these changes, the PW1 in INTERACT_O_3 exhibits a phase shift akin to the GHG effect, but of smaller amplitude (Fig. 7c).

The PW1 pattern of the spring temperature response to GHGs is associated with zonal wind changes of opposite sign in the Eastern Hemisphere and Western Hemisphere (Fig. 5f). The Pacific sector is characterized by a weakening

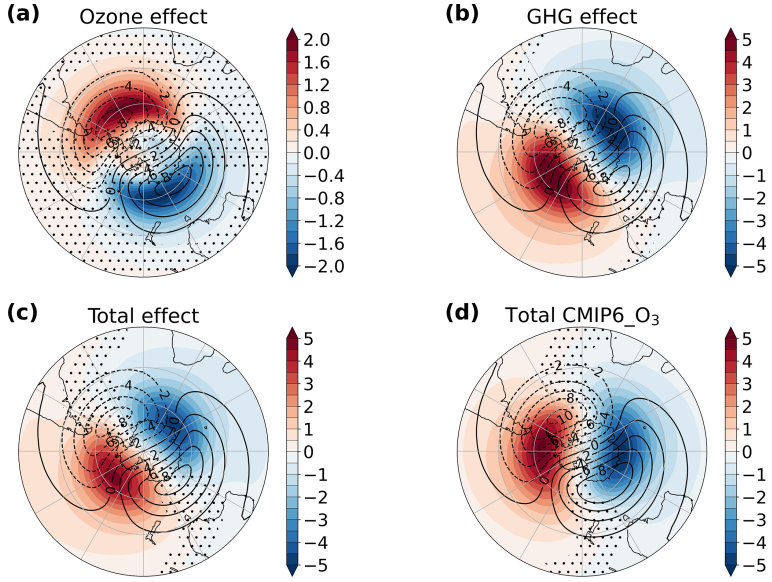

Figure 7. Changes in the temperature PW1 (K) at 50 hPa during October (color shading): effect of ozone recovery **(a)**, effect of GHGs **(b)**, total effect in INTERACT_O_3 **(c)**, and total effect in CMIP6_O_3 **(d)**. The contours depict the current-day (2011–2030) PW1 climatology from INTERACT_O_3 in **(a)**–**(c)** and from CMIP6_O_3 in **(d)**. The stippling masks regions where the changes are not significant at the 95 % confidence interval based on a two-tailed t test.

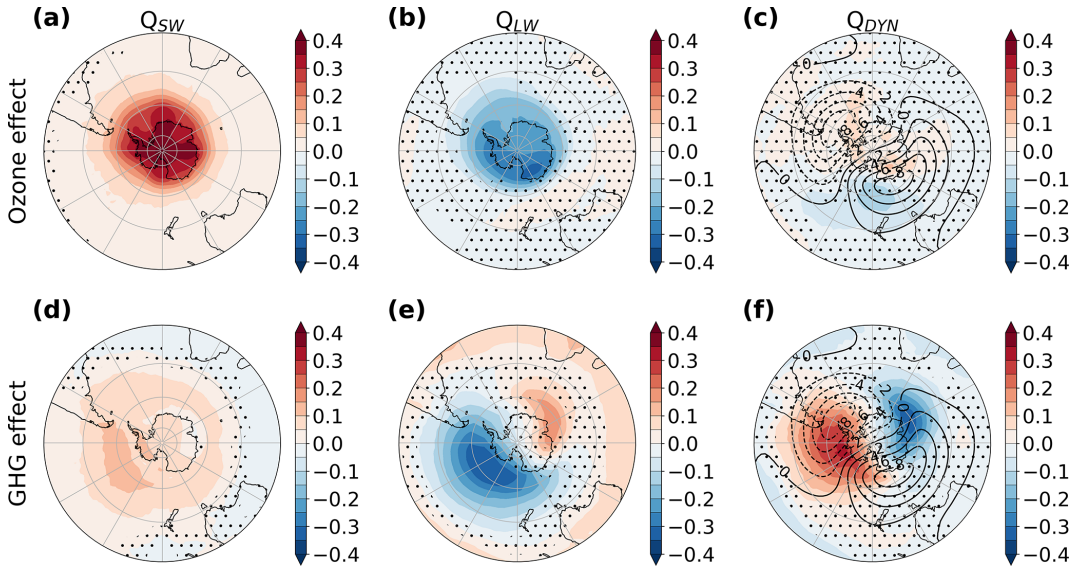

Figure 8. Changes in the SW **(a, d)**, LW **(b, e)**, and dynamical **(c, f)** heating rates (K d^{-1}) at 50 hPa during October due to ozone recovery **(a–c)** and GHGs **(d–f)**. The contours in panels **(c)** and **(f)** depict the current-day (2011–2030) climatology of the temperature deviations from the zonal mean from INTERACT_O_3. The stippling masks regions where the changes are not significant at the 95 % confidence interval based on a two-tailed t test.

of the polar night jet on its equatorward flank and a strengthening on its poleward flank, while the opposite occurs over the Atlantic and Indian sectors. This implies a shift in the polar vortex towards South Africa in austral spring driven by increasing GHGs. In contrast, ozone recovery leads to a circumpolar weakening of the polar night jet (Fig. 5c). The total stratospheric zonal wind change in October (Fig. 6c) consists of a weakening of the polar night jet, which peaks over the Pacific sector, where the GHG effect reinforces the weakening due to ozone recovery. The maximum weakening in this region reaches 16.5 m s^{-1}, or 41 % of the current-day October climatological strength of the polar vortex. At mid-latitudes over the Atlantic and Indian sectors the GHG effect dominates, and the outer flank of the polar vortex strength-

ens, while the easterlies weaken. The maps showing the temperature and zonal wind changes in Figs. 5 and 6 demonstrate that important GHG-induced changes are missed if only changes in zonal-mean fields are investigated.

The total zonal wind change in the CMIP6_O_3 ensemble (Fig. 6f) resembles that caused by GHGs, indicating that the ozone effect is weaker in this ensemble. The magnitude of the polar vortex weakening is significantly larger in INTERACT_O_3 than in CMIP6_O_3 over the Pacific sector (Fig. 6i). At the same time, the strengthening over the Indian sector is weaker in INTERACT_O_3 than in CMIP6_O_3. These differences arise from the different temperature response in the two ensembles (Fig. 6b, e, and h). The total temperature change in CMIP6_O_3 retains more of the PW1 structure caused by GHGs. This suggests that the increase in GHGs plays a more dominant role in driving the temperature changes in this ensemble. The region of increasing temperature is shifted eastward, and the maximum warming is weaker by about 3 K in CMIP6_O_3 compared to INTERACT_O_3. The eastwards shift is even more noticeable in the changes experienced by the PW1 in CMIP6_O_3 compared to INTERACT_O_3 (Fig. 7c and d).

These differences in the temperature response can be partly explained by the patterns of ozone recovery in INTERACT_O_3 and prescribed to CMIP6_O_3 (Fig. 6a and d). There is a stronger increase in ozone over the Pacific sector in INTERACT_O_3 (Fig. 6g), with ozone recovery peaking between the Antarctic Peninsula and the Ross Sea in this ensemble (Fig. 6a). In contrast, ozone recovery peaks over the Weddell Sea in the CMIP6 field (Fig. 6b). The different ozone recovery patterns cause the temperature response to ozone recovery to offset and reinforce the response to increasing GHGs in different regions in the two ensembles. At the same time, the smaller ozone increase in CMIP6_O_3 leads to an overall weaker response to ozone recovery and to GHGs playing a more important role in this ensemble. We also note that the shape and the magnitude of the current-day ozone hole differ between INTERACT_O_3 and CMIP6_O_3 (contours in Fig. 6a and d), with the ozone hole in CMIP6_O_3 being displaced towards South Africa and the ozone hole in INTERACT_O_3 being displaced towards South America.

The total change in the SW heating rate (Fig. 9a and d) illustrates the effect of the differences in ozone recovery on the temperature change in INTERACT_O_3 and CMIP6_O_3. The effect of ozone recovery dominates the total change in the SW heating rate (Fig. 9a), but there is also a small contribution arising from the GHG-driven spring increase in ozone (Fig. 8d). In agreement with the stronger ozone increase in INTERACT_O_3, there is a stronger SW warming over Antarctica and extending to the South Pacific in this ensemble compared to CMIP6_O_3 (Fig. 9a, d, and g). This contributes to the larger temperature increase simulated by INTERACT_O_3 (Fig. 6b). Interestingly, the region over the Pacific sector where ozone levels (Fig. 6g) and SW heating (Fig. 9g) are higher in INTERACT_O_3 compared to CMIP6_O_3 coincides with the region of GHG-induced ozone increase (Fig. 5d). The effect of GHGs on ozone represents a dynamical feedback that cannot be simulated in CMIP6_O_3 because the ozone field is prescribed and therefore cannot react to changes in dynamics. Although this GHG effect is captured in the two CCMs that produced the CMIP6 ozone field prescribed in CMIP6_O_3, and although this ozone field is consistent with the SSP5-8.5 scenario used here, intermodel differences in simulating the ozone response to increasing GHGs and declining ODSs lead to inconsistencies between ozone and dynamical changes when the ozone field obtained from other models is prescribed. This is emphasized by the weak ozone and SW heating rate changes in CMIP6_O_3 in the region where the dynamical increase in ozone driven by GHGs occurs in FOCI.

The pattern of changes in the dynamical heating rate in INTERACT_O_3 is driven by the dynamical response to increasing GHGs (Fig. 8f). The change in the dynamical heating rate due to ozone recovery is weak in October at 50 hPa (Fig. 8c), but it becomes stronger in November, acting to cool the polar cap (Fig. S4l). The region of dynamical warming is larger, and the dynamical cooling is stronger in CMIP6_O_3 (Fig. 9f) than in INTERACT_O_3 (Fig. 9c). These differences in the dynamical heating rate originate from differences in wave activity and in the residual circulation, which are discussed in the following section. The LW heating rate changes act to dampen the warming due to SW and dynamical heating changes in all simulations (Figs. 8b, e and 9b, e).

In summary, ozone recovery during the twenty-first century reverses the effects of ozone depletion. It leads to a springtime warming of the polar cap in the lower stratosphere and an associated weakening of the westerly winds that extends to the surface in austral summer. In contrast, increasing GHGs lead to a cooling of the stratosphere throughout most of the year, an acceleration of the subtropical jet, and enhanced westerly winds throughout the stratosphere. These results are in good agreement with the findings of previous studies (Perlwitz et al., 2008; Karpechko et al., 2010; McLandress et al., 2010; Polvani et al., 2011a). A significant exception to the otherwise rather zonally uniform changes occurs in austral spring, when a dynamical response to increasing GHGs results in contrasting temperature and zonal wind changes over the Pacific and Indo-Atlantic sectors that offset each other in the zonal mean and are not detectable if only zonal-mean fields are investigated. The importance of these GHG-driven changes, which are reported here for the first time, is emphasized by their magnitude, which is similar to the magnitude of the changes due to ozone recovery. In the months and regions where the ozone effect is important, the combined ozone and GHG effect is stronger in the stratosphere in the ensemble with interactive ozone chemistry than in the ensemble with prescribed CMIP6 ozone as the ozone effect is stronger in the former ensemble. This demonstrates the importance of the ozone field in setting the magnitude of

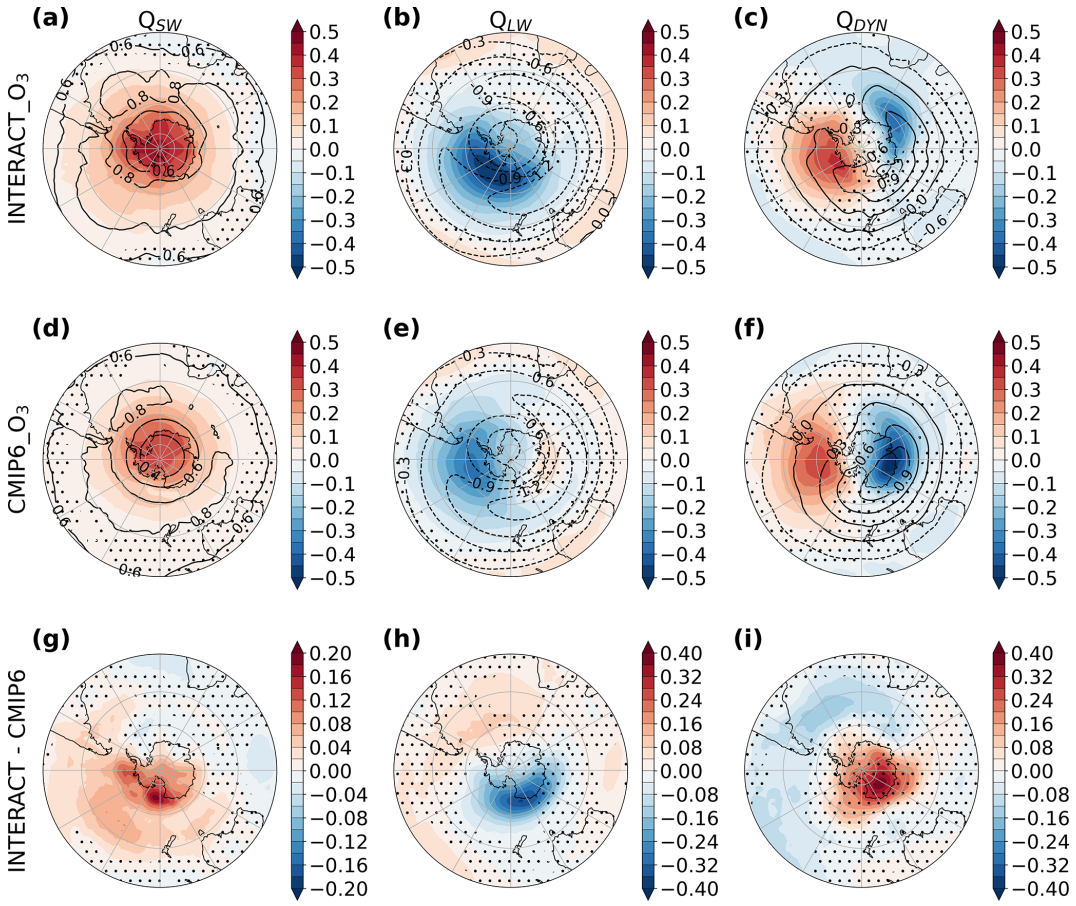

Figure 9. Changes in the SW **(a, d)**, LW **(b, e)**, and dynamical **(c, f)** heating rate ($K\,d^{-1}$) at 50 hPa during October due to ozone recovery and GHGs combined, in INTERACT_O_3 **(a–c)** and CMIP6_O_3 **(d–f)**, and the difference between the INTERACT_O_3 and the CMIP6_O_3 changes **(g–i)**. The stippling in **(a)**–**(f)** masks regions where the changes are not significant at the 95 % confidence interval based on a two-tailed t test, and the stippling in **(g)**–**(i)** masks regions where the difference is lower than 2σ inferred from the spread of the individual ensemble members. The contours in **(a)**–**(f)** show the current-day (2011–2030) climatologies in the respective fields.

the temperature and zonal wind changes during the twenty-first century.

4.1.2 The residual circulation and wave activity

Although the BDC comprises both the mean meridional residual circulation and two-way mixing processes, here we only investigate the contributions of ozone recovery and increasing GHGs to the twenty-first-century changes in the residual circulation. The reduction in ODSs could also theoretically lead to changes in the BDC through the radiative effects of the ODSs. However Abalos et al. (2019) showed that trends in the BDC due to ODSs are mainly explained by ozone changes. We therefore attribute the ODS-induced residual circulation changes in our simulations to ozone recovery. As a first measure of the changes in the strength of the residual circulation, we analyze the tropical upward mass flux and the extratropical downward mass flux in each hemisphere, shown in Fig. 10 at the 50 hPa level for each month.

In both hemispheres, the impact of increasing GHGs is a clear strengthening of the downward mass flux and hence of the BDC, peaking between mid-fall and mid-spring and ceasing in late spring and early summer. For the Northern Hemisphere (NH), the peak GHG-induced strengthening of the BDC in winter agrees with the results of previous studies (e.g., Shepherd and McLandress, 2011; Chrysanthou et al., 2020). For the SH, our results are at odds with those of Chrysanthou et al. (2020), who reported a peak strengthening of the BDC in austral summer in response to a quadrupling of CO_2 in an atmospheric model with prescribed preindustrial ozone. We note that the GHG-induced strengthening of the residual mean stream function is confined north of 55° S in austral winter, unlike in summer, when it reaches the polar region. The magnitude of the strengthening during winter is, however, much larger than that during summer. An important exception to the GHG-induced strengthening occurs in November in the SH, when GHGs lead to a weakening of the mass flux in the lower stratosphere. The upward trop-

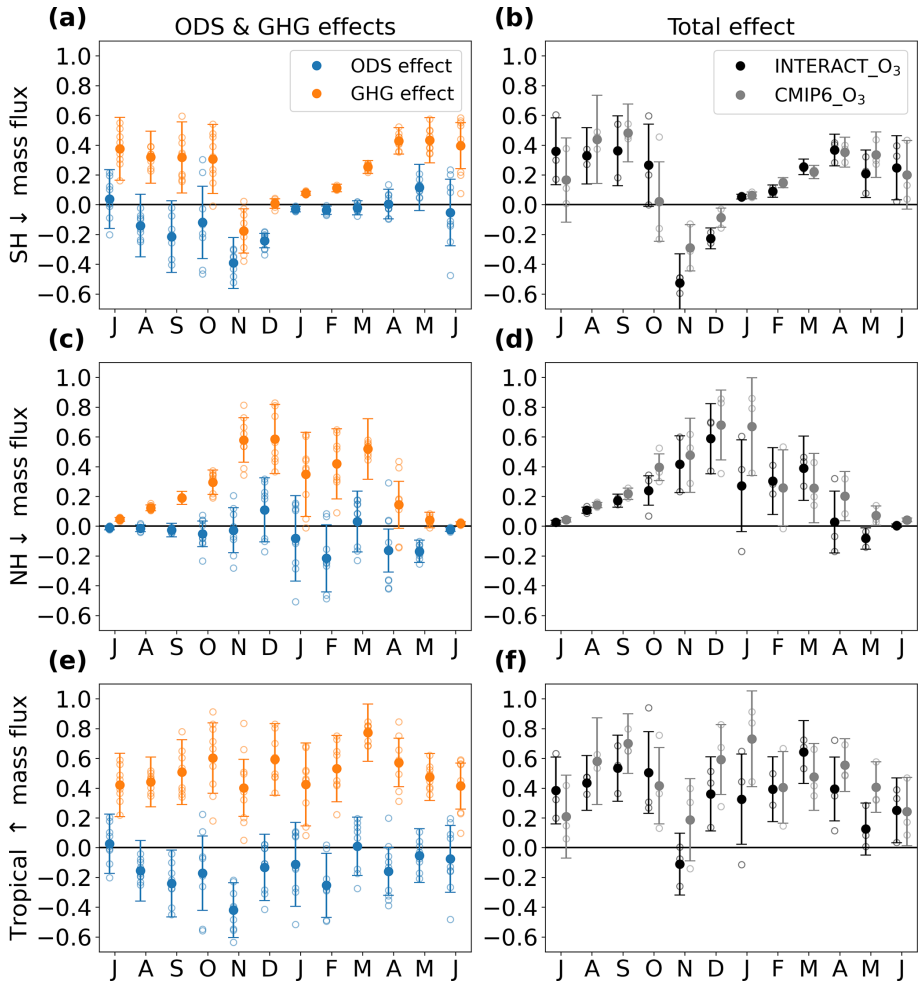

Figure 10. Changes in the SH downward mass flux **(a, b)**, NH downward mass flux **(c, d)**, and tropical upward mass flux **(e, f)** at 50 hPa for each month (10^9 kg s^{-1}). The changes due to ozone recovery are shown in blue, the changes due to GHGs are shown in orange **(a, c, e)**, the total changes in INTERACT_O_3 are shown in black, and the total changes in CMIP6_O_3 are shown in gray **(b, d, f)**. The error bars give the 95 % confidence interval based on a two-tailed t test. Differences between ensemble means are depicted by filled circles, and differences between individual simulations are depicted by hollow circles.

ical mass flux is enhanced by increasing GHGs throughout the year, driven from the NH between November and February, in agreement with the simulations by Oberländer et al. (2013); from the SH between May and July; and from both hemispheres to different extents for the rest of the year. In contrast, ozone recovery weakens the BDC, which is consistent with previous studies (Oman et al., 2009; Lin and Fu, 2013; Oberländer et al., 2013; Polvani et al., 2018, 2019). The ozone effect is strong in the lower stratosphere only in November–December in the SH and April–May in the NH. The largest impact occurs in the SH in November, when the recovery of the Antarctic ozone hole takes place. This is also the only month when the tropical mass flux is significantly affected by ozone recovery.

Throughout most of the year, the total change in the BDC during the twenty-first century follows the change due to increasing GHGs, and the BDC strengthens. In November and December, however, the BDC in the SH weakens, driven by both ozone recovery and increasing GHGs in November and by ozone recovery alone in December. The weakening in the SH offsets the strengthening in the NH during November, leading to an insignificant change in the tropical mass flux. The change in the residual mean stream function shown for November in Fig. S1 in the Supplement reveals that while ozone recovery weakens the BDC throughout the depth of the stratosphere, the increase in GHGs only weakens the lower branch.

The 2 months during which ozone recovery influences the BDC are also the 2 months during which all three members of the INTERACT_O_3 ensemble simulate a stronger weakening than all three members of the CMIP6_O_3 ensemble (hollow circles in Fig. 10b). This once again points to the fact that the effects of ozone recovery are weaker when the CMIP6 ozone field is prescribed. A similar behavior occurs

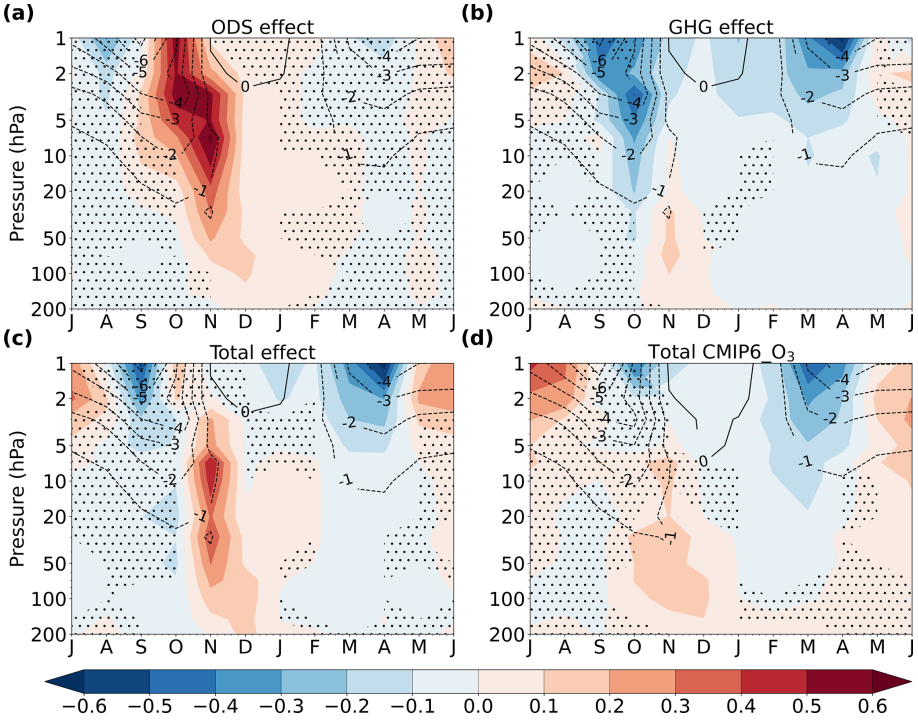

Figure 11. Changes in the polar cap (70–90° S) vertical residual velocity (in mm s^{-1}) for each month and pressure level (color shading): effect of ozone recovery **(a)**, effect of GHGs **(b)**, total effect in INTERACT_O_3 **(c)**, and total effect in CMIP6_O_3 **(d)**. The contours depict the current-day (2011–2030) climatology from INTERACT_O_3 in **(a)**–**(c)** and from CMIP6_O_3 in **(d)**. The stippling masks regions where the changes are not significant at the 95 % confidence interval based on a two-tailed *t* test.

in May in the NH, although the ozone recovery has a weaker effect there. In addition, the November BDC weakening is confined below 20 hPa in CMIP6_O_3, exhibiting a structure more similar to that of the GHG effect, while the weakening in INTERACT_O_3 extends to the upper stratosphere, in accordance with the ozone effect (Fig. S1).

The changes in the residual circulation described above are driven by changes in planetary wave activity in response to ozone recovery and increasing GHGs. In order to better understand the link between the changes in the residual circulation and changes in wave activity, we show in Fig. 11 the changes in the polar cap vertical residual velocity, in Fig. 12 the changes in the divergence of the EP flux, and in Fig. S2 the change in the eddy heat flux for each calendar month. As these diagnostics only offer a zonal-mean view of the simulated changes, we additionally make use of the three-dimensional Plumb flux of wave activity (Plumb, 1985) to obtain the spatial pattern of the changes (Figs. S4 and S5). When zonal averages are considered, the vertical and meridional components of the Plumb flux reduce to the EP flux. Therefore, the zonal-mean eddy heat flux (Fig. S2) is equivalent to the zonal mean of the vertical component of the Plumb flux (Figs. S4 and S5), with negative eddy heat flux values indicating upward wave activity propagation.

In agreement with the ozone-induced weakening of the mass flux (Fig. 10a), the downwelling over the polar cap is considerably reduced in November throughout the stratosphere due to ozone recovery (Fig. 11a), dynamically cooling the polar cap (Fig. S4k and l) and offsetting a part of the radiative warming effect of ozone recovery. This reduction is accompanied by an anomalous divergence of the EP flux (Fig. 12a) and a positive change in the eddy heat flux (Fig. S2a), indicating reduced wave activity propagation. Separating the divergence of the EP flux into contributions from individual zonal wavenumbers reveals that the ozone-induced changes in the residual circulation are primarily mediated through changes in the propagation of the PW1 (Fig. S3a). We showed in Sect. 4.1.1 that ozone recovery reduces the amplitude of the PW1. The weakening of the planetary wave activity flux and the associated weakening of the downwelling are initiated in the upper stratosphere in October over the Atlantic sector and Drake Passage (Fig. S4a) and become more pronounced and circumpolar and extend to the lower stratosphere in November, persisting in the lower stratosphere until February, but with a much lower magnitude (Figs. S4c and d, 11a, and 12a). The changes in the wave activity flux due to ozone recovery are linked to changes in the polar night jet. The region of zero zonal wind velocity represents the critical line for Rossby wave propagation (Dickinson, 1968). As the jet is decelerated in October in response to the ozone-induced polar cap warming (Fig. 5 and contours in Fig. 12), the critical line for Rossby wave propagation mi-

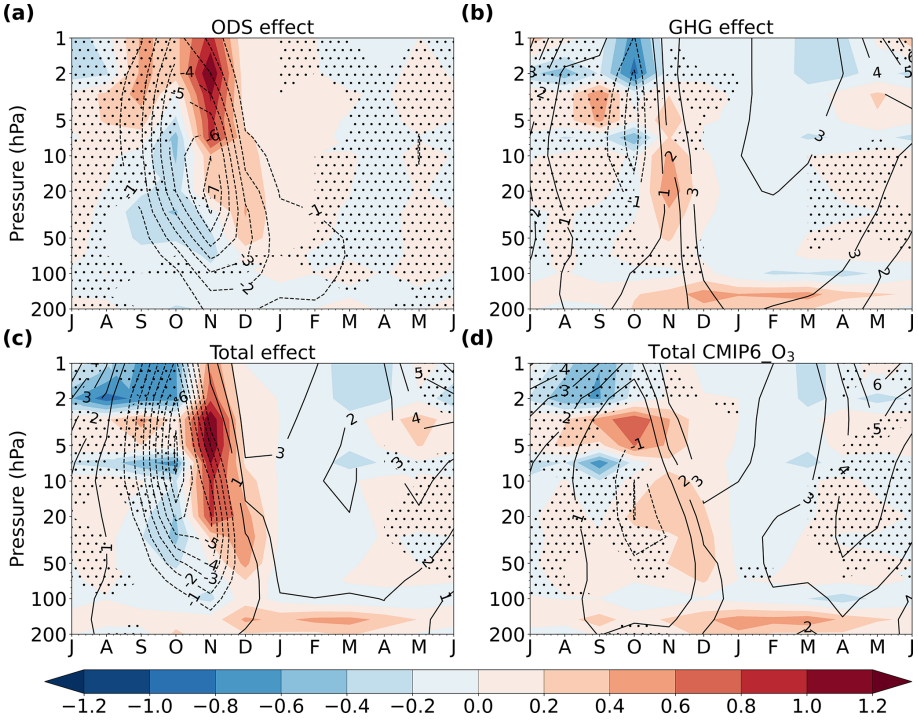

Figure 12. Changes in the divergence of the EP flux averaged over 45–80° S ($m\,s^{-1}\,d^{-1}$) for each month and pressure level (color shading): effect of ozone recovery **(a)**, effect of GHGs **(b)**, total effect in INTERACT_O_3 **(c)**, and total effect in CMIP6_O_3 **(d)**. The contours depict the corresponding changes in the zonal-mean wind averaged over 45–80° S ($m\,s^{-1}$). The stippling masks regions where the changes are not significant at the 95 % confidence interval based on a two-tailed t test.

grates poleward, inhibiting wave propagation. This mechanism is analogous to that demonstrated to be responsible for mediating the effect of increasing GHGs on the BDC in the subtropical lower stratosphere by Shepherd and McLandress (2011). Since the polar vortex in FOCI is displaced towards South America (contours in Fig. 6c), the inhibition of wave propagation is initiated in this region (Fig. S4a). The effect then extends around the Antarctic continent and propagates downward in the following month (Fig. S4c and d) as the polar night jet continues to weaken, and the breakdown of the polar vortex is accelerated by ozone recovery. In summer, the height of the critical line for Rossby wave propagation in the lower stratosphere is decreased in response to ozone recovery (Fig. 12), explaining the weak deceleration of the residual circulation in this season.

We additionally note that ozone recovery leads to anomalous convergence between 50 and 7 hPa in October (Fig. 12a) and a weak but significant strengthening of the lower-stratospheric downwelling (Fig. 11a). This corroborates the results of McLandress et al. (2010), who found an increase in the polar cap downwelling in the lower stratosphere in spring driven by enhanced EP flux convergence due to ozone recovery, changing sign in summer. In our simulations, however, the change in sign occurs already in November. This offers a possible explanation as to why previous studies that looked at seasonally averaged changes did not find an impact of ozone recovery on the BDC in spring (Polvani et al., 2018; Lin and Fu, 2013). The strengthening of the polar downwelling in the lower stratosphere during October agrees with the changes inferred from the Plumb flux and from the dynamical heating rate (Fig. S4a and i): wave propagation is inhibited in the upper stratosphere, and wave breaking occurs at lower levels, leading to a reduction in the downwelling in the upper stratosphere, resulting in dynamical cooling and an enhancement of the downwelling in the lower stratosphere (Fig. 11a).

The increase in GHGs also exerts the largest influence on the SH polar cap downwelling in austral spring (Fig. 11b). The relatively small impact of GHGs on the polar downwelling during the rest of the year might seem at odds with the peak GHG-induced increase in the downward mass flux between April and October (Fig. 10a). This discrepancy is explained by seasonal differences in the latitude range at which the residual circulation is affected by the GHG increase. During winter, although the GHG effect on the residual circulation has the largest magnitude, it is restricted to the low latitudes and midlatitudes as the propagation of wave activity is enhanced towards the Equator (not shown). During spring, the GHG effect extends to the polar latitudes, affecting the polar downwelling, although its overall magnitude is weaker. McLandress et al. (2010) also showed that important changes in the SH downward mass flux caused by increasing GHGs occur outside of the polar cap. Therefore, the season-

ality of the polar downwelling and of the SH total downward mass flux magnitudes is not directly comparable. The effects of ozone recovery on the polar cap downwelling and on the total SH downward mass flux are in better agreement as the ozone-induced residual circulation changes are driven from the polar region.

Figure 11b shows that GHGs strengthen the downwelling above 20 hPa in October. This strengthening is related to enhanced planetary wave propagation (Fig. S2b) and wave breaking (Fig. 12b) in the upper stratosphere, primarily associated with the PW1 (Fig. S3b). The changes in the three-dimensional flux of wave activity (Fig. S4e and f) show that, in fact, the flux of wave activity is enhanced over the Indian Ocean sector and diminished over the Pacific and Atlantic sectors. These changes persist throughout the depth of the stratosphere and indicate that increasing GHGs enable planetary waves to propagate higher into the stratosphere and mesosphere over the Indian Ocean during spring. This results in reduced (enhanced) wave breaking in the middle (upper) stratosphere, which in turn drives a weakening (strengthening) of the downwelling in the middle (upper) stratosphere. Over the Pacific sector, the propagation of wave activity is inhibited by increasing GHGs. Consequently, planetary waves break at lower levels, and the wave drag is enhanced in the middle stratosphere and weakened above, driving stronger downwelling in the lower to middle stratosphere and weaker downwelling in the upper stratosphere. The changes over the Indian Ocean sector have a larger magnitude than those occurring over the Pacific sector and therefore dominate in the zonal mean. As such, the enhanced upward eddy heat flux (Fig. S2b), as well as the enhanced wave drag (Fig. 12b) during October in the upper stratosphere, is consistent with the changes inferred from the Plumb flux. In November, the changes over the Atlantic and Pacific sectors become dominant (Fig. S4h), consistent with the weakened eddy heat flux (Fig. S2b) as well as with the weakened wave breaking (Fig. 12b) in the middle stratosphere that results in the reduced downwelling (Fig. 11b). In fact, as shown in Fig. S1b in the Supplement, the entire lower branch of the BDC in the SH weakens in November, in agreement with the reduction in the downward mass flux (Fig. 10a).

When the combined effect of ozone recovery and increasing GHGs is considered, the weakening of the wave drag and downwelling due to ozone recovery largely offsets the strengthening due to GHGs during October in the upper stratosphere, while in the lower stratosphere the ozone-induced strengthening appears to dominate in INTERACT_O_3 (Figs. 11c and 12c). CMIP6_O_3, however, exhibits a weakening of the downwelling in the lower stratosphere during October (Fig. 11d). During November, INTERACT_O_3 exhibits a strong wave drag reduction extending from 50 hPa to the stratopause and a weakening of the downwelling between 200 and 2 hPa. While the changes in CMIP6_O_3 agree in sign with those in INTERACT_O_3 in November, the magnitude of the changes is weaker in the former ensemble, and, in addition, the changes do not extend as high up as in INTERACT_O_3 (Figs. 11c, d and 12c, d). The weaker magnitude of the changes in CMIP6_O_3 is consistent with the weaker ozone increase in the CMIP6 field. At the same time, the different timing and vertical distribution of the weakening in polar downwelling are explained by differences in the patterns of change in the propagation of planetary waves (Figs. 7c, d and S5). Thus, both the magnitude and the different spatial pattern of the ozone increase in CMIP6_O_3 compared to INTERACT_O_3 contribute to the differences in the dynamical changes between the two ensembles.

In summary, the BDC in the SH strengthens throughout most of the year, driven by the increase in GHGs, but weakens in November and December, driven by both ozone recovery and increasing GHGs in November and by ozone recovery alone in December. An interesting result of our analysis is that, during November, unlike during the rest of the year, the increase in GHGs weakens the BDC in the lower stratosphere. During the months in which ozone recovery significantly affects the BDC, the magnitude of the change in the ensemble with interactive ozone is significantly larger than in the ensemble with prescribed CMIP6 ozone. Furthermore, while the changes in the former ensemble occur throughout the depth of the stratosphere, the changes in the latter ensemble are only significant up to the middle stratosphere. This shows that the effect of ozone recovery on the BDC is weaker when the CMIP6 ozone field is prescribed.

4.1.3 Surface impacts

We now turn our attention to the projected twenty-first-century changes in the surface circulation. As shown in Sect. 4.1.1, the weakening of the stratospheric westerlies due to ozone recovery extends to the surface in November and the austral summer. Figure 13 shows maps of annual changes in the mean sea level pressure (SLP), surface zonal wind, and the associated wind stress curl, in response to ozone recovery and increasing GHGs, separately. We chose to examine the changes occurring over the entire year rather than seasonal subsets as they are the most relevant for the long-term trends in the ocean circulation. For completion, we show additional maps of zonal wind changes during November–January and June–August in Fig. S6. Although occurring during a single season, the ozone effect is still significant in the annual mean and represents a weakening of about 4 % of the current-day annual mean westerlies in the latitude band between 45 and 60° S. In the November–January average, the weakening is larger, reaching 8 %. The change towards more easterly velocities occurs on the poleward flank of the climatological westerlies (contours in Fig. 14b) and implies an equatorward shift in their position. As expected, ozone recovery reverses the strengthening and poleward shift in the westerlies caused in the past by the formation of the Antarctic ozone hole, consistent with previous findings (Perlwitz et al., 2008; McLan-

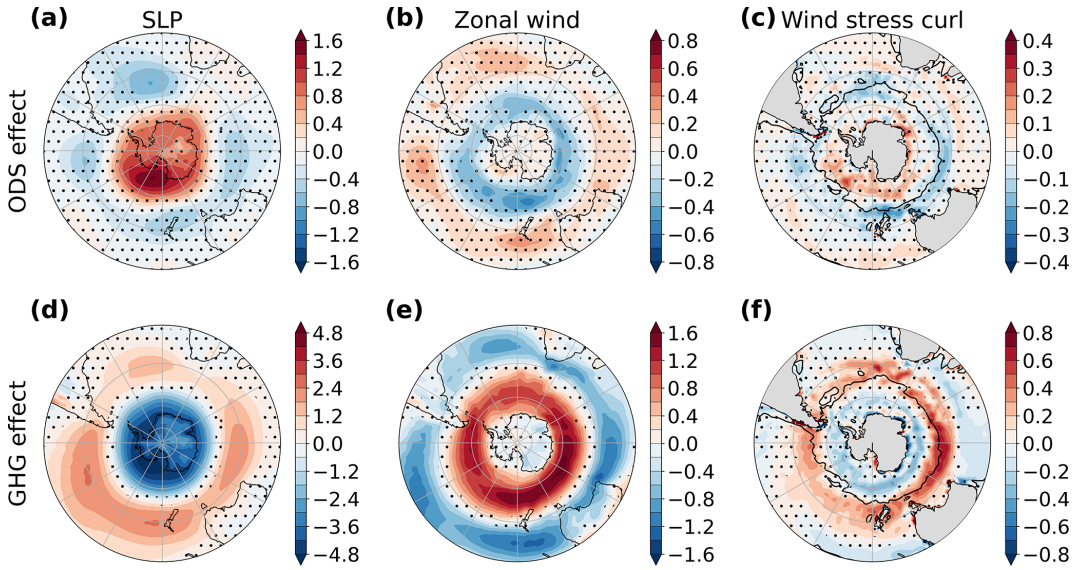

Figure 13. Changes in annual mean sea level pressure (**a**, **d**; hPa), surface zonal wind (**b**, **e**; $\mathrm{m\,s^{-1}}$), and wind stress curl (**c**, **f**; $10^{-7}\,\mathrm{N\,m^{-3}}$) due to ozone recovery **(a–c)** and GHGs **(d–f)**. The stippling masks regions where the changes are not significant at the 95 % confidence interval based on a two-tailed t test. The contour in **(c)** and **(f)** marks the location of zero-wind-stress curl.

dress et al., 2011). This can also be seen in the effect of ozone recovery on SLP (Fig. 13a), which exhibits a strong increase over the Antarctic continent and decreases at mid-latitudes, signaling that the SAM shifts more towards its negative phase. This is confirmed by the negative change in the SAM index shown in Fig. 15a.

Increasing GHGs, in contrast, continue the past trend towards a more positive SAM (Figs. 13d and 15a) and strengthened surface westerlies that shift poleward (Figs. 13e and 15b, c). The magnitude of the GHG effect is much larger than that of the ozone effect on the westerlies in the annual mean, leading to a strengthening of 17 % in the mean over the latitude band between 45 and 60° S. As a consequence, when both effects are considered together (Fig. 14a), the GHG effect dominates, and the westerlies continue to strengthen and shift poleward during the twenty-first century (Fig. 15b and c), accompanied by a shift toward the positive phase of the SAM (Figs. 14a and 15a). There are marked differences between INTERACT_O_3 and CMIP6_O_3 in the magnitude of the total SAM change and in the magnitude of the total westerly wind change (Figs. 14 and 15). Significant differences between the two ensembles occur particularly over the Indian and Pacific oceans for both zonal wind and SLP and additionally over the entire Antarctic continent for SLP, with changes in both signs being stronger in CMIP6_O_3 (Fig. 14). Averaged over 45 and 60° S, the westerlies strengthen by 9 % compared to the current day in INTERACT_O_3, while they strengthen by 16 % in CMIP6_O_3. Given that the difference between INTERACT_O_3 and CMIP6_O_3 lies in the treatment of ozone chemistry, the stronger changes in CMIP6_O_3 in the direction driven by GHGs show that the ozone effect is much weaker in CMIP6_O_3. This is consistent with the results presented in the previous sections for the stratosphere, where the impact of ozone recovery is also weaker in this ensemble.

We stress that the dominance of the GHG effect over the effect of ozone recovery on the surface winds is strongly dependent on the scenario used for GHGs. Here, we use SSP5-8.5, which is characterized by high GHG emissions throughout the twenty-first century. CMIP6 models project that, for the "sustainability" scenario SSP1-2.6, the ozone effect dominates, leading to an overall weakening of the westerly jet, while for the "middle-of-the-road" scenario SSP2-4.5 the two effects compensate each other (Bracegirdle et al., 2020). Our results are consistent with CMIP6 projections for SSP5-8.5 (Bracegirdle et al., 2020). Although the GHG effect dominates if GHG emissions remain high during the twenty-first century, it is important to note the significance of the Montreal Protocol in reducing the impacts of climate change as the changes in the surface westerlies are stronger in the absence of ozone recovery.

In summary, ozone recovery drives a significant weakening of the surface westerlies and a change towards a more negative SAM, reversing the trends caused by ozone depletion, while increasing GHGs drive a continued strengthening of the westerlies and a change towards a more positive SAM. The GHG effect dominates in the annual mean under SSP5-8.5, but there are large differences in the magnitude of the total effect between the ensemble with interactive ozone and the ensemble with prescribed CMIP6 ozone. The effect of the ozone recovery on the surface westerlies and the SAM is weaker in the ensemble with prescribed CMIP6 ozone, lead-

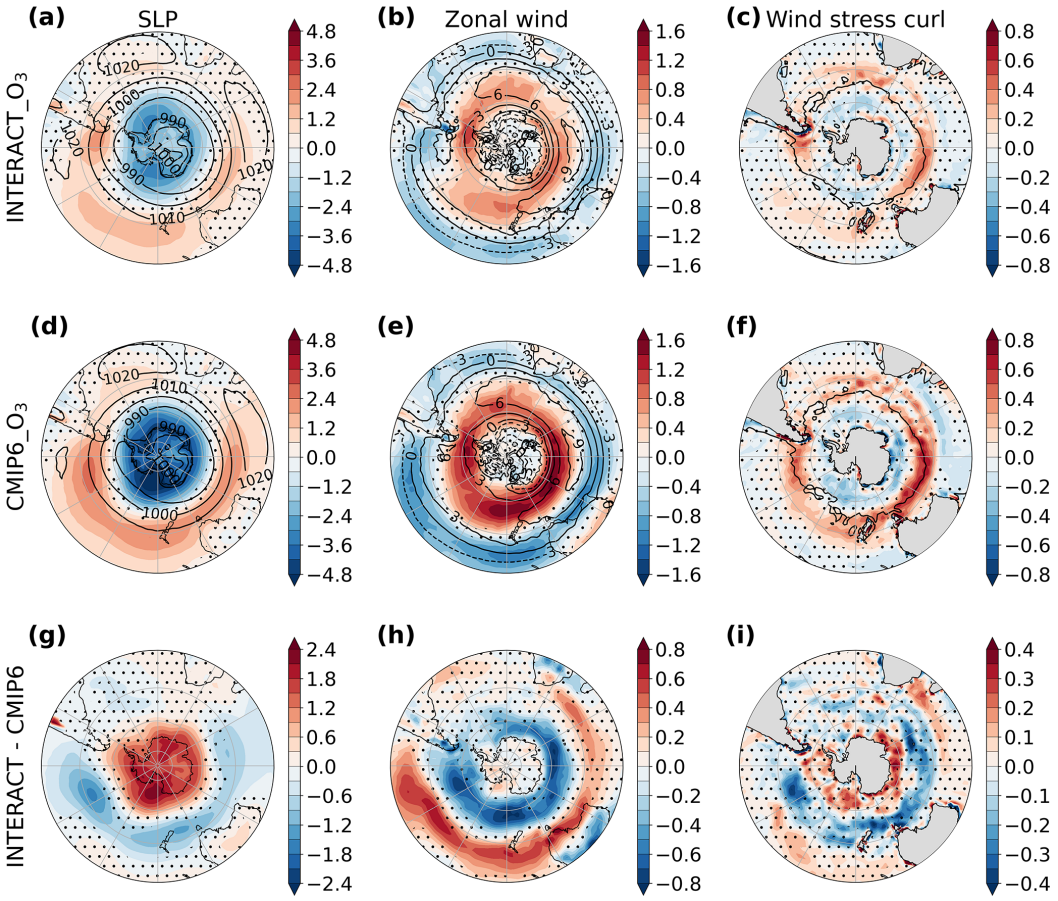

Figure 14. Changes in annual mean sea level pressure (**a**, **d**; hPa), surface zonal wind (**b**, **e**; $\mathrm{m\,s^{-1}}$), and wind stress curl (**c**, **f**; $10^{-7}\,\mathrm{N\,m^{-3}}$) due to ozone recovery and GHGs combined, in INTERACT_O_3 **(a–c)** and CMIP6_O_3 **(d–f)**, and the difference between the INTERACT_O_3 and the CMIP6_O_3 changes **(g–i)**. The stippling in **(a)**–**(f)** masks regions where the changes are not significant at the 95 % confidence interval based on a two-tailed t test, and the stippling in **(g)**–**(i)** masks regions where the difference is lower than 2σ inferred from the spread of the individual ensemble members. The contour in **(c)** and **(f)** marks the location of zero-wind-stress curl, while contours in **(a)**, **(b)**, **(d)**, and **(e)** show the current-day (2011–2030) climatologies in the respective fields.

ing to a greater dominance of the GHG effect and consequently to changes of greater magnitude. The magnitude of the differences between the ensembles with interactive and with prescribed CMIP6 ozone is at least as large as the effect of ozone recovery itself, emphasizing the large uncertainty associated with the ozone field used.

4.2 Ocean circulation changes

4.2.1 Agulhas leakage

The westerly wind changes induced in the past by ozone depletion led to an increase in the inter-ocean exchange of warm and saline waters around South Africa, known as the Agulhas leakage (e.g., Biastoch et al., 2009). In this section, we investigate if the Agulhas leakage will change during the twenty-first century in response to ozone recovery, increasing GHGs, and their combined effects. The Agulhas leakage can be studied using our coupled climate model, owing to the high-resolution ocean nest included in the model, which covers the region of the Agulhas system and resolves the mesoscale features responsible for the leakage. Figure 15f and g show the change in the Agulhas leakage and the Agulhas Current at the end of the century. The current-day (2014–2028) mean Agulhas leakage in the ensemble with interactive ozone is 11.6 Sv ($1\,\mathrm{Sv} = 10^6\,\mathrm{m^3\,s^{-1}}$), lower than the new observational estimate of 21.3 ± 4.7 Sv (Daher et al., 2020) or the older, widely used estimate of 15 Sv (Richardson, 2007) but comparable with the mean values of 11.2 and 12.2 Sv simulated by the high-resolution coupled climate model employed by Cheng et al. (2016, 2018), respectively. For comparison, the mean Agulhas leakage simulated by the ocean component of FOCI, using the same high-resolution nest INALT10X, is 12.2 Sv (Schwarzkopf et al., 2019). The current-day Agulhas Current transport in the FOCI ensemble with interactive ozone is 82.8 Sv, falling within the uncertainty

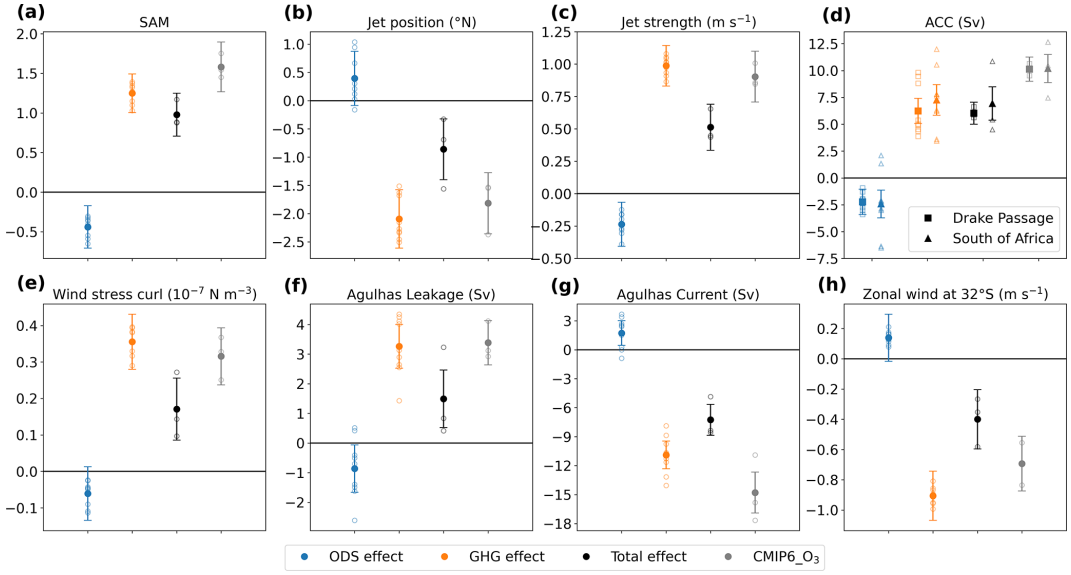

Figure 15. Changes in the annual mean SAM index calculated following the definition of Gong and Wang (1999) as the difference in the normalized zonal-mean SLP between 40 and 65° S **(a)**; surface westerly jet position computed as the latitude of the maximum in the zonal-mean zonal wind between 30 and 65° S (**b**; ° of latitude, positive northward); surface westerly wind strength averaged between 45 and 60° S (**c**; $\mathrm{m\,s^{-1}}$); ACC transport (**d**; Sv) in the Drake Passage, computed as the difference in the barotropic stream function between the Antarctic Peninsula and South America (circles), and south of Africa, computed as the maximum in the barotropic stream function between 20 and 30° E (triangles); wind stress curl averaged between 40 and 55° S and 30 and 120° E (**e**; $10^{-7}\,\mathrm{N\,m^{-3}}$); Agulhas leakage transport (**f**; Sv); Agulhas Current transport (**g**; Sv); and the zonal wind at 32° S averaged between 30 and 120° E (**h**; $\mathrm{m\,s^{-1}}$). Filled symbols depict the change in the ensemble mean, and hollow symbols depict the change in the individual members due to ozone recovery (blue) increasing GHGs (orange), combined forcing in INTERACT_O_3 (black), and combined forcing in CMIP6_O_3 (gray). The error bars denote the 95 % confidence interval based on a two-tailed t test.

range of the observational estimate of 77 ± 32 Sv (Beal and Elipot, 2016). The Agulhas Current transport in the FOCI is slightly larger than the 76.3 Sv reported by Schwarzkopf et al. (2019) from an uncoupled ocean simulation with the INALT10X nest driven by relative wind stress. Although the ocean–atmosphere coupling in FOCI implies that the effect of the ocean circulation on the surface stress is simulated, the much lower resolution of the atmosphere compared to the ocean results in a smoothening of this effect, explaining why the coupled model simulates a larger Agulhas Current transport. Note that, as explained in Sect. 2.3, the calculation of the Agulhas leakage results in a time series ending in 2094, and we adjusted the periods over which we perform our analysis accordingly (see Sect. 2.3 for details). Ozone recovery drives an Agulhas leakage decrease of 0.9 Sv, or about 7 % of the current-day mean transport. This opposes the effect of increasing GHGs, which drive an increase in leakage of 3.3 Sv, or 28 %. The total effect in the ensemble with interactive ozone chemistry, INTERACT_O_3, is an increase in leakage of 1.5 Sv, or 13 %, significantly lower than the increase which would occur from increasing GHGs alone. This highlights the importance of ozone recovery in mitigating some of the ocean circulation changes resulting from increasing GHGs during the twenty-first century. In contrast, in the ensemble with prescribed ozone, CMIP6_O_3, in which the ozone effect is weaker, the Agulhas leakage increases by 3.4 Sv, or 33 %, an increase of similar magnitude to that resulting from the GHG forcing alone when ozone is calculated interactively. These results are consistent with the changes in the westerly winds presented in Sect. 4.1.3 and underline that the choice of how to account for stratospheric ozone changes affects the prediction of not only the tropospheric, but also the oceanic circulation changes. This is further confirmed by the predicted changes in the transport of the Agulhas Current at 32° S, which are rather a response of changes in the trade winds (Fig. 15g). Ozone recovery drives an increase in transport of 1.7 Sv, or 2 %, while increasing GHGs drive a decrease of 10.9 Sv, or 13 % of the current-day mean Agulhas Current transport of 82.8 Sv, resulting in a total decrease of 7.3 Sv, or 9 %, in INTERACT_O_3. In contrast, the decrease in CMIP6_O_3 is 14.8 Sv, or 17 %, significantly greater than that occurring in INTERACT_O_3. It might seem contrary to expectations that the Agulhas leakage increases when the transport of the Agulhas Current decreases, but Loveday et al. (2014) showed that the changes in the Agulhas leakage and Agulhas Current transport appear to be decoupled. While the Agulhas Current changes seem to be driven by the trade winds, the changes in leakage are instead driven by the westerlies (e.g., Durgadoo et al., 2013). In our simulations, there is a good correspondence between the Agulhas Current

transport at 32° S (Fig. 15g) and zonal wind anomalies over the Indian Ocean at the same latitude (Fig. 15h), with ozone-induced westerly wind anomalies associated with an increase in transport and GHG-induced easterly anomalies associated with a decrease in transport. As a result of the zonal wind changes, a decrease in the positive wind stress curl due to increasing GHGs can be seen at this latitude in Figs. 13f and 14f, likely driving the decrease in the Agulhas Current transport.

The mechanism resulting in increased Agulhas leakage has been explored by Durgadoo et al. (2013) in perturbation experiments in which either the intensity or the position of the SH westerlies south of 35° S were varied. Durgadoo et al. (2013) found that strengthening the westerlies leads to more Agulhas leakage, while a poleward shift in the position of the westerlies leads to less Agulhas leakage. They explained the response of the leakage to stronger westerlies through positive wind stress curl anomalies at the latitudes of the westerly winds, which strengthen the positive wind stress curl over the southern part of the Indian Ocean, north of the maximum westerlies. The more positive wind stress curl drives an intensified Ekman pumping and northward Sverdrup transport across the southern part of the subtropical supergyre linking the South Atlantic and Indian oceans, and the Agulhas leakage has to intensify to provide the westward mass transport required by continuity. The changes in wind stress curl simulated by FOCI for the twenty-first century (Figs. 13c and f, 14c and f, and 15e) seem to support this mechanism. The GHG-induced westerly wind changes lead to positive wind stress curl anomalies in the southern part of the Indian Ocean around the latitude of zero-wind-stress curl (maximum westerlies), depicted by the contour in Figs. 13 and 14. Importantly, these anomalies extend to the north of the zero-wind-stress contour, where the climatological wind stress curl is positive, and therefore induce an increase in the equatorward Sverdrup transport. The wind stress curl anomalies are weaker, but still positive when the combined GHG and ozone effect is considered in INTERACT_O_3, the ensemble with interactive ozone (Fig. 14c). They have a similar magnitude to the effect of GHGs in CMIP6_O_3, the ensemble with prescribed CMIP6 ozone (Fig. 14f), consistent with the magnitudes of both the westerly wind changes and the Agulhas leakage changes in these ensembles (Fig. 15). In response to ozone recovery, weak negative wind stress curl anomalies occur that are significant only over limited regions (Figs. 13c and 15e). The Agulhas leakage response is therefore also much weaker compared to the response to increasing GHGs (Fig. 15f).

The relationship between the westerly wind stress and the Agulhas leakage in FOCI is further illustrated in Fig. S7, which shows the decadally averaged Agulhas leakage relative to 2014–2023 plotted against the decadally averaged westerly wind stress. Decades of high Agulhas leakage coincide with decades of high westerly wind stress. Furthermore, Fig. S7 also shows that the relatively small changes in wind stress when the GHGs are fixed result in relatively small changes in leakage (filled dark-blue circles), while the strongest wind stress intensification that occurs in CMIP6_O_3, the ensemble with prescribed ozone, results in the largest increase in leakage (filled dark-red circles). Combined with the good agreement between the changes in the Agulhas leakage and the wind stress curl over the southern part of the Indian Ocean discussed above, this leads us to conclude that ozone recovery and increasing GHGs both impact the Agulhas leakage via their influence on the westerly winds. The two forcings have opposing effects that, when considered together, result in an increase in Agulhas leakage during the twenty-first century.

4.2.2 Effects of an increased Agulhas leakage

An enhanced Agulhas leakage has been previously associated with an increased flux of heat and salt into the Atlantic (Biastoch and Böning, 2013). We performed a composite analysis to investigate the relationship between the Agulhas leakage and changes in South Atlantic salinity and temperature in FOCI during the twenty-first century (Fig. 16). In order to exclude any effects of climate change, we based our analysis on the FixGHG ensemble. Anomalies of potential temperature, and practical salinity were first obtained for each member of the FixGHG ensemble by removing the 2014–2094 time mean at each location. A 5-year low-pass filter was applied to the annual Agulhas leakage, temperature and salinity fields to focus on anomalies associated with decadal Agulhas leakage variations, and a linear trend was removed from each field. Years of high Agulhas leakage transport were then identified using as a threshold the 90th percentile calculated by combining the Agulhas leakage detrended time series of all three members and ensuring that any 2 years are at least 5 years apart. This rendered 11 years of high Agulhas leakage over which the detrended anomalies of temperature and salinity averaged over the upper 1000 m were composited (Fig. 16a and d). Similarly, we composited the temperature and salinity anomalies over a section in the South Atlantic at 35° S between 0 and 20° E (Fig. 16b and c). The significance of the composites was assessed using the Monte Carlo method (e.g., Storch and Zwiers, 1999). A distribution of low-pass-filtered and detrended anomalies was obtained by randomly selecting 11 years (the same number as in the original composite) over all three members, without replacement, 1000 times. The anomalies were deemed significant at the 95 % level if they were greater than the 97.5th or lower than the 2.5th percentile of the distribution.

Figure 16a and d show that periods of increased Agulhas leakage are associated with simultaneous positive temperature and salinity anomalies spreading from the Cape Basin into the South Atlantic. The depth profiles over the section between 0 and 20° E at 35° S (Fig. 16b and c) reveal that these anomalies are largest in the upper 250 m, but they extend down to 1000 m in the case of temperature and to 750 m

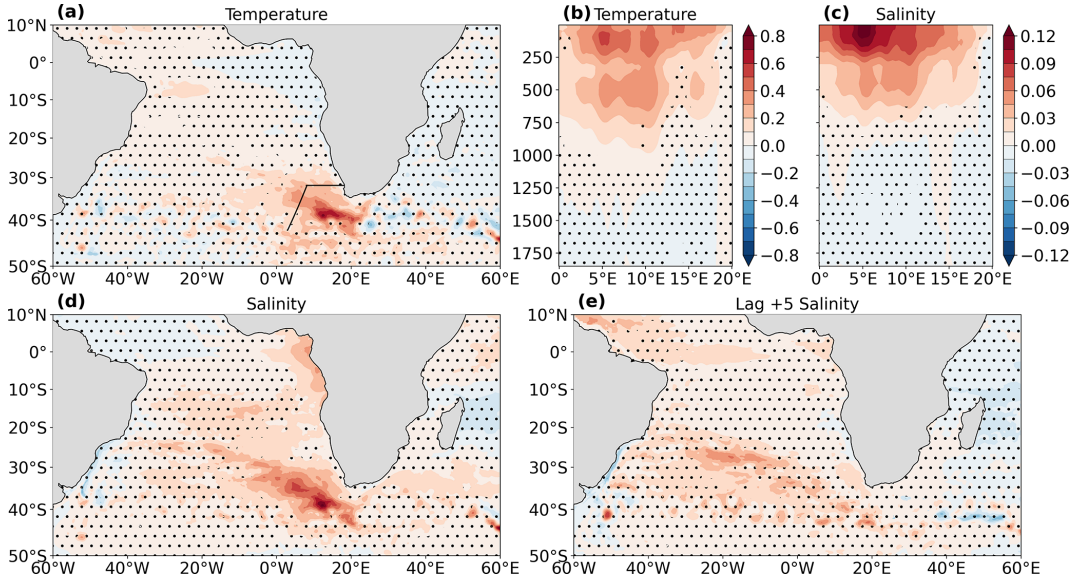

Figure 16. Composites of high Agulhas leakage periods for FixGHG: anomalies with respect to the 2014–2094 mean of potential temperature (**a**; °C) and practical salinity at lag 0 years **(d)** and +5 years **(e)** averaged over the upper 1000 m of the ocean and depth profiles of potential temperature **(b)** and practical salinity **(c)** anomalies between 0 and 20° E at 35° S. The fields are low-pass-filtered to retain only variations with a period above 5 years and detrended by removing a linear trend. The stippling masks anomalies that are not significantly different from the time mean according to the Monte Carlo method (see text for details). The line in panel **(a)** marks the Good Hope section used in calculating the Agulhas leakage.

in the case of salinity. Five years after a period of high Agulhas leakage, positive salinity anomalies are present in the central part of the South Atlantic, indicating that the salinity anomalies are advected northwestward towards the western boundary. No significant temperature anomalies can be detected at this lag (not shown), consistent with the idea that thermal anomalies are damped by heat loss to the atmosphere on their way northwards, while salinity anomalies persist, leading to the development of density anomalies (Weijer et al., 2002). Our results support the findings of Biastoch and Böning (2013) and Weijer and van Sebille (2014) that an advective pathway exists for salinity anomalies associated with the Agulhas leakage to the western boundary and into the North Atlantic. This implies that the increase in Agulhas leakage projected to occur during the twenty-first century under the SSP5-8.5 pathway will result in a salinification and densification of the South Atlantic, potentially reaching the North Atlantic, with consequences for the AMOC.

4.2.3 Antarctic Circumpolar Current

We now investigate whether the changes in the surface westerly jet and the associated changes in wind stress over the Southern Ocean lead to any changes in the transport of the ACC. Figure 15d shows the changes in the ACC transport calculated from the barotropic stream function at two locations, in the Drake Passage and south of Africa. While the Drake Passage is located at the boundary of the high-resolution nest, the region around South Africa is located in the middle of the nest. Following Durgadoo et al. (2013), the ACC transport through the Drake Passage is computed as the difference in the barotropic stream function between the Antarctic Peninsula (60° W and 65° S) and South America (68° W and 55° S), while the ACC transport south of Africa is computed as the maximum in the barotropic stream function between 20 and 30° E. The mean current-day (2011–2030) transport through the Drake Passage is 97.9 and 95.3 Sv in FOCI with interactive ozone chemistry (INTERACT_O_3) and with prescribed CMIP6 ozone (CMIP6_O_3), respectively. This is at the lower end of the CMIP5 range of 90–264 Sv (Meijers et al., 2012) and lower than the observed transport, which ranges from 136.7 ± 7.8 Sv (Cunningham et al., 2003) to 173.3 ± 10.7 Sv (Donohue et al., 2016), although these measurements cover earlier time periods. South of Africa, the current-day ACC transport is 181.8 and 181.2 Sv in INTERACT_O_3 and CMIP6_O_3, respectively.

Ozone depletion results in a weak but statistically significant (at the 95 % level) reduction in the ACC transport at both locations, in line with the weakening of the westerlies. This weakening represents 2 % and 1 % of the current-day mean ACC transport in the Drake Passage and south of Africa, respectively. In contrast, increasing GHGs lead to a strengthening of 6 % and 4 % of the current-day mean ACC transport in the Drake Passage and south of Africa, respectively, as expected from the strengthening of the westerlies. There is a larger spread in the ACC transport changes in the individual

simulations south of Africa compared to the Drake Passage as the former region is located in the middle of the high-resolution nest and is therefore characterized by more vigorous eddy activity. Nevertheless, the magnitudes of the ensemble mean changes are in good agreement at the two locations for all of the ensembles, giving confidence in the results. Interestingly, the combined effect of ozone recovery and increasing GHGs on the ACC is very similar in magnitude to the effect of increasing GHGs alone. The ACC transport in the Drake Passage and south of Africa is stronger by 6.0 and 6.9 Sv, or 6 % and 4 %, respectively, at the end of the twenty-first century compared to today. This points to a non-linear response to the combined forcing. It is known that changes in the ACC transport do not scale with the increase in the wind stress over the Southern Ocean due to eddy saturation (e.g., Farneti et al., 2010). The stronger wind stress increases the northward Ekman transport over the Southern Ocean, resulting in a steepening of isopycnals across the ACC on one hand, and it increases eddy activity, which acts to flatten isopycnals, on the other hand. The two effects offset each other, resulting in only small changes in the transport of the ACC. In addition to the changes in wind stress, the ACC is also sensitive to the density gradient across it (Farneti et al., 2015). FOCI simulates a large spread in this density gradient, which likely also contributes to the similar ACC transport changes due to GHGs alone and due to both GHGs and ozone when ensemble means are considered.

The ACC transport experiences a significantly stronger increase during the twenty-first century when the CMIP6 ozone is prescribed (CMIP6_O_3) compared to when ozone is calculated interactively (INTERACT_O_3; Fig. 15d). This is consistent with the fact that the westerlies strengthen more in CMIP6_O_3 than in INTERACT_O_3 (Figs. 14b, e and 15c), but may seem at odds with the eddy saturation phenomenon. A further exploration of the changes in the ACC is not meaningful since parts of the Southern Ocean south of the ACC (as well as regions upstream of the Drake Passage) are not represented at high resolution and hence only contain eddy effects in the form of parameterizations.

4.2.4 Ocean temperature

The temperature of the global ocean is linked to climate change, and, in addition, there is evidence from modeling studies that the ocean's temperature in the SH was affected by ozone depletion (Ferreira et al., 2015; A. Solomon et al., 2015; Seviour et al., 2016; Li et al., 2021). In addition, the temperature of the ocean feeds back on the global climate, through SST on shorter and through deeper temperatures on longer timescales. Therefore, in this section, we investigate the changes in ocean temperature that can be expected during the twenty-first century in response to increasing GHGs and ozone depletion. Our focus is on the South Atlantic Ocean as this region is covered by the high-resolution nest and therefore benefits from having the effects of mesoscale features properly simulated.

Figure 17 shows the changes in SST in the domain of the high-resolution nest. The increase in GHGs leads to warming over the entire domain, but the warming is not uniform (Fig. 17b), hinting to the fact that circulation changes are modulating the change in SST. The magnitude of the warming is larger south of the tip of Africa, and there is a band of stronger warming extending from this region into the Atlantic. As shown in Fig. 16a, this is exactly the region affected by the Agulhas leakage. Therefore, the increase in leakage due to GHGs is contributing to the stronger warming found in this region. The Agulhas Return Current also exhibits a stronger warming than its surroundings. Additionally, there is a zonal band of strong warming centered at about 45° S. Ozone recovery leads to a cooling peaking in the same zonal band (Fig. 17a), which reverses the warming caused at these latitudes by ozone depletion (e.g., Seviour et al., 2016). The signature of a decreased Agulhas leakage due to ozone recovery can also be seen in the SST response as a cooling extending from the Agulhas retroflection region into the Atlantic. These ozone-induced SST changes, although significant, are weak in comparison with the GHG-induced warming. Therefore, when both effects are considered together (Fig. 17c and d), the pattern of SST changes is dictated by GHGs. However, as was the case for the wind and Agulhas leakage changes, ozone recovery is mitigating the increase in SST caused by GHGs. This mitigating effect is weaker in CMIP6_O_3 than in INTERACT_O_3, in line with the weaker ozone forcing and the resulting stronger surface wind strengthening.

The band of cooling (warming) at 45° S due to ozone recovery (GHGs) extends down to about 1500 m (Fig. 18a and b). Observations and model simulations for the last decades exhibit a similar pattern of warming extending well below the surface (Armour et al., 2016; Li et al., 2016), attributed in part to ozone depletion (Bitz and Polvani, 2012; A. Solomon et al., 2015; Ferreira et al., 2015; Seviour et al., 2016; Li et al., 2021). Ozone recovery reverses this warming, but GHGs intensify it, such that the total effect continues to be an increase in the ocean temperature in this latitude band (Fig. 18c and d). As with the SST change, the warming is stronger in CMIP6_O_3 than in INTERACT_O_3. At this stage, we cannot fully isolate the reason for the warming around 45° S. One one hand, the trade winds (arrows in Fig. S8) are affected by ozone recovery and GHGs. In combination with the changes in the westerlies, this leads to an intensification (weakening) and southward (northward) shift in the subtropical gyre due to GHGs (ozone recovery) (Fig. S9). On the other hand, the warming can also be explained by changes in Ekman transport and pumping associated with the wind changes (Fig. S8). The strengthening in both the westerlies and trades driven by GHGs leads to a stronger Ekman convergence, intensifying the downwelling between 40 and 50° S. Ozone depletion is causing the opposite effects.

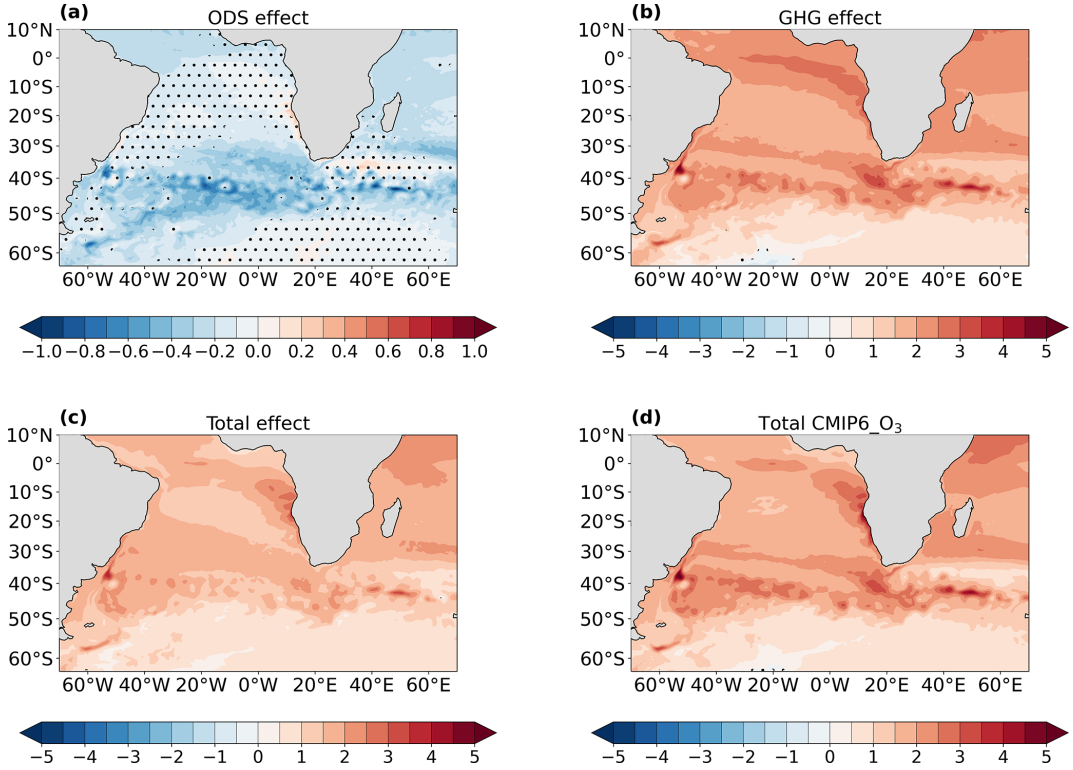

Figure 17. Changes in the SST (°C) for the region covered by the high-resolution nest (63° S–10° N and 70° W–70° E): effect of ozone recovery **(a)**, effect of GHGs **(b)**, total effect in INTERACT_O_3 **(c)**, and total effect in CMIP6_O_3 **(d)**. The stippling masks regions where the changes are not significant at the 95 % confidence interval based on a two-tailed t test.

5 Summary and discussion

The unique ocean–atmosphere coupled climate model FOCI with interactive ozone chemistry and a high-resolution ocean nest was used in this study to separate the effects of ozone recovery and increasing GHGs on the atmospheric and oceanic circulation in the SH during the twenty-first century under the high-emission scenario SSP5-8.5. A special emphasis was placed on the spatial patterns that characterize these effects. In addition, the combined effects of the two forcings were compared between the configuration of FOCI with interactive ozone chemistry and the configuration in which the CMIP6 ozone field consistent with the SSP5-8.5 pathway was prescribed.

The springtime Antarctic total column ozone in FOCI returns to 1980s levels in 2048 as increasing GHGs following SSP5-8.5 accelerate the recovery of the ozone hole by about 2 decades. In the upper stratosphere, the increase in GHGs contributes about half of the total ozone recovery over the twenty-first century in FOCI. This is explained by the GHG-induced cooling, which slows down the reactions involved in destroying ozone, as shown by Haigh and Pyle (1982), Rosenfield et al. (2002), Jonsson et al. (2004), and Revell et al. (2012). At lower-stratospheric levels, GHGs cause an increase in ozone through transport changes associated with an enhanced BDC.

Ozone recovery during the twenty-first century reverses the effects of the past ozone depletion, in agreement with previous studies (e.g., McLandress et al., 2010), leading to a warming of the lower-stratospheric polar cap in austral spring and a weakening of the westerly winds in both the stratosphere and the troposphere. In contrast, increasing GHGs drive a cooling of the stratosphere throughout most of the year and westerly wind anomalies peaking at the top of the subtropical jet and extending vertically to the surface and to the top of the stratosphere.

By analyzing for the first time the spatial patterns of changes during austral spring, we showed that GHGs have an important dynamical impact on the SH stratosphere during austral spring that differs from their effect during the rest of the year. The increase in GHGs leads to changes in the characteristics of planetary waves propagating from the troposphere into the stratosphere, mainly of the PW1, which experiences an eastward phase shift. As a result, despite their symmetric forcing, GHGs induce temperature and zonal wind anomalies of opposite sign over the Pacific and Indo-Atlantic sectors of the Southern Ocean, which are of similar magnitude to the ozone-induced anomalies. Therefore, the ozone and GHG effects reinforce each other over the Pacific

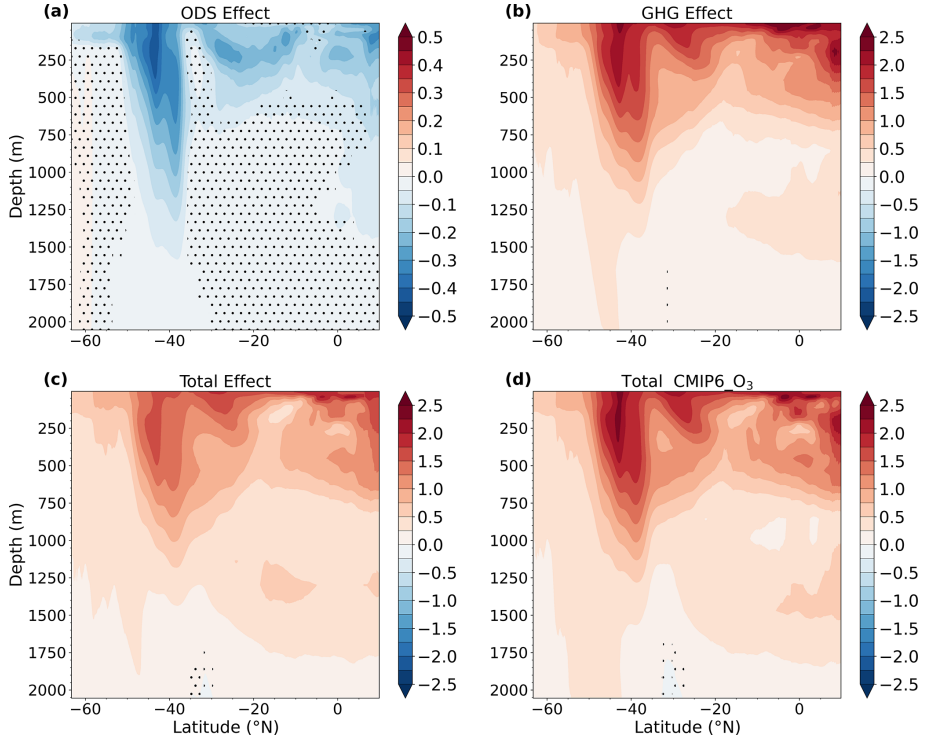

Figure 18. Latitude–depth profile of oceanic potential temperature changes (°C) zonally averaged over the high-resolution nest (70° W–70° E): effect of ozone recovery **(a)**, effect of GHGs **(b)**, total effect in INTERACT_O_3 **(c)**, and total effect in CMIP6_O_3 **(d)**. The stippling masks regions where the changes are not significant at the 95 % confidence interval based on a two-tailed t test.

sector and counteract each other over the Indo-Atlantic sector. Due to the PW1 structure of the stratospheric temperature and zonal wind changes that results from the increase in GHGs, these changes are severely underestimated when zonal or areal mean fields are analyzed. FOCI simulates a statistically insignificant warming in the lower stratosphere during October, when the temperature change due to GHGs is averaged over the polar cap, while Karpechko et al. (2010) reported a significant warming of the Antarctic lower stratosphere in their ensemble forced solely by increasing GHGs. In contrast, Son et al. (2008, 2009) found a weak cooling of the Antarctic lower stratosphere in the CMIP3 models that exclude ozone recovery, in agreement with McLandress et al. (2010), who also found that GHGs drive a weak polar cap lower-stratospheric cooling in their CCM. These contrasting results are likely explained by intermodel differences in simulating the changes in planetary wave activity due to GHGs, which result in temperature and zonal wind responses of different magnitudes in the different models.

Ozone recovery leads to a reduction in the flux of wave activity into the stratosphere during spring by weakening and causing an earlier breakdown of the polar vortex. As the height at which wave drag is being deposited as a result of wave breaking is decreased, the polar downwelling weakens during October in the upper stratosphere and during November and December throughout the entire stratosphere. The resulting dynamical cooling diminishes the warming that occurs due to the radiative effect of ozone in the lower stratosphere and causes an overall cooling of the upper stratosphere in these months. The analysis of the downward mass flux and of the mean residual stream function revealed that the entire residual circulation in the SH is weakened between October and December. Our results add to the body of evidence (Oman et al., 2009; McLandress et al., 2010; Lin and Fu, 2013; Oberländer et al., 2013; Polvani et al., 2018, 2019) that the consequence of ozone recovery during the twenty-first century will be to weaken the BDC and therefore partly offset the strengthening induced by the increase in GHGs. However, all of these studies reported that the contrasting effects on the BDC occur in austral summer. While we also find that GHGs strengthen and ozone recovery weakens the BDC in the SH during summer, the summer changes are small when compared to springtime changes, and, for the case of ozone recovery, they are dominated by changes during December. This result is in line with the presence of climatological easterlies in the middle and upper stratosphere throughout most of the summer that do not support Rossby wave propagation and therefore confine the changes in wave drag to the lower stratosphere, where the zero-wind line is located.

The increase in GHGs drives a strengthening of the SH residual circulation throughout most of the year, with

the exception of November, when it leads to a weakening instead, reinforcing the weakening effect of ozone recovery during this month. Therefore, the combined effect of ozone recovery and increasing GHGs on the residual circulation is a weakening in November and December and a strengthening during the rest of the year. Our results highlight that the increasing GHGs play an important role in the dynamical stratospheric changes that take place in austral spring during the twenty-first century. The changes in the residual circulation and in the stratospheric polar night jet are mediated through changes in the propagation of planetary waves, in particular of the PW1. The exact mechanism through which the increase in GHGs alters the propagation of planetary waves is, however, not known. It is possible that the changes are triggered by the acceleration of the upper flank of the subtropical jet due to the radiative warming (cooling) of the upper troposphere (lower stratosphere) caused by GHGs. The non-linear character of the interactions between planetary waves and the zonal wind makes it difficult to understand how this acceleration then affects planetary wave propagation.

At the surface, our analysis of the twenty-first-century changes in the SH surface westerly winds supports previous findings (Shindell and Schmidt, 2004; Yin, 2005; Perlwitz et al., 2008; McLandress et al., 2011; Polvani et al., 2011a) that ozone recovery drives a weakening and equatorward shift in the westerlies accompanied by a negative change in the SAM during austral summer, while increasing GHGs drive a year-round strengthening and poleward shift accompanied by a positive change in the SAM. Under the high-emission scenario SSP5-8.5, FOCI projects that the GHG effect overwhelms the effect due to ozone recovery both during austral summer and in the annual mean, but the surface changes are weaker when both forcings are considered than those driven by GHGs alone. We note that the total change in the surface westerlies will depend on how much GHGs will increase in the future. Westerly wind changes in studies that also investigated low- to moderate-emission scenarios range from an equatorward shift to no significant changes (Eyring et al., 2013; Barnes et al., 2014; Gerber and Son, 2014; Iglesias-Suarez et al., 2016; Bracegirdle et al., 2020).

The Agulhas leakage is increasing during the twenty-first century. This increase is driven by the wind stress changes associated with the increasing GHGs and is partly offset by the effect of ozone recovery. Our composite analysis revealed that a stronger Agulhas leakage is associated with increased temperature and salinity in the southeastern South Atlantic. Our results are consistent with those of Biastoch et al. (2015) and Cheng et al. (2018), who related an increased Agulhas leakage to higher SSTs extending from the Cape Basin into the South Atlantic. We additionally showed that this relationship is also valid at depth, down to 1000 m. The link between increased Agulhas leakage and higher southeastern Atlantic temperatures simulated in FOCI in the upper 1000 m supports the findings of Lübbecke et al. (2015) that the positive Agulhas leakage trend in the second half of the twentieth century contributed to the warming of the eastern tropical Atlantic. However, the temperature anomalies are not detectible anymore in FOCI after 5 years. This could be partly explained by loss of heat to the atmosphere that damps the temperature anomalies, as reported by Weijer et al. (2002) and Biastoch and Böning (2013). The salinity anomalies, in contrast, are advected northwestward and can be detected in the central part of the South Atlantic at a lag of 5 years. This results in the development of positive density anomalies that are advected towards the North Atlantic and that can potentially be important for the stability of the AMOC as they have the ability to partially compensate the changes in density resulting from a freshening of the North Atlantic due to climate-change-induced ice sheet melting that causes less deepwater formation and hence a weaker AMOC. Unfortunately, in the current study, we cannot isolate the impact of the increase in Agulhas leakage on the AMOC from other effects of the increasing GHGs. Nevertheless, there is compelling evidence from previous studies that salinity anomalies related to an increased Agulhas leakage reach the subtropical North Atlantic within 2 to 4 decades (Biastoch and Böning, 2013; Weijer and van Sebille, 2014). In addition, 40 % of the Agulhas leakage was found to reach 24° N within 2 decades (Rühs et al., 2013). Therefore, the twenty-first-century increase in Agulhas leakage has the potential to alter the thermohaline structure of the AMOC. In addition to the temperature and salinity changes arising from increased Agulhas leakage, we see a local effect driven by changes in the Ekman transport due to changing westerlies and trades. Ozone recovery reverses the warming caused by ozone loss north of the ACC and extending to intermediate depths (Ferreira et al., 2015; A. Solomon et al., 2015; Seviour et al., 2016; Li et al., 2021). In contrast, GHGs lead to warming in the same regions. The pattern of cooling due to ozone recovery closely matches the pattern of warming due to GHGs because they are both modulated by the respective changes in the surface wind stress, which have opposing signs and thus result in opposing circulation changes. The GHG effect is dominant, and when both drivers are considered together, the entire South Atlantic is warming.

The transport of the ACC in the Drake Passage and south of Africa is decreased by ozone recovery and increased by climate change, in agreement with the findings of Sigmond et al. (2011), but changes in transport are rather small, with a maximum of 6 %. The combined effect of ozone recovery and increasing GHGs equals the effect of GHGs alone. This result is consistent with the fact that the ACC is in an eddy-saturated state (e.g., Farneti et al., 2010; Morrison and Hogg, 2013) as the effects of an increase in eddy activity and of an increase in northward Ekman transport offset each other, rendering the ACC only weakly sensitive to changes in wind stress. Typically, coupled climate models such as those used for the different phases of CMIP have too low a resolution to

simulate mesoscale eddies and rely on eddy parametrization schemes based on Gent and Mcwilliams (1990) to account for eddy effects (e.g., Downes and Hogg, 2013). CMIP5 models do not agree on the sign of the change in ACC transport during the twenty-first century under RCP8.5, with about half of the models simulating an increase and the other half simulating a decrease in transport (Downes and Hogg, 2013). Additionally, there is no statistically significant relationship between the change in the strength of the zonal wind stress and the change in ACC transport among the CMIP5 models (Meijers et al., 2012; Downes and Hogg, 2013). The ACC transport changes in the Drake Passage of about 6 % and 11 % in FOCI with interactive ozone and with prescribed CMIP6 ozone, respectively, fall within the range of changes of about ±15 % simulated by CMIP5 models under RCP8.5 (Downes and Hogg, 2013). Unlike the CMIP5 models, however, FOCI has a higher oceanic resolution, $1/2°$ globally and $1/10°$ within the high-resolution nest, INALT10X. The mesoscale eddies are resolved in the Atlantic sector and in part of the Indian sector of the Southern Ocean, and because of the two-way nesting technique used in FOCI, the information about the presence of the eddies is transmitted to the global ocean model. Therefore, we can assume that this configuration of FOCI captures the eddy saturation effect better than the CMIP-class models. Bishop et al. (2016) performed a perturbation experiment with another coupled climate model that uses a $1/10°$ oceanic resolution in which they increased the zonal wind stress over the Southern Ocean by 50 % and found only a 6 % strengthening in the ACC transport through the Drake Passage in response. In our simulations, a 6 % and an 11 % ACC transport increase is obtained for the wind stress increases of 10 % and 17 % in INTERACT_O_3 and CMIP6_O_3, respectively, implying that the sensitivity of the ACC transport to wind stress changes is stronger in our model. Although our results are not directly comparable with those of Bishop et al. (2016) because their simulation does not include changes in buoyancy due to, for example, climate change, this suggests that the degree of eddy saturation is further increased if the oceanic resolution is eddy-resolving over the entire Southern Ocean.

The comparison of the combined ozone and GHG effect between the ensemble with interactive ozone chemistry, INTERACT_O_3, and the ensemble in which the CMIP6 ozone field is prescribed, CMIP6_O_3, revealed that the ozone effect is weaker, and the GHG effect is more dominant in the latter ensemble, in agreement with the weaker increase in the ozone field in CMIP6. Significant differences were found in all of the examined fields. In the stratosphere, differences in both the magnitude and the spatial pattern of the total response occur. The magnitude of the difference at the surface and in the oceanic circulation is comparable to or greater than the ozone effect itself. This hints at the fact that other factors likely contribute to these differences, in addition to the difference in the ozone fields. Such possible factors are the interpolation of the prescribed monthly mean ozone field in time, which causes an underestimation of the spring ozone changes (Sassi et al., 2005; Neely et al., 2014); the feedbacks between the ozone field, radiation, and dynamics that cannot occur if the ozone field is prescribed and are therefore not properly captured (Haase et al., 2020); and the inconsistencies between the prescribed ozone field and the dynamics in the model (Ivanciu et al., 2021). In addition, the combined effect when the ozone field is prescribed is in some cases larger than the GHG effect simulated alone in the ensemble in which the ozone field is calculated interactively. This suggests that the GHG effect is affected by the response of the ozone field and is greater when the ozone is prescribed. The studies by Morgenstern et al. (2014) and Chiodo and Polvani (2016) showed that there are important dynamical changes resulting from the response of the ozone field to GHGs and that these changes offset part of the direct influence of GHGs on the SH dynamics. Although the prescribed CMIP6 ozone field is consistent with the increase in GHGs under SSP5-8.5, it cannot react to the changes in GHG concentrations during the simulations to which it is prescribed and may therefore be less sensitive to the GHG changes than in the ensemble in which it evolves interactively. This, in turn, could result in a lower degree of compensation between the direct GHG effect on the dynamics and the GHG effect mediated by the ozone field. While including interactive ozone chemistry is the only way to ensure that all ozone-related processes are simulated and that the ozone field is spatially and temporally consistent with the simulated dynamics, we showed that even larger uncertainties in future projections are related to estimates of ozone recovery itself. The CMIP6 ozone field has been produced by two CCMs, yet the Antarctic ozone returns to 1980s values in 2089, much later than in FOCI (2048) or in the CCMI ensemble average (2060; Dhomse et al., 2018). This shows how large the spread in ozone recovery rates is among CCMs. As a result, the magnitude of the effects of ozone recovery also exhibits a large spread, as demonstrated here using the same model with two different ozone fields.

The differences in the circulation response to ozone recovery and increasing GHGs between INTERACT_O_3 and CMIP6_O_3 show that the choice of the ozone field can affect the prediction of changes not only in the atmospheric but also in the oceanic circulation. This adds to the evidence provided by Ferreira et al. (2015), Li et al. (2016), and Seviour et al. (2016) that the ozone field affects the SH oceanic circulation. Furthermore, it suggests that the ozone field may introduce a source of uncertainty in the predictions for the twenty-first century.

While in the stratosphere the effects of ozone recovery and increasing GHGs reinforce each other in some regions and counteract each other in other regions, the GHG effect clearly dominates the changes at the surface and in the oceanic circulation under the high-emission scenario used here. However, these changes are considerably weaker in the presence of ozone recovery than in its absence, highlighting the im-

portance of the Montreal Protocol in mitigating some of the impacts of climate change.

Code and data availability. The output of the model simulations used in this study can be found at https://doi.org/10.5281/zenodo.5013716 (Ivanciu, 2021). The scientific code used to perform the analysis can be obtained upon request from Ioana Ivanciu (iivanciu@geomar.de).

Supplement. The supplement related to this article is available online at: https://doi.org/10.5194/wcd-3-139-2022-supplement.

Author contributions. II, KM, and AB designed the study and the setup of the simulations. II, SW, and JH performed the model simulations. II carried out the analysis, and all authors discussed the results. II wrote the manuscript with contributions from all co-authors.

Competing interests. The contact author has declared that neither they nor their co-authors have any competing interests.

Disclaimer. Publisher's note: Copernicus Publications remains neutral with regard to jurisdictional claims in published maps and institutional affiliations.

Acknowledgements. The model simulations used in this study were performed with resources provided by the North German Supercomputing Alliance (HLRN). The authors thank Siren Rühs and Franziska Schwarzkopf for helpful discussions regarding the analysis of the surface and oceanic circulation.

Financial support. This study has been funded by the German Federal Ministry of Education and Research through the SPACES-II CASISAC project (grant no. 03F0796A).

Review statement. This paper was edited by Thomas Birner and reviewed by two anonymous referees.

References

Abalos, M., Polvani, L., Calvo, N., Kinnison, D., Ploeger, F., Randel, W., and Solomon, S.: New Insights on the Impact of Ozone-Depleting Substances on the Brewer–Dobson Circulation, J. Geophys. Res.-Atmos., 124, 2435–2451, https://doi.org/10.1029/2018JD029301, 2019.

Amos, M., Young, P. J., Hosking, J. S., Lamarque, J.-F., Abraham, N. L., Akiyoshi, H., Archibald, A. T., Bekki, S., Deushi, M., Jöckel, P., Kinnison, D., Kirner, O., Kunze, M., Marchand, M., Plummer, D. A., Saint-Martin, D., Sudo, K., Tilmes, S., and Yamashita, Y.: Projecting ozone hole recovery using an ensemble of chemistry–climate models weighted by model performance and independence, Atmos. Chem. Phys., 20, 9961–9977, https://doi.org/10.5194/acp-20-9961-2020, 2020.

Andrews, D. G., Holton, J. R., and Leovy, C. B.: Middle Atmosphere Dynamics, in: vol. 40 of International Geophysics Serie, Academic Press, ISBN 9780120585762, 1987.

Armour, K. C., Marshall, J., Scott, J. R., Donohoe, A., and Newsom, E. R.: Southern Ocean warming delayed by circumpolar upwelling and equatorward transport, Nat. Geosci., 9, 549–554, https://doi.org/10.1038/ngeo2731, 2016.

Banerjee, A., Fyfe, J. C., Polvani, L. M., Waugh, D., and Chang, K.-L.: A pause in Southern Hemisphere circulation trends due to the Montreal Protocol, Nature, 579, 544–548, https://doi.org/10.1038/s41586-020-2120-4, 2020.

Barnes, E. A., Barnes, N. W., and Polvani, L. M.: Delayed Southern Hemisphere Climate Change Induced by Stratospheric Ozone Recovery, as Projected by the CMIP5 Models, J. Climate, 27, 852–867, https://doi.org/10.1175/JCLI-D-13-00246.1, 2014.

Beal, L. M. and Elipot, S.: Broadening not strengthening of the Agulhas Current since the early 1990s, Nature, 540, 570–573, https://doi.org/10.1038/nature19853, 2016.

Biastoch, A. and Böning, C. W.: Anthropogenic impact on Agulhas leakage, Geophys. Res. Lett., 40, 1138–1143, https://doi.org/10.1002/grl.50243, 2013.

Biastoch, A., Böning, C. W., and Lutjeharms, J. R. E.: Agulhas leakage dynamics affects decadal variability in Atlantic overturning circulation, Nature, 456, 489–492, https://doi.org/10.1038/nature07426, 2008.

Biastoch, A., Böning, C. W., Schwarzkopf, F. U., and Lutjeharms, J. R. E.: Increase in Agulhas leakage due to poleward shift of Southern Hemisphere westerlies, Nature, 462, 495–498, https://doi.org/10.1038/nature08519, 2009.

Biastoch, A., Durgadoo, J. V., Morrison, A. K., van Sebille, E., Weijer, W., and Griffies, S. M.: Atlantic multi-decadal oscillation covaries with Agulhas leakage, Nat. Commun., 6, 10082, https://doi.org/10.1038/ncomms10082, 2015.

Bishop, S. P., Gent, P. R., Bryan, F. O., Thompson, A. F., Long, M. C., and Abernathey, R.: Southern Ocean Overturning Compensation in an Eddy-Resolving Climate Simulation, J. Phys. Oceanogr., 46, 1575–1592, https://doi.org/10.1175/JPO-D-15-0177.1, 2016.

Bitz, C. M. and Polvani, L. M.: Antarctic climate response to stratospheric ozone depletion in a fine resolution ocean climate model, Geophys. Res. Lett., 39, L20705, https://doi.org/10.1029/2012GL053393, 2012.

Blanke, B. and Raynaud, S.: Kinematics of the Pacific Equatorial Undercurrent: An Eulerian and Lagrangian Approach from GCM Results, J. Phys.

Oceanogr., 27, 1038–1053, https://doi.org/10.1175/1520-0485(1997)027<1038:KOTPEU>2.0.CO;2, 1997.

Blanke, B., Arhan, M., Madec, G., and Roche, S.: Warm Water Paths in the Equatorial Atlantic as Diagnosed with a General Circulation Model, J. Phys. Oceanogr., 29, 2753–2768, https://doi.org/10.1175/1520-0485(1999)029<2753:WWPITE>2.0.CO;2, 1999.

Böning, C. W., Dispert, A., Visbeck, M., Rintoul, S. R., and Schwarzkopf, F. U.: The response of the Antarctic Circumpolar Current to recent climate change, Nat. Geosci., 1, 864–869, https://doi.org/10.1038/ngeo362, 2008.

Bracegirdle, T. J., Krinner, G., Tonelli, M., Haumann, F. A., Naughten, K. A., Rackow, T., Roach, L. A., and Wainer, I.: Twenty first century changes in Antarctic and Southern Ocean surface climate in CMIP6, Atmos. Sci. Lett., 21, e984, https://doi.org/10.1002/asl.984, 2020.

Brovkin, V., Raddatz, T., Reick, C. H., Claussen, M., and Gayler, V.: Global biogeophysical interactions between forest and climate, Geophys. Res. Lett., 36, L07405, https://doi.org/10.1029/2009GL037543, 2009.

Cheng, Y., Putrasahan, D., Beal, L., and Kirtman, B.: Quantifying Agulhas Leakage in a High-Resolution Climate Model, J. Climate, 29, 6881–6892, https://doi.org/10.1175/JCLI-D-15-0568.1, 2016.

Cheng, Y., Beal, L. M., Kirtman, B. P., and Putrasahan, D.: Interannual Agulhas Leakage Variability and Its Regional Climate Imprints, J. Climate, 31, 10105–10121, https://doi.org/10.1175/JCLI-D-17-0647.1, 2018.

Chiodo, G. and Polvani, L. M.: Reduction of Climate Sensitivity to Solar Forcing due to Stratospheric Ozone Feedback, J. Climate, 29, 4651–4663, https://doi.org/10.1175/JCLI-D-15-0721.1, 2016.

Chiodo, G., Polvani, L. M., Marsh, D. R., Stenke, A., Ball, W., Rozanov, E., Muthers, S., and Tsigaridis, K.: The Response of the Ozone Layer to Quadrupled CO_2 Concentrations, J. Climate, 31, 3893–3907, https://doi.org/10.1175/JCLI-D-17-0492.1, 2018.

Chipperfield, M. P., Bekki, S., Dhomse, S., Harris, N. R. P., Hossaini, R., Steinbrecht, W., Thiéblemont, R., and Weber, M.: Detecting recovery of the stratospheric ozone layer, Nature, 549, 211–218, https://doi.org/10.1038/nature23681, 2017.

Chrysanthou, A., Maycock, A. C., and Chipperfield, M. P.: Decomposing the response of the stratospheric Brewer–Dobson circulation to an abrupt quadrupling in CO_2, Weather Clim. Dynam., 1, 155–174, https://doi.org/10.5194/wcd-1-155-2020, 2020.

Cunningham, S. A., Alderson, S. G., King, B. A., and Brandon, M. A.: Transport and variability of the Antarctic Circumpolar Current in Drake Passage, J. Geophys. Res.-Oceans, 108, 8084, https://doi.org/10.1029/2001JC001147, 2003.

Daher, H., Beal, L. M., and Schwarzkopf, F. U.: A New Improved Estimation of Agulhas Leakage Using Observations and Simulations of Lagrangian Floats and Drifters, J. Geophys. Res.-Oceans, 125, e2019JC015753, https://doi.org/10.1029/2019JC015753, 2020.

Debreu, L., Vouland, C., and Blayo, E.: AGRIF: Adaptive grid refinement in Fortran, Comput. Geosci., 34, 8–13, https://doi.org/10.1016/j.cageo.2007.01.009, 2008.

Dhomse, S. S., Kinnison, D., Chipperfield, M. P., Salawitch, R. J., Cionni, I., Hegglin, M. I., Abraham, N. L., Akiyoshi, H., Archibald, A. T., Bednarz, E. M., Bekki, S., Braesicke, P., Butchart, N., Dameris, M., Deushi, M., Frith, S., Hardiman, S. C., Hassler, B., Horowitz, L. W., Hu, R.-M., Jöckel, P., Josse, B., Kirner, O., Kremser, S., Langematz, U., Lewis, J., Marchand, M., Lin, M., Mancini, E., Marécal, V., Michou, M., Morgenstern, O., O'Connor, F. M., Oman, L., Pitari, G., Plummer, D. A., Pyle, J. A., Revell, L. E., Rozanov, E., Schofield, R., Stenke, A., Stone, K., Sudo, K., Tilmes, S., Visioni, D., Yamashita, Y., and Zeng, G.: Estimates of ozone return dates from Chemistry-Climate Model Initiative simulations, Atmos. Chem. Phys., 18, 8409–8438, https://doi.org/10.5194/acp-18-8409-2018, 2018.

Dickinson, R. E.: Planetary Rossby Waves Propagating Vertically Through Weak Westerly Wind Wave Guides, J. Atmos. Sci., 25, 984–1002, https://doi.org/10.1175/1520-0469(1968)025<0984:PRWPVT>2.0.CO;2, 1968.

Donners, J. and Drijfhout, S. S.: The Lagrangian View of South Atlantic Interocean Exchange in a Global Ocean Model Compared with Inverse Model Results, J. Phys. Oceanogr., 34, 1019–1035, https://doi.org/10.1175/1520-0485(2004)034<1019:TLVOSA>2.0.CO;2, 2004.

Donohue, K. A., Tracey, K. L., Watts, D. R., Chidichimo, M. P., and Chereskin, T. K.: Mean Antarctic Circumpolar Current transport measured in Drake Passage, Geophys. Res. Lett., 43, 11760–11767, https://doi.org/10.1002/2016GL070319, 2016.

Downes, S. M. and Hogg, A. M.: Southern Ocean Circulation and Eddy Compensation in CMIP5 Models, J. Climate, 26, 7198–7220, https://doi.org/10.1175/JCLI-D-12-00504.1, 2013.

Durgadoo, J. V., Loveday, B. R., Reason, C. J. C., Penven, P., and Biastoch, A.: Agulhas Leakage Predominantly Responds to the Southern Hemisphere Westerlies, J. Phys. Oceanogr., 43, 2113–2131, https://doi.org/10.1175/JPO-D-13-047.1, 2013.

Eyring, V., Cionni, I., Lamarque, J. F., Akiyoshi, H., Bodeker, G. E., Charlton-Perez, A. J., Frith, S. M., Gettelman, A., Kinnison, D. E., Nakamura, T., Oman, L. D., Pawson, S., and Yamashita, Y.: Sensitivity of 21st century stratospheric ozone to greenhouse gas scenarios, Geophys. Res. Lett., 37, L16807, https://doi.org/10.1029/2010GL044443, 2010.

Eyring, V., Arblaster, J. M., Cionni, I., Sedláček, J., Perlwitz, J., Young, P. J., Bekki, S., Bergmann, D., Cameron-Smith, P., Collins, W. J., Faluvegi, G., Gottschaldt, K.-D., Horowitz, L. W., Kinnison, D. E., Lamarque, J.-F., Marsh, D. R., Saint-Martin, D., Shindell, D. T., Sudo, K., Szopa, S., and Watanabe, S.: Long-term ozone changes and associated climate impacts in CMIP5 simulations, J. Geophys. Res.-Atmos., 118, 5029–5060, https://doi.org/10.1002/jgrd.50316, 2013.

Farneti, R., Delworth, T. L., Rosati, A. J., Griffies, S. M., and Zeng, F.: The Role of Mesoscale Eddies in the Rectification of the Southern Ocean Response to Climate Change, J. Phys. Oceanogr., 40, 1539–1557, https://doi.org/10.1175/2010JPO4353.1, 2010.

Farneti, R., Downes, S. M., Griffies, S. M., Marsland, S. J., Behrens, E., Bentsen, M., Bi, D., Biastoch, A., Böning, C., Bozec, A., Canuto, V. M., Chassignet, E., Danabasoglu, G., Danilov, S., Diansky, N., Drange, H., Fogli, P. G., Gusev, A., Hallberg, R. W., Howard, A., Ilicak, M., Jung, T., Kelley, M., Large, W. G., Leboissetier, A., Long, M., Lu, J., Masina, S., Mishra, A., Navarra, A., George Nurser, A., Patara, L., Samuels, B. L., Sidorenko, D., Tsujino, H., Uotila, P., Wang, Q., and Yeager, S. G.: An assessment of Antarctic Circumpolar Current and Southern Ocean meridional overturning circulation during 1958–2007

in a suite of interannual CORE-II simulations, Ocean Model., 93, 84–120, https://doi.org/10.1016/j.ocemod.2015.07.009, 2015.

Ferreira, D., Marshall, J., Bitz, C. M., Solomon, S., and Plumb, A.: Antarctic Ocean and Sea Ice Response to Ozone Depletion: A Two-Time-Scale Problem, J. Climate, 28, 1206–1226, https://doi.org/10.1175/JCLI-D-14-00313.1, 2015.

Fichefet, T. and Maqueda, M. A. M.: Sensitivity of a global sea ice model to the treatment of ice thermodynamics and dynamics, J. Geophys. Res.-Oceans, 102, 12609–12646, https://doi.org/10.1029/97JC00480, 1997.

Fyfe, J. C. and Saenko, O. A.: Simulated changes in the extratropical Southern Hemisphere winds and currents, Geophys. Res. Lett., 33, L06701, https://doi.org/10.1029/2005GL025332, 2006.

Gent, P. R. and Mcwilliams, J. C.: Isopycnal Mixing in Ocean Circulation Models, J. Phys. Oceanogr., 20, 150–155, https://doi.org/10.1175/1520-0485(1990)020<0150:IMIOCM>2.0.CO;2, 1990.

Gerber, E. P. and Son, S.-W.: Quantifying the Summertime Response of the Austral Jet Stream and Hadley Cell to Stratospheric Ozone and Greenhouse Gases, J. Climate, 27, 5538–5559, https://doi.org/10.1175/JCLI-D-13-00539.1, 2014.

Gillett, N. P. and Thompson, D. W. J.: Simulation of Recent Southern Hemisphere Climate Change, Science, 302, 273–275, https://doi.org/10.1126/science.1087440, 2003.

Gong, D. and Wang, S.: Definition of Antarctic Oscillation index, Geophys. Res. Lett., 26, 459–462, https://doi.org/10.1029/1999GL900003, 1999.

Gordon, A. L., Weiss, R. F., Smethie Jr., W. M., and Warner, M. J.: Thermocline and intermediate water communication between the south Atlantic and Indian oceans, J. Geophys. Res.-Oceans, 97, 7223–7240, https://doi.org/10.1029/92JC00485, 1992.

Grytsai, A. V., Evtushevsky, O. M., Agapitov, O. V., Klekociuk, A. R., and Milinevsky, G. P.: Structure and long-term change in the zonal asymmetry in Antarctic total ozone during spring, Ann. Geophys., 25, 361–374, https://doi.org/10.5194/angeo-25-361-2007, 2007.

Haase, S., Fricke, J., Kruschke, T., Wahl, S., and Matthes, K.: Sensitivity of the southern hemisphere tropospheric jet response to Antarctic ozone depletion: prescribed versus interactive chemistry, Atmos. Chem. Phys., 20, 14043–14061, https://doi.org/10.5194/acp-20-14043-2020, 2020.

Haigh, J. D. and Pyle, J. A.: Ozone perturbation experiments in a two-dimensional circulation model, Q. J. Roy. Meteorol. Soc., 108, 551–574, https://doi.org/10.1002/qj.49710845705, 1982.

Hegglin, M., Kinnison, D., Lamarque, J.-F., and Plummer, D.: CCMI ozone in support of CMIP6 – version 1.0, ESGF, https://doi.org/10.22033/ESGF/input4MIPs.1115, 2016.

Hogg, A. M., Meredith, M. P., Chambers, D. P., Abrahamsen, E. P., Hughes, C. W., and Morrison, A. K.: Recent trends in the Southern Ocean eddy field, J. Geophys. Res.-Oceans, 120, 257–267, https://doi.org/10.1002/2014JC010470, 2015.

Iglesias-Suarez, F., Young, P. J., and Wild, O.: Stratospheric ozone change and related climate impacts over 1850–2100 as modelled by the ACCMIP ensemble, Atmos.Chem. Phys., 16, 343–363, https://doi.org/10.5194/acp-16-343-2016, 2016.

Ivanciu, I.: FOCI model output used in the study by Ivanciu et al. – Twenty-first century Southern Hemisphere impacts of ozone recovery and climate change from the stratosphere to the ocean, Zenodo [data set], https://doi.org/10.5281/zenodo.5013716, 2021.

Ivanciu, I., Matthes, K., Wahl, S., Harlaß, J., and Biastoch, A.: Effects of prescribed CMIP6 ozone on simulating the Southern Hemisphere atmospheric circulation response to ozone depletion, Atmos. Chem. Phys., 21, 5777–5806, https://doi.org/10.5194/acp-21-5777-2021, 2021.

Jonsson, A. I., de Grandpré, J., Fomichev, V. I., McConnell, J. C., and Beagley, S. R.: Doubled CO_2-induced cooling in the middle atmosphere: Photochemical analysis of the ozone radiative feedback, J. Geophys. Res.-Atmos., 109, D24103, https://doi.org/10.1029/2004JD005093, 2004.

Kang, S. M., Polvani, L. M., Fyfe, J. C., and Sigmond, M.: Impact of Polar Ozone Depletion on Subtropical Precipitation, Science, 332, 951–954, https://doi.org/10.1126/science.1202131, 2011.

Karpechko, A. Y., Gillett, N. P., Gray, L. J., and Dall'Amico, M.: Influence of ozone recovery and greenhouse gas increases on Southern Hemisphere circulation, J. Geophys. Res.-Atmos., 115, D22117, https://doi.org/10.1029/2010JD014423, 2010.

Keeble, J., Braesicke, P., Abraham, N. L., Roscoe, H. K., and Pyle, J. A.: The impact of polar stratospheric ozone loss on Southern Hemisphere stratospheric circulation and climate, Atmos. Chem. Phys., 14, 13705–13717, https://doi.org/10.5194/acp-14-13705-2014, 2014.

Kinnison, D. E., Brasseur, G. P., Walters, S., Garcia, R. R., Marsh, D. R., Sassi, F., Harvey, V. L., Randall, C. E., Emmons, L., Lamarque, J. F., Hess, P., Orlando, J. J., Tie, X. X., Randel, W., Pan, L. L., Gettelman, A., Granier, C., Diehl, T., Niemeier, U., and Simmons, A. J.: Sensitivity of chemical tracers to meteorological parameters in the MOZART-3 chemical transport model, J. Geophys. Res.-Atmos., 112, D20302, https://doi.org/10.1029/2006JD007879, 2007.

Kushner, P. J., Held, I. M., and Delworth, T. L.: Southern Hemisphere Atmospheric Circulation Response to Global Warming, J. Climate, 14, 2238–2249, https://doi.org/10.1175/1520-0442(2001)014<0001:SHACRT>2.0.CO;2, 2001.

Langematz, U., Kunze, M., Krüger, K., Labitzke, K., and Roff, G. L.: Thermal and dynamical changes of the stratosphere since 1979 and their link to ozone and CO_2 changes, J. Geophys. Res.-Atmos., 108, ACL 9-1–ACL 9-13, https://doi.org/10.1029/2002JD002069, 2003.

Le Bars, D., Durgadoo, J. V., Dijkstra, H. A., Biastoch, A., and De Ruijter, W. P. M.: An observed 20-year time series of Agulhas leakage, Ocean Sci., 10, 601–609, https://doi.org/10.5194/os-10-601-2014, 2014.

Li, F., Austin, J., and Wilson, J.: The Strength of the Brewer–Dobson Circulation in a Changing Climate: Coupled Chemistry-Climate Model Simulations, J. Climate, 21, 40–57, https://doi.org/10.1175/2007JCLI1663.1, 2008.

Li, F., Newman, P. A., and Stolarski, R. S.: Relationships between the Brewer–Dobson circulation and the southern annular mode during austral summer in coupled chemistry-climate model simulations, J. Geophys. Res.-Atmos., 115, D15106, https://doi.org/10.1029/2009JD012876, 2010.

Li, F., Vikhliaev, Y. V., Newman, P. A., Pawson, S., Perlwitz, J., Waugh, D. W., and Douglass, A. R.: Impacts of Interactive Stratospheric Chemistry on Antarctic and Southern Ocean Climate Change in the Goddard Earth Observ-

ing System, Version 5 (GEOS-5), J. Climate, 29, 3199–3218, https://doi.org/10.1175/JCLI-D-15-0572.1, 2016.

Li, S., Liu, W., Lyu, K., and Zhang, X.: The effects of historical ozone changes on Southern Ocean heat uptake and storage, Clim. Dynam., 57, 2269–2285, https://doi.org/10.1007/s00382-021-05803-y, 2021.

Lin, P. and Fu, Q.: Changes in various branches of the Brewer–Dobson circulation from an ensemble of chemistry climate models, J. Geophys. Res.-Atmos., 118, 73–84, https://doi.org/10.1029/2012JD018813, 2013.

Loveday, B. R., Durgadoo, J. V., Reason, C. J. C., Biastoch, A., and Penven, P.: Decoupling of the Agulhas Leakage from the Agulhas Current, J. Phys. Oceanogr., 44, 1776–1797, https://doi.org/10.1175/JPO-D-13-093.1, 2014.

Lübbecke, J. F., Durgadoo, J. V., and Biastoch, A.: Contribution of Increased Agulhas Leakage to Tropical Atlantic Warming, J. Climate, 28, 9697–9706, https://doi.org/10.1175/JCLI-D-15-0258.1, 2015.

Madec, G. and the NEMO team: NEMO ocean engine – version 3.6, Note du Pôle de modélisation, Institut Pierre-Simon Laplace (IPSL), Zenodo [code], https://doi.org/10.5281/zenodo.3248739, 2016.

Matthes, K., Funke, B., Andersson, M. E., Barnard, L., Beer, J., Charbonneau, P., Clilverd, M. A., Dudok de Wit, T., Haberreiter, M., Hendry, A., Jackman, C. H., Kretzschmar, M., Kruschke, T., Kunze, M., Langematz, U., Marsh, D. R., Maycock, A. C., Misios, S., Rodger, C. J., Scaife, A. A., Seppälä, A., Shangguan, M., Sinnhuber, M., Tourpali, K., Usoskin, I., van de Kamp, M., Verronen, P. T., and Versick, S.: Solar forcing for CMIP6 (v3.2), Geosci. Model Dev., 10, 2247–2302, https://doi.org/10.5194/gmd-10-2247-2017, 2017.

Matthes, K., Biastoch, A., Wahl, S., Harlaß, J., Martin, T., Brücher, T., Drews, A., Ehlert, D., Getzlaff, K., Krüger, F., Rath, W., Scheinert, M., Schwarzkopf, F. U., Bayr, T., Schmidt, H., and Park, W.: The Flexible Ocean and Climate Infrastructure version 1 (FOCI1): mean state and variability, Geosci. Model Dev., 13, 2533–2568, https://doi.org/10.5194/gmd-13-2533-2020, 2020.

McLandress, C., Jonsson, A. I., Plummer, D. A., Reader, M. C., Scinocca, J. F., and Shepherd, T. G.: Separating the Dynamical Effects of Climate Change and Ozone Depletion. Part I: Southern Hemisphere Stratosphere, J. Climate, 23, 5002–5020, https://doi.org/10.1175/2010JCLI3586.1, 2010.

McLandress, C., Shepherd, T. G., Scinocca, J. F., Plummer, D. A., Sigmond, M., Jonsson, A. I., and Reader, M. C.: Separating the Dynamical Effects of Climate Change and Ozone Depletion. Part II: Southern Hemisphere Troposphere, J. Climate, 24, 1850–1868, https://doi.org/10.1175/2010JCLI3958.1, 2011.

Meijers, A. J. S., Shuckburgh, E., Bruneau, N., Sallee, J.-B., Bracegirdle, T. J., and Wang, Z.: Representation of the Antarctic Circumpolar Current in the CMIP5 climate models and future changes under warming scenarios, J. Geophys. Res.-Oceans, 117, C12008, https://doi.org/10.1029/2012JC008412, 2012.

Meinshausen, M., Nicholls, Z. R. J., Lewis, J., Gidden, M. J., Vogel, E., Freund, M., Beyerle, U., Gessner, C., Nauels, A., Bauer, N., Canadell, J. G., Daniel, J. S., John, A., Krummel, P. B., Luderer, G., Meinshausen, N., Montzka, S. A., Rayner, P. J., Reimann, S., Smith, S. J., van den Berg, M., Velders, G. J. M., Vollmer, M. K., and Wang, R. H. J.: The shared socioeconomic pathway (SSP) greenhouse gas concentrations and their extensions to 2500, Geosci. Model Dev., 13, 3571–3605, https://doi.org/10.5194/gmd-13-3571-2020, 2020.

Min, S.-K. and Son, S.-W.: Multimodel attribution of the Southern Hemisphere Hadley cell widening: Major role of ozone depletion, J. Geophys. Res.-Atmos., 118, 3007–3015, https://doi.org/10.1002/jgrd.50232, 2013.

Morgenstern, O., Zeng, G., Dean, S. M., Joshi, M., Abraham, N. L., and Osprey, A.: Direct and ozone-mediated forcing of the Southern Annular Mode by greenhouse gases, Geophys. Res. Lett., 41, 9050–9057, https://doi.org/10.1002/2014GL062140, 2014.

Morgenstern, O., Stone, K. A., Schofield, R., Akiyoshi, H., Yamashita, Y., Kinnison, D. E., Garcia, R. R., Sudo, K., Plummer, D. A., Scinocca, J., Oman, L. D., Manyin, M. E., Zeng, G., Rozanov, E., Stenke, A., Revell, L. E., Pitari, G., Mancini, E., Di Genova, G., Visioni, D., Dhomse, S. S., and Chipperfield, M. P.: Ozone sensitivity to varying greenhouse gases and ozone-depleting substances in CCMI-1 simulations, Atmos. Chem. Phys., 18, 1091–1114, https://doi.org/10.5194/acp-18-1091-2018, 2018.

Morrison, A. K. and Hogg, A. M.: On the Relationship between Southern Ocean Overturning and ACC Transport, J. Phys. Oceanogr., 43, 140–148, https://doi.org/10.1175/JPO-D-12-057.1, 2013.

Neely, R. R., Marsh, D. R., Smith, K. L., Davis, S. M., and Polvani, L. M.: Biases in southern hemisphere climate trends induced by coarsely specifying the temporal resolution of stratospheric ozone, Geophys. Res. Lett., 41, 8602–8610, https://doi.org/10.1002/2014GL061627, 2014.

Oberländer, S., Langematz, U., and Meul, S.: Unraveling impact factors for future changes in the Brewer-Dobson circulation, J. Geophys. Res.-Atmos., 118, 10296–10312, https://doi.org/10.1002/jgrd.50775, 2013.

Oberländer-Hayn, S., Meul, S., Langematz, U., Abalichin, J., and Haenel, F.: A chemistry-climate model study of past changes in the Brewer–Dobson circulation, J. Geophys. Res.-Atmos., 120, 6742–6757, https://doi.org/10.1002/2014JD022843, 2015.

Oke, P. R. and England, M. H.: Oceanic Response to Changes in the Latitude of the Southern Hemisphere Subpolar Westerly Winds, J. Climate, 17, 1040–1054, https://doi.org/10.1175/1520-0442(2004)017<1040:ORTCIT>2.0.CO;2, 2004.

Oman, L., Waugh, D. W., Pawson, S., Stolarski, R. S., and Newman, P. A.: On the influence of anthropogenic forcings on changes in the stratospheric mean age, J. Geophys. Res.-Atmos., 114, D03105, https://doi.org/10.1029/2008JD010378, 2009.

Patara, L., Böning, C. W., and Biastoch, A.: Variability and trends in Southern Ocean eddy activity in $1/12^\circ$ ocean model simulations, Geophys. Res. Lett., 43, 4517–4523, https://doi.org/10.1002/2016GL069026, 2016.

Perlwitz, J., Pawson, S., Fogt, R. L., Nielsen, J. E., and Neff, W. D.: Impact of stratospheric ozone hole recovery on Antarctic climate, Geophys. Res. Lett., 35, L08714, https://doi.org/10.1029/2008GL033317, 2008.

Plumb, R. A.: On the Three-Dimensional Propagation of Stationary Waves, J. Atmos. Sci., 42, 217–229, https://doi.org/10.1175/1520-0469(1985)042<0217:OTTDPO>2.0.CO;2, 1985.

Polvani, L. M., Previdi, M., and Deser, C.: Large cancellation, due to ozone recovery, of future Southern Hemisphere atmo-

spheric circulation trends, Geophys. Res. Lett., 38, L04707, https://doi.org/10.1029/2011GL046712, 2011a.

Polvani, L. M., Waugh, D. W., Correa, G. J. P., and Son, S.-W.: Stratospheric Ozone Depletion: The Main Driver of Twentieth-Century Atmospheric Circulation Changes in the Southern Hemisphere, J. Climate, 24, 795–812, https://doi.org/10.1175/2010JCLI3772.1, 2011b.

Polvani, L. M., Abalos, M., Garcia, R., Kinnison, D., and Randel, W. J.: Significant Weakening of Brewer-Dobson Circulation Trends Over the 21st Century as a Consequence of the Montreal Protocol, Geophys. Res. Lett., 45, 401–409, https://doi.org/10.1002/2017GL075345, 2018.

Polvani, L. M., Wang, L., Abalos, M., Butchart, N., Chipperfield, M. P., Dameris, M., Deushi, M., Dhomse, S. S., Jöckel, P., Kinnison, D., Michou, M., Morgenstern, O., Oman, L. D., Plummer, D. A., and Stone, K. A.: Large Impacts, Past and Future, of Ozone-Depleting Substances on Brewer-Dobson Circulation Trends: A Multimodel Assessment, J. Geophys. Res.-Atmos., 124, 6669–6680, https://doi.org/10.1029/2018JD029516, 2019.

Portmann, R. W. and Solomon, S.: Indirect radiative forcing of the ozone layer during the 21st century, Geophys. Res. Lett., 34, L02813, https://doi.org/10.1029/2006GL028252, 2007.

Previdi, M. and Polvani, L. M.: Climate system response to stratospheric ozone depletion and recovery, Q. J. Roy. Meteorol. Soc., 140, 2401–2419, https://doi.org/10.1002/qj.2330, 2014.

Reick, C. H., Raddatz, T., Brovkin, V., and Gayler, V.: Representation of natural and anthropogenic land cover change in MPI-ESM, J. Adv. Model. Earth Syst., 5, 459–482, https://doi.org/10.1002/jame.20022, 2013.

Revell, L. E., Bodeker, G. E., Huck, P. E., Williamson, B. E., and Rozanov, E.: The sensitivity of stratospheric ozone changes through the 21st century to N_2O and CH_4, Atmos. Chem. Phys., 12, 11309–11317, https://doi.org/10.5194/acp-12-11309-2012, 2012.

Richardson, P. L.: Agulhas leakage into the Atlantic estimated with subsurface floats and surface drifters, Deep-Sea Res. Pt. I, 54, 1361–1389, https://doi.org/10.1016/j.dsr.2007.04.010, 2007.

Rosenfield, J. E., Douglass, A. R., and Considine, D. B.: The impact of increasing carbon dioxide on ozone recovery, J. Geophys. Res.-Atmos., 107, ACH 7-1–ACH 7-9, https://doi.org/10.1029/2001JD000824, 2002.

Rouault, M., Penven, P., and Pohl, B.: Warming in the Agulhas Current system since the 1980's, Geophys. Res. Lett., 36, L12602, https://doi.org/10.1029/2009GL037987, 2009.

Rühs, S., Durgadoo, J. V., Behrens, E., and Biastoch, A.: Advective timescales and pathways of Agulhas leakage, Geophys. Res. Lett., 40, 3997–4000, https://doi.org/10.1002/grl.50782, 2013.

Rühs, S., Schwarzkopf, F. U., Speich, S., and Biastoch, A.: Cold vs. warm water route – sources for the upper limb of the Atlantic Meridional Overturning Circulation revisited in a high-resolution ocean model, Ocean Sci., 15, 489–512, https://doi.org/10.5194/os-15-489-2019, 2019.

Sassi, F., Boville, B. A., Kinnison, D., and Garcia, R. R.: The effects of interactive ozone chemistry on simulations of the middle atmosphere, Geophys. Res. Lett., 32, L07811, https://doi.org/10.1029/2004GL022131, 2005.

Schwarzkopf, F. U., Biastoch, A., Böning, C. W., Chanut, J., Durgadoo, J. V., Getzlaff, K., Harlaß, J., Rieck, J. K., Roth, C., Scheinert, M. M., and Schubert, R.: The INALT family – a set of high-resolution nests for the Agulhas Current system within global NEMO ocean/sea-ice configurations, Geosci. Model Dev., 12, 3329–3355, https://doi.org/10.5194/gmd-12-3329-2019, 2019.

Seviour, W. J. M., Gnanadesikan, A., and Waugh, D. W.: The Transient Response of the Southern Ocean to Stratospheric Ozone Depletion, J. Climate, 29, 7383–7396, https://doi.org/10.1175/JCLI-D-16-0198.1, 2016.

Seviour, W. J. M., Codron, F., Doddridge, E. W., Ferreira, D., Gnanadesikan, A., Kelley, M., Kostov, Y., Marshall, J., Polvani, L. M., Thomas, J. L., and Waugh, D. W.: The Southern Ocean Sea Surface Temperature Response to Ozone Depletion: A Multimodel Comparison, J. Climate, 32, 5107–5121, https://doi.org/10.1175/JCLI-D-19-0109.1, 2019.

Shepherd, T. G. and McLandress, C.: A Robust Mechanism for Strengthening of the Brewer–Dobson Circulation in Response to Climate Change: Critical-Layer Control of Subtropical Wave Breaking, J. Atmos. Sci., 68, 784–797, https://doi.org/10.1175/2010JAS3608.1, 2011.

Shindell, D. T. and Schmidt, G. A.: Southern Hemisphere climate response to ozone changes and greenhouse gas increases, Geophys. Res. Lett., 31, L18209, https://doi.org/10.1029/2004GL020724, 2004.

Sigmond, M., Reader, M. C., Fyfe, J. C., and Gillett, N. P.: Drivers of past and future Southern Ocean change: Stratospheric ozone versus greenhouse gas impacts, Geophys. Res. Lett., 38, L12601, https://doi.org/10.1029/2011GL047120, 2011.

Solomon, A., Polvani, L. M., Smith, K. L., and Abernathey, R. P.: The impact of ozone depleting substances on the circulation, temperature, and salinity of the Southern Ocean: An attribution study with CESM1(WACCM), Geophys. Res. Lett., 42, 5547–5555, https://doi.org/10.1002/2015GL064744, 2015.

Solomon, S., Kinnison, D., Bandoro, J., and Garcia, R.: Simulation of polar ozone depletion: An update, J. Geophys. Res.-Atmos., 120, 7958–7974, https://doi.org/10.1002/2015JD023365, 2015.

Solomon, S., Ivy, D. J., Kinnison, D., Mills, M. J., Neely, R. R., and Schmidt, A.: Emergence of healing in the Antarctic ozone layer, Science, 353, 269–274, https://doi.org/10.1126/science.aae0061, 2016.

Solomon, S., Ivy, D., Gupta, M., Bandoro, J., Santer, B., Fu, Q., Lin, P., Garcia, R. R., Kinnison, D., and Mills, M.: Mirrored changes in Antarctic ozone and stratospheric temperature in the late 20th versus early 21st centuries, J. Geophys. Res.-Atmos., 122, 8940–8950, https://doi.org/10.1002/2017JD026719, 2017.

Son, S.-W., Polvani, L. M., Waugh, D. W., Akiyoshi, H., Garcia, R., Kinnison, D., Pawson, S., Rozanov, E., Shepherd, T. G., and Shibata, K.: The Impact of Stratospheric Ozone Recovery on the Southern Hemisphere Westerly Jet, Science, 320, 1486–1489, https://doi.org/10.1126/science.1155939, 2008.

Son, S.-W., Tandon, N. F., Polvani, L. M., and Waugh, D. W.: Ozone hole and Southern Hemisphere climate change, Geophys. Res. Lett., 36, L15705, https://doi.org/10.1029/2009GL038671, 2009.

Son, S.-W., Gerber, E. P., Perlwitz, J., Polvani, L. M., Gillett, N. P., Seo, K.-H., Eyring, V., Shepherd, T. G., Waugh, D., Akiyoshi, H., Austin, J., Baumgaertner, A., Bekki, S., Braesicke, P., Brühl, C., Butchart, N., Chipperfield, M. P., Cugnet, D., Dameris, M., Dhomse, S., Frith, S., Garny, H., Garcia, R., Hardiman, S. C., Jöckel, P., Lamarque, J. F., Mancini, E., Marchand, M., Michou, M., Nakamura, T., Morgenstern, O., Pitari, G., Plummer, D. A.,

Pyle, J., Rozanov, E., Scinocca, J. F., Shibata, K., Smale, D., Teyssèdre, H., Tian, W., and Yamashita, Y.: Impact of stratospheric ozone on Southern Hemisphere circulation change: A multimodel assessment, J. Geophys. Res.-Atmos., 115, D00M07, https://doi.org/10.1029/2010JD014271, 2010.

Stevens, B., Giorgetta, M., Esch, M., Mauritsen, T., Crueger, T., Rast, S., Salzmann, M., Schmidt, H., Bader, J., Block, K., Brokopf, R., Fast, I., Kinne, S., Kornblueh, L., Lohmann, U., Pincus, R., Reichler, T., and Roeckner, E.: Atmospheric component of the MPI-M Earth System Model: ECHAM6, J. Adv. Model. Earth Syst., 5, 146–172, https://doi.org/10.1002/jame.20015, 2013.

Storch, H. V. and Zwiers, F. W.: Statistical Analysis in Climate Research, Cambridge University Press, Cambridge, https://doi.org/10.1017/CBO9780511612336, 1999.

Thompson, D. W. J. and Solomon, S.: Interpretation of Recent Southern Hemisphere Climate Change, Science, 296, 895–899, https://doi.org/10.1126/science.1069270, 2002.

Thompson, D. W. J., Solomon, S., Kushner, P. J., England, M. H., Grise, K. M., and Karoly, D. J.: Signatures of the Antarctic ozone hole in Southern Hemisphere surface climate change, Nat. Geosci., 4, 741–749, https://doi.org/10.1038/ngeo1296, 2011.

Treguier, A. M., Held, I. M., and Larichev, V. D.: Parameterization of Quasigeostrophic Eddies in Primitive Equation Ocean Models, J. Phys. Oceanogr., 27, 567–580, https://doi.org/10.1175/1520-0485(1997)027<0567:POQEIP>2.0.CO;2, 1997.

van Sebille, E., Biastoch, A., van Leeuwen, P. J., and de Ruijter, W. P. M.: A weaker Agulhas Current leads to more Agulhas leakage, Geophys. Res. Lett., 36, L03601, https://doi.org/10.1029/2008GL036614, 2009.

Viebahn, J. and Eden, C.: Towards the impact of eddies on the response of the Southern Ocean to climate change, Ocean Model., 34, 150–165, https://doi.org/10.1016/j.ocemod.2010.05.005, 2010.

Waugh, D. W., Randel, W. J., Pawson, S., Newman, P. A., and Nash, E. R.: Persistence of the lower stratospheric polar vortices, J. Geophys. Res.-Atmos., 104, 27191–27201, https://doi.org/10.1029/1999JD900795, 1999.

Waugh, D. W., Oman, L., Kawa, S. R., Stolarski, R. S., Pawson, S., Douglass, A. R., Newman, P. A., and Nielsen, J. E.: Impacts of climate change on stratospheric ozone recovery, Geophys. Res. Lett., 36, L03805, https://doi.org/10.1029/2008GL036223, 2009a.

Waugh, D. W., Oman, L., Newman, P. A., Stolarski, R. S., Pawson, S., Nielsen, J. E., and Perlwitz, J.: Effect of zonal asymmetries in stratospheric ozone on simulated Southern Hemisphere climate trends, Geophys. Res. Lett., 36, L18701, https://doi.org/10.1029/2009GL040419, 2009b.

Waugh, D. W., Primeau, F., DeVries, T., and Holzer, M.: Recent Changes in the Ventilation of the Southern Oceans, Science, 339, 568–570, https://doi.org/10.1126/science.1225411, 2013.

Waugh, D. W., Garfinkel, C. I., and Polvani, L. M.: Drivers of the Recent Tropical Expansion in the Southern Hemisphere: Changing SSTs or Ozone Depletion?, J. Climate, 28, 6581–6586, https://doi.org/10.1175/JCLI-D-15-0138.1, 2015.

Weijer, W. and van Sebille, E.: Impact of Agulhas Leakage on the Atlantic Overturning Circulation in the CCSM4, J. Climate, 27, 101–110, https://doi.org/10.1175/JCLI-D-12-00714.1, 2014.

Weijer, W., De Ruijter, W. P., Sterl, A., and Drijfhout, S. S.: Response of the Atlantic overturning circulation to South Atlantic sources of buoyancy, Global Planet. Change, 34, 293–311, https://doi.org/10.1016/S0921-8181(02)00121-2, 2002.

World Meteorological Organization: Scientific Assessment of Ozone Depletion: 2018, Global Ozone Research and Monitoring Project – Report No. 58, WMO, UNEP, Geneva, Switzerland, 2018.

Yin, J. H.: A consistent poleward shift of the storm tracks in simulations of 21st century climate, Geophys. Res. Lett., 32, L18701, https://doi.org/10.1029/2005GL023684, 2005.

Supplement of Weather Clim. Dynam., 3, 139–171, 2022
https://doi.org/10.5194/wcd-3-139-2022-supplement

Supplement of

Twenty-first-century Southern Hemisphere impacts of ozone recovery and climate change from the stratosphere to the ocean

Ioana Ivanciu et al.

Correspondence to: Ioana Ivanciu (iivanciu@geomar.de)

1 Plumb flux calculation

We use the three-dimensional flux of wave activity defined by Plumb (1985) to study the spatial patterns of planetary wave propagation. The Plumb flux is defined as follows:

$$\boldsymbol{F}_s = \frac{p\,cos\phi}{p_o} \times \left\{ \begin{array}{l} \frac{1}{2a^2\,cos^2\phi}\left[\left(\frac{\partial\psi'}{\partial\lambda}\right)^2 - \psi'\frac{\partial^2\psi'}{\partial\lambda^2}\right] \\ \frac{1}{2a^2\,cos\phi}\left(\frac{\partial\psi'}{\partial\lambda}\frac{\partial\psi'}{\partial\phi} - \psi'\frac{\partial^2\psi'}{\partial\lambda\partial\phi}\right) \\ \frac{2\Omega^2\,sin^2\phi}{N^2 a\,cos\phi}\left(\frac{\partial\psi'}{\partial\lambda}\frac{\partial\psi'}{\partial z} - \psi'\frac{\partial^2\psi'}{\partial\lambda\partial z}\right) \end{array} \right\} \tag{1}$$

where ψ is the quasi-geostrophic streamfunction, N^2 is the buoyancy frequency, a is the radius of the Earth, Ω is the rotation rate of the Earth, ϕ and λ are the latitude and the longitude respectively, p is the pressure, with p_o taken as 1000 hPa, and the primes denote departures from the zonal mean.

2 Supplementary Figures

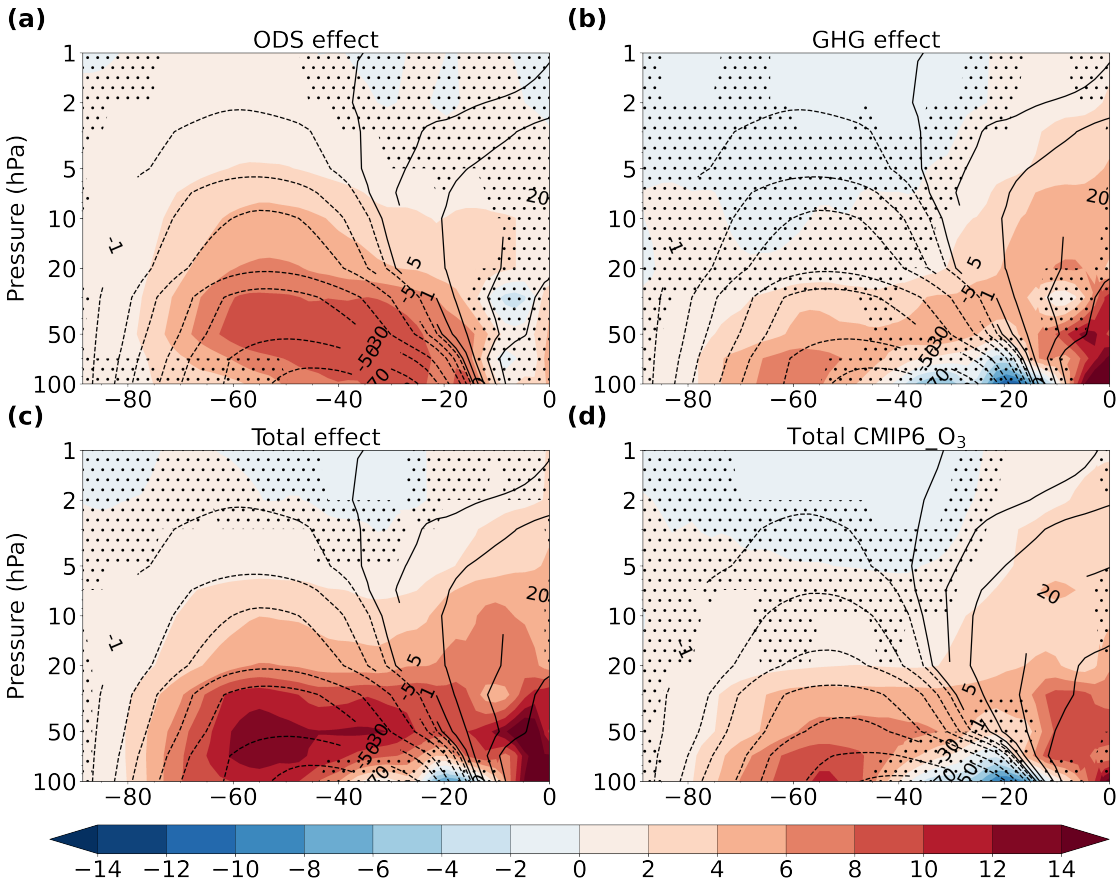

Figure S1. Changes in the mean residual streamfunction (kg m^{-1} s^{-1}) during November for each latitude and pressure level (color shading): effect of ozone recovery (a), effect of GHGs (b), total effect in INTERACT_O_3 (c) and total effect CMIP6_O_3 (d). The contours depict the current day (2011-2030) November climatology from INTERACT_O_3 in a-c and from CMIP6_O_3 in d. The stippling masks regions where the changes are not significant at the 95% confidence interval based on a two-tailed t-test.

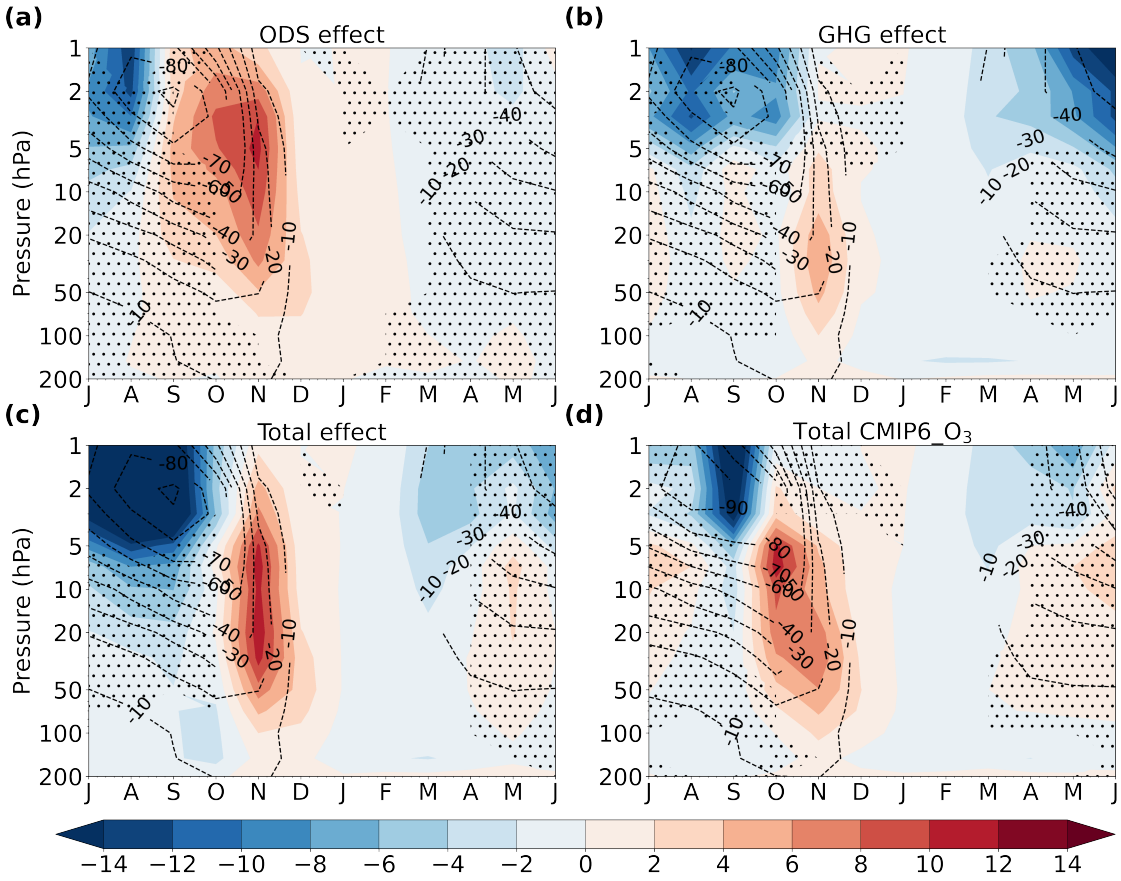

Figure S2. Changes in the eddy heat flux averaged over 45°S-80°S (kg m s^{-2}) for each month and pressure level (color shading): effect of ozone recovery (a), effect of GHGs (b), total effect in INTERACT_O_3 (c) and total effect in CMIP6_O_3 (d). The contours depict the current day (2011-2030) climatology from INTERACT_O_3 in a-c and from CMIP6_O_3 in d. The stippling masks regions where the changes are not significant at the 95% confidence interval based on a two-tailed t-test.

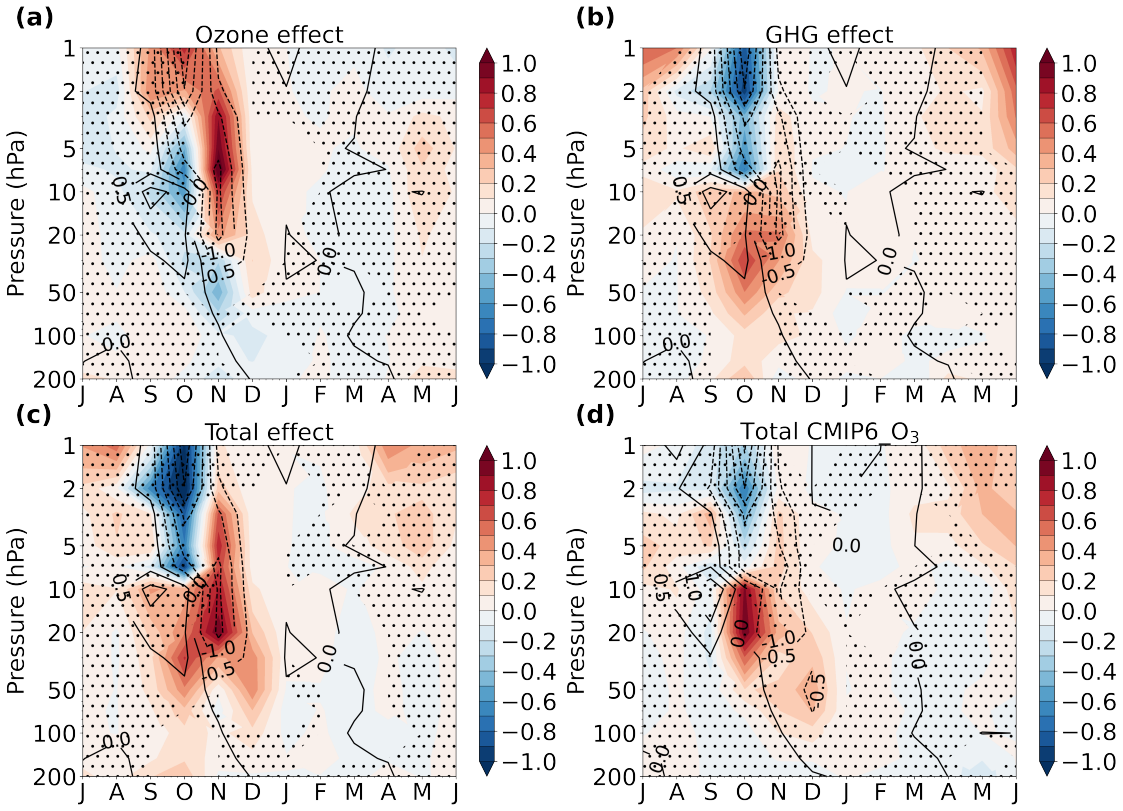

Figure S3. Changes in the divergence of the EP flux associated with the PW1 averaged over 45°S-80°S ($\mathrm{m\ s^{-1}\ day^{-1}}$) for each month and pressure level (color shading): effect of ozone recovery (a), effect of GHGs (b), total effect in INTERACT_O_3 (c) and total effect in CMIP6_O_3 (d). The contours depict the current day (2011-2030) climatology from INTERACT_O_3 in a-c and from CMIP6_O_3 in d. The stippling masks regions where the changes are not significant at the 95% confidence interval based on a two-tailed t-test.

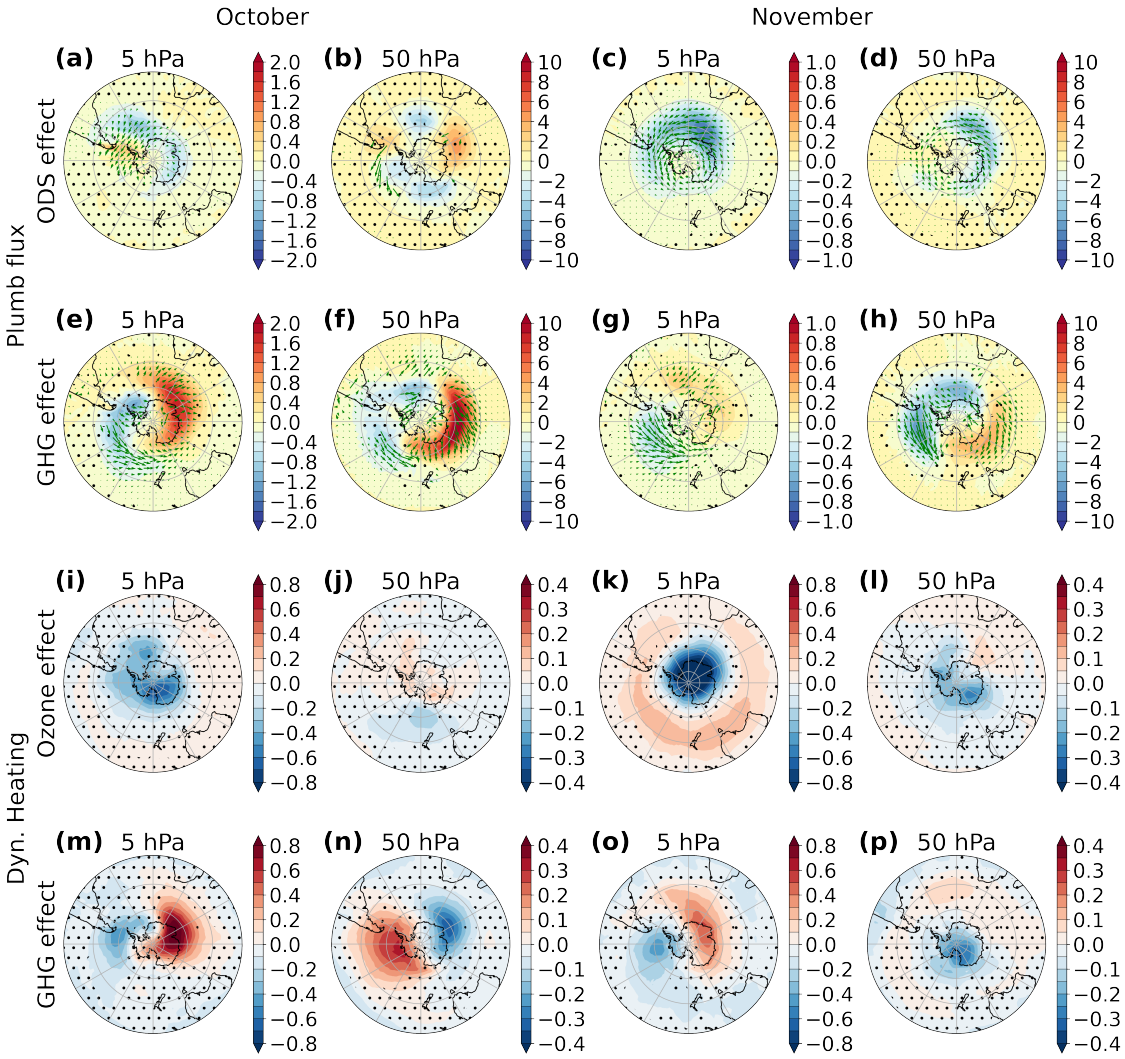

Figure S4. Changes in the flux of wave activity (a-h) and in the dynamical heating rate (i-p; K day^{-1}) at 50 hPa (b, d, f, h, j, l, n and p) and 5 hPa (a, c, e, g, i, k, m and o) during October (a, b, e, f, i, j, m and n) and November (c, d, g, h, k, l, o and p) due to ozone recovery (a-d and i-l) and increasing GHGs (e-h and m-p). The color shading in a-h shows the change in the vertical (10^{-3} m^2 s^{-2}) and the vectors show the change in the horizontal (m^2 s^{-2}) component of the flux. The stippling masks regions where the changes are not significant at the 95% confidence interval based on a two-tailed t-test.

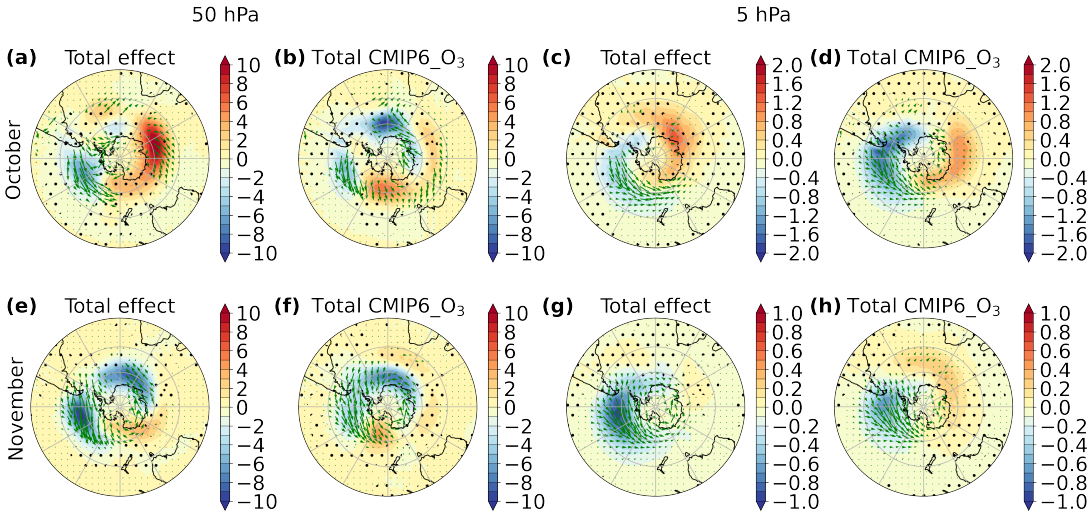

Figure S5. Changes in the flux of wave activity at 50 hPa (a, b, e and f) and at 5 hPa (c, d, g and h) during October (a, b, c and d) and November (e, f, g and h) due to ozone recovery and increasing GHGs combined, in INTERACT_O_3 (a, c, e and g) and CMIP6_O_3 (b, d, f and h). The color shading shows the change in the vertical (10^{-3} m^2 s^{-2}) and the vectors show the change in the horizontal (m^2 s^{-2}) component of the flux. The stippling masks regions where the changes are not significant at the 95% confidence interval based on a two-tailed t-test.

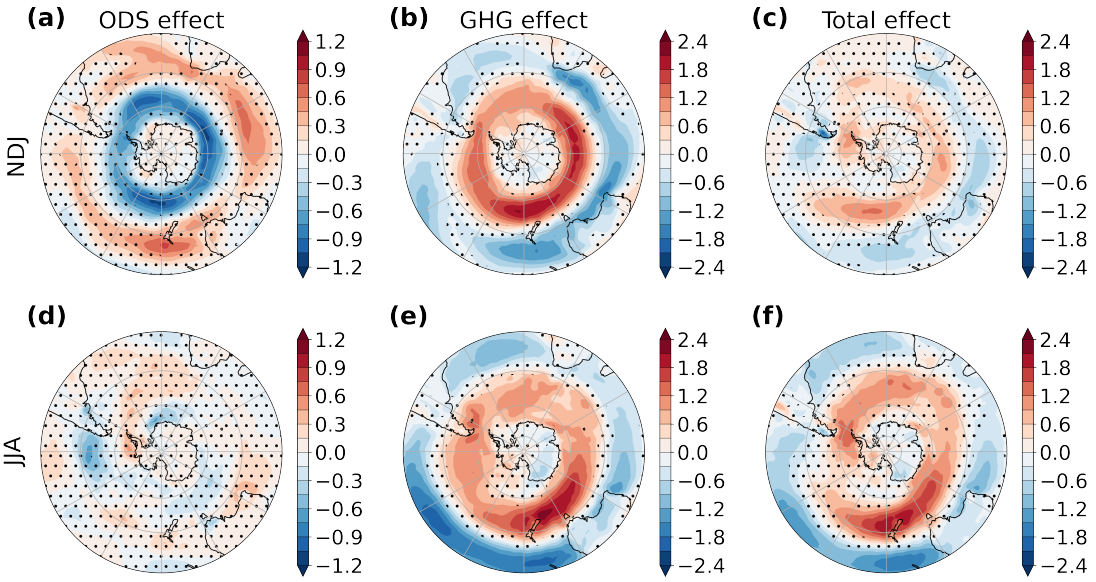

Figure S6. Changes in the surface zonal wind ($\mathrm{m\ s^{-1}}$) during November-January (a-c) and June-August (d-f) due to ozone recovery (a and d), GHGs (b and e) and their combined effect in INTERACT_O_3 (c and f). The stippling masks regions where the changes are not significant at the 95% confidence interval based on a two-tailed t-test.

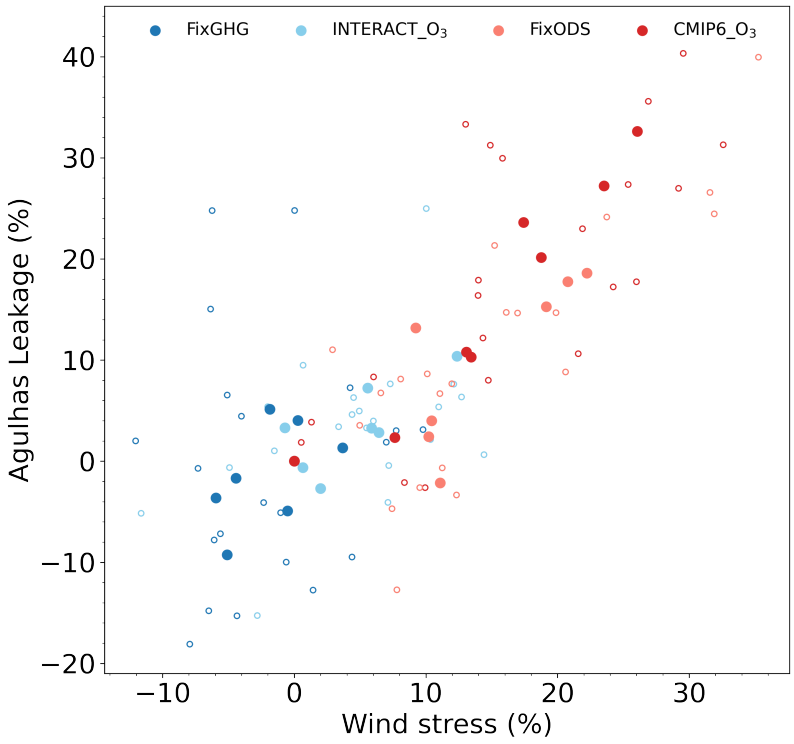

Figure S7. Decadal changes in Agulhas leakage versus decadal changes in wind stress over 45°S and 65°S and 30°E and 120°E (% change relative to 2014-2023). Each circle represents the change of each separate decade starting with 2014-2023 and ending with 2083-2094 relative to 2014-2023 in FixGHG (dark blue), INTERACT_O_3 (light blue), FixODS (light red) and CMIP6_O_3 (dark red). Filled circles denote ensemble means and small, hollow circles denote individual members.

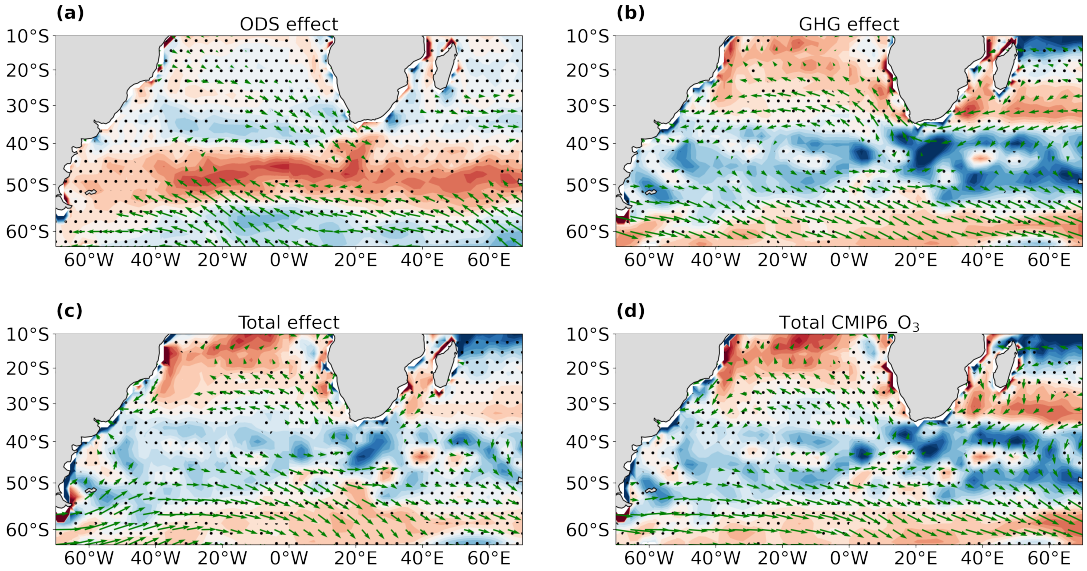

Figure S8. Changes in surface winds (arrows, in $\mathrm{m\ s^{-1}}$) and Ekman pumping (color shading, in $\mathrm{cm\ day^{-1}}$, positive upward) due to ozone recovery during NDJ (a), GHGs (b) and their combined effect in INTERACT_O_3 (c) and CMIP6_O_3 (d) during the entire year. Only significant (95% confidence interval) wind changes are shown and the Ekman pumping changes that are not significant are stippled.

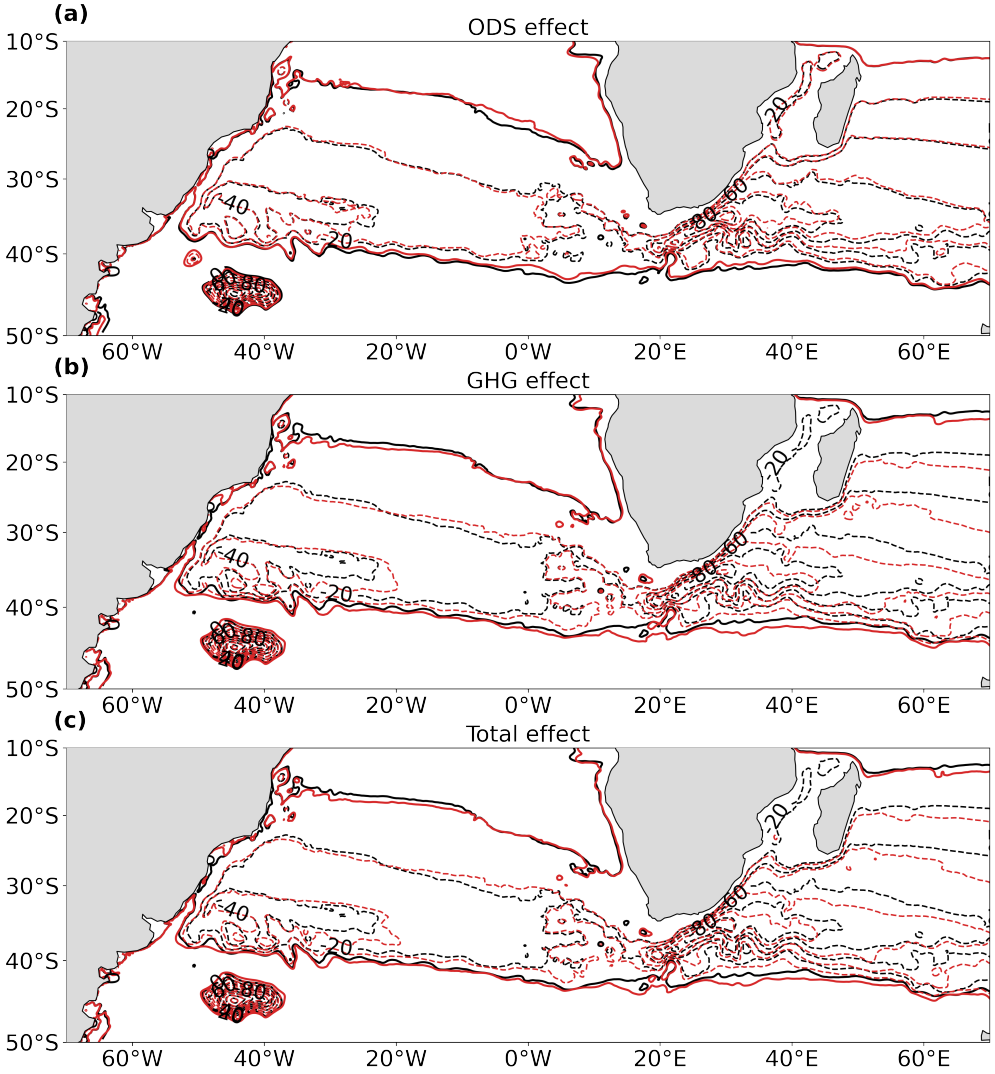

Figure S9. Changes in the subtropical gyre: the barotropic streamfunction for the current day is depicted by the black contours in all panels, while the red contours depict the streamfunction at the end of the twenty-first century in the ensemble with only ozone recovery (a), only increasing GHGs (b) and in the ensemble with both drivers (c). Only negative contours are shown and the zero contours marking the extent of the gyre is depicted by the thicker lines.

Chapter 5

On the ridging of the South Atlantic Anticyclone over South Africa: the impact of Rossby wave breaking and of climate change

The focus of this chapter is the Southern African region, in particular the ridging of the South Atlantic Anticyclone over South Africa, the associated precipitation and the future changes in these events. Ridging highs are categorized for the first time based on whether they are accompanied by RWB or not and the differences in the precipitation contributed by the two types of events are reported. The role played by RWB in the ridging process is investigated and it is found to be particularly important in mediating the future changes experienced by ridging highs. A separation of the contributions from increasing GHGs and ozone recovery to these changes reveals that they are solely driven by the increase in GHGs.

Citation: Ivanciu, I., Ndarana, T., Matthes, K. and Wahl, S.: On the ridging of the South Atlantic Anticyclone over South Africa: the impact of Rossby wave breaking and of climate change, Geophysical Research Letters, in revision, 2022.

Candidate's contributions to this publication:

- She designed the experimental set-up and performed eleven of the simulations.
- She performed all of the analyses.
- She produced all the figures.
- She wrote the manuscript, from the first draft to the final version.

On the ridging of the South Atlantic Anticyclone over South Africa: the impact of Rossby wave breaking and of climate change

Ioana Ivanciu[1], Thando Ndarana[2], Katja Matthes[1]and Sebastian Wahl[1]

[1]GEOMAR Helmholtz Centre for Ocean Research Kiel, Germany
[2]Department of Geography, Geoinformatics and Meteorology, University of Pretoria, South Africa

Key Points:

- Ridging South Atlantic Anticyclones are accompanied by Rossby wave breaking aloft in 44% of the cases
- Ridging highs that are accompanied by Rossby wave breaking lead to more precipitation over South Africa than those that are not
- Ridging highs will bring more precipitation over the southern and less precipitation over the northeastern part of South Africa in the future due to climate change

Corresponding author: Ioana Ivanciu, iivanciu@geomar.de

Abstract

Ridging South Atlantic Anticyclones contribute an important amount of precipitation over South Africa. Here, we use a global coupled climate model and the ERA5 reanalysis to separate for the first time ridging highs based on whether they occur together with Rossby wave breaking (RWB) or not. We show that the former type of ridging highs are associated with more precipitation than the latter type. The mean sea level pressure anomalies caused by the two types of ridging highs are characterized by distinct patterns, leading to differences in the flow of moisture-laden air onto land. We additionally find that RWB mediates the effect of climate change on ridging highs during the twenty-first century. Consequently, ridging highs occurring without RWB exhibit little change, while those occurring with RWB contribute more precipitation over the southern and less precipitation over the northeastern South Africa in the future.

Plain Language Summary

The high pressure system located above the South Atlantic Ocean occasionally extends eastward over South Africa, leading to winds that blow onshore and carry moisture from the warm waters of the Southwest Indian Ocean to the coast. These events, termed ridging highs, bring an important contribution to precipitation over the southern and eastern parts of South Africa. Their occurrence is related to the propagation and breaking of atmospheric waves at the boundary between the troposphere and the stratosphere. This study categorizes ridging highs based on the behaviour of atmospheric waves above and shows that events that are accompanied by wave breaking result in more precipitation over South Africa. In addition, model simulations are used to investigate the impact of climate change during the twenty-first century on ridging highs and the associated precipitation. Although the model predicts that in total South Africa will experience dryer conditions in the future, ridging highs contribute to this drying trend only in the northeastern part of the country. In the southern part of South Africa, the model simulates that ridging highs will bring more precipitation in the future.

1 Introduction

Semi-arid South Africa receives most of its annual precipitation during the summer months over the eastern part of the country (Roffe et al., 2019). Winter rainfall occurs in the southwestern part of the country and the southeastern coast receives rainfall through the entire year (C. J. Engelbrecht et al., 2015; Roffe et al., 2019). These rainfall patterns are caused by mesoscale convective complexes (Blamey & Reason, 2012) and synoptic scale weather systems. The latter include the all-season cut-off low pressure systems (COLs) (Favre et al., 2013), tropical temperate troughs (TTTs) (Harrison, 1984; Hart et al., 2012) and ridging South Atlantic Anticyclones (henceforth, ridging highs). A ridging high occurs when the anticyclone extends east and wraps around the southern tip of Africa (Tyson & Preston-Whyte, 2000). In some cases the leading edge of the ridging component breaks off from the parent South Atlantic Anticyclone and amalgamates with the Indian Ocean high pressure system. In other cases the whole anticyclone propagates east and eventually becomes integrated into the Indian Ocean high (Ndarana et al., 2022).

Ridging highs are central to the moisture budget of South Africa because they are the main mechanism that facilitates the transport of moisture from the Southwest Indian Ocean (SWIO) (Dyson, 2015; Ndarana et al., 2021), and therefore critical to rainfall occurrence in the region. The warm waters of the Agulhas Current, flowing along the east coast of South Africa in the SWIO, result in high evaporation (Lee-Thorp et al., 1999; Rouault et al., 2000; Rapolaki et al., 2020) and provide an important source of moisture (Rouault et al., 2002; Singleton & Reason, 2006; Nkwinkwa Njouodo et al., 2018, 2021). Southerly and southeasterly onshore winds caused by ridging highs, advect the

moisture and lead to precipitation on land (Blamey & Reason, 2009; Rapolaki et al., 2020). As a result, ridging highs contribute 60% of the summer rainfall days in the summer rainfall region (Ndarana et al., 2021) and 46% of the annual rainfall in the all-year rainfall region (C. J. Engelbrecht et al., 2015). COLs and TTTs, which co-occur with ridging highs, provide dynamical lifting mechanisms of moist air. COLs contribute the most to the annual rainfall during spring (Favre et al., 2013) and about 16% to the all-year rainfall region (Molekwa et al., 2014; C. J. Engelbrecht et al., 2015), while TTTs contribute 30% to the summer rainfall from October to March, increasing to 40% in the middle of the season (Hart et al., 2013).

Several recent studies considered the upper level dynamics that might influence the initiation of the ridging process and found that they are associated with synoptic Rossby wave trains aloft that propagate from the Drake Passage (Ndarana et al., 2018, 2022). These Rossby waves may venture into non-linear regimes and break (McIntyre & Palmer, 1983), a process referred to as Rossby wave breaking (RWB). RWB can be viewed as a dissipating mechanism of wave packets (Wirth et al., 2018). Ndarana et al. (2018) showed that ridging highs may be associated with RWB in the upper troposphere and lower stratosphere, lasting for the entire evolution of the ridging process, and causing positive upper tropospheric potential vorticity (PV) anomalies that induce an anticyclonic circulation. These positive anomalies, in turn, extend to the surface to induce the ridging process (Ndarana et al., 2022). However, precisely what proportion of RWB events are associated with ridging highs and whether the behavior of the latter differs according to whether there is RWB aloft are still open questions. Further more, the influence of increasing concentrations of greenhouse gases (GHGs) in the twenty-first century on this relationship has not been explored yet. Thus, the questions we explore are

1. What proportion of ridging highs are accompanied by RWB?
2. Do ridging highs occurring with RWB differ from those occurring without RWB in their evolution and in their effect on precipitation?
3. Will ridging highs and their impact on precipitation change in the twenty-first century in response to climate change?

The latter question, investigated here for the first time, is of particular importance given that models predict a reduction in precipitation under climate change in the southern part of Africa (Dosio et al., 2019; Rojas et al., 2019; Almazroui et al., 2020) and considering the contribution of ridging highs to precipitation in this region.

2 Data and Methodology

We analyze ridging highs in the coupled climate model FOCI (Matthes et al., 2020) and in the ERA5 reanalysis (Hersbach et al., 2018). FOCI distinguishes itself from other global coupled climate models through its capability to combine a module for simulating the ozone chemistry in the atmosphere, MOZART3 (Kinnison et al., 2007) with an ocean nest, INALT10X (Schwarzkopf et al., 2019), that enhances the ocean resolution around southern Africa to 0.1°. Therefore, the model resolves the mesoscale features of the Agulhas System and, at the same time, simulates an ozone field consistent with the atmospheric dynamics. The increased ocean resolution is important for the latent and sensible heat fluxes over the Agulhas Current (Rouault et al., 2003) and for precipitation (Singleton & Reason, 2006).

One historical and three twenty-first century ensembles are analyzed, each comprising three members. The historical ensemble is the same as the "REF" ensemble described by Ivanciu et al. (2021), which we analyze for the 1980-2009 period and we denote PAST. The first twenty-first century ensemble, FUTURE, represents continuations of the PAST simulations into the future under the high emission scenario SSP585. The second ensemble, GHG, also follows SSP585, but ozone depleting substances are kept con-

stant at their 1991-2000 mean, such that the ozone hole does not recover and only GHGs drive changes in this ensemble. In the third ensemble, OZONE, GHGs are instead kept constant at their 1991-2000 mean, such that ozone recovery is the sole driver of changes. The three twenty-first century ensembles were used by Ivanciu et al. (2022) to extensively analyze the impacts of ozone recovery and increasing GHGs in the Southern Hemisphere. Here, we focus our analysis on the 2070-2099 period.

To validate our model results for the historical period against observations, we employ the ERA5 mean sea level pressure (MSLP), temperature, horizontal winds and geopotential on pressure levels (Hersbach et al., 2018) and the CPC Global Unified Precipitation data provided by the NOAA/OAR/ESRL PSL, Boulder, Colorado, USA, at 0.5° horizontal resolution.

Ridging highs over South Africa are identified based on MSLP using the method of (Ndarana et al., 2018). RWB events are identified following the algorithm of Ndarana and Waugh (2011), using PV between -2.5 PVU to -1.5 PVU (1 PVU = 10^6 K m^2 s^{-1} kg^{-1}) interpolated to isentropic surfaces according to Edouard et al. (1997). Then, for every ridging high, we test if it is accompanied by a RWB event by checking if RWB occurs in the domain 20°W - 40°E and in the time interval from two days prior to two days after the inception of the ridging. A detailed description of the identification algorithms for ridging highs and RWB can be found in the supporting information.

3 Results and Discussion

A connection between ridging highs over South Africa and RWB aloft was reported by Ndarana et al. (2018) in reanalysis data. We first test if this relationship is captured by our coupled climate model. Figure 1 shows the evolution of a ridging event in the model, starting one day prior to the ridging. The South Atlantic Anticyclone extends progressively over South Africa until day 2, when a high pressure system breaks off from it and advances eastward over the Indian Ocean (black contours in Fig. 1). This evolution is in good agreement with the ridging highs described by Ndarana et al. (2018). Simultaneously with the ridging, RWB occurs over the Atlantic Ocean close to the tropopause. The -2 PVU contour on the 350 K isentropic surface, depicted in red in Fig. 1, is severely deformed throughout the evolution of the ridging event, signaling that RWB is taking place. This demonstrates that FOCI is capable of simulating ridging highs accompanied by RWB. Fig. 1 also depicts how the ridging high brings onshore wind anomalies along the southern and eastern coasts of South Africa, transporting moisture on land and leading to positive precipitation anomalies that advance northward along the coast as the ridging progresses.

As Fig. 1 depicts a single ridging event, the question of how often the ridging highs are accompanied by RWB arises. Out of 1872 (1969) ridging highs identified in FOCI (ERA5) over the period 1980-2009, 43 % (44 %) occurred together with RWB aloft and 57 % (56 %) occurred without RWB. These results are remarkably robust between the model and the reanalysis and show that an important proportion of events are accompanied by RWB. There is a slight change in these percentages at the end of the twenty-first century, when 38 % and 62 % of the 1936 ridging highs identified between 2070 and 2099 occur with and without RWB, respectively. The decrease in the proportion of ridging highs with RWB is consistent with the poleward shift in RWB that accompanies the poleward shift of the midlatitude jet under climate change in FOCI (Ivanciu et al., 2022), in agreement with Barnes and Hartmann (2012).

3.1 Characterization of Ridging Highs with and without Rossby Wave Breaking

We now wish to understand the differences between ridging highs occurring with and without RWB in FOCI. To this end, we composite ridging highs with RWB and ridging highs without RWB, separately, for the PAST ensemble and we show in Fig. 2 a-d anomalies in MSLP and 200 hPa PV for days zero and one of each composite. Day zero represents the day when the South Atlantic Anticyclone first extends eastward of 25°E. Similar composites obtained for ERA5 are shown in Fig. S1 in the supporting information and they are in good agreement with the model composites.

Both categories of ridging highs are characterized by positive MSLP anomalies in the Southeastern Atlantic Ocean, negative MSLP anomalies southeast of Africa, and positive MSLP anomalies farther east, that migrate eastward as the ridging progresses. There are however important differences in the shape and extent of these anomalies. In the case of ridging highs with RWB, the positive anomalies are elongated in the zonal direction, being flanked by negative anomalies south of 50°S. The positive anomalies occurring without RWB have a much larger meridional extent, reaching not only farther south, but also deeper inland. In fact, the entire South Africa is covered by positive MSLP anomalies at day 1, in contrast to the composites with RWB, where the positive anomalies are mostly confined south of the continent and negative anomalies cover most of southern Africa. This has important consequences for the flow and precipitation over the region, as discussed below.

MSLP anomalies seem to be well connected to PV anomalies aloft (contours in Fig. 2) for ridging highs with RWB, but not as much for ridging high without RWB. Strong positive PV anomalies occur above the positive MSLP anomalies in Fig. 2 a and c, while weaker negative PV anomalies are found south of 40°S in the region of the negative MSLP anomalies. The dominant PV anomalies for the case without RWB are instead negative. There are no positive PV anomalies accompanying the positive MSLP anomalies between 0°and 40°E, suggesting that there is no clear connection between the ridging and the PV anomalies above.

To get a better understanding of the vertical coupling between PV and MSLP anomalies, Fig. 3 shows the vertical profile of PV and geopotential height anomalies for the composites with and without RWB. The vertical profiles of composites using ERA5 are shown in Fig. S2 in the supporting information and are, as before, in good agreement with the model composites. The succession of positive, negative and again positive PV anomalies seen in Fig. 3a clearly reveals the occurrence of RWB. These anomalies maximize around 200 hPa and extended between 400 and 100 hPa, inducing geopotential height anomalies of the same sign, in accordance with the PV invertibility principle (Hoskins et al., 1985). The geopotential height anomalies extend to the surface where they result in ridging. It thus appears that RWB close to the tropopause can induce ridging highs over South Africa. As discussed above, ridging highs also occur in the absence of RWB. While PV anomalies can also be seen in this case (Fig. 3d), indicating that the PV contours are undulating as Rossby waves propagate without breaking, the positive anomalies between 0°and 30°E, where the ridging occurs, are much weaker. The positive geopotential height anomalies found at these longitudes seem to have their origin at lower levels, unlike in the case with RWB, and the ridging appears to be less influenced by the PV anomalies aloft.

We demonstrated that ridging highs occurring with and without RWB are characterized by different patterns of MSLP anomalies, which naturally affect the flow of moist air from the warm Indian Ocean towards South Africa. In the next section, we explore the influence of these differences on precipitation.

3.2 Implications for Precipitation

Figure 4 shows composites of precipitation and 850 hPa winds for ridging highs with and without RWB. As there is less agreement between model and observations regarding the precipitation anomalies compared to other fields, we discuss both model and observations in the following.

Ridging highs with RWB are related to precipitation in both the all-year rainfall region and in the summer rainfall region in observations. At day 0 southerly onshore wind anomalies associated with the ridging bring moisture along the south coast resulting in positive precipitation anomalies (Fig. 4a). As the ridging matures, positive MSLP anomalies are found south of the continent (Fig. 2c) and the southerly wind anomalies are confined to the eastern part of South Africa (Fig. 4b), while to the west southeasterly wind anomalies are present. Consequently, positive precipitation anomalies occur in the east, extending into Mozambique, while negative anomalies occur along the western coast. The model shows similar results, but overestimates the extent of the negative anomalies and underestimates the extent of the positive anomalies (Fig. 4c), likely due to the low resolution of its atmospheric component (1.8°). The southerly wind anomalies induced by the ridging high with RWB are consistent with the ridging-associated circulation reported during extreme precipitation events by Crimp and Mason (1999) and Blamey and Reason (2009) that advects moisture to the eastern coast.

Ridging highs without RWB lead to more precipitation over the southwestern coast at day 0 (Fig. 4d) compared to ridging high with RWB, but elsewhere they contribute significantly less precipitation over South Africa. At day 1, negative precipitation anomalies cover most of the country, with the exception of the eastern coast where positive anomalies occur, though weaker than in the case with RWB. This is the consequence of the positive MSLP anomalies extending over the continent at day 1 (Fig. 2d) and resulting in weaker onshore wind anomalies that transport less moisture on land (Fig. 4e). The dryer conditions that occur in the absence of RWB are further explained by the fact that RWB promotes precipitation by leading to strong uplift to the east of its trough. Despite simulating similar wind anomalies as found in the reanalysis, FOCI overestimates the amount of precipitation associated with ridging highs without RWB (Fig. 4f). Climate models are known to overestimate precipitation in the region, particularly over the eastern part of South Africa (F. A. Engelbrecht et al., 2009; Jury, 2012; Dedekind et al., 2016; Almazroui et al., 2020). The use of convective parameterisation schemes that do not represent the diurnal cycle in convective rainfall realistically (Nikulin et al., 2012), is a source of this overestimation that likely also explains the rainfall bias found in FOCI.

3.3 Impact of Climate Change

We examine the future changes in ridging highs and their associated precipitation over the twenty-first century by taking the difference between composites for the FUTURE and the PAST ensembles, separately for ridging highs with and without RWB. As the westerly jet shifts poleward under climate change (McLandress et al., 2011; Ivanciu et al., 2022), so does RWB on the equatorward flank of the jet (Barnes & Hartmann, 2012). The pattern of negative PV change centered at 35°S and positive PV change centered at 50°S shown in Fig. 2e illustrate the shift in RWB clearly. The positive PV anomalies induce as before positive geopotential height anomalies that reach the surface (Fig. 3b), such that the positive MSLP anomalies associated with ridging highs in the future extend farther south (Fig. 2e). This hints to an increase in the number of Type-S ridging highs (Ndarana et al., 2022) in the future.

The negative PV anomaly accompanying ridging highs without RWB also moves poleward in the future causing negative MSLP anomalies (Figs. 2f and 3e), but there is no change in the positive anomalies south of Africa, associated with the ridging. RWB

thus mediates the impact of climate change on ridging highs and ridging highs that occur without RWB are less impacted in the future.

The differences between composites for the GHG and PAST ensemble (Fig. 2g, h and Fig. 3c, f) reveal that the increase in GHGs is responsible for the majority of the changes described above, while the differences between OZONE and PAST (not shown) are mostly not significant. Ivanciu et al. (2022) showed that changes in the westerly jet due to ozone recovery are considerably weaker than changes due to increased GHGs following SSP585, likely explaining why ozone recovery does not affect ridging highs.

Twenty-first century model simulations predict a decrease in precipitation over the entire southern Africa (Dosio et al., 2019; Rojas et al., 2019). The changes in ridging highs with RWB discussed above contribute to the drying in the summer rainfall region (Fig. 4g). In contrast, in the all-year rainfall region along the south coast they lead to an increase in precipitation, therefore weakening the total drying trend. The GHG-induced precipitation changes associated with ridging highs (Fig. 4h) match the changes shown in Fig. 4g very well, demonstrating that the increase in GHGs is driving these changes. The simulated precipitation changes come with the caveat that there are differences between the observed and modeled precipitation associated with ridging highs, as discussed above.

4 Conclusions

This study separated ridging highs over South Africa for the first time based on whether they occur together with RWB at tropopause levels or not in a state-of-the-art global coupled climate model and in the ERA5 reanalysis. In 43% (44%) of the cases RWB occurred together with the ridging highs in the model (reanalysis), a robust result.

Positive PV anomalies associated with RWB induce positive geopotential height anomalies that reach to the surface and cause the South Atlantic Anticyclone to ridge. Ridging highs can also occur in the absence of RWB. The patterns of MSLP anomalies related to ridging highs with and without RWB differ. Stronger southerly and southeasterly wind anomalies occur in the presence of RWB. Previous studies showed that such wind anomalies advect moisture-laden air from above the warm Agulhas Current into South Africa (Crimp & Mason, 1999; Blamey & Reason, 2009; Rapolaki et al., 2020). Therefore, ridging highs with RWB lead to increased precipitation in the all-year rainfall region at day 0 and in the summer rainfall region at days 0 and 1. The observational-based composites demonstrated that ridging highs that occur accompanied by RWB bring more precipitation over southern Africa than ridging highs without RWB. Although there is good agreement between the model and ERA5 with respect to most fields, larger differences arise with respect to precipitation, with the model underestimating (overestimating) the extent of the positive (negative) anomalies associated with ridging highs with RWB and exhibiting a positive precipitation bias for ridging highs without RWB. Climate models have known difficulties in correctly simulating the precipitation in the region, attributed to their convective parameterization schemes that do not represent the diurnal cycle realistically (Nikulin et al., 2012).

The twenty-first century changes in ridging highs were additionally investigated for the first time. RWB on the equatorward side of the westerly jet shifts poleward with the jet in the future, mediating the effect of climate change on ridging highs. Accordingly, the positive MSLP anomalies associated with the ridging extend farther south. Ridging highs that occur without RWB experience little change. The model predicts that ridging highs with RWB will bring more precipitation over the south coast and less precipitation in the summer rainfall region in the future. The increase in GHGs according to the SSP585 scenario is the main driver of the future changes, while ozone recovery does

not affect ridging highs, likely because its effect on the westerly jet is considerably weaker (Ivanciu et al., 2022).

5 Data Availability Statement

The model output used in this study is available at https://doi.org/10.5281/zenodo.6523956 (Ivanciu, 2022). The ERA5 hourly data on pressure levels from 1979 to present (Hersbach et al., 2018) is publicly available from the Copernicus Climate Change Service (C3S) Climate Data Store (CDS) at https://cds.climate.copernicus.eu/cdsapp!/dataset/reanalysis-era5-pressure-levels?tab=overview (accessed on 16.05.2020). The CPC Global Unified Precipitation data is provided by the NOAA/OAR/ESRL PSL, Boulder, Colorado, USA, from their Web site at https://psl.noaa.gov/data/gridded/data.cpc.globalprecip.html (accessed on 16.05.2022).

Acknowledgments
This study has been funded by the German Federal Ministry of Education and Research through the SPACES-II CASISAC project (grant no. 03F0796) and by the Water Research Commission of South Africa (grant no. C2020/2023-00653). The model simulations used in this study were performed with resources provided by the North-German Supercomputing Alliance (HLRN).

References

Almazroui, M., Saeed, F., Saeed, S., Nazrul Islam, M., Ismail, M., Klutse, N. A. B., & Siddiqui, M. H. (2020). Projected Change in Temperature and Precipitation Over Africa from CMIP6. *Earth Systems and Environment*, *4*, 455-475. doi: 10.1007/s41748-020-00161-x

Barnes, E. A., & Hartmann, D. L. (2012). Detection of Rossby wave breaking and its response to shifts of the midlatitude jet with climate change. *Journal of Geophysical Research: Atmospheres*, *117*(D9). doi: 10.1029/2012JD017469

Blamey, R. C., & Reason, C. J. C. (2009). Numerical simulation of a mesoscale convective system over the east coast of South Africa. *Tellus A: Dynamic Meteorology and Oceanography*, *61*(1), 17–34. doi: 10.1111/j.1600-0870.2007.00366.x

Blamey, R. C., & Reason, C. J. C. (2012). Mesoscale Convective Complexes over Southern Africa. *Journal of Climate*, *25*(2), 753 - 766. doi: 10.1175/JCLI-D-10-05013.1

Crimp, S. J., & Mason, S. J. (1999). The Extreme Precipitation Event of 11 to 16 February 1996 over South Africa. *Meteorology and Atmospheric Physics*, *70*, 29 - 42. doi: 10.1007/s007030050023

Dedekind, Z., Engelbrecht, F. A., & van der Merwe, J. (2016). Model simulations of rainfall over southern Africa and its eastern escarpment. *Water SA*, *42*(1), 129-143. doi: 10.4314/wsa.v42i1.13

Dosio, A., Jones, R. G., Jack, C., Lennard, C., Nikulin, G., & Hewitson, B. (2019). What can we know about future precipitation in Africa? Robustness, significance and added value of projections from a large ensemble of regional climate models. *Climate Dynamics*, *53*, 5833 - 5858. doi: 10.1007/s00382-019-04900-3

Dyson, L. L. (2015). A heavy rainfall sounding climatology over Gauteng, South Africa, using self-organising maps. *Climate Dynamics*, *45*, 3051-3065. doi: 10.1007/s00382-015-2523-3

Edouard, S., Vautard, R., & Brunet, G. (1997). On the maintenance of potential vorticity in isentropic coordinates. *Quarterly Journal of the Royal Meteorological Society*, *123*(543), 2069-2094. doi: 10.1002/qj.49712354314

Engelbrecht, C. J., Landman, W. A., Engelbrecht, F. A., & Malherbe, J. (2015). A synoptic decomposition of rainfall over the Cape south coast of South Africa.

Climate Dynamics, *44*, 2589-2607. doi: 10.1007/s00382-014-2230-5

Engelbrecht, F. A., McGregor, J. L., & Engelbrecht, C. J. (2009). Dynamics of the Conformal-Cubic Atmospheric Model projected climate-change signal over southern Africa. *International Journal of Climatology*, *29*(7), 1013-1033. doi: 10.1002/joc.1742

Favre, A., Hewitson, B., Lennard, C., Cerezo-Mota, R., & Tadross, M. (2013). Cut-off Lows in the South Africa region and their contribution to precipitation. *Climate Dynamics*, *41*, 2331-2351. doi: 10.1007/s00382-012-1579-6

Harrison, M. S. J. (1984). A generalized classification of South African summer rain-bearing synoptic systems. *Journal of Climatology*, *4*(5), 547-560. doi: 10.1002/joc.3370040510

Hart, N. C. G., Reason, C. J. C., & Fauchereau, N. (2012). Building a Tropical–Extratropical Cloud Band Metbot. *Monthly Weather Review*, *140*(12), 4005 - 4016. doi: 10.1175/MWR-D-12-00127.1

Hart, N. C. G., Reason, C. J. C., & Fauchereau, N. (2013). Cloud bands over southern Africa: seasonality, contribution to rainfall variability and modulation by the MJO. *Climate Dynamics*, *41*, 1199-1212. doi: 10.1007/s00382-012-1589-4

Hersbach, H., Bell, B., Berrisford, P., Biavati, G., Horányi, A., Muñoz Sabater, J., ... Thépaut, J.-N. (2018). *ERA5 hourly data on pressure levels from 1979 to present. Copernicus Climate Change Service (C3S) Climate Data Store (CDS).* [dataset]. (Accessed on 16.05.2022) doi: 10.24381/cds.bd0915c6

Hoskins, B. J., McIntyre, M. E., & Robertson, A. W. (1985). On the use and significance of isentropic potential vorticity maps. *Quarterly Journal of the Royal Meteorological Society*, *111*(470), 877-946. doi: 10.1002/qj.49711147002

Ivanciu, I. (2022). *FOCI model output used in the study by Ivanciu et al. - On the ridging of the South Atlantic Anticyclone over South Africa: the impact of Rossby wave breaking and of climate change* [dataset]. Zenodo. doi: 10.5281/zenodo.6523955

Ivanciu, I., Matthes, K., Biastoch, A., Wahl, S., & Harlaß, J. (2022). Twenty-first-century Southern Hemisphere impacts of ozone recovery and climate change from the stratosphere to the ocean. *Weather and Climate Dynamics*, *3*(1), 139–171. doi: 10.5194/wcd-3-139-2022

Ivanciu, I., Matthes, K., Wahl, S., Harlaß, J., & Biastoch, A. (2021). Effects of prescribed CMIP6 ozone on simulating the Southern Hemisphere atmospheric circulation response to ozone depletion. *Atmospheric Chemistry and Physics*, *21*(8), 5777–5806. doi: 10.5194/acp-21-5777-2021

Jury, M. R. (2012). An inter-comparison of model-simulated east–west climate gradients over South Africa. *Water SA*, *38*(4), 467-478. doi: 10.4314/wsa.v38i4.1

Kinnison, D. E., Brasseur, G. P., Walters, S., Garcia, R. R., Marsh, D. R., Sassi, F., ... Simmons, A. J. (2007). Sensitivity of chemical tracers to meteorological parameters in the MOZART-3 chemical transport model. *Journal of Geophysical Research: Atmospheres*, *112*(D20). doi: 10.1029/2006JD007879

Lee-Thorp, A. M., Rouault, M., & Lutjeharms, J. R. E. (1999). Moisture uptake in the boundary layer above the Agulhas Current: A case study. *Journal of Geophysical Research: Oceans*, *104*(C1), 1423-1430. doi: 10.1029/98JC02375

Matthes, K., Biastoch, A., Wahl, S., Harlaß, J., Martin, T., Brücher, T., ... Park, W. (2020). The Flexible Ocean and Climate Infrastructure Version 1 (FOCI1): Mean State and Variability. *Geoscientific Model Development Discussions*, *2020*, 1–53. doi: 10.5194/gmd-13-2533-2020

McIntyre, M. E., & Palmer, T. N. (1983). Breaking planetary waves in the stratosphere. *Nature*, *305*, 593-600. doi: 10.1038/305593a0

McLandress, C., Shepherd, T. G., Scinocca, J. F., Plummer, D. A., Sigmond, M., Jonsson, A. I., & Reader, M. C. (2011). Separating the Dynamical Effects of Climate Change and Ozone Depletion. Part II: Southern Hemisphere Troposphere. *Journal of Climate*, *24*(6), 1850-1868. doi: 10.1175/2010JCLI3958.1

Molekwa, S., Engelbrecht, C. J., & Rautenbach, C. J. W. (2014). Attributes of cut-off low induced rainfall over the Eastern Cape Province of South Africa. *Theoretical and Applied Climatology*, *118*, 307-318. doi: 10.1007/s00704-013-1061-3

Ndarana, T., Bopape, M.-J., Waugh, D., & Dyson, L. (2018). The Influence of the Lower Stratosphere on Ridging Atlantic Ocean Anticyclones over South Africa. *Journal of Climate*, *31*(15), 6175 - 6187. doi: 10.1175/JCLI-D-17-0832.1

Ndarana, T., Mpati, S., Bopape, M.-J., Engelbrecht, F., & Chikoore, H. (2021). The flow and moisture fluxes associated with ridging South Atlantic Ocean anticyclones during the subtropical southern African summer. *International Journal of Climatology*, *41*(S1), E1000-E1017. doi: 10.1002/joc.6745

Ndarana, T., Rammopo, T. S., Reason, C. J., Bopape, M.-J., Engelbrecht, F., & Chikoore, H. (2022). Two types of ridging South Atlantic Ocean anticyclones over South Africa and the associated dynamical processes. *Atmospheric Research*, *265*, 105897. doi: 10.1016/j.atmosres.2021.105897

Ndarana, T., & Waugh, D. W. (2011). A Climatology of Rossby Wave Breaking on the Southern Hemisphere Tropopause. *Journal of the Atmospheric Sciences*, *68*(4), 798 - 811. doi: 10.1175/2010JAS3460.1

Nikulin, G., Jones, C., Giorgi, F., Asrar, G., Büchner, M., Cerezo-Mota, R., ... Sushama, L. (2012). Precipitation Climatology in an Ensemble of CORDEX-Africa Regional Climate Simulations. *Journal of Climate*, *25*(18), 6057 - 6078. doi: 10.1175/JCLI-D-11-00375.1

Nkwinkwa Njouodo, A. S., Koseki, S., Keenlyside, N., & Rouault, M. (2018). Atmospheric Signature of the Agulhas Current. *Geophysical Research Letters*, *45*(10), 5185-5193. doi: 10.1029/2018GL077042

Nkwinkwa Njouodo, A. S., Rouault, M., Keenlyside, N., & Koseki, S. (2021). Impact of the Agulhas Current on southern Africa precipitation: a modelling study. *Journal of Climate*, 1 - 50. doi: 10.1175/JCLI-D-20-0627.1

Rapolaki, R. S., Blamey, R. C., Hermes, J. C., & Reason, C. J. C. (2020). Moisture sources associated with heavy rainfall over the Limpopo River Basin, southern Africa. *Climate Dynamics*, *55*, 1473 - 1487. doi: 10.1007/s00382-020-05336-w

Roffe, S., Fitchett, J., & Curtis, C. (2019). Classifying and mapping rainfall seasonality in South Africa: a review. *South African Geographical Journal*, *101*(2), 158-174. doi: 10.1080/03736245.2019.1573151

Rojas, M., Lambert, F., Ramirez-Villegas, J., & Challinor, A. J. (2019). Emergence of robust precipitation changes across crop production areas in the 21st century. *Proceedings of the National Academy of Sciences*, *116*(14), 6673-6678. doi: 10.1073/pnas.1811463116

Rouault, M., Lee-Thorp, A. M., & Lutjeharms, J. R. E. (2000). The Atmospheric Boundary Layer above the Agulhas Current during Alongcurrent Winds. *Journal of Physical Oceanography*, *30*(1), 40 - 50. doi: 10.1175/1520-0485(2000)030⟨0040:TABLAT⟩2.0.CO;2

Rouault, M., Reason, C. J. C., Lutjeharms, J. R. E., & Beljaars, A. C. M. (2003). Underestimation of Latent and Sensible Heat Fluxes above the Agulhas Current in NCEP and ECMWF Analyses. *Journal of Climate*, *16*(4), 776 - 782. doi: 10.1175/1520-0442(2003)016⟨0776:UOLASH⟩2.0.CO;2

Rouault, M., White, S. A., Reason, C. J. C., Lutjeharms, J. R. E., & Jobard, I. (2002). Ocean–Atmosphere Interaction in the Agulhas Current Region and a South African Extreme Weather Event. *Weather and Forecasting*, *17*(4), 655 - 669. doi: 10.1175/1520-0434(2002)017⟨0655:OAIITA⟩2.0.CO;2

Schwarzkopf, F. U., Biastoch, A., Böning, C. W., Chanut, J., Durgadoo, J. V., Getzlaff, K., ... Schubert, R. (2019). The INALT family – a set of high-resolution nests for the Agulhas Current system within global NEMO ocean/sea-ice configurations. *Geoscientific Model Development*, *12*(7), 3329–3355. doi: 10.5194/gmd-12-3329-2019

Singleton, A. T., & Reason, C. J. C. (2006). Numerical simulations of a severe rainfall event over the Eastern Cape coast of South Africa: sensitivity to sea surface temperature and topography. *Tellus A: Dynamic Meteorology and Oceanography*, *58*(3), 335-367. doi: 10.1111/j.1600-0870.2006.00180.x

Tyson, P. D., & Preston-Whyte, R. A. (2000). *Weather and climate of southern Africa*. Oxford University Press.

Wirth, V., Riemer, M., Chang, E. K. M., & Martius, O. (2018). Rossby Wave Packets on the Midlatitude Waveguide—A Review. *Monthly Weather Review*, *146*(7), 1965 - 2001. doi: 10.1175/MWR-D-16-0483.1

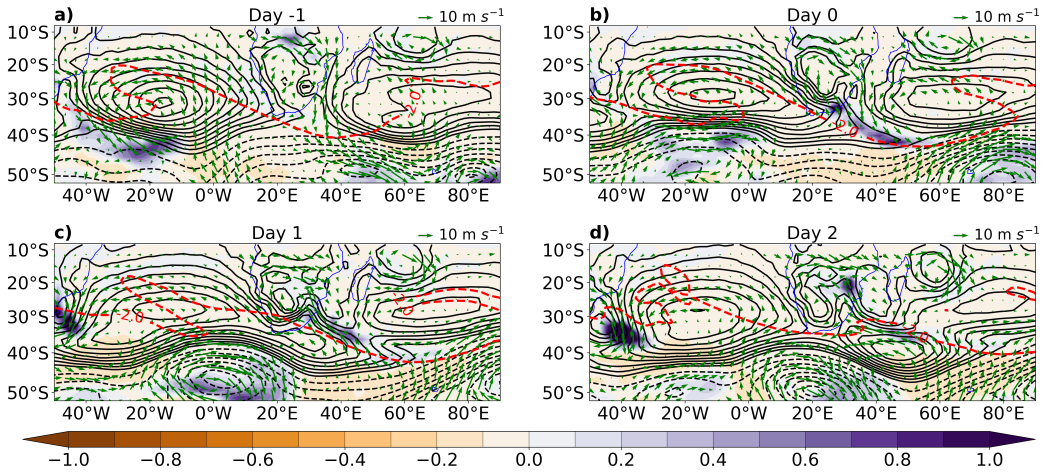

Figure 1. Example of ridging high accompanied by RWB in FOCI: black contours depict the MSLP, every 2 hPa starting at 1010 hPa (solid) and every 5 hPa below (dashed), the color shading depicts precipitation anomalies (mm day^{-1}), the arrows depict the wind anomalies at 850 hPa (m s^{-1}) and the red dashed contour shows -2 PVU on the 350 K isentrop. The evolution of the event is shown from day -1 (a) to day +2 (d).

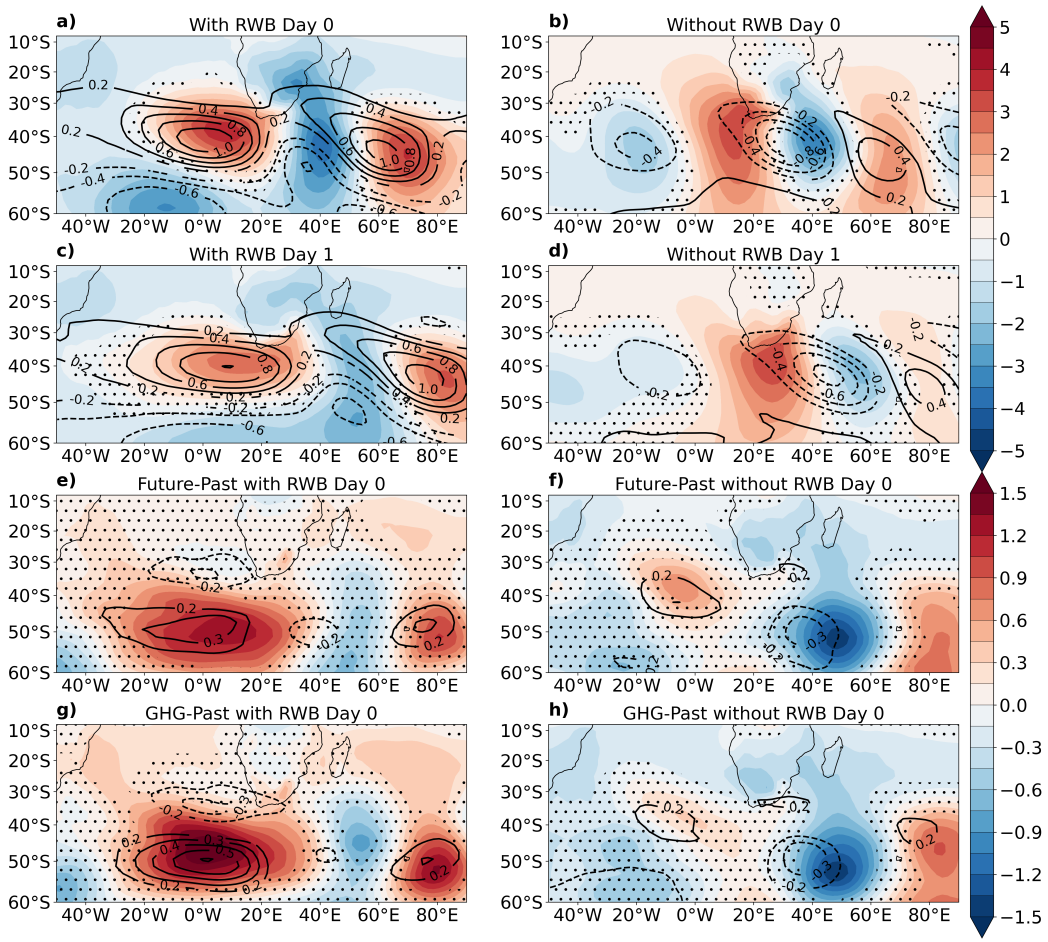

Figure 2. Composites of ridging highs with (a,c) and without (b,d) RWB at day 0 (a,b) and day 1 (c,d) of the ridging for the period 1980-2009. Anomalies of MSLP (hPa) and of 200 hPa PV (PVU) are depicted by the color shading and by the contours, respectively. Total (e,f) and GHG-induced (g,h) change, between 2070-2099 and 1980-2009, in the day 0 anomalies associated with ridging highs with (e,g) and without (f,h) RWB. The stippling masks anomalies that are not significant at the 95 % confidence interval based on the Monte Carlo method. Only significant PV anomalies are plotted.

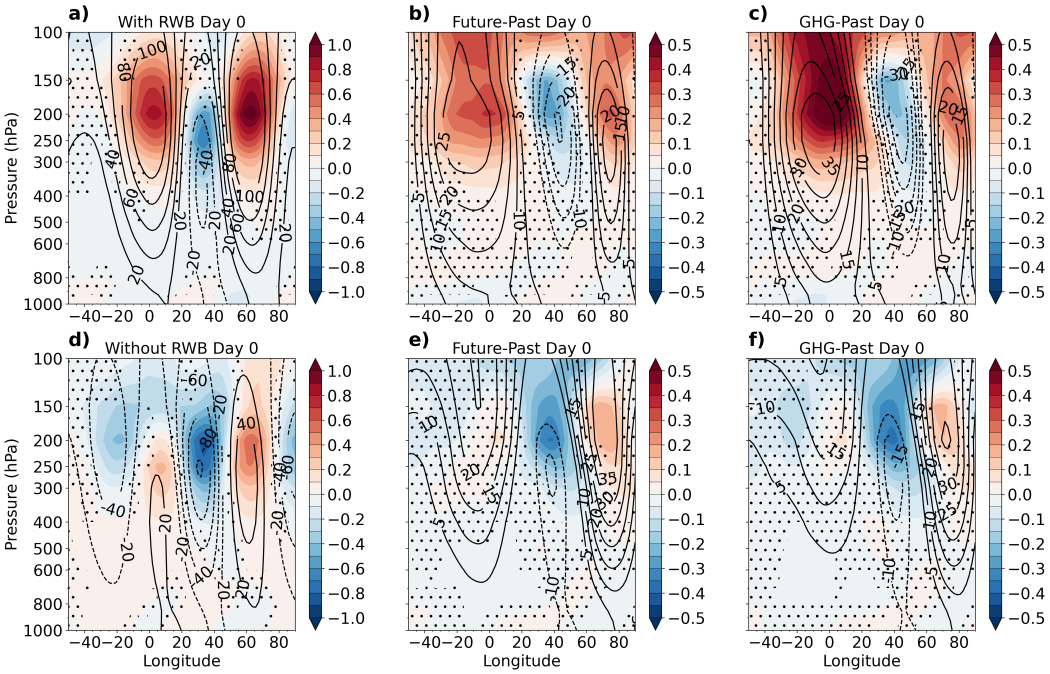

Figure 3. Composites of ridging highs at day 0 with (a) and without (d) RWB for the period 1980-2009. Anomalies of PV (PVU) and of geopotential height (m) at 45°S are depicted by the color shading and by the contours, respectively. Total (b,e) and GHG-induced (c,f) change, between 2070-2099 and 1980-2009 at 50°S, in the anomalies associated with ridging highs with (b,c) and without (e,f) RWB. The stippling masks anomalies that are not significant at the 95 % confidence interval based on the Monte Carlo method. Only significant geopotential height anomalies are plotted.

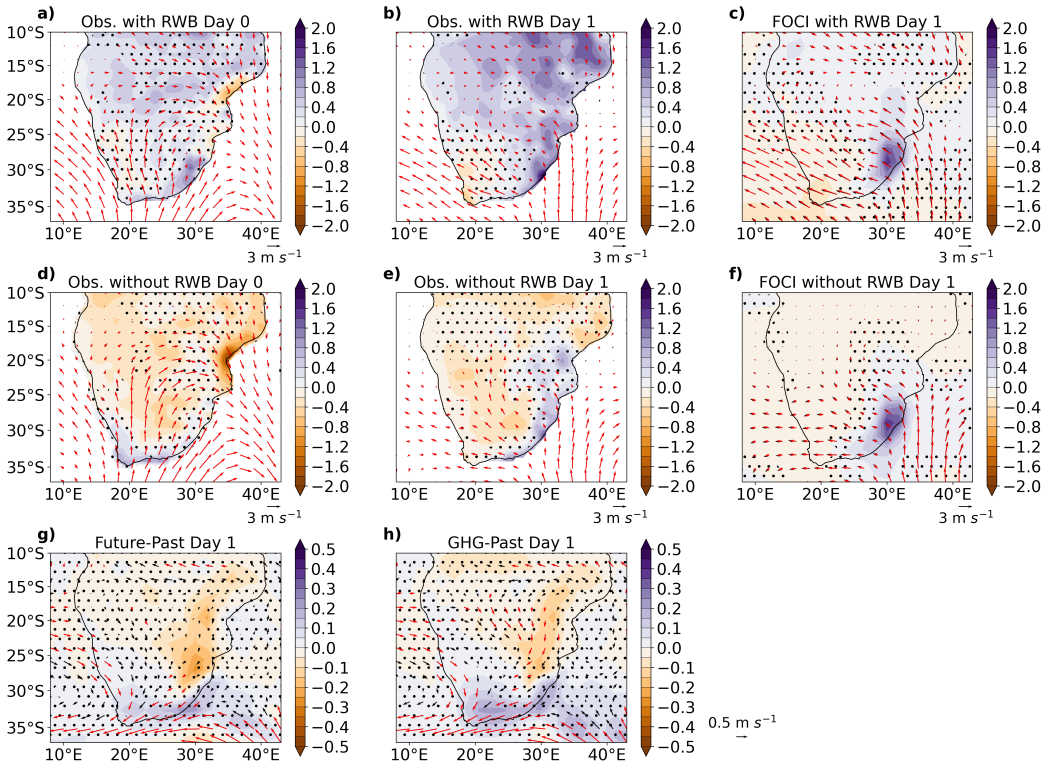

Figure 4. Composites of ridging highs with (a-c) and without (d-f) RWB from observations (a,b,d,e) and from FOCI (c,f) at day 0 (a,d) and day 1 (b,c,e,f) for the period 1980-2009. Anomalies of precipitation (mm day^{-1}) and of 850 hPa winds (m s^{-1}) are depicted by the color shading and by the vectors, respectively. Total (g) and GHG-induced (h) change, between 2070-2099 and 1980-2009, in the day 1 anomalies associated with ridging highs with RWB. The stippling masks anomalies that are not significant at the 95 % confidence interval based on the Monte Carlo method. The red vectors depict significant wind anomalies.

Supporting Information for "On the ridging of the South Atlantic Anticyclone over South Africa: the impact of Rossby wave breaking and of climate change"

Ioana Ivanciu[1], Thando Ndarana[2], Katja Matthes[1]and Sebastian Wahl[1]

[1]GEOMAR Helmholtz Centre for Ocean Research Kiel, Germany

[2]Department of Geography, Geoinformatics and Meteorology, University of Pretoria, South Africa

Contents of this file

1. Text S1 and S2
2. Figures S1 and S2

Introduction The supporting material provides detailed descriptions of the algorithms used to identify ridging highs and Rossby wave breaking (RWB) in the South African sector. Additionally, composites of ridging highs with and without Rossby wave breaking based on the ERA5 reanalysis are provided for comparison and validation of the results based on the coupled climate model FOCI.

Corresponding author: I. Ivanciu, GEOMAR Helmholtz Centre for Ocean Research Kiel, Düsternbrooker Weg 20, 24105 Kiel, Germany. (iivanciu@geomar.de)

S1. Ridging Highs Identification

We identify the ridging of the South Atlantic Anticyclone over South Africa based on MSLP using the method of (Ndarana et al., 2018). For each day, contours are generated, in 1 hPa intervals, from the minimum to the maximum MSLP in the domain 0°- 60°S and 60°W - 60°E. Only closed contours originating in the South Atlantic Ocean and having a diameter of at least 10° are kept, in order to exclude sub-synoptic-scale processes and to ensure that we only consider the South Atlantic Anticyclone and not other high pressure systems. The eastward extension of the contours is then checked starting from the contour with the lowest MSLP and, if a contour extends eastward of 25°E, a ridging event is considered to have occurred. This contour is then saved together with all the contours concentric with it, for that respective day. Since a ridging event can last more than a day, consecutive days with contours extending past 25°E are considered to be part of the same event.

S2. Rossby Wave Breaking Identification

RWB events that are relevant for the South Atlantic Anticyclone are identified using potential vorticity (PV) between -2.5 PVU to -1.5 PVU (1 PVU = 10^6 K m^2 s^{-1} kg^{-1}) on the 330, 340 and 350 K isentropic surfaces. We follow the algorithm proposed by Ndarana and Waugh (2011) with the additional condition that PV contours need to have an S-like shape, as detailed below.

First, we compute PV on pressure levels:

$$PV = g\Big[f + \frac{1}{acos\phi}\frac{\partial v}{\partial \lambda} - \frac{1}{acos\phi}\frac{\partial (ucos\phi)}{\partial \phi}\Big]\Big(-\frac{\partial \theta}{\partial p}\Big) \tag{1}$$

where g is the gravitational acceleration, f is the Coriolis parameter, a is the radius of the earth, u and v are the zonal and meridional velocity components, respectively, θ is the potential temperature, p is the pressure and ϕ and λ are the latitude and longitude, respectively. Then we linearly interpolate the PV to isentropic surfaces following Edouard, Vautard, and Brunet (1997) and we apply a spatial 3-point running mean. PV contours are generated every 0.1 PVU for each day and isentropic surface. Only contours that are equal to a latitude circle or longer are included in order to exclude isolated PV anomalies that are likely to be remnants of old RWB events. RWB occurs when all the following conditions are met: a meridian intersects a contour at least at three distinct latitudes, the meridional PV gradient is negative and the contour has an S-like shape in the respective region. Additionally, the contour segment has to be at least 20° long. If these conditions are met at the same location for several contours, on several isentropic surfaces or for consecutive day, a single event is considered to have occurred.

References

Edouard, S., Vautard, R., & Brunet, G. (1997). On the maintenance of potential vorticity in isentropic coordinates. *Quarterly Journal of the Royal Meteorological Society*, *123*(543), 2069-2094. doi: 10.1002/qj.49712354314

Ndarana, T., Bopape, M.-J., Waugh, D., & Dyson, L. (2018). The Influence of the Lower Stratosphere on Ridging Atlantic Ocean Anticyclones over South Africa. *Journal of Climate*, *31*(15), 6175 - 6187. doi: 10.1175/JCLI-D-17-0832.1

Ndarana, T., & Waugh, D. W. (2011). A Climatology of Rossby Wave Breaking on the Southern Hemisphere Tropopause. *Journal of the Atmospheric Sciences*, *68*(4), 798

- 811. doi: 10.1175/2010JAS3460.1

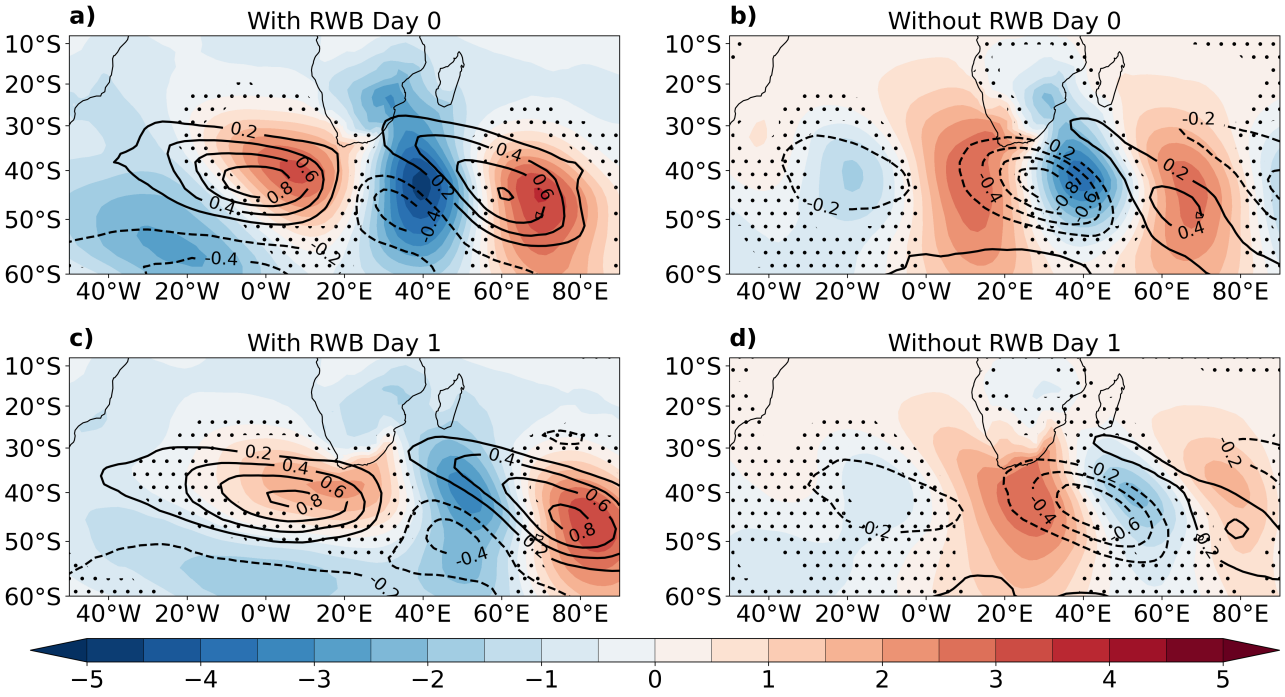

Figure S1. ERA5 composites of ridging highs with (a,c) and without (b,d) RWB at day 0 (a,b) and day 1 (c,d) of the ridging for the period 1980-2009. Anomalies of MSLP (hPa) and of 200 hPa PV (PVU) are depicted by the color shading and by the contours, respectively. The stippling masks anomalies that are not significant at the 95 % confidence interval based on the Monte Carlo method. Only significant PV anomalies are plotted.

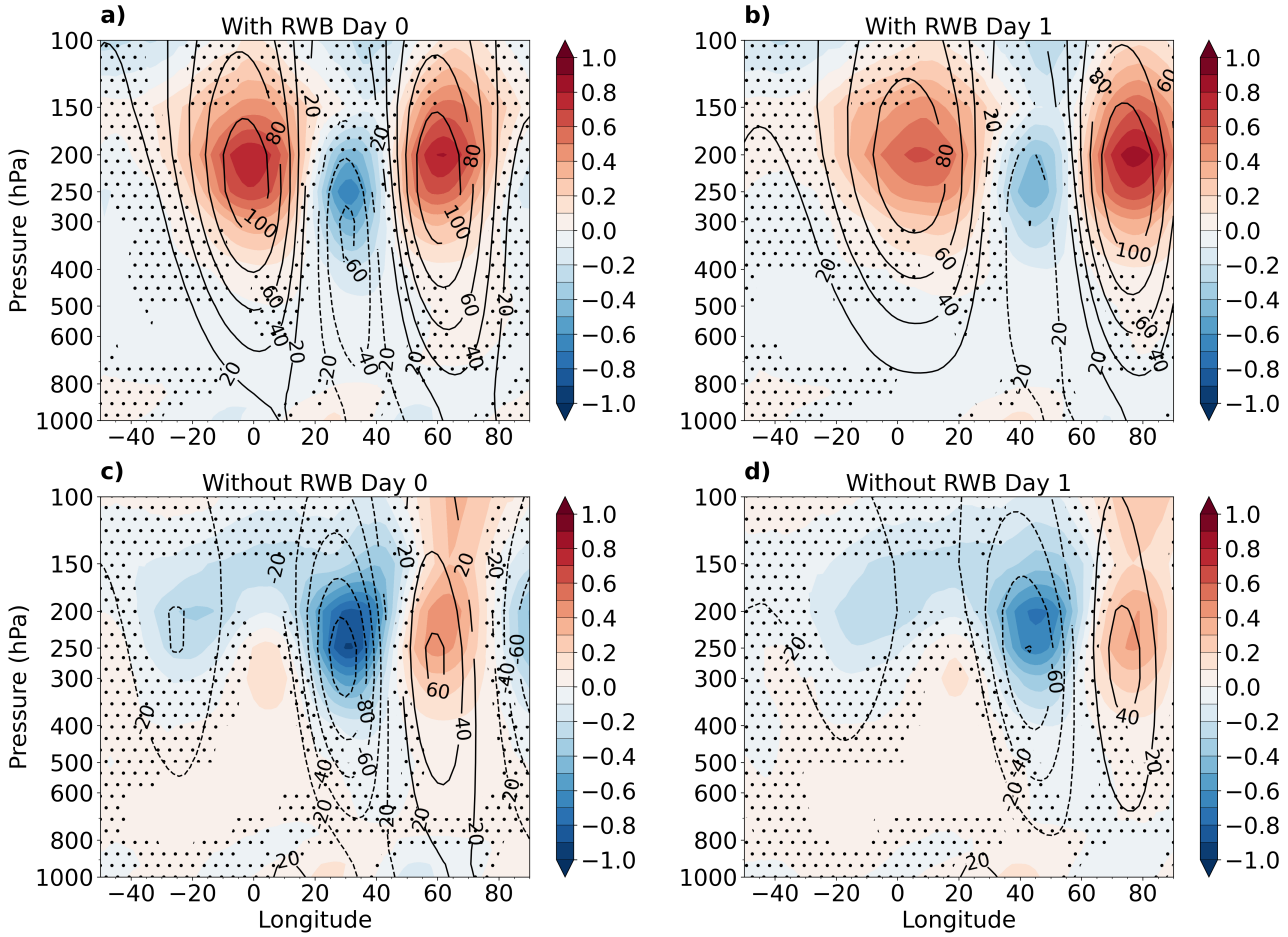

Figure S2. ERA5 composites of ridging highs with (a,b) and without (c,d) RWB at day 0 (a,c) and day 1 (b,d) for the period 1980-2009. Anomalies of PV (PVU) and of geopotential height (m) at 45°S are depicted by the color shading and by the contours, respectively. The stippling masks anomalies that are not significant at the 95 % confidence interval based on the Monte Carlo method. Only significant geopotential height anomalies are plotted.

Chapter 6

Summary and Outlook

This thesis separated the effects that the increase in anthropogenic greenhouse gases (GHGs) and the changes in stratospheric ozone concentrations have on the atmospheric and oceanic circulation in the Southern Hemisphere during the second half of the twentieth century and the twenty-first century. The dominant forcing was identified for each of the two periods and the total change driven by both forcings together was reported. The model employed for this purpose is the coupled climate model FOCI, described in Chapter 2. Two special features of FOCI recommended it for this study. First, FOCI includes an optional module for interactively simulating the ozone chemistry, enabling the ozone field to be consistent with the simulated dynamics and the GHG emission scenario used, and making it an appropriate tool for the study of ozone changes and their associated impacts. Second, FOCI allows for an increased resolution in an ocean area of interest, thus resolving the mesoscale oceanic features that play an important role for ocean dynamics.

The first step of the analysis involved assessing if FOCI accurately simulates the known past changes in the Southern Hemisphere dynamics and the contributions of ozone depletion and increasing GHGs to these changes, reported from observations and previous modeling studies. Thus, the first question this thesis answered was:

1. **How well does the coupled climate model FOCI simulate the changes caused in the second half of the twentieth century in the Southern Hemisphere by ozone depletion and increasing levels of anthropogenic GHGs?**

This question was addressed in Chapter 3. It was shown that FOCI captures all the effects of the past increase in GHGs and of ozone depletion on the Southern Hemisphere atmospheric circulation reported in previous studies (*Randel and Wu*, 1999; *Thompson and Solomon*, 2002; *Gillett and Thompson*, 2003; *Arblaster and Meehl*, 2006; *Li et al.*, 2008; *McLandress et al.*, 2010; *Son et al.*, 2010; *Polvani et al.*, 2011; *Keeble et al.*, 2014;

Oberländer-Hayn et al., 2015). The stratosphere experienced a general cooling, which peaked in the lower stratosphere during austral spring, when the ozone hole occurred. The polar upper stratosphere cooled by about 1 to 2 K in FOCI, driven primarily by the increase in GHGs. In austral spring however, a warming of up to 2 K occurred in the middle to upper stratosphere, as the dynamical effect of ozone depletion dominated the cooling due to GHGs. The polar lower stratosphere has cooled by up to 4 K in austral spring. The effect of ozone depletion was greater, reaching over 7 K, but at these levels during spring GHGs led to a warming of up to 4 K that offset part of the ozone effect. In response to the temperature changes, the polar vortex strengthened and became more persistent. The trends in the westerly winds extended from the stratosphere into the troposphere and to the surface. The tropospheric westerlies experienced a poleward strengthening and the Southern Annular Mode (SAM) experienced a positive trend. The strengthening of the polar vortex and of the subtropical jet altered the propagation of planetary waves from the troposphere into the stratosphere, resulting in an overall strengthening of the Brewer-Dobson circulation (BDC) in the middle and upper stratosphere. In the lower stratosphere during austral spring, FOCI correctly captures the weakening of the wave drag and the resulting weakening of the polar downwelling, which reverses its sign in austral summer. This weakening of the residual circulation in the lower stratosphere was found in modeling studies by *McLandress et al.* (2010), *Orr et al.* (2012) and *Lubis et al.* (2016) and was recently confirmed in reanalyses (*Orr et al.*, 2021). In FOCI, the dynamical cooling associated with the weaker downwelling enhances the temperature reduction due to the radiative effect of ozone loss in the polar lower stratosphere during spring, in agreement with the results of *Orr et al.* (2013). Thus, FOCI simulates all the known changes experienced by the atmospheric dynamics in the second half of the twentieth century.

The isolation of the changes that occurred due to ozone depletion from the changes that occurred due to increasing GHGs revealed that FOCI attributes the past circulation changes primarily to ozone depletion, in agreement with previous studies (*McLandress et al.*, 2010; *Polvani et al.*, 2011; *Abalos et al.*, 2019). This demonstrates that FOCI correctly identifies the cause of the past Southern Hemisphere atmospheric changes. Due to the seasonality of the ozone hole, the stratospheric changes occurred in austral spring, while the tropospheric changes lagged by about two months, occurring in austral summer. The past increase in GHGs had relatively weak impacts on the atmospheric circulation, being associated with a cooling of the stratosphere and a strengthening of the subtropical jet on its upper flank throughout the year. At the surface, GHGs enhanced the effect of ozone depletion, but in the absence of the ozone effects they resulted only in insignificant trends in the surface westerly jet strength and the SAM.

The good agreement between the past circulation changes simulated by FOCI and those reported by previous observational and modeling studies gave confidence in the future changes projected by FOCI under the high-emission scenario SSP5-8.5, which were presented in Chapter 4.

The fact that changes in both ozone and GHG concentrations affected the Southern Hemisphere dynamics in the past suggests that they will continue to do so in the future, giving rise to the second question of this thesis. In the future, the ozone hole recovers in FOCI in 2048, as ozone depleting substances (ODSs) are being phased out, as mandated by the Montreal Protocol and its amendments and adjustments. Atmospheric levels of GHGs, in contrast, continue to rise. Ozone recovery implies that a continuation and intensification of the past trends in Southern Hemisphere dynamics cannot simply be assumed. At the same time, the continued increase in GHGs implies that a simple reversal of the past trends cannot be expected. Chapter 4, therefore studied the future impacts of increasing GHGs and ozone recovery, both in isolation and in combination, in order to answer the questions:

2. **How will increasing concentrations of GHGs and the recovery of stratospheric ozone impact the atmospheric and oceanic circulation in the Southern Hemisphere in the twenty-first century? What will the net effect of these changes in atmospheric composition be?**

When answering this question, one needs to keep in mind that GHGs affect the concentration and distribution of stratospheric ozone and therefore their increase leads to ozone changes. This is because GHGs affect ozone chemistry, lead to temperature changes that impact the temperature dependent ozone depleting reactions and alter the BDC and hence the transport of ozone from low latitudes. FOCI predicts that GHGs accelerate the recovery of the Antarctic ozone hole by approximately two decades. Thus, the dynamical changes driven by GHGs summarized below include both a direct effect due the interaction of GHGs with radiation and an indirect effect mediated through GHG-driven changes in stratospheric ozone, in agreement with *Morgenstern et al.* (2014) and *Chiodo and Polvani* (2016). At the same time, the changes occurring due to ozone recovery in response solely to the elimination of ODSs do not include the effect of the increase in ozone due to increasing GHGs.

Particular attention was paid in Chapter 4 to the spatial patterns exhibited by the future dynamical changes. The austral spring changes in stratospheric dynamics were found to be weakly asymmetric for ozone recovery and strongly asymmetric for the increase in GHGs. The recovery of the Antarctic ozone hole leads to a warming of the entire lower stratospheric polar cap in austral spring, which extends more towards the Atlantic Ocean and which is accompanied by a circumpolar weakening of the polar vortex. Although the GHG forcing

itself is approximately symmetric, the temperature and zonal wind response to this forcing exhibits a planetary wavenumber 1 (PW1) pattern, characterized by warming in the Western and cooling in the Eastern Hemisphere and by a shift of the polar vortex towards the Eastern Hemisphere. This PW1 pattern, which only occurs in austral spring, was reported here for the first time and was found to be dynamically and not radiatively driven. The magnitudes of the temperature and zonal wind responses to the GHG and ozone forcings are comparable, highlighting that GHGs also play an important role in the future changes in stratospheric dynamics during austral spring. Since the GHG-induced stratospheric changes in the Eastern and the Western Hemisphere have opposite signs, they compensate each other in the zonal mean. Hence, the importance of the GHG-induced stratospheric changes during austral spring is strongly underestimated if only zonal mean changes are analyzed.

The discovery of this asymmetric response to the increase in GHGs leads to the following two questions: why does a symmetric GHG forcing lead to an asymmetric dynamical response and why does this only occur in austral spring? The seasonality of the response is likely explained by the fact that the Southern Hemisphere stratosphere is most active during austral spring. The answer to the first question likely lies in the non-linear dynamics involving the interaction between waves and the mean flow interaction, but the exact mechanism could not be elucidated in this thesis and cannot be easily revealed. This is therefore still an open question.

The BDC was also found to respond to both the GHG and the ozone forcing. Ozone recovery drives a weakening of the BDC in the Southern Hemsiphere during austral spring and early summer. GHGs drive a strengthening of the BDC during most of the year, but a weakening in November, reinforcing the effect of ozone recovery. The net change in the BDC therefore consists of a strengthening in all months but November and December when a weakening occurs instead.

At the surface, the recovery of the Antarctic ozone hole induces a weakening of the poleward flank of the westerly jet representing 4%, in the annual mean, and 8%, in the November-January mean, of the jet's current day strength. This weakening is accompanied by a negative trend in the SAM. The increase in GHGs according to the SSP5-8.5 scenario induces a positive trend in the SAM and an annual-mean poleward strengthening of the westerly jet representing 17% of the jet's current day strength. The total change in the westerly jet is dominated by the influence of GHGs and amounts to a strengthening of 9% in the annual mean. Nevertheless, ozone recovery brings an important contribution to the future trends in the surface westerly winds, mitigating the effect of increasing GHGs by at least 4%.

The Southern Ocean circulation responds to the changes in surface winds associated with ozone recovery and the increase in GHGs in the future. The Antarctic Circumpolar Current

(ACC) is in an ”eddy-saturated” state (e.g., *Farneti et al.*, 2010) and, therefore, its transport does not scale with the surface wind change. Still, the ACC transport changes exhibit the same sign as the wind changes. Ozone recovery drives a decrease and GHGs drive an increase in the ACC transport, with the GHG effect being stronger. In total, FOCI predicts an increase in the ACC transport at the end of the century of 6% in the Drake Passage and of 4% south of the African continent. The Drake Passage is located on the boundary of the domain covered by the high-resolution ocean nest, while the sector of the Southern Ocean south of Africa is located in the center of the nest. A better representation of the ”eddy-saturation” effect can therefore be expected in the latter location.

While FOCI includes a better representation of the eddy effects compared to the climate models participating in CMIP6, owing to its high-resolution nest and to its variable eddy parametrization scheme, using a climate model with a global high-resolution ocean would be desirable to achieve a higher degree of confidence in the projections of future ACC change. The high-resolution nest used in FOCI only covers the Indo-Atlantic sector of the Southern Ocean and terminates at 63°S, therefore not covering the regions of deep water formation in the Weddell and Ross Seas. The formation and spreading of deep waters might not be accurate as a result. This might affect the density gradient across the ACC and hence the projected future changes in the ACC. To date, the only study that used a coupled climate model with a 0.1° global ocean to investigate changes in the ACC (*Bishop et al.*, 2016), applied only a 50% increase in the surface wind stress over the Southern Ocean as forcing. The resulting increase in ACC transport amounted to 6%, but this increase stemmed only from changes in surface momentum fluxes. The buoyancy forcing associated with changes in surface heat and freshwater fluxes, as well as remote influences that affect the global pycnocline and hence the slope of isopycnals across the ACC, such as the rate of deep water formation in the North Atlantic (*Fučkar and Vallis*, 2007) or remote diapycnal mixing (*Munday et al.*, 2011), were not considered. The approach used in this thesis includes all these factors that have an influence on the ACC transport. It would therefore be of interest to study the response of the ACC to the twenty-first century ozone recovery and increase in GHGs in a climate model with a 0.1° global ocean. Since such simulations are still computationally expensive, particularly when ensembles of several simulations are required due to the high internal variability in coupled climate models, an alternative would be to use increased ocean resolution only in the Southern Ocean. Such a study would not only provide the most realistic projection of the future ACC change, under a wind stress forcing that is in line with the ozone and GHG changes, but it would also provide a measure of how close projections from models like FOCI are to projections of fully eddy-resolving models.

Ozone recovery and the increase in GHGs during the twenty-first century were found to have opposing effects on the ocean temperature in the Southern Hemisphere. The large scale GHG-induced warming, reaching 4°C in some regions, overwhelms the large scale ozone-induced cooling of up to 1°C, but the effect of ozone recovery acts to mitigate the warming. The net change in SST therefore reaches up to 3°C. Both the ozone- and the GHG-induced temperature trends are particularly pronounced and reach the greatest depths around 40°S. These trends are related to changes in the Southern Ocean circulation. To better understand the mechanisms that lead to these temperature trends, a future study should investigate the response of the Southern Ocean meridional overturning circulation (MOC) to ozone recovery and increasing GHGs. Due to the "eddy compensation" of changes in the MOC, such a study should ideally also resolve the mesoscale variability, at least in the Southern Ocean. The approach should be to differentiate between the Eulerian MOC, characterized by the Deacon Cell, and the eddy-driven MOC, which opposes the Eulerian MOC. Summing up the two gives the residual MOC, which provides the net change in transport. It is the change in the residual MOC that could help to better understand the mechanism behind the trends in ocean temperature. In addition, changes in surface heat fluxes could also be investigated, to shed further light on the origin of the ocean temperature trends.

This thesis placed a special focus on the Southern African region. This is a highly-populated region whose climate is shaped by the warm waters of the Agulhas Current System. Chapters 4 and 5 addressed the questions:

3. **How are the Southern African region and the adjacent oceans impacted by the increases in GHGs and ozone in the twenty-first century? Do ridging highs over South Africa that are accompanied by Rossby wave breaking at the tropopause bring a different contribution to precipitation in the region than ridging highs that are not?**

This thesis investigated for the first time the response of the Agulhas Current System to ozone recovery and increasing GHGs during the twenty-first century. The Agulhas Current, as well as its leakage into the Atlantic Ocean were found to respond to future changes in GHGs and stratospheric ozone. Ozone recovery drives a strengthening of the Agulhas Current of 2% and a decrease in leakage of 7%, while increasing GHGs drive a weakening of the Agulhas Current of 13% and an increase in leakage of 28% until the end of the century. The result is a net increase in Agulhas leakage of 13% of its current day transport. The role played by ozone recovery in mitigating the effects of the increase in GHGs is also noticeable for the changes in the Agulhas Current System. *Durgadoo et al.* (2013) showed that changes in the surface westerly winds alter the Agulhas leakage via the interior Sverdrup transport in

the Southern Indian Ocean. Chapter 4 also showed a close relationship between the westerly wind stress over the Indian Ocean and Agulhas leakage and attributed the future increase in leakage to the net strengthening of the westerly jet.

Agulhas leakage variations were found to alter the thermohaline properties of the Atlantic Ocean. Chapter 4 showed that periods characterized by high Agulhas leakage exhibit positive temperature and salinity anomalies extending from the Agulhas retroflection into the South Atlantic Ocean. These anomalies reach down to 1000 m depth. While the temperature anomalies are dampened by heat loss to the atmosphere, the salinity anomalies are advected northwestwards and can be detected in the central part of the South Atlantic Ocean after 5 years. The total temperature change during the twenty-first century, summarized in the answer to question 2, exhibits a region of pronounced warming extending from the Agulhas retroflection into the South Atlantic, much like the leakage-related anomalies. These results suggest that the future increase in leakage contributes to the South Atlantic temperature trends. However this contribution, as well as the contribution to changes in salinity, could not be quantified in this thesis, because the Agulhas leakage is only one element that responds to the GHG and ozone forcing. Changes in the Atlantic Meridional Overturning Circulation (AMOC), in surface heat fluxes, as well as regional changes, such as changes in upwelling are among the factors that can contribute to the temperature trends and that could not be separated from the Agulhas contribution. Nevertheless, the composite analysis presented in Chapter 4 showed that an increased Agulhas leakage is accompanied by a warmer and saltier South Atlantic Ocean.

Thus, an open question arising from this thesis concerns the amount that the increase in Agulhas leakage contributes to the overall changes in Atlantic Ocean temperature and salinity. A related question is whether the increase in leakage affects the strength and stability of the AMOC in the future. This issue is of particular importance since the melting of the Greenland ice sheet due to increasing GHGs is expected to have a destabilizing effect on the AMOC, and an increase in Atlantic Ocean density due to the increased Agulhas leakage could have a compensatory effect. It is however difficult to test this hypothesis in climate models. One option would be to impose temperature and salinity anomalies akin to those induced by an increase in leakage in the Cape Basin, to track their advection in the Atlantic Ocean and to assess the resulting changes in the stability of the AMOC. However, this is problematic. First, one would need to know the magnitude of the anomalies associated with a certain increase in leakage. Second, imposing such anomalies would alter the circulation in the region and possibly the Agulhas leakage itself. Alternatively, the Agulhas leakage itself could be increased, but as the leakage is not a continuous current it is not clear how

this could be accomplished. Increasing the Agulhas leakage by strengthening the westerlies would result in other effects on the AMOC driven directly by the change in the winds.

Aside from their importance for the Atlantic Ocean circulation, the warm waters of the Agulhas Current System also give rise to high moisture and heat fluxes into the atmosphere. One mechanism through which the moisture originating from the Agulhas System is transported on land to result in precipitation is the ridging of the South Atlantic Anticyclone over South Africa. In Chapter 5 these ridging highs were categorized for the first time based on whether they are accompanied by Rossby wave breaking (RWB) aloft or not. It was found that 44% of ridging highs occur together with RWB aloft and that RWB impacts the evolution of the ridging highs, the amount of precipitation they result in and their response to increasing GHGs. Ridging highs accompanied by RWB result in more than double the precipitation contributed by ridging highs without RWB in the summer rainfall regions of South Africa. They are also more affected by the future increase in GHGs than ridging highs that occur on their own, contributing more precipitation over the south coast and less precipitation in the summer rainfall region in the future. Ridging highs occurring without RWB do not exhibit significant future changes in their contribution to precipitation. This is because the effect of GHGs on ridging highs is mediated by RWB. The poleward shift in the westerly jet in the future is accompanied by a poleward shift of the region where RWB occurs. At the surface, this alters the sea level pressure anomalies associated with ridging highs such that the winds become more easterly and are more suitable for transporting moisture from above the Agulhas Current, therefore leading to more precipitation.

The investigation of past and future Southern Hemispheric changes offered the opportunity to study the role played by the method used to represent the ozone field in accurately simulating these changes. Simulations with interactively calculated ozone chemistry were compared to simulations in which the ozone field recommended for CMIP6 was prescribed, with the aim of answering the question:

4. **How does the representation of stratospheric ozone in climate models affect the simulated dynamics and what are the implications for future climate model intercomparison projects?**

In both past (Chapter 3) and future (Chapter 4) simulations, the effects of changes in stratospheric ozone were found to be weaker when the CMIP6 ozone field was prescribed compared to when the ozone field was calculated interactively. However, the primary cause of the weaker ozone impacts differs between past and future simulations. The differences in the simulated changes between simulations with interactive and simulations with prescribed CMIP6 ozone and the causes of these differences are first summarized in the following, before a recommendation for future climate model intercomparison projects is offered.

For the past simulations, the ozone hole is stronger in the CMIP6 field than in FOCI, but the associated cooling of the polar lower stratosphere is weaker when the CMIP6 ozone is prescribed. As a result of the weaker polar cap cooling, the strengthening of the polar vortex is also weaker when the CMIP6 ozone is prescribed. This implies that the difference in the magnitude of ozone depletion does not drive the difference in the magnitude of the temperature and dynamical changes. Instead, it was shown that the polar lower stratosphere is dynamically cooled in austral spring in the simulations with interactive ozone, but this cooling is absent when the CMIP6 is prescribed. This dynamical cooling enhances the direct, radiative cooling due to ozone loss in the simulations with interactive ozone and results in a stronger total temperature decrease in these simulations, despite a weaker ozone loss. In the time mean, the CMIP6 ozone hole was found to exhibit a different displacement from the polar cap than that simulated by FOCI, demonstrating that the prescribed ozone hole is not consistent with the simulated polar vortex. The fact that the prescribed ozone hole is not collocated with the simulated polar vortex alters the propagation of wave activity from the troposphere and leads to the absence of this dynamical effect in the simulations with prescribed CMIP6 ozone.

In contrast, the future ozone recovery is much weaker in the CMIP6 field than in FOCI, or other chemistry-climate models (CCMs). In a recent study published after the publication presented in Chapter 4, *Revell et al.* (2022) pointed out that the GHG concentrations used to produce the twenty-first century CMIP6 ozone followed the old emission scenarios used in CMIP5, the RCPs. While the RCPs have the same increase in radiative forcing at the end of the century as their equivalent SSPs, their concentrations of the individual GHGs differ from the SSPs. *Revell et al.* (2022) argued that this is the cause for the slower ozone recovery in the CMIP6 field compared to CCMs. In line with the weaker ozone forcing, the dynamical changes driven by ozone recovery are weaker when the CMIP6 ozone field is prescribed in FOCI, mitigating the effects of the increasing in GHGs to a lesser extent and resulting in significantly stronger net changes. The study by *Revell et al.* (2022) confirmed that these results, obtained using a single model in this thesis, also hold for the models participating in CMIP6: the models that prescribed the CMIP6 ozone field simulated significantly weaker ozone effects than the models that calculated the ozone field interactively.

Chapter 4 highlighted that the impacts of the slower ozone recovery in the CMIP6 field are not confined to the stratosphere, but extend to the surface and to the ocean circulation. The choice of ozone field thus also affects the future projections for the ocean circulation. In fact, for the future changes in the surface westerly jet, in the Agulhas leakage and in the ACC, the magnitude of the difference between simulations with interactive and simulations with prescribed ozone is at least as large as the magnitude of the ozone-driven change in

these fields. This implies that the weaker ozone recovery exhibited by the CMIP6 ozone field is not the sole reason for the differences in the simulated changes between simulations with interactive and simulations with prescribed ozone. It is proposed that additional contributions come from the inconsistencies between the prescribed ozone field and the simulated dynamics, as was the case for the historical simulations, from lack of feedbacks between ozone and dynamics when ozone is prescribed (*Haase et al.*, 2020) and from the temporal interpolation of the prescribed monthly ozone field (*Sassi et al.*, 2005; *Neely et al.*, 2014).

The differences between simulations with prescribed and simulations with interactive ozone highlighted in this thesis raise the question: which method of representing the ozone field is preferable in climate simulations? In terms of which method rendered the changes for the past period that were closest to observations, the answer differs depending on the field of interest. Calculating the ozone interactively resulted in stratospheric temperature changes that are closer to those from observations and reanalyses. In contrast, the results regarding the westerly wind changes depend on the calendar month and on height, making it difficult to draw a clear conclusion.

Additional complications arise from the large internal variability of coupled climate models, as well as from large inter-model differences. The latter explain the difficulty in detecting significant differences in the tropospheric westerly jet trends between the multi-model mean of models with interactive and of models with prescribed ozone, reported by *Son et al.* (2018). The inter-model differences in simulating dynamical changes are larger than differences arising from the use of different ozone fields. In addition, there is a large spread in the ozone fields and in their trends simulated by different CCMs (e.g., *Dhomse et al.*, 2018). This underlines the large uncertainties in the magnitude of future dynamical changes. Therefore, while the choice of ozone field does make a significant difference in the simulated dynamics and their trends, if the focus of a study is on the tropospheric or on the oceanic dynamics, prescribing the ozone field will likely lead to results within the spread of CCMs. Prescribing the ozone field to a single model does lead to differences to the interactive chemistry version of that model, but these differences appear to be within the spread of CCMs.

If the focus of a study is on the stratospheric processes, the ozone field should preferably be calculated interactively, as ozone plays a key role in the stratospheric dynamics, both affecting the circulation through its interaction with radiation and being affected by dynamical changes. In the stratosphere, the differences between the simulations with interactive and the simulations with prescribed ozone were not limited to the magnitude of trends, but also affected the spatial patterns of the dynamics. At present, interactively simulating the ozone

field is the only way to ensure that the ozone field is consistent with the simulated dynamics and that feedbacks between ozone and dynamics can occur.

For future coupled model intercomparison projects, using an interactively calculated ozone field is recommended based on the results of this thesis. Nevertheless, if the ozone field is to be prescribed, an ozone field that includes ozone asymmetries, that has a daily temporal resolution and that is consistent with the intended GHG emission scenario should be used. Furthermore, the recovery of the ozone field should be representative of the multi-model mean simulated by CCMs and not of one end of the distribution, as it is currently the case for the twenty-first century CMIP6 ozone field whose recovery is among the slowest simulated by CCMs.

On the whole, this thesis furthered the current understanding of the effects of the increase in anthropogenic GHGs and of changes in stratospheric ozone on the atmospheric and oceanic circulation in the Southern Hemisphere. In addition, it provided compelling evidence that the choice of the ozone field plays an important role in simulating these effects. The novel insights contributed by this thesis include:

1. the spatial pattern of the springtime stratospheric response to the increase in GHGs, which bears the signature of a PW1;

2. the future changes in the Agulhas Current System;

3. the importance of RWB for the future changes in the ridging of the South Atlantic Anticyclone over South Africa and the associated precipitation changes.

4. the differences in the simulated circulation changes under interactive ozone forcing and under prescribed CMIP6 ozone forcing, and the implications of these differences for future projections.

Several open questions arose from the results of this thesis and were identified in this section. Depending on where the interest lies, future research could explore one of the following topics:

1. The mechanism leading to the PW 1 response in austral spring to increasing GHGs and the reason behind the seasonality of this response. The presence of this response should first be confirmed with more CCMs. CCMs are needed in such a study as the chemical, thermal and dynamical effects of increasing GHGs impact the concentration and distribution of ozone and the GHG-induced ozone changes could contribute to this response. When pursuing this topic, the challenge lies in identifying why the propagation of planetary waves is promoted in certain regions and prohibited in others.

The non-linear nature of the interactions between waves and the mean flow adds complexity to this issue and makes solving it difficult.

2. The response of the ACC to future GHG and ozone forcing in a climate model with an ocean that resolves the mesoscale features globally, or at least over the entire Southern Ocean. This thesis showed that the representation of stratospheric ozone impacts the ocean circulation, implying that interactive ozone chemistry is desirable for such a study. However, a climate model with a global high resolution ocean and interactive ozone chemistry is very expensive computationally. Since for this topic resolving the oceanic mesoscale takes precedence, it is suggested that the daily future ozone field obtained from FOCI in this thesis could be prescribed to a version of the model with high resolution at least in the entire Southern Ocean, to maximize the consistency between the ozone field and the simulated stratospheric dynamics, while also minimizing the computational costs. Such a study would provide the most realistic projection of ACC changes to date, to my knowledge. Comparing the results with the future ACC changes identified in this thesis will additionally provide valuable insights into the performance of the current configuration of FOCI.

3. The impact of future GHG and ozone changes on the Southern Ocean MOC and the contribution of the MOC response to the trends in ocean temperature. The same argumentation and recommendation regarding the oceanic resolution and the ozone chemistry as for the previous point hold here too. In fact, the same ensemble of simulations could be used to study the future of both the ACC and the Southern Ocean MOC. The Eulerian MOC and the eddy-driven MOC would need to be calculated in order to obtain the future change in the residual MOC, representing the net change in transport.

4. The impact of the future increase in Agulhas leakage on the Atlantic Ocean circulation and the potential of offsetting the effects of the melting Greenland ice sheet on the AMOC. Such a study would require a high resolution ocean and would face challenges in separating the contribution of the increase in Agulhas leakage from other effects of climate change. A method to mimic the increase in leakage without altering other aspects of the circulation in the process would first have to be developed.

5. The role played by the ozone-related feedbacks in the future changes in atmospheric circulation. While this thesis revealed large differences between the future predictions obtained with interactive and with prescribed ozone, several factors contributed to these differences and the role played solely by feedbacks involving ozone could not

be isolated. The twenty-first century simulations analyzed in this thesis could be compared to another ensemble of simulations in which the daily ozone field simulated by the interactive ozone chemistry version of the model is prescribed. This would eliminate the effects of prescribing a monthly ozone field that is not consistent with the model dynamics and with the GHG scenario and would reveal the importance of the ozone-related feedbacks.

References

Abalos, M., B. Legras, F. Ploeger, and W. J. Randel (2015), Evaluating the advective Brewer-Dobson circulation in three reanalyses for the period 1979–2012, *Journal of Geophysical Research: Atmospheres*, *120*(15), 7534–7554, doi:10.1002/2015JD023182.

Abalos, M., L. Polvani, N. Calvo, D. Kinnison, F. Ploeger, W. Randel, and S. Solomon (2019), New Insights on the Impact of Ozone-Depleting Substances on the Brewer-Dobson Circulation, *Journal of Geophysical Research: Atmospheres*, *124*(5), 2435–2451, doi:10.1029/2018JD029301.

Abalos, M., N. Calvo, S. Benito-Barca, H. Garny, S. C. Hardiman, P. Lin, M. B. Andrews, N. Butchart, R. Garcia, C. Orbe, D. Saint-Martin, S. Watanabe, and K. Yoshida (2021), The Brewer–Dobson circulation in CMIP6, *Atmospheric Chemistry and Physics*, *21*(17), 13,571–13,591, doi:10.5194/acp-21-13571-2021.

Abernathey, R., J. Marshall, and D. Ferreira (2011), The Dependence of Southern Ocean Meridional Overturning on Wind Stress, *Journal of Physical Oceanography*, *41*(12), 2261 – 2278, doi:10.1175/JPO-D-11-023.1.

Allison, L. C., H. L. Johnson, D. P. Marshall, and D. R. Munday (2010), Where do winds drive the Antarctic Circumpolar Current?, *Geophysical Research Letters*, *37*(12), doi:10.1029/2010GL043355.

Amos, M., P. J. Young, J. S. Hosking, J.-F. Lamarque, N. L. Abraham, H. Akiyoshi, A. T. Archibald, S. Bekki, M. Deushi, P. Jöckel, D. Kinnison, O. Kirner, M. Kunze, M. Marchand, D. A. Plummer, D. Saint-Martin, K. Sudo, S. Tilmes, and Y. Yamashita (2020), Projecting ozone hole recovery using an ensemble of chemistry–climate models weighted by model performance and independence, *Atmospheric Chemistry and Physics*, *20*(16), 9961–9977, doi:10.5194/acp-20-9961-2020.

Andrews, D. G., J. R. Holton, and C. B. Leovy (1987), *Middle Atmosphere Dynamics*, *International Geophysics Series*, vol. 40, 489 pp., Academic Press.

Arblaster, J. M., and G. A. Meehl (2006), Contributions of External Forcings to Southern Annular Mode Trends, *Journal of Climate*, *19*(12), 2896–2905, doi:10.1175/JCLI3774.1.

Arrhenius, P. S. (1896), On the influence of carbonic acid in the air upon the temperature of the ground, *The London, Edinburgh, and Dublin Philosophical Magazine and Journal of Science*, *41*(251), 237–276, doi:10.1080/14786449608620846.

Arrhenius, S. (1908), *Worlds in the Making: the Evolution of the Universe / by Svante Arrhenius; translated to English by H. Borns*, xiii, 229 pp., Harper & Brothers New York and London.

Austin, J., N. Butchart, and K. P. Shine (1992), Possibility of an Arctic ozone hole in a doubled-CO2 climate, *Nature*, *60*, 221–22, doi:10.1038/360221a0.

Baldwin, M. P., and T. J. Dunkerton (2001), Stratospheric Harbingers of Anomalous Weather Regimes, *Science*, *294*(5542), 581–584, doi:10.1126/science.1063315.

Banerjee, A., J. C. Fyfe, L. M. Polvani, D. Waugh, and K.-L. Chang (2020), A pause in Southern Hemisphere circulation trends due to the Montreal Protocol, *Nature*, *579*, 544–548, doi:10.1038/s41586-020-2120-4.

Barnes, E. A., and L. Polvani (2013), Response of the Midlatitude Jets, and of Their Variability, to Increased Greenhouse Gases in the CMIP5 Models, *Journal of Climate*, *26*(18), 7117 – 7135, doi:10.1175/JCLI-D-12-00536.1.

Beal, L. M., and S. Elipot (2016), Broadening not strengthening of the Agulhas Current since the early 1990s, *Nature*, *540*, 570–573, doi:10.1038/nature19853.

Beal, L. M., W. P. De Ruijter, A. Biastoch, R. Zahn, M. Cronin, J. Hermes, J. Lutjeharms, G. Quartly, T. Tozuka, S. Baker-Yeboah, T. Bornman, P. Cipollini, H. Dijkstra, I. Hall, W. Park, F. Peeters, P. Penven, H. Ridderinkhof, J. Zinke, and S. W. G. 136 (2011), On the role of the Agulhas system in ocean circulation and climate, *Nature*, *472*, 429–436, doi:10.1038/nature09983.

Beal, L. M., S. Elipot, A. Houk, and G. M. Leber (2015), Capturing the Transport Variability of a Western Boundary Jet: Results from the Agulhas Current Time-Series Experiment (ACT), *Journal of Physical Oceanography*, *45*(5), 1302 – 1324, doi:10.1175/JPO-D-14-0119.1.

Biastoch, A., and C. W. Böning (2013), Anthropogenic impact on Agulhas leakage, *Geophysical Research Letters*, *40*(6), 1138–1143, doi:10.1002/grl.50243.

Biastoch, A., and W. Krauss (1999), The Role of Mesoscale Eddies in the Source Regions of the Agulhas Current, *Journal of Physical Oceanography*, *29*(9), 2303 – 2317, doi:10.1175/1520-0485(1999)029<2303:TROMEI>2.0.CO;2.

Biastoch, A., C. W. Böning, and J. R. E. Lutjeharms (2008), Agulhas leakage dynamics affects decadal variability in Atlantic overturning circulation, *Nature*, *456*, 489–492, doi:10.1038/nature07426.

Biastoch, A., C. W. Böning, F. U. Schwarzkopf, and J. R. E. Lutjeharms (2009), Increase in Agulhas leakage due to poleward shift of Southern Hemisphere westerlies, *Nature*, *462*(7272), 495–498, doi:10.1038/nature08519.

Biastoch, A., J. V. Durgadoo, A. K. Morrison, E. van Sebille, W. Weijer, and S. M. Griffies (2015), Atlantic multi-decadal oscillation covaries with Agulhas leakage, *Nature Communications*, *6*, 10,082, doi:10.1038/ncomms10082.

Birner, T., and H. Bönisch (2011), Residual circulation trajectories and transit times into the extratropical lowermost stratosphere, *Atmospheric Chemistry and Physics*, *11*(2), 817–827, doi:10.5194/acp-11-817-2011.

Bishop, S. P., P. R. Gent, F. O. Bryan, A. F. Thompson, M. C. Long, and R. Abernathey (2016), Southern Ocean Overturning Compensation in an Eddy-Resolving Climate Simulation, *Journal of Physical Oceanography*, *46*(5), 1575 – 1592, doi:10.1175/JPO-D-15-0177.1.

Blamey, R. C., and C. J. C. Reason (2009), Numerical simulation of a mesoscale convective system over the east coast of South Africa, *Tellus A: Dynamic Meteorology and Oceanography*, *61*(1), 17–34, doi:10.1111/j.1600-0870.2007.00366.x.

Blamey, R. C., and C. J. C. Reason (2012), Mesoscale Convective Complexes over Southern Africa, *Journal of Climate*, *25*(2), 753 – 766, doi:10.1175/JCLI-D-10-05013.1.

Boebel, O., T. Rossby, J. Lutjeharms, W. Zenk, and C. Barron (2003a), Path and variability of the Agulhas Return Current, *Deep Sea Research Part II: Topical Studies in Oceanography*, *50*(1), 35–56, doi:10.1016/S0967-0645(02)00377-6.

Boebel, O., J. Lutjeharms, C. Schmid, W. Zenk, T. Rossby, and C. Barron (2003b), The Cape Cauldron: a regime of turbulent inter-ocean exchange, *Deep Sea Research Part II: Topical Studies in Oceanography*, *50*(1), 57–86, doi:10.1016/S0967-0645(02)00379-X.

Bönisch, H., A. Engel, T. Birner, P. Hoor, D. W. Tarasick, and E. A. Ray (2011), On the structural changes in the Brewer-Dobson circulation after 2000, *Atmospheric Chemistry and Physics*, *11*(8), 3937–3948, doi:10.5194/acp-11-3937-2011.

Brasseur, G. P., and S. Solomon (2005), *Aeronomy of the Middle Atmosphere*, 646 pp., Springer, Dordrecht, doi:10.1007/1-4020-3824-0.

Brasseur, G. P., J. J. Orlando, and G. S. Tyndall (1999), *Atmospheric chemistry and global change*, Oxford University Press.

Brewer, A. W. (1949), Evidence for a world circulation provided by the measurements of helium and water vapour distribution in the stratosphere, *Quarterly Journal of the Royal Meteorological Society*, *75*(326), 351–363, doi:10.1002/qj.49707532603.

Brovkin, V., T. Raddatz, C. H. Reick, M. Claussen, and V. Gayler (2009), Global biogeophysical interactions between forest and climate, *Geophysical Research Letters*, *36*(7), L07,405, doi:10.1029/2009GL037543.

Burls, N. J., R. C. Blamey, B. A. Cash, E. T. Swenson, A. a. Fahad, M.-J. M. Bopape, D. M. Straus, and C. J. C. Reason (2019), The Cape Town "Day Zero" drought and Hadley cell expansion, *npj Climate and Atmospheric Science*, *2*, 27, doi:10.1038/s41612-019-0084-6.

Butchart, N. (2014), The Brewer-Dobson circulation, *Reviews of Geophysics*, *52*(2), 157–184, doi:10.1002/2013RG000448.

Butchart, N., and A. A. Scaife (2001), Removal of chlorofluorocarbons by increased mass exchange between the stratosphere and troposphere in a changing climate, *Nature*, *410*, 799 – 802, doi:10.1038/35071047.

Böning, C. W., A. Dispert, M. Visbeck, S. R. Rintoul, and F. U. Schwarzkopf (2008), The response of the Antarctic Circumpolar Current to recent climate change, *Nature Geoscience*, *1*, 864–869, doi:10.1038/ngeo362.

Calvo, N., and R. R. Garcia (2009), Wave Forcing of the Tropical Upwelling in the Lower Stratosphere under Increasing Concentrations of Greenhouse Gases, *Journal of the Atmospheric Sciences*, *66*(10), 3184 – 3196, doi:10.1175/2009JAS3085.1.

Casanova-Masjoan, M., J. L. Pelegrí, P. Sangrà, A. Martínez, D. Grisolía-Santos, M. D. Pérez-Hernández, and A. Hernández-Guerra (2017), Characteristics and evolution of an Agulhas ring, *Journal of Geophysical Research: Oceans*, *122*(9), 7049–7065, doi:10.1002/2017JC012969.

Charlton, A. J., and L. M. Polvani (2007), A New Look at Stratospheric Sudden Warmings. Part I: Climatology and Modeling Benchmarks, *Journal of Climate*, *20*(3), 449 – 469, doi:10.1175/JCLI3996.1.

Charlton, A. J., A. O'Neill, W. A. Lahoz, and P. Berrisford (2005), The Splitting of the Stratospheric Polar Vortex in the Southern Hemisphere, September 2002: Dynamical Evolution, *Journal of the Atmospheric Sciences*, *62*(3), 590 – 602, doi:10.1175/JAS-3318.1.

Charney, J. G., and P. G. Drazin (1961), Propagation of planetary-scale disturbances from the lower into the upper atmosphere, *Journal of Geophysical Research (1896-1977)*, *66*(1), 83–109.

Chidichimo, M. P., K. A. Donohue, D. R. Watts, and K. L. Tracey (2014), Baroclinic Transport Time Series of the Antarctic Circumpolar Current Measured in Drake Passage, *Journal of Physical Oceanography*, *44*(7), 1829 – 1853, doi:10.1175/JPO-D-13-071.1.

Chiodo, G., and L. M. Polvani (2016), Reduction of Climate Sensitivity to Solar Forcing due to Stratospheric Ozone Feedback, *Journal of Climate*, *29*(12), 4651 – 4663, doi:10.1175/JCLI-D-15-0721.1.

Chiodo, G., L. M. Polvani, D. R. Marsh, A. Stenke, W. Ball, E. Rozanov, S. Muthers, and K. Tsigaridis (2018), The Response of the Ozone Layer to Quadrupled CO2 Concentrations, *Journal of Climate*, *31*(10), 3893 – 3907, doi:10.1175/JCLI-D-17-0492.1.

Chrysanthou, A., A. C. Maycock, and M. P. Chipperfield (2020), Decomposing the response of the stratospheric Brewer–Dobson circulation to an abrupt quadrupling in CO_2, *Weather and Climate Dynamics*, *1*(1), 155–174, doi:10.5194/wcd-1-155-2020.

Cionni, I., V. Eyring, J. F. Lamarque, W. J. Randel, D. S. Stevenson, F. Wu, G. E. Bodeker, T. G. Shepherd, D. T. Shindell, and D. W. Waugh (2011), Ozone database in support of CMIP5 simulations: results and corresponding radiative forcing, *Atmospheric Chemistry and Physics*, *11*(21), 11,267–11,292, doi:10.5194/acp-11-11267-2011.

Cordero, E. C., and P. M. D. F. Forster (2006), Stratospheric variability and trends in models used for the IPCC AR4, *Atmospheric Chemistry and Physics*, *6*(12), 5369–5380, doi:10.5194/acp-6-5369-2006.

Crimp, S. J., and S. J. Mason (1999), The Extreme Precipitation Event of 11 to 16 February 1996 over South Africa, *Meteorology and Atmospheric Physics*, *70*, 29 – 42, doi:10.1007/s007030050023.

Crook, J. A., N. P. Gillett, and S. P. E. Keeley (2008), Sensitivity of Southern Hemisphere climate to zonal asymmetry in ozone, *Geophysical Research Letters*, *35*(7), L07,806, doi:10.1029/2007GL032698.

Cunningham, S. A., S. G. Alderson, B. A. King, and M. A. Brandon (2003), Transport and variability of the Antarctic Circumpolar Current in Drake Passage, *Journal of Geophysical Research: Oceans*, *108*(C5), 8084, doi:10.1029/2001JC001147.

Daher, H., L. M. Beal, and F. U. Schwarzkopf (2020), A New Improved Estimation of Agulhas Leakage Using Observations and Simulations of Lagrangian Floats and Drifters, *Journal of Geophysical Research: Oceans*, *125*(4), e2019JC015,753, doi:10.1029/2019JC015753.

De Ruijter, W. P. M., A. Biastoch, S. S. Drijfhout, J. R. E. Lutjeharms, R. P. Matano, T. Pichevin, P. J. van Leeuwen, and W. Weijer (1999a), Indian-Atlantic interocean exchange: Dynamics, estimation and impact, *Journal of Geophysical Research: Oceans*, *104*(C9), 20,885–20,910, doi:https://doi.org/10.1029/1998JC900099.

De Ruijter, W. P. M., P. J. van Leeuwen, and J. R. E. Lutjeharms (1999b), Generation and Evolution of Natal Pulses: Solitary Meanders in the Agulhas Current, *Journal of Physical Oceanography*, *29*(12), 3043 – 3055, doi:10.1175/1520-0485(1999)029<3043:GAEONP>2.0.CO;2.

Debreu, L., C. Vouland, and E. Blayo (2008), AGRIF: Adaptive grid refinement in Fortran, *Computers & Geosciences*, *34*(1), 8–13, doi:10.1016/j.cageo.2007.01.009.

Dhomse, S. S., D. Kinnison, M. P. Chipperfield, R. J. Salawitch, I. Cionni, M. I. Hegglin, N. L. Abraham, H. Akiyoshi, A. T. Archibald, E. M. Bednarz, S. Bekki, P. Braesicke, N. Butchart, M. Dameris, M. Deushi, S. Frith, S. C. Hardiman, B. Hassler, L. W. Horowitz, R.-M. Hu, P. Jöckel, B. Josse, O. Kirner, S. Kremser, U. Langematz, J. Lewis, M. Marchand, M. Lin, E. Mancini, V. Marécal, M. Michou, O. Morgenstern, F. M. O'Connor, L. Oman, G. Pitari, D. A. Plummer, J. A. Pyle, L. E. Revell, E. Rozanov, R. Schofield, A. Stenke, K. Stone, K. Sudo, S. Tilmes, D. Visioni, Y. Yamashita, and G. Zeng (2018), Estimates of ozone return dates from Chemistry-Climate Model Initiative simulations, *Atmospheric Chemistry and Physics*, *18*(11), 8409–8438, doi:10.5194/acp-18-8409-2018.

Diallo, M., B. Legras, and A. Chédin (2012), Age of stratospheric air in the ERA-Interim, *Atmospheric Chemistry and Physics*, *12*(24), 12,133–12,154, doi:10.5194/acp-12-12133-2012.

Diallo, M., M. Ern, and F. Ploeger (2021), The advective Brewer–Dobson circulation in the ERA5 reanalysis: climatology, variability, and trends, *Atmospheric Chemistry and Physics*, *21*(10), 7515–7544, doi:10.5194/acp-21-7515-2021.

Dickinson, R. E. (1968), Planetary Rossby Waves Propagating Vertically Through Weak Westerly Wind Wave Guides, *Journal of Atmospheric Sciences*, *25*(6), 984 – 1002, doi:10.1175/1520-0469(1968)025<0984:PRWPVT>2.0.CO;2.

Dobson, G. M. B. (1956), Origin and distribution of the polyatomic molecules in the atmosphere, *Proceedings of the Royal Society of London*, *236*(1205), 187–193, doi: 10.1098/rspa.1956.0127.

Dobson, G. M. B., D. N. Harrison, and J. Lawrence (1929), Measurements of the amount of ozone in the Earth's atmosphere and its relation to other geophysical conditions. Part III, *Proceedings of the Royal Society of London*, *122*(790), 456–486, doi:10.1098/rspa.1929.0034.

Donohue, K. A., K. L. Tracey, D. R. Watts, M. P. Chidichimo, and T. K. Chereskin (2016), Mean Antarctic Circumpolar Current transport measured in Drake Passage, *Geophysical Research Letters*, *43*(22), 11,760–11,767, doi:10.1002/2016GL070319.

Durgadoo, J. V., B. R. Loveday, C. J. C. Reason, P. Penven, and A. Biastoch (2013), Agulhas Leakage Predominantly Responds to the Southern Hemisphere Westerlies, *Journal of Physical Oceanography*, *43*(10), 2113–2131, doi:10.1175/JPO-D-13-047.1.

Durgadoo, J. V., S. Rühs, A. Biastoch, and C. W. B. Böning (2017), Indian Ocean sources of Agulhas leakage, *Journal of Geophysical Research: Oceans*, *122*(4), 3481–3499, doi:10.1002/2016JC012676.

Döös, K., and D. J. Webb (1994), The Deacon Cell and the Other Meridional Cells of the Southern Ocean, *Journal of Physical Oceanography*, *24*(2), 429 – 442, doi:10.1175/1520-0485(1994)024<0429:TDCATO>2.0.CO;2.

Elipot, S., and L. M. Beal (2015), Characteristics, Energetics, and Origins of Agulhas Current Meanders and Their Limited Influence on Ring Shedding, *Journal of Physical Oceanography*, *45*(9), 2294 – 2314, doi:10.1175/JPO-D-14-0254.1.

Elipot, S., and L. M. Beal (2018), Observed Agulhas Current Sensitivity to Interannual and Long-Term Trend Atmospheric Forcings, *Journal of Climate*, *31*(8), 3077 – 3098, doi:10.1175/JCLI-D-17-0597.1.

Engel, A., T. Möbius, H. Bönisch, U. Schmidt, R. Heinz, I. Levin, E. Atlas, S. Aoki, T. Nakazawa, S. Sugawara, F. Moore, D. Hurst, J. Elkins, S. Schauffler, A. Andrews, and K. Boering (2009), Age of stratospheric air unchanged within uncertanties over the past 30 years, *Nature Geoscience*, *2*, 28 – 31, doi:10.1038/ngeo388.

Engel, A., H. Bönisch, M. Ullrich, R. Sitals, O. Membrive, F. Danis, and C. Crevoisier (2017), Mean age of stratospheric air derived from AirCore observations, *Atmospheric Chemistry and Physics*, *17*(11), 6825–6838, doi:10.5194/acp-17-6825-2017.

Engelbrecht, C. J., W. A. Landman, F. A. Engelbrecht, and J. Malherbe (2015), A synoptic decomposition of rainfall over the Cape south coast of South Africa, *Climate Dynamics*, *44*, 2589–2607, doi:10.1007/s00382-014-2230-5.

Eyring, V., J. M. Arblaster, I. Cionni, J. Sedláček, J. Perlwitz, P. J. Young, S. Bekki, D. Bergmann, P. Cameron-Smith, W. J. Collins, G. Faluvegi, K.-D. Gottschaldt, L. W. Horowitz, D. E. Kinnison, J.-F. Lamarque, D. R. Marsh, D. Saint-Martin, D. T. Shindell, K. Sudo, S. Szopa, and S. Watanabe (2013), Long-term ozone changes and associated climate impacts in CMIP5 simulations, *Journal of Geophysical Research: Atmospheres*, *118*(10), 5029–5060, doi:10.1002/jgrd.50316.

Farman, J. C., B. G. Gardiner, and J. D. Shanklin (1985), Large losses of total ozone in Antarctica reveal seasonal ClOx/NOx interaction, *Nature*, *315*, 207–210, doi:10.1038/315207a0.

Farneti, R., and T. L. Delworth (2010), The Role of Mesoscale Eddies in the Remote Oceanic Response to Altered Southern Hemisphere Winds, *Journal of Physical Oceanography*, *40*(10), 2348 – 2354, doi:10.1175/2010JPO4480.1.

Farneti, R., T. L. Delworth, A. J. Rosati, S. M. Griffies, and F. Zeng (2010), The Role of Mesoscale Eddies in the Rectification of the Southern Ocean Response to Climate Change, *Journal of Physical Oceanography*, *40*(7), 1539 – 1557, doi:10.1175/2010JPO4353.1.

Favre, A., B. Hewitson, C. Lennard, R. Cerezo-Mota, and M. Tadross (2013), Cut-off Lows in the South Africa region and their contribution to precipitation, *Climate Dynamics*, *41*, 2331–2351, doi:10.1007/s00382-012-1579-6.

Ferreira, D., J. Marshall, C. M. Bitz, S. Solomon, and A. Plumb (2015), Antarctic Ocean and Sea Ice Response to Ozone Depletion: A Two-Time-Scale Problem, *Journal of Climate*, *28*(3), 1206 – 1226, doi:10.1175/JCLI-D-14-00313.1.

Fichefet, T., and M. A. M. Maqueda (1997), Sensitivity of a global sea ice model to the treatment of ice thermodynamics and dynamics, *Journal of Geophysical Research: Oceans*, *102*(C6), 12,609–12,646, doi:10.1029/97JC00480.

Fishman, J., V. Ramanathan, P. J. Crutzen, and S. C. Liu (1979), Tropospheric ozone and climate, *Nature*, *282*, 818–820, doi:10.1038/282818a0.

Fleming, E. L., C. H. Jackman, R. S. Stolarski, and A. R. Douglass (2011), A model study of the impact of source gas changes on the stratosphere for 1850–2100, *Atmospheric Chemistry and Physics*, *11*(16), 8515–8541, doi:10.5194/acp-11-8515-2011.

Fleming, J. R. (1998), *Historical Perspectives on Climate Change*, Oxford University Press, doi:10.1093/oso/9780195078701.001.0001.

Foote, E. (1856), Circumstances Affecting the Heat of the Sun‘s Rays, *The American Journal of Science and Arts*, *66*, 383–384.

Fu, Q., P. Lin, S. Solomon, and D. L. Hartmann (2015), Observational evidence of strengthening of the Brewer-Dobson circulation since 1980, *Journal of Geophysical Research: Atmospheres*, *120*(19), 10,214–10,228, doi:https://doi.org/10.1002/2015JD023657.

Fu, Q., S. Solomon, H. A. Pahlavan, and P. Lin (2019), Observed changes in Brewer–Dobson circulation for 1980–2018, *Environmental Research Letters*, *14*(11), 114,026, doi:10.1088/1748-9326/ab4de7.

Fučkar, N. S., and G. K. Vallis (2007), Interhemispheric influence of surface buoyancy conditions on a circumpolar current, *Geophysical Research Letters*, *34*(14), doi:10.1029/2007GL030379.

Fyfe, J. C., and O. A. Saenko (2006), Simulated changes in the extratropical Southern Hemisphere winds and currents, *Geophysical Research Letters*, *33*(6), L06,701, doi:10.1029/2005GL025332.

Gallego, D., P. Ribera, R. Garcia-Herrera, E. Hernandez, and L. Gimeno (2005), A new look for the Southern Hemisphere jet stream, *Climate Dynamics*, *24*, 607 – 621, doi: 10.1007/s00382-005-0006-7.

Garcia, R. R., and W. J. Randel (2008), Acceleration of the Brewer–Dobson Circulation due to Increases in Greenhouse Gases, *Journal of the Atmospheric Sciences*, *65*(8), 2731 – 2739, doi:10.1175/2008JAS2712.1.

Garcia, R. R., D. E. Kinnison, and D. R. Marsh (2012), "World avoided" simulations with the whole atmosphere community climate model, *Journal of Geophysical Research: Atmospheres*, *117*(D23), doi:10.1029/2012JD018430.

Gent, P. R. (2016), Effects of Southern Hemisphere Wind Changes on the Meridional Overturning Circulation in Ocean Models, *Annual Review of Marine Science*, *8*(1), 79–94, doi:10.1146/annurev-marine-122414-033929.

Gent, P. R., and J. C. Mcwilliams (1990), Isopycnal Mixing in Ocean Circulation Models, *Journal of Physical Oceanography*, *20*(1), 150 – 155, doi:10.1175/1520-0485(1990)020<0150:IMIOCM>2.0.CO;2.

Giglio, D., and G. C. Johnson (2016), Subantarctic and Polar Fronts of the Antarctic Circumpolar Current and Southern Ocean Heat and Freshwater Content Variability: A View from Argo, *Journal of Physical Oceanography*, *46*(3), 749 – 768, doi: 10.1175/JPO-D-15-0131.1.

Gille, J. C., and L. V. Lyjak (1986), Radiative Heating and Cooling Rates in the Middle Atmosphere, *Journal of Atmospheric Sciences*, *43*(20), 2215 – 2229, doi:10.1175/1520-0469(1986)043<2215:RHACRI>2.0.CO;2.

Gillett, N. P., and D. W. J. Thompson (2003), Simulation of Recent Southern Hemisphere Climate Change, *Science*, *302*(5643), 273–275, doi:10.1126/science.1087440.

Gillett, N. P., J. F. Scinocca, D. A. Plummer, and M. C. Reader (2009), Sensitivity of climate to dynamically-consistent zonal asymmetries in ozone, *Geophysical Research Letters*, *36*(10), L10,809, doi:10.1029/2009GL037246.

Giulivi, C. F., and A. L. Gordon (2006), Isopycnal displacements within the Cape Basin thermocline as revealed by the Hydrographic Data Archive, *Deep Sea Research Part I: Oceanographic Research Papers*, *53*(8), 1285–1300, doi:https://doi.org/10.1016/j.dsr.2006.05.011.

Gordon, A. L. (1986), Interocean exchange of thermocline water, *Journal of Geophysical Research: Oceans*, *91*(C4), 5037–5046, doi:https://doi.org/10.1029/JC091iC04p05037.

Gordon, A. L. (2003), The brawniest retroflection, *Nature*, *421*, 904 – 905, doi:10.1038/421904a.

Gordon, A. L., J. R. Lutjeharms, and M. L. Gründlingh (1987), Stratification and circulation at the Agulhas Retroflection, *Deep Sea Research Part A. Oceanographic Research Papers*, *34*(4), 565–599, doi:10.1016/0198-0149(87)90006-9.

Gordon, A. L., R. F. Weiss, W. M. Smethie Jr., and M. J. Warner (1992), Thermocline and intermediate water communication between the south Atlantic and Indian oceans, *Journal of Geophysical Research: Oceans*, *97*(C5), 7223–7240, doi:10.1029/92JC00485.

Grytsai, A. V., O. M. Evtushevsky, O. V. Agapitov, A. R. Klekociuk, and G. P. Milinevsky (2007), Structure and long-term change in the zonal asymmetry in Antarctic total ozone during spring, *Annales Geophysicae*, *25*(2), 361–374.

Gutenberg, B. (1949), New Data on the Lower Stratosphere, *Bulletin of the American Meteorological Society*, *30*(2), 62–64.

Haarsma, R. J., E. J. D. Campos, S. Drijfhout, W. Hazeleger, and C. Severijns (2011), Impacts of interruption of the Agulhas leakage on the tropical Atlantic in coupled ocean–atmosphere simulations, *Climate Dynamics*, *36*, 989–1003, doi:10.1007/s00382-009-0692-7.

Haase, S., and K. Matthes (2019), The importance of interactive chemistry for stratosphere–troposphere coupling, *Atmospheric Chemistry and Physics*, *19*(5), 3417–3432, doi:10.5194/acp-19-3417-2019.

Haase, S., K. Matthes, M. Latif, and N.-E. Omrani (2018), The Importance of a Properly Represented Stratosphere for Northern Hemisphere Surface Variability in the Atmosphere and the Ocean, *Journal of Climate*, *31*(20), 8481 – 8497, doi:10.1175/JCLI-D-17-0520.1.

Haase, S., J. Fricke, T. Kruschke, S. Wahl, and K. Matthes (2020), Sensitivity of the southern hemisphere tropospheric jet response to Antarctic ozone depletion: prescribed versus interactive chemistry, *Atmospheric Chemistry and Physics*, *20*(22), 14,043–14,061, doi:10.5194/acp-20-14043-2020.

Haigh, J. D., and J. A. Pyle (1982), Ozone perturbation experiments in a two-dimensional circulation model, *Quarterly Journal of the Royal Meteorological Society*, *108*(457), 551–574, doi:10.1002/qj.49710845705.

Hallberg, R., and A. Gnanadesikan (2006), The Role of Eddies in Determining the Structure and Response of the Wind-Driven Southern Hemisphere Overturning: Results from the Modeling Eddies in the Southern Ocean (MESO) Project, *Journal of Physical Oceanography*, *36*(12), 2232 – 2252, doi:10.1175/JPO2980.1.

Harrison, M. S. J. (1984), A generalized classification of South African summer rain-bearing synoptic systems, *Journal of Climatology*, *4*(5), 547–560, doi:10.1002/joc.3370040510.

Hart, N. C. G., C. J. C. Reason, and N. Fauchereau (2010), Tropical–Extratropical Interactions over Southern Africa: Three Cases of Heavy Summer Season Rainfall, *Monthly Weather Review*, *138*(7), 2608 – 2623, doi:10.1175/2010MWR3070.1.

Hart, N. C. G., C. J. C. Reason, and N. Fauchereau (2013), Cloud bands over southern Africa: seasonality, contribution to rainfall variability and modulation by the MJO, *Climate Dynamics*, *41*, 1199–1212, doi:10.1007/s00382-012-1589-4.

Hartmann, D. L. (2007), The Atmospheric General Circulation and Its Variability, *Journal of the Meteorological Society of Japan*, *85B*, 123–143, doi:10.2151/jmsj.85B.123.

Haynes, P. H., M. E. McIntyre, T. G. Shepherd, C. J. Marks, and K. P. Shine (1991), On the "Downward Control" of Extratropical Diabatic Circulations by Eddy-Induced Mean Zonal Forces, *Journal of the Atmospheric Sciences*, *48*(4), 651–678, doi:10.1175/1520-0469(1991)048<0651:OTCOED>2.0.CO;2.

Hegglin, M., D. Kinnison, J.-F. Lamarque, and D. Plummer (2016), CCMI ozone in support of CMIP6 - version 1.0, doi:10.22033/ESGF/input4MIPs.1115.

Held, I. M., and A. Y. Hou (1980), Nonlinear Axially Symmetric Circulations in a Nearly Inviscid Atmosphere, *Journal of Atmospheric Sciences*, *37*(3), 515 – 533, doi:10.1175/1520-0469(1980)037<0515:NASCIA>2.0.CO;2.

Hogg, A. M. (2010), An Antarctic Circumpolar Current driven by surface buoyancy forcing, *Geophysical Research Letters*, *37*(23), doi:10.1029/2010GL044777.

Hogg, A. M. C., M. P. Meredith, J. R. Blundell, and C. Wilson (2008), Eddy Heat Flux in the Southern Ocean: Response to Variable Wind Forcing, *Journal of Climate*, *21*(4), 608 – 620, doi:10.1175/2007JCLI1925.1.

Holton, J. R., P. H. Haynes, M. E. McIntyre, A. R. Douglass, R. B. Rood, and L. Pfister (1995), Stratosphere-troposphere exchange, *Reviews of Geophysics*, *33*(4), 403–439, doi:10.1029/95RG02097.

Hoskins, B. J., M. E. McIntyre, and A. W. Robertson (1985), On the use and significance of isentropic potential vorticity maps, *Quarterly Journal of the Royal Meteorological Society*, *111*(470), 877–946, doi:10.1002/qj.49711147002.

Hughes, C. W., and E. R. Ash (2001), Eddy forcing of the mean flow in the Southern Ocean, *Journal of Geophysical Research: Oceans*, *106*(C2), 2713–2722, doi:10.1029/2000JC900332.

IPCC (2013), Contribution of Working Group I to the Fifth Assessment Report of the Intergovernmental Panel on Climate Change, in *Climate Change 2013: The Physical Science Basis.*, edited by T. Stocker, D. Qin, G.-K. Plattner, M. Tignor, S. Allen, J. Boschung, A. Nauels, Y. Xia, V. Bex, and P. Midgley, p. 1535, Cambridge University Press, Cambridge, United Kingdom and New York, NY, USA.

IPCC (2021), *Climate Change 2021: The Physical Science Basis. Contribution of Working Group I to the Sixth Assessment Report of the Intergovernmental Panel on Climate Change*, vol. In Press, Cambridge University Press, Cambridge, United Kingdom and New York, NY, USA, doi:10.1017/9781009157896.

Johnson, G. C., and H. L. Bryden (1989), On the size of the Antarctic Circumpolar Current, *Deep Sea Research Part A. Oceanographic Research Papers*, *36*(1), 39–53, doi:10.1016/0198-0149(89)90017-4.

Jonsson, A. I., J. de Grandpré, V. I. Fomichev, J. C. McConnell, and S. R. Beagley (2004), Doubled CO2-induced cooling in the middle atmosphere: Photochemical analysis of the ozone radiative feedback, *Journal of Geophysical Research: Atmospheres*, *109*(D24), D24,103, doi:10.1029/2004JD005093.

Jucker, M., T. Reichler, and D. W. Waugh (2021), How Frequent Are Antarctic Sudden Stratospheric Warmings in Present and Future Climate?, *Geophysical Research Letters*, *48*(11), e2021GL093,215, doi:10.1029/2021GL093215.

Jury, M. R., H. R. Valentine, and J. R. E. Lutjeharms (1993), Influence of the Agulhas Current on Summer Rainfall along the Southeast Coast of South Africa, *Journal of Applied Meteorology and Climatology*, *32*(7), 1282 – 1287, doi:10.1175/1520-0450(1993)032<1282:IOTACO>2.0.CO;2.

Keeble, J., P. Braesicke, N. L. Abraham, H. K. Roscoe, and J. A. Pyle (2014), The impact of polar stratospheric ozone loss on Southern Hemisphere stratospheric circulation and climate, *Atmospheric Chemistry and Physics*, *14*(24), 13,705–13,717, doi:10.5194/acp-14-13705-2014.

Keeling, C. D. (1960), The Concentration and Isotopic Abundances of Carbon Dioxide in the Atmosphere, *Tellus*, *12*(2), 200–203, doi:https://doi.org/10.1111/j.2153-3490.1960.tb01300.x.

Kennicutt, M. C., D. Bromwich, D. Liggett, B. Njåstad, L. Peck, S. R. Rintoul, C. Ritz, M. J. Siegert, A. Aitken, C. M. Brooks, J. Cassano, S. Chaturvedi, D. Chen, K. Dodds, N. R. Golledge, C. Le Bohec, M. Leppe, A. Murray, P. C. Nath, M. N. Raphael, M. Rogan-Finnemore, D. M. Schroeder, L. Talley, T. Travouillon, D. G. Vaughan, L. Wang, A. T. Weatherwax, H. Yang, and S. L. Chown (2019), Sustained Antarctic Research: A 21st Century Imperative, *One Earth*, *1*(1), 95–113, doi:10.1016/j.oneear.2019.08.014.

Kinnison, D. E., G. P. Brasseur, S. Walters, R. R. Garcia, D. R. Marsh, F. Sassi, V. L. Harvey, C. E. Randall, L. Emmons, J. F. Lamarque, P. Hess, J. J. Orlando, X. X. Tie, W. Randel, L. L. Pan, A. Gettelman, C. Granier, T. Diehl, U. Niemeier, and A. J. Simmons (2007), Sensitivity of chemical tracers to meteorological parameters in the MOZART-3 chemical transport model, *Journal of Geophysical Research: Atmospheres*, *112*(D20), doi:10.1029/2006JD007879.

Knorr, G., and G. Lohmann (2003), Southern Ocean origin for the resumption of Atlantic thermohaline circulation during deglaciation, *Nature*, *424*, 532–536, doi:10.1038/nature01855.

Labitzke, K. (1974), The temperature in the upper stratosphere: Differences between hemispheres, *Journal of Geophysical Research (1896-1977)*, *79*(15), 2171–2175, doi:10.1029/JC079i015p02171.

Labitzke, K. (1977), Interannual Variability of the Winter Stratosphere in the Northern Hemisphere, *Monthly Weather Review*, *105*(6), 762 – 770, doi:10.1175/1520-0493(1977)105<0762:IVOTWS>2.0.CO;2.

Labitzke, K. G., and H. van Loon (1999), *The Stratosphere: Phenomena, History, and Relevance*, 180 pp., Springer Berlin, Heidelberg.

Langematz, U., M. Kunze, K. Krüger, K. Labitzke, and G. L. Roff (2003), Thermal and dynamical changes of the stratosphere since 1979 and their link to ozone and CO2 changes, *Journal of Geophysical Research: Atmospheres*, *108*(D1), ACL 9–1–ACL 9–13, doi:10.1029/2002JD002069.

Le Bars, D., J. V. Durgadoo, H. A. Dijkstra, A. Biastoch, and W. P. M. De Ruijter (2014), An observed 20-year time series of Agulhas leakage, *Ocean Science*, *10*(4), 601–609, doi:10.5194/os-10-601-2014.

Lee, S., and H. Kim (2003), The Dynamical Relationship between Subtropical and Eddy-Driven Jets, *Journal of the Atmospheric Sciences*, *60*(12), 1490 – 1503, doi:10.1175/1520-0469(2003)060<1490:TDRBSA>2.0.CO;2.

Lee, S.-K., W. Park, E. van Sebille, M. O. Baringer, C. Wang, D. B. Enfield, S. G. Yeager, and B. P. Kirtman (2011), What caused the significant increase in Atlantic Ocean heat content since the mid-20th century?, *Geophysical Research Letters*, *38*(17), L17,607, doi:10.1029/2011GL048856.

Lee-Thorp, A. M., M. Rouault, and J. R. E. Lutjeharms (1999), Moisture uptake in the boundary layer above the Agulhas Current: A case study, *Journal of Geophysical Research: Oceans*, *104*(C1), 1423–1430, doi:10.1029/98JC02375.

Li, F., J. Austin, and J. Wilson (2008), The Strength of the Brewer-Dobson Circulation in a Changing Climate: Coupled Chemistry-Climate Model Simulations, *Journal of Climate*, *21*(1), 40–57, doi:10.1175/2007JCLI1663.1.

Li, F., R. S. Stolarski, and P. A. Newman (2009), Stratospheric ozone in the post-CFC era, *Atmospheric Chemistry and Physics*, *9*(6), 2207–2213, doi:10.5194/acp-9-2207-2009.

Li, F., Y. V. Vikhliaev, P. A. Newman, S. Pawson, J. Perlwitz, D. W. Waugh, and A. R. Douglass (2016), Impacts of Interactive Stratospheric Chemistry on Antarctic and Southern Ocean Climate Change in the Goddard Earth Observing System, Version 5 (GEOS-5), *Journal of Climate*, *29*(9), 3199–3218, doi:10.1175/JCLI-D-15-0572.1.

Li, F., P. Newman, S. Pawson, and J. Perlwitz (2018), Effects of Greenhouse Gas Increase and Stratospheric Ozone Depletion on Stratospheric Mean Age of Air in 1960-2010, *Journal of Geophysical Research: Atmospheres*, *123*(4), 2098–2110, doi:10.1002/2017JD027562.

Lin, P., and Q. Fu (2013), Changes in various branches of the Brewer–Dobson circulation from an ensemble of chemistry climate models, *Journal of Geophysical Research: Atmospheres*, *118*(1), 73–84, doi:10.1029/2012JD018813.

Lin, P., D. Paynter, L. Polvani, G. J. P. Correa, Y. Ming, and V. Ramaswamy (2017), Dependence of model-simulated response to ozone depletion on stratospheric polar vortex climatology, *Geophysical Research Letters*, *44*(12), 6391–6398, doi:10.1002/2017GL073862.

Liou, K.-N. (2002), *An Introduction to Atmospheric Radiation*, International geophysics series ; v. 84, 2nd ed., 583 pp., Academic Press, Amsterdam ;.

Loveday, B. R., J. V. Durgadoo, C. J. C. Reason, A. Biastoch, and P. Penven (2014), Decoupling of the Agulhas Leakage from the Agulhas Current, *Journal of Physical Oceanography*, *44*(7), 1776 – 1797, doi:10.1175/JPO-D-13-093.1.

Loveday, B. R., P. Penven, and C. J. C. Reason (2015), Southern Annular Mode and westerly-wind-driven changes in Indian-Atlantic exchange mechanisms, *Geophysical Research Letters*, *42*(12), 4912–4921, doi:10.1002/2015GL064256.

Lubis, S. W., N.-E. Omrani, K. Matthes, and S. Wahl (2016), Impact of the Antarctic Ozone Hole on the Vertical Coupling of the Stratosphere–Mesosphere–Lower Thermosphere System, *Journal of the Atmospheric Sciences*, *73*(6), 2509–2528, doi:10.1175/JAS-D-15-0189.1.

Lumpkin, R., and K. Speer (2007), Global Ocean Meridional Overturning, *Journal of Physical Oceanography*, *37*(10), 2550 – 2562, doi:10.1175/JPO3130.1.

Lutjeharms, J., and J. Cooper (1996), Interbasin leakage through Agulhas current filaments, *Deep Sea Research Part I: Oceanographic Research Papers*, *43*(2), 213–238, doi:10.1016/0967-0637(96)00002-7.

Lutjeharms, J. R. E. (2006), *The Agulhas Current*, 329 pp., Springer Berlin, Heidelberg, doi:10.1007/3-540-37212-1.

Lutjeharms, J. R. E. (2007), Three decades of research on the greater Agulhas Current, *Ocean Science*, *3*(1), 129–147, doi:10.5194/os-3-129-2007.

Lutjeharms, J. R. E., and H. R. Roberts (1988), The Natal pulse: An extreme transient on the Agulhas Current, *Journal of Geophysical Research: Oceans*, *93*(C1), 631–645, doi:https://doi.org/10.1029/JC093iC01p00631.

Lübbecke, J. F., J. V. Durgadoo, and A. Biastoch (2015), Contribution of Increased Agulhas Leakage to Tropical Atlantic Warming, *Journal of Climate*, *28*(24), 9697 – 9706, doi:10.1175/JCLI-D-15-0258.1.

Madec, G., and the NEMO team (2016), *NEMO ocean engine - version 3.6*, p. 406 pp., Note du Pôle de modélisation, Institut Pierre-Simon Laplace (IPSL).

Mahlman, J. D., L. J. Umscheid, and J. P. Pinto (1994), Transport, Radiative, and Dynamical Effects of the Antarctic Ozone Hole: A GFDL "SKYHI" Model Experiment, *Journal of the Atmospheric Sciences*, *51*(4), 489–508, doi:10.1175/1520-0469(1994)051<0489:TRADEO>2.0.CO;2.

Manney, G. L., M. L. Santee, M. Rex, N. J. Livesey, M. C. Pitts, E. R. Veefkind, Pepijn and-Nash, I. Wohltmann, R. Lehmann, L. Froidevaux, L. R. Poole, M. R. Schoeberl, D. P. Haffner, J. Davies, V. Dorokhov, H. Gernandt, B. Johnson, R. Kivi, E. Kyrö, N. Larsen, P. F. Levelt, A. Makshtas, C. T. McElroy, H. Nakajima, M. C. Parrondo, D. W. Tarasick, P. von der Gathen, K. A. Walker, and N. S. Zinoviev (2011), Unprecedented Arctic ozone loss in 2011, *Nature*, *478*, 469–475, doi:10.1038/nature10556.

Manzini, E., B. Steil, C. Brühl, M. A. Giorgetta, and K. Krüger (2003), A new interactive chemistry-climate model: 2. Sensitivity of the middle atmosphere to ozone depletion and increase in greenhouse gases and implications for recent stratospheric cooling, *Journal of Geophysical Research: Atmospheres*, *108*(D14), doi:10.1029/2002JD002977.

Marshall, D. P., M. H. P. Ambaum, J. R. Maddison, D. R. Munday, and L. Novak (2017), Eddy saturation and frictional control of the Antarctic Circumpolar Current, *Geophysical Research Letters*, *44*(1), 286–292, doi:10.1002/2016GL071702.

Marshall, J., and T. Radko (2003), Residual-Mean Solutions for the Antarctic Circumpolar Current and Its Associated Overturning Circulation, *Journal of Physical Oceanography*, *33*(11), 2341 – 2354, doi:10.1175/1520-0485(2003)033<2341:RSFTAC>2.0.CO;2.

Marshall, J., and K. Speer (2012), Closure of the meridional overturning circulation through Southern Ocean upwelling, *Nature Geoscience*, *5*, 171–180, doi:10.1038/ngeo1391.

Matthes, K., B. Funke, M. E. Andersson, L. Barnard, J. Beer, P. Charbonneau, M. A. Clilverd, T. Dudok de Wit, M. Haberreiter, A. Hendry, C. H. Jackman, M. Kretzschmar, T. Kruschke, M. Kunze, U. Langematz, D. R. Marsh, A. C. Maycock, S. Misios, C. J. Rodger, A. A. Scaife, A. Seppälä, M. Shangguan, M. Sinnhuber, K. Tourpali, I. Usoskin, M. van de Kamp, P. T. Verronen, and S. Versick (2017), Solar forcing for CMIP6 (v3.2), *Geoscientific Model Development*, *10*(6), 2247–2302, doi:10.5194/gmd-10-2247-2017.

Matthes, K., A. Biastoch, S. Wahl, J. Harlaß, T. Martin, T. Brücher, A. Drews, D. Ehlert, K. Getzlaff, F. Krüger, W. Rath, M. Scheinert, F. U. Schwarzkopf, T. Bayr, H. Schmidt, and W. Park (2020), The Flexible Ocean and Climate Infrastructure version 1 (FOCI1): mean state and variability, *Geoscientific Model Development*, *13*(6), 2533–2568, doi:10.5194/gmd-13-2533-2020.

McCormick, M. P., H. M. Steele, P. Hamill, W. P. Chu, and T. J. Swissler (1982), Polar Stratospheric Cloud Sightings by SAM II, *Journal of Atmospheric Sciences*, *39*(6), 1387 – 1397, doi:10.1175/1520-0469(1982)039<1387:PSCSBS>2.0.CO;2.

McIntyre, M. E., and T. N. Palmer (1983), Breaking planetary waves in the stratosphere, *Nature*, *305*, 593–600, doi:10.1038/305593a0.

McIntyre, M. E., and T. N. Palmer (1984), The 'surf zone' in the stratosphere, *Journal of Atmospheric and Terrestrial Physics*, *46*(9), 825–849, doi:10.1016/0021-9169(84)90063-1.

McLandress, C., and T. G. Shepherd (2009), Simulated Anthropogenic Changes in the Brewer–Dobson Circulation, Including Its Extension to High Latitudes, *Journal of Climate*, *22*(6), 1516–1540, doi:10.1175/2008JCLI2679.1.

McLandress, C., A. I. Jonsson, D. A. Plummer, M. C. Reader, J. F. Scinocca, and T. G. Shepherd (2010), Separating the Dynamical Effects of Climate Change and Ozone Depletion. Part I: Southern Hemisphere Stratosphere, *Journal of Climate*, *23*(18), 5002–5020, doi:10.1175/2010JCLI3586.1.

McLandress, C., T. G. Shepherd, J. F. Scinocca, D. A. Plummer, M. Sigmond, A. I. Jonsson, and M. C. Reader (2011), Separating the Dynamical Effects of Climate Change and Ozone Depletion. Part II: Southern Hemisphere Troposphere, *Journal of Climate*, *24*(6), 1850–1868, doi:10.1175/2010JCLI3958.1.

Meinshausen, M., Z. R. J. Nicholls, J. Lewis, M. J. Gidden, E. Vogel, M. Freund, U. Beyerle, C. Gessner, A. Nauels, N. Bauer, J. G. Canadell, J. S. Daniel, A. John, P. B. Krummel, G. Luderer, N. Meinshausen, S. A. Montzka, P. J. Rayner, S. Reimann, S. J. Smith, M. van den Berg, G. J. M. Velders, M. K. Vollmer, and R. H. J. Wang (2020), The shared socio-economic pathway (SSP) greenhouse gas concentrations and their extensions to 2500, *Geoscientific Model Development*, *13*(8), 3571–3605, doi:10.5194/gmd-13-3571-2020.

Meredith, M. P., and A. M. Hogg (2006), Circumpolar response of Southern Ocean eddy activity to a change in the Southern Annular Mode, *Geophysical Research Letters*, *33*(16), doi:10.1029/2006GL026499.

Meredith, M. P., P. L. Woodworth, T. K. Chereskin, D. P. Marshall, L. C. Allison, G. R. Bigg, K. Donohue, K. J. Heywood, C. W. Hughes, A. Hibbert, A. M. Hogg, H. L. Johnson, L. Jullion, B. A. King, H. Leach, Y.-D. Lenn, M. A. Morales Maqueda, D. R. Munday, A. C. Naveira Garabato, C. Provost, J.-B. Sallée, and J. Sprintall (2011), Sustained Monitoring of the Southern Ocean at Drake Passage: Past Achievements and Future Priorities, *Reviews of Geophysics*, *49*(4), doi:10.1029/2010RG000348.

Meredith, M. P., A. C. N. Garabato, A. M. Hogg, and R. Farneti (2012), Sensitivity of the Overturning Circulation in the Southern Ocean to Decadal Changes in Wind Forcing, *Journal of Climate*, *25*(1), 99 – 110, doi:10.1175/2011JCLI4204.1.

Molina, M. J., and F. S. Rowland (1974), Stratospheric sink for chlorofluoromethanes: chlorine atom-catalysed destruction of ozone, *Nature*, *249*, 810 – 812, doi:10.1038/249810a0.

Morake, D. M., R. C. Blamey, and C. J. C. Reason (2021), Long-Lived Mesoscale Convective Systems over Eastern South Africa, *Journal of Climate*, *34*(15), 6421 – 6439, doi:10.1175/JCLI-D-20-0851.1.

Morgenstern, O. (2021), The Southern Annular Mode in 6th Coupled Model Intercomparison Project Models, *Journal of Geophysical Research: Atmospheres*, *126*(5), e2020JD034,161, doi:10.1029/2020JD034161.

Morgenstern, O., G. Zeng, S. M. Dean, M. Joshi, N. L. Abraham, and A. Osprey (2014), Direct and ozone-mediated forcing of the Southern Annular Mode by greenhouse gases, *Geophysical Research Letters*, *41*(24), 9050–9057, doi:10.1002/2014GL062140.

Morgenstern, O., K. A. Stone, R. Schofield, H. Akiyoshi, Y. Yamashita, D. E. Kinnison, R. R. Garcia, K. Sudo, D. A. Plummer, J. Scinocca, L. D. Oman, M. E. Manyin, G. Zeng, E. Rozanov, A. Stenke, L. E. Revell, G. Pitari, E. Mancini, G. Di Genova, D. Visioni, S. S. Dhomse, and M. P. Chipperfield (2018), Ozone sensitivity to varying greenhouse gases and ozone-depleting substances in CCMI-1 simulations, *Atmospheric Chemistry and Physics*, *18*(2), 1091–1114, doi:10.5194/acp-18-1091-2018.

Morrison, A. K., and A. M. Hogg (2013), On the Relationship between Southern Ocean Overturning and ACC Transport, *Journal of Physical Oceanography*, *43*(1), 140 – 148, doi:10.1175/JPO-D-12-057.1.

Munday, D. R., L. C. Allison, H. L. Johnson, and D. P. Marshall (2011), Remote forcing of the Antarctic Circumpolar Current by diapycnal mixing, *Geophysical Research Letters*, *38*(8), doi:10.1029/2011GL046849.

Munday, D. R., H. L. Johnson, and D. P. Marshall (2013), Eddy Saturation of Equilibrated Circumpolar Currents, *Journal of Physical Oceanography*, *43*(3), 507 – 532, doi:10.1175/JPO-D-12-095.1.

Munk, W. H., and E. Palmén (1951), Note on the Dynamics of the Antarctic Circumpolar Current, *Tellus*, *3*(1), 53–55, doi:10.1111/j.2153-3490.1951.tb00776.x.

Ndarana, T., and D. W. Waugh (2010), The link between cut-off lows and Rossby wave breaking in the Southern Hemisphere, *Quarterly Journal of the Royal Meteorological Society*, *136*(649), 869–885, doi:10.1002/qj.627.

Ndarana, T., M.-J. Bopape, D. Waugh, and L. Dyson (2018), The Influence of the Lower Stratosphere on Ridging Atlantic Ocean Anticyclones over South Africa, *Journal of Climate*, *31*(15), 6175 – 6187, doi:10.1175/JCLI-D-17-0832.1.

Ndarana, T., S. Mpati, M.-J. Bopape, F. Engelbrecht, and H. Chikoore (2021), The flow and moisture fluxes associated with ridging South Atlantic Ocean anticyclones during the subtropical southern African summer, *International Journal of Climatology*, *41*(S1), E1000–E1017, doi:10.1002/joc.6745.

Ndarana, T., T. S. Rammopo, C. J. Reason, M.-J. Bopape, F. Engelbrecht, and H. Chikoore (2022), Two types of ridging South Atlantic Ocean anticyclones over South Africa and the associated dynamical processes, *Atmospheric Research*, *265*, 105,897, doi:10.1016/j.atmosres.2021.105897.

Neely, R. R., D. R. Marsh, K. L. Smith, S. M. Davis, and L. M. Polvani (2014), Biases in Southern Hemisphere climate trends induced by coarsely specifying the temporal resolution of stratospheric ozone, *Geophysical Research Letters*, *41*(23), 8602–8610, doi:10.1002/2014GL061627.

Newman, P. A., L. D. Oman, A. R. Douglass, E. L. Fleming, S. M. Frith, M. M. Hurwitz, S. R. Kawa, C. H. Jackman, N. A. Krotkov, E. R. Nash, J. E. Nielsen, S. Pawson, R. S. Stolarski, and G. J. M. Velders (2009), What would have happened to the ozone layer if chlorofluorocarbons (CFCs) had not been regulated?, *Atmospheric Chemistry and Physics*, *9*(6), 2113–2128, doi:10.5194/acp-9-2113-2009.

Nkwinkwa Njouodo, A. S., S. Koseki, N. Keenlyside, and M. Rouault (2018), Atmospheric Signature of the Agulhas Current, *Geophysical Research Letters*, *45*(10), 5185–5193, doi:10.1029/2018GL077042.

Nkwinkwa Njouodo, A. S., M. Rouault, N. Keenlyside, and S. Koseki (2021), Impact of the Agulhas Current on southern Africa precipitation: a modelling study, *Journal of Climate*, pp. 1 – 50, doi:10.1175/JCLI-D-20-0627.1.

Oberländer, S., U. Langematz, and S. Meul (2013), Unraveling impact factors for future changes in the Brewer-Dobson circulation, *Journal of Geophysical Research: Atmospheres*, *118*(18), 10,296–10,312, doi:10.1002/jgrd.50775.

Oberländer-Hayn, S., S. Meul, U. Langematz, J. Abalichin, and F. Haenel (2015), A chemistry-climate model study of past changes in the Brewer-Dobson circulation, *Journal of Geophysical Research: Atmospheres*, *120*(14), 6742–6757, doi:10.1002/2014JD022843.

Olbers, D., D. Borowski, C. Völker, and J.-O. Wölff (2004), *Antarctic Science*, *16*(4), 439–470, doi:10.1017/S0954102004002251.

Oman, L., D. W. Waugh, S. Pawson, R. S. Stolarski, and P. A. Newman (2009), On the influence of anthropogenic forcings on changes in the stratospheric mean age, *Journal of Geophysical Research: Atmospheres*, *114*(D3), doi:10.1029/2008JD010378.

Orr, A., T. J. Bracegirdle, J. S. Hosking, T. Jung, J. D. Haigh, T. Phillips, and W. Feng (2012), Possible Dynamical Mechanisms for Southern Hemisphere Climate Change due to the Ozone Hole, *Journal of the Atmospheric Sciences*, *69*(10), 2917–2932, doi:10.1175/JAS-D-11-0210.1.

Orr, A., T. J. Bracegirdle, J. S. Hosking, W. Feng, H. K. Roscoe, and J. D. Haigh (2013), Strong Dynamical Modulation of the Cooling of the Polar Stratosphere Associated with the Antarctic Ozone Hole, *Journal of Climate*, *26*(2), 662–668, doi:10.1175/JCLI-D-12-00480.1.

Orr, A., H. Lu, P. Martineau, E. P. Gerber, G. J. Marshall, and T. J. Bracegirdle (2021), Is our dynamical understanding of the circulation changes associated with the Antarctic ozone hole sensitive to the choice of reanalysis dataset?, *Atmospheric Chemistry and Physics*, *21*(10), 7451–7472, doi:10.5194/acp-21-7451-2021.

Orsi, A. H., T. Whitworth, and W. D. Nowlin (1995), On the meridional extent and fronts of the Antarctic Circumpolar Current, *Deep Sea Research Part I: Oceanographic Research Papers*, *42*(5), 641–673, doi:10.1016/0967-0637(95)00021-W.

Ou, H. W. O., and W. P. M. De Ruijter (1986), Separation of an Inertial Boundary Current from a Curved Coastline, *Journal of Physical Oceanography*, *16*(2), 280 – 289, doi:10.1175/1520-0485(1986)016<0280:SOAIBC>2.0.CO;2.

Palmer, C. E. (1959), The stratospheric polar vortex in winter, *Journal of Geophysical Research (1896-1977)*, *64*(7), 749–764, doi:10.1029/JZ064i007p00749.

Panetta, R. L. (1993), Zonal Jets in Wide Baroclinically Unstable Regions: Persistence and Scale Selection, *Journal of Atmospheric Sciences*, *50*(14), 2073 – 2106, doi:10.1175/1520-0469(1993)050<2073:ZJIWBU>2.0.CO;2.

Peeters, F. J. C., R. Acheson, G.-J. A. Brummer, W. P. M. de Ruijter, R. R. Schneider, G. M. Ganssen, E. Ufkes, and D. Kroon (2004), Vigorous exchange between the Indian and Atlantic oceans at the end of the past five glacial periods, *Nature*, *430*, 661–665, doi:10.1038/nature02785.

Perlwitz, J., S. Pawson, R. L. Fogt, J. E. Nielsen, and W. D. Neff (2008), Impact of stratospheric ozone hole recovery on Antarctic climate, *Geophysical Research Letters*, *35*(8), 10.1029/2008GL033,317.

Petty, G. W. (2006), *A first course in atmospheric radiation*, 2nd ed., 459 pp., Sundog Publishing, Madison, Wisconsin.

Ploeger, F., B. Legras, E. Charlesworth, X. Yan, M. Diallo, P. Konopka, T. Birner, M. Tao, A. Engel, and M. Riese (2019), How robust are stratospheric age of air trends from different reanalyses?, *Atmospheric Chemistry and Physics*, *19*(9), 6085–6105, doi:10.5194/acp-19-6085-2019.

Plumb, R. A. (2002), Stratospheric transport, *Journal of the Meteorological Society of Japan. Ser. II*, *80*(4B), 793–809, doi:10.2151/jmsj.80.793.

Plumb, R. A. (2007), Tracer interrelationships in the stratosphere, *Reviews of Geophysics*, *45*(4), doi:10.1029/2005RG000179.

Polvani, L. M., D. W. Waugh, G. J. P. Correa, and S.-W. Son (2011), Stratospheric Ozone Depletion: The Main Driver of Twentieth-Century Atmospheric Circulation Changes in the Southern Hemisphere, *Journal of Climate*, *24*(3), 795–812, doi:10.1175/2010JCLI3772.1.

Polvani, L. M., L. Wang, M. Abalos, N. Butchart, M. P. Chipperfield, M. Dameris, M. Deushi, S. S. Dhomse, P. Jöckel, D. Kinnison, M. Michou, O. Morgenstern, L. D. Oman, D. A. Plummer, and K. A. Stone (2019), Large Impacts, Past and Future, of Ozone-Depleting Substances on Brewer-Dobson Circulation Trends: A Multimodel Assessment, *Journal of Geophysical Research: Atmospheres*, *124*(13), 6669–6680, doi:10.1029/2018JD029516.

Portmann, R. W., and S. Solomon (2007), Indirect radiative forcing of the ozone layer during the 21st century, *Geophysical Research Letters*, *34*(2), L02,813, doi:10.1029/2006GL028252.

Previdi, M., and L. M. Polvani (2014), Climate system response to stratospheric ozone depletion and recovery, *Quarterly Journal of the Royal Meteorological Society*, *140*(685), 2401–2419, doi:10.1002/qj.2330.

Randel, W. J., and F. Wu (1999), Cooling of the Arctic and Antarctic Polar Stratospheres due to Ozone Depletion, *Journal of Climate*, *12*(5), 1467–1479, doi:10.1175/1520-0442(1999)012<1467:COTAAA>2.0.CO;2.

Rapolaki, R. S., R. C. Blamey, J. C. Hermes, and C. J. C. Reason (2020), Moisture sources associated with heavy rainfall over the Limpopo River Basin, southern Africa, *Climate Dynamics*, *55*, 1473 – 1487, doi:10.1007/s00382-020-05336-w.

Reason, C., and H. Mulenga (1999), Relationships between South African rainfall and SST anomalies in the Southwest Indian Ocean, *International Journal of Climatology*, *19*(15), 1651–1673, doi:10.1002/(SICI)1097-0088(199912)19:15<1651::AID-JOC439>3.0.CO;2-U.

Reason, C. J. C. (2001), Evidence for the Influence of the Agulhas Current on Regional Atmospheric Circulation Patterns, *Journal of Climate*, *14*(12), 2769 – 2778, doi:10.1175/1520-0442(2001)014<2769:EFTIOT>2.0.CO;2.

Reick, C. H., T. Raddatz, V. Brovkin, and V. Gayler (2013), Representation of natural and anthropogenic land cover change in MPI-ESM, *Journal of Advances in Modeling Earth Systems*, *5*(3), 459–482, doi:10.1002/jame.20022.

Revell, L. E., G. E. Bodeker, P. E. Huck, B. E. Williamson, and E. Rozanov (2012), The sensitivity of stratospheric ozone changes through the 21st century to N_2O and CH_4, *Atmospheric Chemistry and Physics*, *12*(23), 11,309–11,317, doi:10.5194/acp-12-11309-2012.

Revell, L. E., F. Robertson, H. Douglas, O. Morgenstern, and D. Frame (2022), Influence of Ozone Forcing on 21st Century Southern Hemisphere Surface Westerlies in CMIP6 Models, *Geophysical Research Letters*, *49*(6), e2022GL098,252, doi:10.1029/2022GL098252.

Richardson, P. L. (2007), Agulhas leakage into the Atlantic estimated with subsurface floats and surface drifters, *Deep Sea Research Part I: Oceanographic Research Papers*, *54*(8), 1361–1389, doi:10.1016/j.dsr.2007.04.010.

Rind, D., R. Suozzo, N. K. Balachandran, and M. J. Prather (1990), Climate Change and the Middle Atmosphere. Part I: The Doubled CO2 Climate, *Journal of Atmospheric Sciences*, *47*(4), 475 – 494, doi:10.1175/1520-0469(1990)047<0475:CCATMA>2.0.CO;2.

Rintoul, S. R., and C. E. da Silva (2019), Antarctic Circumpolar Current, in *Encyclopedia of Ocean Sciences (Third Edition)*, edited by J. K. Cochran, H. J. Bokuniewicz, and P. L. Yager, third edition ed., pp. 248–261, Academic Press, Oxford, doi: 10.1016/B978-0-12-409548-9.11298-9.

Rintoul, S. R., and A. C. Naveira Garabato (2013), Chapter 18 - Dynamics of the Southern Ocean Circulation, in *Ocean Circulation and Climate*, *International Geophysics*, vol. 103, edited by G. Siedler, S. M. Griffies, J. Gould, and J. A. Church, pp. 471–492, Academic Press, doi:10.1016/B978-0-12-391851-2.00018-0.

Rintoul, S. R., C. W. Hughes, and D. Olbers (2001), Chapter 4.6 The Antarctic Circumpolar Current System, in *Ocean Circulation and Climate*, *International Geophysics*, vol. 77, edited by G. Siedler, J. Church, and J. Gould, pp. 271–XXXVI, Academic Press, doi: 10.1016/S0074-6142(01)80124-8.

Roffe, S., J. Fitchett, and C. Curtis (2019), Classifying and mapping rainfall seasonality in South Africa: a review, *South African Geographical Journal*, *101*(2), 158–174, doi: 10.1080/03736245.2019.1573151.

Roscoe, H. K., J. D. Shanklin, and S. R. Colwell (2005), Has the Antarctic Vortex Split before 2002?, *Journal of the Atmospheric Sciences*, *62*(3), 581 – 588, doi:10.1175/JAS-3331.1.

Rosenfield, J. E., A. R. Douglass, and D. B. Considine (2002), The impact of increasing carbon dioxide on ozone recovery, *Journal of Geophysical Research: Atmospheres*, *107*(D6), ACH 7–1–ACH 7–9, doi:10.1029/2001JD000824.

Rouault, M., A. M. Lee-Thorp, and J. R. E. Lutjeharms (2000), The Atmospheric Boundary Layer above the Agulhas Current during Alongcurrent Winds, *Journal of Physical Oceanography*, *30*(1), 40 – 50, doi:10.1175/1520-0485(2000)030<0040:TABLAT>2.0.CO;2.

Rouault, M., P. Penven, and B. Pohl (2009), Warming in the Agulhas Current system since the 1980's, *Geophysical Research Letters*, *36*(12), L12,602, doi:10.1029/2009GL037987.

Rühs, S., F. U. Schwarzkopf, S. Speich, and A. Biastoch (2019), Cold vs. warm water route – sources for the upper limb of the Atlantic Meridional Overturning Circulation revisited in a high-resolution ocean model, *Ocean Science*, *15*(3), 489–512, doi:10.5194/os-15-489-2019.

Sassi, F., B. A. Boville, D. Kinnison, and R. R. Garcia (2005), The effects of interactive ozone chemistry on simulations of the middle atmosphere, *Geophysical Research Letters*, *32*(7), doi:10.1029/2004GL022131.

Scherhag, R. (1948), *Neue Methoden der Wetteranalyse und Wetterprognose*, 424 pp., Springer Berlin, Heidelberg.

Scherhag, R. (1952), Die explosionsartige Stratosphärenerwärmung des Spätwinters 1951/52., *Berichte des Deutschen Wetterdienstes in der US-Zone*, *38*, 51–63.

Schoeberl, M., and P. Newman (2015), Middle Atmosphere: Polar Vortex, in *Encyclopedia of Atmospheric Sciences (Second Edition)*, edited by G. R. North, J. Pyle, and F. Zhang, second edition ed., pp. 12–17, Academic Press, Oxford, doi:10.1016/B978-0-12-382225-3.00228-0.

Schoeberl, M. R., and D. L. Hartmann (1991), The Dynamics of the Stratospheric Polar Vortex and Its Relation to Springtime Ozone Depletions, *Science*, *251*(4989), 46–52, doi:10.1126/science.251.4989.46.

Schouten, M. W., W. P. M. de Ruijter, P. J. van Leeuwen, and J. R. E. Lutjeharms (2000), Translation, decay and splitting of Agulhas rings in the southeastern Atlantic Ocean, *Journal of Geophysical Research: Oceans*, *105*(C9), 21,913–21,925, doi:https://doi.org/10.1029/1999JC000046.

Schultz, M. G., S. Stadtler, S. Schröder, D. Taraborrelli, B. Franco, J. Krefting, A. Henrot, S. Ferrachat, U. Lohmann, D. Neubauer, C. Siegenthaler-Le Drian, S. Wahl, H. Kokkola, T. Kühn, S. Rast, H. Schmidt, P. Stier, D. Kinnison, G. S. Tyndall, J. J. Orlando, and C. Wespes (2018), The chemistry-climate model ECHAM6.3-HAM2.3-MOZ1.0, *Geoscientific Model Development*, *11*(5), 1695–1723, doi:10.5194/gmd-11-1695-2018.

Schwarzkopf, F. U., A. Biastoch, C. W. Böning, J. Chanut, J. V. Durgadoo, K. Getzlaff, J. Harlaß, J. K. Rieck, C. Roth, M. M. Scheinert, and R. Schubert (2019), The INALT family – a set of high-resolution nests for the Agulhas Current system within global NEMO ocean/sea-ice configurations, *Geoscientific Model Development*, *12*(7), 3329–3355, doi:10.5194/gmd-12-3329-2019.

Seviour, W. J. M., A. Gnanadesikan, and D. W. Waugh (2016), The Transient Response of the Southern Ocean to Stratospheric Ozone Depletion, *Journal of Climate*, *29*(20), 7383 – 7396, doi:10.1175/JCLI-D-16-0198.1.

Seviour, W. J. M., F. Codron, E. W. Doddridge, D. Ferreira, A. Gnanadesikan, M. Kelley, Y. Kostov, J. Marshall, L. M. Polvani, J. L. Thomas, and D. W. Waugh (2019), The Southern Ocean Sea Surface Temperature Response to Ozone Depletion: A Multimodel Comparison, *Journal of Climate*, *32*(16), 5107 – 5121, doi:10.1175/JCLI-D-19-0109.1.

Shannon, L. V. (1985), The Benguela ecosystem. I: Evolution of the Benguela physical features and processes, *Oceanography and Marine Biology*, *23*, 105–182.

Singleton, A. T., and C. J. C. Reason (2006), Numerical simulations of a severe rainfall event over the Eastern Cape coast of South Africa: sensitivity to sea surface temperature and topography, *Tellus A: Dynamic Meteorology and Oceanography*, *58*(3), 335–367, doi:10.1111/j.1600-0870.2006.00180.x.

Singleton, A. T., and C. J. C. Reason (2007a), Variability in the characteristics of cut-off low pressure systems over subtropical southern Africa, *International Journal of Climatology*, *27*(3), 295–310, doi:10.1002/joc.1399.

Singleton, A. T., and C. J. C. Reason (2007b), A Numerical Model Study of an Intense Cutoff Low Pressure System over South Africa, *Monthly Weather Review*, *135*(3), 1128 – 1150, doi:10.1175/MWR3311.1.

Solomon, A., L. M. Polvani, K. L. Smith, and R. P. Abernathey (2015), The impact of ozone depleting substances on the circulation, temperature, and salinity of the Southern Ocean: An attribution study with CESM1(WACCM), *Geophysical Research Letters*, *42*(13), 5547–5555, doi:https://doi.org/10.1002/2015GL064744.

Solomon, S. (1999), Stratospheric ozone depletion: A review of concepts and history, *Reviews of Geophysics*, *37*(3), 275–316, doi:10.1029/1999RG900008.

Solomon, S., R. R. Garcia, F. S. Rowland, and D. J. Wuebbles (1986), On the depletion of Antarctic ozone, *Nature*, *321*, 755–758, doi:10.1038/321755a0.

Solomon, S., D. J. Ivy, D. Kinnison, M. J. Mills, R. R. Neely, and A. Schmidt (2016), Emergence of healing in the Antarctic ozone layer, *Science*, *353*(6296), 269–274, doi:10.1126/science.aae0061.

Solomon, S., D. Ivy, M. Gupta, J. Bandoro, B. Santer, Q. Fu, P. Lin, R. R. Garcia, D. Kinnison, and M. Mills (2017), Mirrored changes in Antarctic ozone and stratospheric temperature in the late 20th versus early 21st centuries, *Journal of Geophysical Research: Atmospheres*, *122*(16), 8940–8950, doi:10.1002/2017JD026719.

Son, S.-W., L. M. Polvani, D. W. Waugh, H. Akiyoshi, R. Garcia, D. Kinnison, S. Pawson, E. Rozanov, T. G. Shepherd, and K. Shibata (2008), The Impact of Stratospheric Ozone Recovery on the Southern Hemisphere Westerly Jet, *Science*, *320*(5882), 1486–1489, doi:10.1126/science.1155939.

Son, S.-W., E. P. Gerber, J. Perlwitz, L. M. Polvani, N. P. Gillett, K.-H. Seo, V. Eyring, T. G. Shepherd, D. Waugh, H. Akiyoshi, J. Austin, A. Baumgaertner, S. Bekki, P. Braesicke, C. Brühl, N. Butchart, M. P. Chipperfield, D. Cugnet, M. Dameris, S. Dhomse, S. Frith, H. Garny, R. Garcia, S. C. Hardiman, P. Jöckel, J. F. Lamarque, E. Mancini, M. Marchand, M. Michou, T. Nakamura, O. Morgenstern, G. Pitari, D. A. Plummer, J. Pyle, E. Rozanov, J. F. Scinocca, K. Shibata, D. Smale, H. Teyssèdre, W. Tian, and Y. Yamashita (2010), Impact of stratospheric ozone on Southern Hemisphere circulation change: A multimodel assessment, *Journal of Geophysical Research: Atmospheres*, *115*(D3), doi:10.1029/2010JD014271.

Son, S.-W., B.-R. Han, C. I. Garfinkel, S.-Y. Kim, R. Park, N. L. Abraham, H. Akiyoshi, A. T. Archibald, N. Butchart, M. P. Chipperfield, M. Dameris, M. Deushi, S. S. Dhomse, S. C. Hardiman, P. Jöckel, D. Kinnison, M. Michou, O. Morgenstern, F. M. O'Connor, L. D. Oman, D. A. Plummer, A. Pozzer, L. E. Revell, E. Rozanov, A. Stenke, K. Stone, S. Tilmes, Y. Yamashita, and G. Zeng (2018), Tropospheric jet response to Antarctic ozone depletion: An update with Chemistry-Climate Model Initiative (CCMI) models, *Environmental Research Letters*, *13*(5), 054,024, doi:10.1088/1748-9326/aabf21.

Speer, K., S. R. Rintoul, and B. Sloyan (2000), The Diabatic Deacon Cell, *Journal of Physical Oceanography*, *30*(12), 3212 – 3222, doi:10.1175/1520-0485(2000)030<3212:TDDC>2.0.CO;2.

Speich, S., B. Blanke, and G. Madec (2001), Warm and cold water routes of an O.G.C.M. thermohaline conveyor belt, *Geophysical Research Letters*, *28*(2), 311–314, doi:10.1029/2000GL011748.

Stevens, B., M. Giorgetta, M. Esch, T. Mauritsen, T. Crueger, S. Rast, M. Salzmann, H. Schmidt, J. Bader, K. Block, R. Brokopf, I. Fast, S. Kinne, L. Kornblueh, U. Lohmann, R. Pincus, T. Reichler, and E. Roeckner (2013), Atmospheric component of the MPI-M Earth System Model: ECHAM6, *Journal of Advances in Modeling Earth Systems*, *5*(2), 146–172, doi:10.1002/jame.20015.

Stiller, G. P., T. von Clarmann, F. Haenel, B. Funke, N. Glatthor, U. Grabowski, S. Kellmann, M. Kiefer, A. Linden, S. Lossow, and M. López-Puertas (2012), Observed temporal evolution of global mean age of stratospheric air for the 2002 to 2010 period, *Atmospheric Chemistry and Physics*, *12*(7), 3311–3331, doi:10.5194/acp-12-3311-2012.

Stramma, L., and J. R. E. Lutjeharms (1997), The flow field of the subtropical gyre of the South Indian Ocean, *Journal of Geophysical Research: Oceans*, *102*(C3), 5513–5530, doi:10.1029/96JC03455.

Straub, D. N. (1993), On the Transport and Angular Momentum Balance of Channel Models of the Antarctic Circumpolar Current, *Journal of Physical Oceanography*, *23*(4), 776 – 782, doi:10.1175/1520-0485(1993)023<0776:OTTAAM>2.0.CO;2.

Thompson, D. W. J., and S. Solomon (2002), Interpretation of Recent Southern Hemisphere Climate Change, *Science*, *296*(5569), 895–899, doi:10.1126/science.1069270.

Thompson, D. W. J., and J. M. Wallace (2000), Annular Modes in the Extratropical Circulation. Part I: Month-to-Month Variability, *Journal of Climate*, *13*(5), 1000 – 1016, doi:10.1175/1520-0442(2000)013<1000:AMITEC>2.0.CO;2.

Thompson, D. W. J., S. Solomon, P. J. Kushner, M. H. England, K. M. Grise, and D. J. Karoly (2011), Signatures of the Antarctic ozone hole in Southern Hemisphere surface climate change, *Nature Geoscience*, *4*, 741–749, doi:10.1038/ngeo1296.

Tim, N., E. Zorita, F. U. Schwarzkopf, S. Rühs, K.-C. Emeis, and A. Biastoch (2018), The Impact of Agulhas Leakage on the Central Water Masses in the Benguela Upwelling System From A High-Resolution Ocean Simulation, *Journal of Geophysical Research: Oceans*, *123*(12), 9416–9428, doi:10.1029/2018JC014218.

Treguier, A. M., I. M. Held, and V. D. Larichev (1997), Parameterization of Quasigeostrophic Eddies in Primitive Equation Ocean Models, *Journal of Physical Oceanography*, *27*(4), 567 – 580, doi:10.1175/1520-0485(1997)027<0567:POQEIP>2.0.CO;2.

Tyndall, J. (1859), On the transmission of heat of different qualities through gases of different kinds, *Proceedings of the Royal Institution of Great Britain*, *3*, 155–158.

Tyndall, J. (1861), The Bakerian Lecture: On the absorption and radiation of heat by gases and vapours, and on the physical connexion of radiation, absorption and conduction, *Philosophical Transactions of the Royal Society of London*, *151*, 1–36, doi:10.1098/rstl.1861.0001.

Van Aken, H. M., A. K. Van Veldhoven, C. Veth, W. P. De Ruijter, P. J. Van Leeuwen, S. S. Drijfhout, C. P. Whittle, and M. Rouault (2003), Observations of a young Agulhas ring, Astrid, during MARE in March 2000, *Deep. Res. Part II Top. Stud. Oceanogr.*, *50*(1), 167–195, doi:10.1016/S0967-0645(02)00383-1.

van Leeuwen, P. J., W. P. M. de Ruijter, and J. R. E. Lutjeharms (2000), Natal pulses and the formation of Agulhas rings, *Journal of Geophysical Research: Oceans*, *105*(C3), 6425–6436, doi:10.1029/1999JC900196.

van Sebille, E., A. Biastoch, P. J. van Leeuwen, and W. P. M. de Ruijter (2009), A weaker Agulhas Current leads to more Agulhas leakage, *Geophysical Research Letters*, *36*(3), L03,601, doi:10.1029/2008GL036614.

Walker, N. D. (1990), Links between South African summer rainfall and temperature variability of the Agulhas and Benguela Current systems, *Journal of Geophysical Research: Oceans*, *95*(C3), 3297–3319, doi:10.1029/JC095iC03p03297.

Ward, M. L., and A. M. Hogg (2011), Establishment of momentum balance by form stress in a wind-driven channel, *Ocean Modelling*, *40*(2), 133–146, doi:10.1016/j.ocemod.2011.08.004.

Waugh, D. W., and L. M. Polvani (2010), Stratospheric Polar Vortices, in *The Stratosphere: Dynamics, Transport, and Chemistry*, edited by L. Polvani, A. Sobel, and D. Waugh, pp. 43–57, American Geophysical Union, doi:10.1002/9781118666630.ch3.

Waugh, D. W., and W. J. Randel (1999), Climatology of Arctic and Antarctic Polar Vortices Using Elliptical Diagnostics, *Journal of the Atmospheric Sciences*, *56*(11), 1594 – 1613, doi:10.1175/1520-0469(1999)056<1594:COAAAP>2.0.CO;2.

Waugh, D. W., W. J. Randel, S. Pawson, P. A. Newman, and E. R. Nash (1999), Persistence of the lower stratospheric polar vortices, *Journal of Geophysical Research: Atmospheres*, *104*(D22), 27,191–27,201, doi:10.1029/1999JD900795.

Waugh, D. W., L. Oman, S. R. Kawa, R. S. Stolarski, S. Pawson, A. R. Douglass, P. A. Newman, and J. E. Nielsen (2009a), Impacts of climate change on stratospheric ozone recovery, *Geophysical Research Letters*, *36*(3), L03,805, doi:https://doi.org/10.1029/2008GL036223.

Waugh, D. W., L. Oman, P. A. Newman, R. S. Stolarski, S. Pawson, J. E. Nielsen, and J. Perlwitz (2009b), Effect of zonal asymmetries in stratospheric ozone on simulated Southern Hemisphere climate trends, *Geophysical Research Letters*, *36*(18), doi:10.1029/2009GL040419.

Waugh, D. W., A. H. Sobel, and L. M. Polvani (2017), What Is the Polar Vortex and How Does It Influence Weather?, *Bulletin of the American Meteorological Society*, *98*(1), 37 – 44, doi:10.1175/BAMS-D-15-00212.1.

Weijer, W., and E. van Sebille (2014), Impact of Agulhas Leakage on the Atlantic Overturning Circulation in the CCSM4, *Journal of Climate*, *27*(1), 101 – 110, doi:10.1175/JCLI-D-12-00714.1.

Weijer, W., W. P. De Ruijter, A. Sterl, and S. S. Drijfhout (2002), Response of the Atlantic overturning circulation to South Atlantic sources of buoyancy, *Global and Planetary Change*, *34*(3), 293–311, doi:10.1016/S0921-8181(02)00121-2.

Weijer, W., V. Zharkov, D. Nof, H. A. Dijkstra, W. P. M. de Ruijter, A. T. van Scheltinga, and F. Wubs (2013), Agulhas ring formation as a barotropic instability of the retroflection, *Geophysical Research Letters*, *40*(20), 5435–5438, doi:https://doi.org/10.1002/2013GL057751.

Whitworth, T. (1983), Monitoring the Transport of the Antarctic Circumpolar Current at Drake Passage, *Journal of Physical Oceanography*, *13*(11), 2045 – 2057, doi:10.1175/1520-0485(1983)013<2045:MTTOTA>2.0.CO;2.

Whitworth, T., and R. G. Peterson (1985), Volume Transport of the Antarctic Circumpolar Current from Bottom Pressure Measurements, *Journal of Physical Oceanography*, *15*(6), 810 – 816, doi:10.1175/1520-0485(1985)015<0810:VTOTAC>2.0.CO;2.

World Meteorological Organization (2014), *Scientific Assessment of Ozone Depletion: 2014, Global Ozone Research and Monitoring Project–Report No. 55*, 416 pp., WMO, UNEP, Geneva, Switzerland.

World Meteorological Organization (2018), *Scientific Assessment of Ozone Depletion: 2018, Global Ozone Research and Monitoring Project–Report No. 58*, 588 pp., WMO, UNEP, Geneva, Switzerland.

Acknowledgements

First and foremost I would like to express my sincere gratitude to Prof. Dr. Katja Matthes, for her continuous guidance and fantastic supervision. Thank you for giving me the opportunity to work on this exciting topic allowing me to continue to pursue my passion for both Atmospheric Physics and Physical Oceanography. Your extraordinary support and constant encouragement empowered me to become the scientist I am today. You have been not only a supervisor, but also you will always be a role model for me.

I am extremely grateful to Prof. Dr. Arne Biastoch for his input regarding the ocean circulation, for his advice and for sharing his excellent knowledge about the Agulhas Current System.

I thank PD Dr. Joke Lübbecke and Dr. Susann Tegtmeier for their constructive feedback and advice during the advisory committee meetings in the framework of the Integrated School of Ocean Sciences (ISOS).

I express thanks to Dr. Thando Ndarana for introducing the importance of ridging highs and helping with their identification and for numerous constructive discussions.

I greatly appreciate the support throughout my doctorate of my colleagues in the Maritime Meteorology and Ocean Dynamics departments at Geomar. I thank Dr. Sebastian Wahl for the great technical support and for answering all my questions about the climate model FOCI; Dr. Jan Harlaß for the help with the INALT10X nest; Dr. Franziska Schwarzkopf for her support in the CASISAC project, especially with writing the reports in German; Dr. Sabine Haase for sharing her expertise on ozone - dynamics interactions and for her feedback on this thesis; Dr. Robin Pilch Kedzierski and Dr. Wenjuan Huo for fruitful discussions about the stratosphere; Silke Gesinn for her help in organizing all the trips I took during my doctorate;

Funding from the Bundesministerium für Bildung und Forschung (BMBF) through the SPACES-II CASISAC project is gratefully acknowledged.

Completing my doctorate would never have been possible without the unwavering support of my family and close friends. To my parents, Cristina Ionescu and Grabriel Ivanciu, thank you for believing in me and for making my studies possible. To my partner, Dr. Moritz Behrend, thank you for helping me stay in balance and for always keeping life outside work

exciting. And to my dear friends, Lena Ebsen, Megan Metcalfe and Hajar Al Balushi for sharing your thoughts on this thesis and for always being there for me.

Declaration

I hereby declare that the content and design of this thesis is my own work apart from the guidance and acknowledged assistance of my supervisors, Prof. Dr. Katja Matthes and Prof. Dr. Arne Biastoch. This thesis has not been submitted either partially or wholly as part of a doctoral degree to another examining body. This is a cumulative thesis. Chapter 3 has been published in the journal Atmospheric Chemistry and Physics, Chapter 4 has been published in the journal Weather and Climate Dynamics and Chapter 5 has been submitted for publication in Geophysical Research Letters. This thesis has been prepared in accordance with the Rules of Good Scientific Practice of the German Research Foundation. An academic degree has never been withdrawn from me.

Ioana Ivanciu
Kiel, 16 September 2022